TESIS DE LA UNIVERSIDAD DE ZARAGOZA
2016
108

Lidia Vlassova

Land Surface Temperature (LST) estimated from Landsat images: applications in burnt areas and tree-grass woodlands (dehesas)

Departamento
Geografía y Ordenación del Territorio

Director/es
Pérez Cabello, Fernando

ISSN 2254-7606

Prensas de la Universidad
Universidad Zaragoza

ISSN 2254-7606

Universidad Zaragoza
1542

Tesis Doctoral

LAND SURFACE TEMPERATURE (LST) ESTIMATED FROM LANDSAT IMAGES: APPLICATIONS IN BURNT AREAS AND TREE-GRASS WOODLANDS (DEHESAS)

Autor

Lidia Vlassova

Director/es

Pérez Cabello, Fernando

UNIVERSIDAD DE ZARAGOZA

Geografía y Ordenación del Territorio

2016

Universidad Zaragoza
1542

Tesis Doctoral

LAND SURFACE TEMPERATURE (LST) ESTIMATED FROM LANDSAT IMAGES: APPLICATIONS IN BURNT AREAS AND TREE-GRASS WOODLANDS (DEHESAS)

Autora

Lidia Vlassova

Director

Dr. Fernando Pérez Cabello

UNIVERSIDAD DE ZARAGOZA

Departamento de Geografía y Ordenación del Territorio

2015

La autora de esta tesis es becaria del Programa ACADEMIA-2010 del SENESCYT, Ecuador. Para la realización de esta tesis contó, además, con el apoyo financiero de la Universidad Técnica Estatal de Quevedo, Ecuador; el acuerdo de colaboración entre el Gobierno de Aragón y la Obra Social "La Caixa" (DGA-La Caixa, GA-LC-042/2011); el Ministerio de Ciencia e Innovación y el Ministerio de Economía y Competitividad en el marco de los proyectos BIOSPEC (CGL2008-02301/CLI) y FLUXPEC (CGL2012-34383).

Agradecimientos

Quiero agradecer a todas las personas que me ayudaron a empezar y llegar a culminar mi Doctorado que fueron tantos que no podría nombrarlas todas.

En primer lugar agradezco a mi director de tesis, Fernando Pérez Cabello por su confianza, paciencia y constante apoyo durante todo el tiempo que duró el trabajo, por las ideas que ha compartido conmigo y el tiempo que ha dedicado/sacrificado para que el trabajo siga adelante.

Agradezco también a Juan de Riva, el Director del Grupo de Investigación GEOFOREST-IUCA porque a pesar de su gran carga de trabajo nunca se negó a escuchar las inquietudes relacionadas con la investigación y la vida diaria, y por su capacidad de encontrar solución a (casi) cualquier problema de logística.

A Angel Pueyo, Director del Departamento de Geografía y Ordenación del Territorio cuando inicié el Doctorado y a Maite Echeverría, la Directora del Departamento actual por su ayuda en tantas gestiones administrativas que tiene que solventar un becario extranjero.

A los participantes de proyectos BIOSPEC y FLUXPEC y especialmente a Pilar Martin que me permitió colaborar con los proyectos y fue muy generosa al compartir los datos, conocimientos e ideas; a Hector Nieto y David Riaño, mis coautores en la primera publicación, por revisar y hacer sugerencias sobre el artículo.

A todos los becarios del Departamento y del Laboratorio de Espectro-radiometría y Teledetección Ambiental por el agradable ambiente de trabajo.

Este trabajo está dedicado a mi familia

Making use of the possibility offered by the University of Zaragoza, this thesis is presented as compendium of scientific articles, being the Ph.D. student **Lidia Vlassova** the author responsible for all of them:

1. Vlassova, L.; Perez-Cabello, F.; Nieto, H.; Martin, P.; Riaño, D.; de la Riva, J. (2014). Assessment of methods for land surface temperature retrieval from Landsat-5 TM images applicable to MultiscaleTree-Grass Ecosystem Modeling. Remote Sensing6, 4345-4368, DOI: 10.3390/rs6054345.

   Status: published

   JCR Impact factor: 3.18 (Q1, "Remote sensing")

2. Vlassova, L.; Perez-Cabello, F.; Rodrigues Mimbrero, M.; Montorio Lloveria, R.; García-Martin, A. (2014). Analysis of the relationship between land surface temperatureand wildfire severity in a series of Landsat images. Remote Sensing 6, 6136-6162, DOI: 10.3390/rs6076136.

   Status: published

   JCR Impact factor: 3.18 (Q1, "Remote sensing")

3. Vlassova, L.; Perez-Cabello, F. (2016). Effects of post-fire wood management strategies on vegetation recovery and land surface temperature (LST) estimated from Landsat images. International Journal of Applied Earth Observation and Geoinformation 44, 171-183, DOI: 10.1016/j.jag.2015.08.011.

   Status: accepted (published on-line)

   JCR Impact factor: 3.47 (Q1, "Remote sensing")

4. Vlassova, L.; Rosero Tufiño, P.; Montorio Llovería, R. (2016). Variabilidad espacio-temporal de la temperatura de superficie en ecosistema de dehesa estimada mediante imágenes Landsat TM: el papel del arbolado. Geographicalia 68.ISSN: 0210-8380; EISSN: 2386-3021.

   Status: accepted

   JCR Impact factor: NA

Haciendo uso de la posibilidad que ofrece la Universidad de Zaragoza, esta tesis doctoral se presenta como un compendio de artículos científicos, siendo la estudiante de doctorado**Lidia Vlassova**la autora principal de todos ellos:

1. Vlassova, L.; Perez-Cabello, F.; Nieto, H.; Martin, P.; Riaño, D.; de la Riva, J. (2014). Assessment of methods for land surface temperature retrieval from Landsat-5 TM images applicable to MultiscaleTree-Grass Ecosystem Modeling. Remote Sensing6, 4345-4368, DOI:10.3390/rs6054345.

   Status: publicado

   JCR Factor de impacto (2014): 3.18 (Q1, "Remote sensing")

2. Vlassova, L.; Perez-Cabello, F.; Rodrigues Mimbrero, M.; Montorio Lloveria, R.; García-Martin, A. (2014). Analysis of the relationship between land surface temperatureand wildfire severity in a series of Landsat images. Remote Sensing 6, 6136-6162, DOI:10.3390/rs6076136.

   Status: publicado

   JCR Factor de impacto (2014): 3.18 (Q1, "Remote sensing")

3. Vlassova, L.; Perez-Cabello, F. (2016). Effects of post-fire wood management strategies on vegetation recovery and land surface temperature (LST) estimated from Landsat images. International Journal of Applied Earth Observation and Geoinformation 44, 171-183, DOI: 10.1016/j.jag.2015.08.011.

   Status: aceptado (publicado en web)

   JCR Factor de impacto (2014): 3.47 (Q1, "Remote sensing")

4. Vlassova, L.; Rosero Tufiño, P.; Montorio Llovería, R. (2016). Variabilidad espacio-temporal de la temperatura de superficie en ecosistema de dehesa estimada mediante imágenes Landsat TM: el papel del arbolado. Geographicalia 68.ISSN: 0210-8380; EISSN: 2386-3021.

   Status: aceptado

   JCR Impact factor: NA

Resumen

A lo largo de los últimos 40 años, las diferentes misiones del proyecto Landsat han proporcionado una gran cantidad de información espectral sobre la superficie terrestre. Las imágenes obtenidas por estos satélites se caracterizan por una resolución espacial de tipo medio, bandas espectrales situadas en diferentes regiones del espectro electromagnético (ópticas y térmicas) y una amplia cobertura terrestre.

Si bien las bandas del óptico han sido utilizadas con éxito en numerosas aplicaciones, el uso del térmico ha sido mucho más limitado, a pesar de la gran importancia que representa el parámetro de la temperatura de superficie para numerosas aplicaciones ambientales, especialmente para aquellas relacionadas con la modelización de los flujos de energía en el sistema suelo-vegetación-atmósfera y con el cambio global.

En este contexto, el objetivo principal de la presente investigación es explorar el potencial de la temperatura de superficie terrestre (siglas en inglés - LST), derivada de imágenes Landsat, en el estudio de ecosistemas heterogéneos, concretamente (i) áreas afectadas por los incendios forestales y (ii) ecosistemas de dehesa,formaciones constituidas por los árboles dispersos y pastizal/cultivos.

En primer lugar, en el marco del proyecto BIOSPEC "*Linking spectral information at different spatial scales with biophysical parameters of Mediterranean vegetation in the context of Global Change*" (http://www.lineas.cchs.csic.es/biospec) se comparan las diferentes metodologías disponibles para la estimación de la LST a partir de la banda térmica de Landsat. Los mejores resultados, en condiciones atmosféricas caracterizadas por niveles medios de contenido de vapor, se obtuvieron usando el método mono-banda (en inglés - *SingleChannel*) (Jiménez-Muñoz *et al.*, 2003), con un error de estimación menor de 1 K.

En el siguiente paso de la investigación la información sobre la distribución de LST derivada del sensor *Thematic Mapper* se utilizó en el análisis de la severidad del fuego en una zona forestal de Las Hurdes(Extremadura, España), y en el estudio de los efectos ocasionados por los diferentes tratamientos post-incendio en una zona quemada, esta vez localizada en los Montes de Zuera (Zaragoza, España).

En relación con la severidad del fuego analizada en diferentes fechas post-incendio, se han detectado diferencias estadísticamente significativas entre los valores de LST correspondientes a las categorías de severidad establecidas a partir del índice espectral ΔNBR (Key y Benson, 2006).Los niveles de LST más elevados se observaron en las zonas donde la severidad del fuego fue mayor, debido a la menor emisividad de los productos de combustión y los cambios en el balance de energía relacionados con la ausencia de vegetación.

En cuanto a las consecuencias de los tratamientos de madera quemada en la regeneración vegetal, se han observado diferencias estadísticamente significativas entre las áreas intervenidas y no intervenidas. En este sentido, en las áreas no intervenidas se registraron valores de LST ~1 K más bajos y niveles de recubrimiento vegetal ~10% más altos que en las intervenidas.

En otro ámbito de aplicación, los datos de LST obtenidos mediante imágenes de Landsat-5 TM (período 2009-2011), se utilizaron en el análisis de los patrones espacio-temporales de la LST y su relación con el grado de ocupación de la fracción arbórea en ecosistemas de *dehesa*. Se ha detectado una relación negativa entre la LST y la cobertura arbórea, con diferencias a nivel estacional debido al dinamismo del ciclo fenológico del pastizal.

Los resultados de la investigación permiten afirmar que la LST puede ser obtenida mediante las imágenes Landsat con el error alrededor de 1 K, aceptable para modelización de procesos en los ecosistemas mediterráneos heterogéneos.

Abstract

Landsat missions have been providing spectral data for research of land surface processes for more than 40 years. Landsatprovides global coverage with multispectral images, which include optical and thermal bands at the medium spatial resolution.

While optical bands have been successfully used in a wide range of applications, the use of thermal data has been much more limited, in spite of a great importance of land surface temperature (LST) for environmental applications, especially those related to modeling energy fluxes in soil-vegetation-atmosphere systems and terrestrial global change research.

In this context, the main goal of this research is to explore the potential of Landsat-derived LST in heterogeneous ecosystems of (i) the areas affected by wildfire burns and (ii) tree-grass woodlands (Spanish *dehesas*).

First, different methods currently used for LST estimation from Landsat thermal bandare compared in the frame of BIOSPEC *"Linking spectral information at different spatial scales with biophysical parameters of Mediterranean vegetation in the context of global change"* project (http://www.lineas.cchs.csic.es/biospec). The best results with an error below 1 K were obtainedusing Single Channel method (Jiménez-Muñoz et al., 2003) in atmospheric condition characterized by low/moderate levels of atmospheric water content.

Next, data on LST distribution derived from the *Thematic Mapper* sensorwere used in assessment ofburn severity in the Las Hurdes forest burn (Extremadura, Spain) and in analysis of effects of different post-fire treatments in the Montes de Zuera burn (Zaragoza, España).

In respect of burn severity analyzed at different moments after the fire, statistically significant differences in LST have been detected between burn severity categories established based on ΔNBR spectral index (Key y Benson, 2006).Higher LST levels were observed in zones of greater fire severity, due to the lower emissivity of combustion products and changes in the energy balance related to vegetation removal.

In regard to the consequences of post-fire wood treatment on vegetation recovery,statistically significant differences wereobserved between the intervened and not intervened areas two years.Thus, LST registered in the not intervened areas were on average 1 °C lower and vegetation cover was 10% higher than in the intervened zones.

Besides, LST data retrieved fromLandsat 5 TM images acquired between 2009 and 2011 were used in analysis of relation between spatio-temporal patterns of LST and the tree cover in ecosystems of *dehesa*. Negative relation has been detected between LST values and the levels of tree cover linked to the seasonal dynamicsof pasture fenology.

Based on the results it is possible to affirm that LST can be retrieved from Landsat images with an error closet to 1 K, which is acceptable for modeling surface processes in heterogeneous ecosystems of Mediterranean.

TABLE OF CONTENTS

1. Background, objectives and structure

Land surface temperature (LST) plays a crucial role in land surface processes and is included in the list of high-priority parameters of the International Geosphere and Biosphere Program (IGBP) (Townshend et al., 1994). The link between LST and surface environmental variables is the surface energy balance equation.

LST is related to the transport of heat between the land surface and the atmospheric boundary layer (Kustas and Anderson, 2009), and makes possible estimation of sensible heat flux (Jia et al., 2001) and latent heat flux, or evapotranspiration (Anderson et al., 2012). Energy absorption and emission by atmospheric water vapor, clouds and greenhouse gases affect radiative balance. The increased concentrations of some of these gases, such as CO_2, contribute to the climate change. Continuous LST monitoring on a global scale is necessary for characterization of such changes in climate and explains an increased interest in operational LST estimation.

LST provides information about variations of the surface equilibrium state and is vital for many applications (Kerr et al., 2004). Thus, LST is a key input to models in hydrology (Ambast et al., 2008; Liang, 2004), climate (Wild, 2005), weather forecast (Van Den Hurk et al, 2002) and ecology (Gamon et al., 2004) at multiple scales. LST influences all the stages of plant development and is an indicator of vegetation health (Moran, 2004; Zarco-Tejada et al., 2003), due to a close relation between the canopy temperature and hydric stress which causes plant stomata closure. Being an indicator of vegetation water content, LST is one of the variables used for fire danger evaluation in forest environments (Chuvieco et al., 2004; García et al., 2008): areas having lower water content present greater probability of fire ignition and propagation. LST can also serve as a proxy of air temperature, assuming that the temperature of a full cover canopy approaches the temperature of the air within the canopy (Prihodko and Goward, 1997; Nieto et al., 2011).

Local modeling relies heavily on field data, while at the regional and global scales remote sensing has become the main source for LST data retrieval. The history of temperature measurements from remote platforms began in the late 50s (King, 1956) and the first remote measurements of LST were performed by Television and Infrared Observation Satellite in 1960s (TIROS) (Bandeen et al., 1961). However, regular acquisition and distribution of LST data has been established at the beginning of the 1980s (Price, 1984).

Last decades have seen a considerable increase in the use of remote sensing for estimation of land surface biophysical properties (Houbourg et al., 2011; Kalma et al., 2008). Satellite-

derived LST is among the products most required for operational monitoring of land surface systems (Townshend and Justice, 2002).Because LST is highly variable in space and time, ground measurements cannot adequately characterize its temporal and spatial distribution. Moreover, remote sensing overcomes the limitations imposed by sparse networks of meteorological and ground-based monitoring stations, particularly in areas having harsh climates (Westermann, 2011) or difficult access (Neteler, 2010). One more advantage of remote sensing is the possibility of obtaining homogeneous and continuous data over big areas at spatial and temporal resolution suitable for various application types. It also provides a framework for coupled modeling approaches to energy, carbon and water exchange studies (French et al., 2000), and has a potential for data integration through upscaling and downscaling (Gamon et al., 2004).

The current state-of-the-art of surface temperature retrieval allows quantification of the atmospheric and surface effects fairly well. However, the approach has achieved a routine performance only for the sea surface temperature (SST) estimation (McMillin, 1975). At present, the reported accuracy of SST retrieved from MODIS data made available by a fully operational schemeis about 0.26ºC. However, estimation of LST resulted more complicated. It is generally accepted that to be useful for studying surface systems and processes at regional and local scale, LST should be retrieved with accuracy of 1 K or better. It is quite a challenge because compared to the oceans where most of the surface is covered with water, land cover types present different structure, composition and dynamics posing additional challenges to LST estimation.

Main difficulties for LST can be summarized in the following way: (i) surface-emitted radiance is altered by atmosphere before reaching TOA sensors; (ii) a direct separation of temperature from surface radiance is not possible because of the problem indetermination: for a sensor with N spectral channels, there are N measurements but N+1 unknowns (i.e. N spectral emissivities and the surface temperature). Therefore, the corresponding system of equations has no unique solution. The combined effect of atmospheric perturbations and varying emissivity increases the difficulty. For resolving this ill-posed problem, additional assumptions are necessary to constrain the extra degree-of-freedom. (iii) LST validation is also a challenge: while LST derived from remote sensing images is representative for the whole pixel, it is not true for the point temperature measurements which can vary over short distances (Prata et al., 1995). It is not unusual for LST to vary by more than 10 K over just a few centimeters of distance or by more than 1 K in less than a minute over certain cover

types. Hence, a field validation is possible only for homogeneous areas, such as dense vegetation or desert, for other areas validation is performed using simulated data or accuracies are inferred from results of field validation over homogeneous areas, such as lakes, deserts, and densely vegetated (Coll et al., 2009; Hook et al., 2004).

Over last decades techniques for measuring surface temperature from remote sensing data have improved in terms of method, instrumentation and computation efficiency. Satellites providing global data from the thermal region of the spectrum at different scales include MODIS (Wan et al., 2004) and Spinning Enhanced Visible and Infrared Imager (SEVIRI) (DaCamara, 2006). These satellites,for which LST products are available on a regular basis, are characterized by low spatial and high temporal resolutions. At the medium spatial scale Landsat has provided global brightness temperatures since 1984, with Landsat 8 launched at the beginning of 2013 giving continuity to the data record (Roy et al., 2014). Landsat can provide LST at a spatial detail much higher than MODIS, but only once in 16 days compared to daily image acquisition by MODIS. Thus, integration of the data from these two satellites would be highly beneficial given the spatial resolution of the former and the temporal resolution of the latter. However there are still challenges and persisting uncertainties related to the use of Landsat for LST estimation, especially in heterogeneous environments (Cleugh et al., 2007).

In this context the research goal of this thesis is to explore the applicability of Landsat-derived land surface temperature in the study of heterogeneous Mediterranean ecosystems resulting from wildfire and traditional agrosilvopastoril management (dehesa).The main objective was approached through the work on four specific objectives:

(1) Compare single band algorithms for LST estimation from satellite images in Mediterranean ecosystems with partial tree cover (dehesa);

(2) Analyze spatio-temporal patterns of Landsat LST in Mediterranean forests affected by wildfires and its relationship with burn severity;

(3) Study the effects of different post-fire wood treatments on vegetation recovery (through NDVI) and LST;

(4) Analyze spatio-temporal patterns of Landsat LST in Mediterranean tree-grass ecosystem (dehesa) and their relationship with vegetation fenology.

The thesis contains eleven chapters. Chapter 1 presents the scientific context of research and its objectives. Chapter 2 reviews the basic theory andmethods used for LST estimation from remote sensing data. Chapter 3 describes study area, while Chapter 4 gives details on data and materials used in the study. Chapters 5 presents the methods applied to achieve research objectives. Chapters from 6 to 9 constitute the body of the research in form of the original versions of the published articles. Finally, Chapters 10 and 11 summarize the most relevant results and future research in English and Spanish, respectively. The Thesis also includes the sections of References for Chapters 1-5 and Appendices, which include information on contribution of the PhD student to the published papers and documents certifying that the four presented articles are authorized for the exclusive use in this thesis.

2. LST estimation from remotely-sensed data

2.1. Basic theory

Temperature is the measure of internal energy (kinetic heat) of the object expressed in units or degrees at a standard scale. This temperature also referred to as thermodynamic temperature can be measured with thermometers. Objects with temperature above absolute zero emit electromagnetic energy converted from internal kinetic heat. Blackbody, which is an ideal energy absorber, is also an ideal emitter (Howell et al., 2010). The relationship between surface temperature and the spectral radiance emitted by the blackbody is described by Planck's law.

The blackbody temperature is known as brightness temperature. Because natural objects are not perfect emitters and do not behave as blackbodies, it is necessary to take into account their emissivity (Li et al., 2013b), which is defined as the ratio between the target's emitting capacity and that of a blackbody at the same temperature. Brightness temperature corrected for emissivity is known as radiometric temperature.

Radiance emitted by the surface can be registered by remote sensing and is used to estimate LST. Earth emits radiance in thermal infrared region of the electromagnetic spectrum at the wavelengths between 3μm and 14 μm (Tang and Li, 2014). At an average temperature of about 300 K Earth's peak of electromagnetic emittance is located in the thermal infrared(TIR) domain at about 9.7 μm. It is possible to use remote sensing devices to detect infrared energy in these regions because the atmosphere allows a portion of the infrared energy to be transmitted from the terrain to the detectors. To avoid water vapor (H_2O), carbon dioxide (CO_2), and ozone (O_3) absorption bands satellites usually record thermal infrared data in the region from 10.5μm to 12.5 μm (Jensen, 2009).

Sensors on remote platforms register solar radiation reflected and emitted by the Earth surface, as well as radiation scattered and emitted by the atmosphere. The proportion of radiation affected by each of these processes in the signal registered by the sensor depends of the spectral region: reflection dominates in the optical region of the spectrum with wavelengths in the range of 0.4 – 3.0 μm, while Earth-emitted energy dominates in the TIR range (3.0 – 14.0 μm). Because emitted radiation is related to the object temperature (Stefan-Boltzman law) LST can be estimated from the remotely-sensed thermal signal using radiation transfer equation.

LST estimated from remote sensors is the `surface radiometric temperature´ (Li et al., 2013a). When a surface is homogeneous and isothermal, its radiometric temperature is equal

to thermodynamic temperature. Otherwise, those temperatures are different, and surface temperature estimated from remote sensors is not equivalent to the temperature measured by a thermometer. Moreover, ground-based radiometric point measurements cannot provide LST estimates on a pixel scale. Even in high-resolution remote sensing images a pixel can include various surface types with different temperatures and emissivities, which presents additional challenge for interpretation of the retrieved LST.

2.2. Radiative Transfer Equation

Earlier explanation makes it clear that LST cannot be directly measured with remote sensors and is derived from the surface-emitted thermal radiance. The greatest difficulty of the process consists in estimation and correction of signal distortion due mainly to the energy absorption by atmospheric water vapor (Song et al., 2001) and the need to take into account differences in thermal emitting capacity of earth landcovers (Valor and Caselles, 1996). The required corrections can be realized using algorithms based on Radiative Transfer Equation (RTE) applied to the thermal infrared region of the electromagnetic spectrum:

$$L_{sensor} = \tau\varepsilon B(T_s) + L_u + \tau(1-\varepsilon)L_d \quad (1)$$

where L_{sensor} is at-sensor radiance, B – Planck law, $T_s$is the land surface temperature (LST), L_u and $L_d$are upwelling and downwelling atmospheric radiances, respectively, τ is atmospheric transmittance and ε is land surface transmissivity.

When $B(T_S)$ is known, the land surface temperature can be calculated by inversion of Planck's law:

$$T_S = \frac{c_2}{\lambda ln\left(\frac{c_1}{\lambda^5 L_T}+1\right)} \quad (2)$$

where T_s is the land surface temperature (LST) in K, c_1 (1.19104×10^8 W μm ^{4} m^{-2} sr^{-1}) and c_2 (1.43877×10^4 μm K) are calibration constants, and λ=11.457 μm is an effective wavelength for the Landsat-5 TM thermal band (Jiménez-Muñoz and Sobrino, 2003).

2.3. Methods for LST estimation from multispectral images

Since thermal satellite data became available researchers have tested various approaches for LST estimation. Recent review of existing algorithms presented in Tang and Li (2014) updates and complements earlier surveys (Dash et al., 2002; Li et al., 2013a; Prata et al.,

1995). Currently used algorithms can be roughly grouped in single channel, multi-channel and multi-angle algorithms, all requiring an *a priori* knowledge of surface emissivity. There are also methods using techniques different to those already mentioned (e.g. Becker and Li, 1990; Sun and Pinker, 2003). In each particular case the choice of the method depends on the availability and characteristics of images and ancillary data and the required quality of the results.

2.3.1. Single-channel methods

There are several methods successfully used for LST estimation from a single band. Among the commonly used procedures are a direct inversion of the Radiative Transfer Equation (RTE), mono-window method (Qin et al, 2001) and a single-channel algorithm (Jiménez-Muñoz and Sobrino, 2003).

LST can be obtained through a direct inversion of RTE using Planck's law. In this case it is necessary to know parameters characterizing atmospheric conditions at the moment of satellite overpass, which can be calculated from atmospheric profiles and radiative transfer codes (models). It is possible to obtain this information through the on-line web tool developed and implemented by Barsi et al. (2003).

Other two methods often used for LST retrieval from the unique thermal band are ETR approximations which avoid dependence on actual atmospheric profiles. Mono-window method (Qin et al, 2001) incorporates calculation of two empirical coefficients based on the atmospheric water content and near-surface air temperature, while single-channel method (Jiménez-Muñoz and Sobrino, 2003) requires only knowledge of atmospheric water content to compute three atmospheric functions. Both algorithms are capable of obtaining LST with errors close to 1 K for clear-sky images when water vapor content in the atmosphere is in the range of 0.4 g/cm^2 and 2.5 g/cm^2.

2.3.2. Multi-channel methods

Multi-channel method also known as split-window algorithm uses radiances in two thermal bands with different atmospheric absorption to estimate the effect of atmosphere on the signal. The technique was first proposed by Anding and Kauth (1970);it was applied for estimating surface temperatureof sea/ocean (e.g., Njoku, 1985) and land (e.g., Sobrino et al., 2006). The method is based on the fact that atmospheric attenuation of the signal is proportional to the difference of the radiances simultaneously measured in two thermal channels. Algorithm adapted for LST estimation by Sobrino et al. (1991) along with

atmospheric attenuation due to water vapor absorption, also estimates the effect of much greater heterogeneity of land surface emissivity on LST. The errors reported by researchers who applied split-window method for LST estimation from several multi- and hyperspectral sensors is ~1 K (Li et al., 2013a; Sobrino et al., 2006).

2.3.3. Multi-angle methods

Multi-angle algorithm is based on the same principle as the split-window method, but the differences in absorption are due to the differences in signal path on its way to the sensor registered in the images taken at different angles (Chedin et al., 1982). Assuming that emissivity does not vary if the difference in the viewing angles is less than 60º, Prata (1993) has developed dual-angle method for ATSR. Sobrino et al. (1996) improved the method through incorporation of spectral and angular variations of land surface emissivity. However, besides the assumption that atmospheric profiles maintain spatial uniformity, the algorithm requires that the radiances registered at the two angles have significantly different paths, otherwise the algorithm becomes unstable (Prata, 1993). Moreover, one more condition is the knowledge of the anisotropy of the radiance due to the surface structure, which is very difficult to satisfy.

2.4. Emissivity estimation

LST estimation requires precise knowledge of land surface emissivity (LSE), which is an intrinsic characteristic of material composition. Because land surface is heterogeneous its emissivity range is greater than that of the oceans; it varies with landcover type, surface moisture, roughness, and viewing angle (Salisbury and D'Aria, 1992; Sobrino et al., 2008). Surface emissivity is a critical variable for separation of surface influence and that of the atmosphere in LST retrieval. Recent review by Li et al. (2013b) and Tang and Li (2014) present a detailed explanation of proposed methods for emissivity estimation grouped in multi-channel, physically-based and semi-empirical methods. For example, the temperature-emissivity separation method (TES) (Gillespie et al., 1998) requires at least 4-5 infrared (IR) channels within 10-12 nanometers. It uses an empirical relationship to predict the minimum emissivity from the spectral contrast of the ratioed values and recover the emissivity spectrum. Another attractive solution is to use one of the physical methods based on spectral indices almost independent on LST, such as a method of temperature independent thermal infrared spectral indices (TISI) (Becker and Li, 1990). It is obvious that neither TES, nor TISI can be employed to estimate LST from sensors with one thermal band.

On the contrary, semi-empirical methods based on either land-cover information (Peres and DaCamara, 2004; Snyder et al., 1998) or NDVI do not have this limitation. Classification-based methods work well with high-resolution imagery when each of the pixels can be unambiguously assigned one of the established classes. However, the performance is hampered when dealing with images of medium or coarse spatial resolution because most of the pixels present a mixture of different landcover classes with contrasting emissivity levels (Snyder et al., 1998). Methods for emissivity estimation based on NDVI use direct links between emissivity and NDVI (Van de Griend and Owe, 1993), or exploit the relationship between surface emissivity, the amount and structure of vegetation, and surface roughness (Sobrino and Raissouni, 2000; Valor and Caselles, 1996). The empirical expression suggested by Van de Griend and Owe (1993) is often used (e.g. Liu and Zhang, 2011) because of simplicity. On the other hand, the equation of Valor and Caselles (1996) is more general and supported by a theoretical model validated under differing environmental conditions. Valor and Caselles (1996) showed that emissivity depends on surface structure, the components contributing to emissivity (soil and vegetation), and the viewing geometry. They also demonstrated that there is no universal relationship between emissivity and NDVI, and hence the same equation cannot be applied to areas having dissimilar characteristics. Validation experiments conducted in Mediterranean areas have confirmed the applicability of the model to heterogeneous, fully vegetated or bare soil areas, as well as for areas where more than one vegetation type or more than one soil type are present (Sobrino et al., 2008).

2.5. Atmospheric correction of optical bands

When emissivity estimation is basedon NDVI, it becomes necessary to perform atmospheric correction of optical bands involved in the index calculation, i.e. red and near-infrared. Because the effect of the atmospheric scattering and absorption on the signal depends on the wavelength, methods of atmospheric corrections of the radiances in the optical region are different from those applied for correction of the thermal spectral region.

Atmospheric correction methods can be relative and absolute (Thome et al., 1997). Relative atmospheric correction methods avoid estimation of atmospheric parameters. In this case reflectivity is compared with that of the reference pixels in the image. For example, Empirical Line Correction requires selection in the scene and spectral characterization of two pixels with contrasting radiances used as calibration standards, i.e. it assumes previous familiarity with each of the selected locations. Empirical correction compares image radiance values with those of the spectral standards calculating correction coefficients for each band,

which are later applied to all the pixels in the corresponding band. When no field radiometric data are available the reference spectra are obtained from the spectral libraries. This method cannot be applied when there is no previous knowledge on spectral properties of landcover types present in the image.

Dark Object Subtraction method is another method successfully applied to correct the effects of atmospheric attenuation (Chavez, 1996; Song, 2001). The method assumes that black objects do not reflect light and, therefore, radiance values they present result from atmospheric scattering. These radiance values are subtracted from the radiances of all the rest of the scene pixels. The method is relatively easy to apply and uses only image data for correction.

More sophisticatedabsolute atmospheric correction methods use radiation transfer codes (e.g. LOWTRAN, MODTRAN, 6S) for modeling optical properties of the atmosphere under conditions observed at the moment of image acquisition removing the effects of atmospheric absorption and scattering, as well as those caused by observation geometry.

2.6. LST validation

The final challenge in LST retrieval is its validation. The main difficulty is to be able to obtain ground measurements which are synchronous with image acquisition and representative of at the image scale because of great temporal and spatial LST fluctuations. Existing approaches to LST validation include temperature-based, radiance-based and cross-validation methods (Li et al., 2013a). In temperature-based method retrieved LST values are compared to those obtained by ground sensors. Measurements are taken in areas homogeneous at the pixel scale or representative of the landcover components (e.g. grass, sun-lit tree canopy, tree shadows, and bare soil).

Although comparison between satellite LST and field LST seems to be the most obvious validation method, it is almost impossible to perform because of the difficulty in locating of the suitable areas. Thus, regional and global LST is often validated using radiance-based method, in which reference LST is simulated using radiative transfer modeling (Sobrino et al., 2004). The success of this approach depends on the quality of the inputs: data on emissivity and atmospheric profiles. When data on atmospheric conditions are not available, LST quality can be assessed through cross validation, consisting in comparison of obtained LST with LST derived from other sensors. Since sensors have different spectral, spatial and temporal characteristics, and different observation geometry, these differences should be taken into account.

3. Study area

Research was conducted in two types of settings in central and northeastern Spain: (1) tree-grass woodlands known as *dehesas* and (2) areas affected by wildfires (Figure 1).

Dehesa is an integrated agroforestry ecosystem with complex vegetation structure typical foropen savannah. It occupies large areas on Iberian Peninsula with more than 30000 km^2 in Spain (Olea et al., 2005).Dehesas developed as a result of human interaction with original forests thinned to create areas for agricultural, and are included in the EU Directive 92/43 because of their high ecological and cultural value.

Figure 1. Location of the study sites.

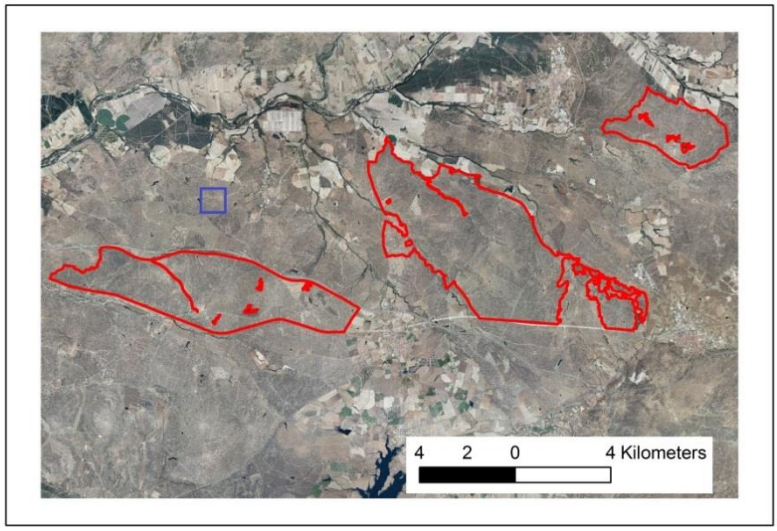

Figure 2. Orthophoto of dehesa study sites: (1) blue line indicates the site used for methods assessment of LST estimation methods, and (2) red linesshow polygons (SIOSE) used in the study of LST variability.

The work on the first specific objective dealing with comparison of methods for LST estimation from Landsat images was performed in a 1 km^2 dehesa sitenear Las Majadas del Tietar (Lat 39°56′26″N, Long 5°46′29″W)(blue-line rectangle in Figure 2).

The area located at 400 m above sea level is flat and includes FLUXNET tower operated by the Mediterranean Center for Environmental Studies (CEAM). FLUXNET is a network of micrometeorological observation stations established to perform continuous measurement of exchange fluxes in the soil–vegetation–atmosphere system (Baldocchi et al., 2001).The climate (Csa according to Köppen classification) is characterized by an annual average temperature of 16 °C. Annual precipitation of about 550 mm is unevenly distributed through the year and there is a four-month hot dry period from June to September (Nuñez and Sosa, 2001).Vegetation structure typical for dehesa consists of two main vegetation strata: grass covering 75% of the area and holm oak trees (Quercus ilex ssp. *rotundifolia*) over the 25% of the surface (Figure 3).

Figure 3. Views of the study sites: dehesa (left) and wildfire burn (right).

This site is a part of much more extensive area of dehesas in the province of Cáceres, Spain (Figures 1). Part of this area consisting of three polygons(Figure 2) with a total area of ~70 km^2 was used to develop the second specific objective dealing with the study of spatio-temporal patterns of LST. Although tree and grass layers are present in any *dehesa*, their proportion in this study area vary from 5% to more than 90%, which is not unusual for this ecosystem (Moreno and Pulido, 2009).

Spatio-temporal patterns of LST distribution were also studied in areas affected by wildfires (Figure 1). Wildfires are a major disturbance of Mediterranean forests (Pausas and Vallejo, 1999) which in Spain occupy over 1.5 million km^2. The number of fires is steadily growing. Due to the global warming and changes in socio-economic conditions big forest

fires are becoming more frequent (Pausas and Vallejo, 1999). In this context, monitoring of wildfire effects on landscapes and development of new indicators and metrics for assessment of post-fire vegetation recovery is of primary importance.

Responding to this demand, the relationship between LST and fire severity (third specific objective) was studied in the hilly area of the Las Hurdes 2009 wildfire (40°19′–40°24′N, 6°10′–6°15′W) located in the province of Cáceres, Spain, 100 km northeast of the study site used for the work on the first specific objective of this research (Figure 1). More than 3000 ha of pine forest (*Pinus pinaster*) were burned between 25 and 28 of July 2009. *Pinus pinaster*is one of the most common Spanish conifer (occupies more than 1.5 million ha) and is the species most affected by wildfires (27.96% of the burned area) (EGIF, 2008). High species resilience to the recurrent fires is explained by its adaptation strategy known as serotony (Vallejo et al., 2012). The seed production is generally related to the fire regime. Stands suffering recurrent, high-intensity fires show more serotinous cones and a large aerial seed bank compared to stands where crown fires are not frequent (Tapias et al., 2001).

Another studied burn used for the work on the fourth specific objectiveoccurred in August 2008 in the Zuera Mountains, NE Spain (41º56'- 4º58'N, 0º55'- 1º0'W). In some aspects (size – 2500 ha, generally high fire severity) it is similar to the las Hurdes fire described earlier.In this case wildfire destroyed forest dominated by *Pinus halepensis* Mill. on sandy-loam soils over Rendzic Phaeozem (Badía et al., 2014). The understory is rich in typical Mediterranean species, such as *Quercus coccifera* L., *Juniperus oxycedrus* L., *Rosmarinus officinalis* L. and *Genista Scorpius* (L.)DC. Forests are interspersed with patches of shrublands dominated by *Quercus coccifera*, *Genista scorpius* and *Brachipodium retusum*.Figure 3 shows typical vegetation cover in the study area at the moment of sampling in August of 2014. Vegetation is characterized by the presence of evergreen sclerophyllous shrublands (< 1.5 m tall), sclerophyllous pastures dominated by *Brachypodium retosum* (a rhizomatous perennial grass resprouting after fire), areas of bare soil, and *Pinus halepensis* saplings (<1 m tall) (~75 plants per hectare). Shrub species with the highest contribution to the vegetation cover are: *Quercus coccifera* (kermes oak) (~30%) –an obligate resprouter-, and *Rosmarinus officinalis* (~20%) and *Genista scorpius* (15-20%) –obligate seeders-, representative species constituting a typical garrigue plant community.

4. Materials and data

4.1. Satellite images

4.1.1. Landsat

Beginning with the first mission in 1972 Landsat satellites have been monitoring Earth environment building up regularly updated global archive. Due to their spatial (30 m for optical and 60-120 m for thermal bands), spectral (7 or more bands including 1 or 2 thermal infrared) and temporal (16 days revisiting period) resolution Landsat images are the most widely used source of remote sensing data (Miller et al., 2013). Landsat has provided global brightness temperature since the launch of Thematic Mapper (TM) instrument on board of Landsat-4 in 1982. Landsat-5 mission equipped with TM sensor acquired data for more than 27 years until the system failure in November 2011. The latest Landsat-8 mission put on orbit in February 2013 carries OLI (Optical land Imager) and TIRS (Thermal Infrared Scanner) instruments ensuring continuity of data collection. With the current calibration parameters and processing algorithms, the thermal bands of these sensors are calibrated to within 1 K (Schott et al., 2012). Landsat images are especially suitable for multitemporal studies and research of ecosystem disturbances, e.g. deforestation or wildfires. A number of indices currently used to assess the degree of damage and post-fire vegetation recovery, such as NBR (normalized burn ratio) and dNBR (differenced Normalized Burn Ratio), are tailored to the characteristics of Landsat bands (Key and Benson, 2006).

The study used 22 clear sky images from the three Landsat missions: Landsat-5 TM, Landsat-7 ETM+ (Enhanced Thematic Mapper Plus) and Landsat-8 OLI (Optical Land Imager) and TIRS (Thermal Infrared Scanner). Spectral and spatial resolution of the bands used in analysis is presented in Table 1. Two sets of images processed by the NLAPS (National Land Archive Production System–USGS) were downloaded from NASA website at http://glovis.usgs.gov/ (Table 2). The first group (path 202/row 32) covers the area of study sites in dehesa and Las Hurdes burn; the second group of images (Path 199; Row 31) corresponds to the area of the Zuera burn. Optical (red and near infrared) and thermal data were used in this research. Landsat-8 has two thermal bands, but only one of them (band 10) was used for LST estimation, because of elevated uncertainties detected in the data from another band (http://landsat.usgs.gov/calibration_notices.php).

Table 1. Specification of Landsat bands used in the study.

Satellite and sensor	**Band**	**Spectral range (micrometers)**	**Spatial resolution (m)**
Landsat-5 TM	3 (Red)	0.63 - 0.69	30
	4 (NIR)	0.76 - 0.90	30
	7 (SWIR 2)	2.064 - 2.345	30
	6 (Thermal IR)	10.40 - 12.50	120
Landsat-7 ETM+	3 (Red)	0.63 - 0.69	30
	4 (NIR)	0.76 - 0.90	30
	7 (SWIR 2)	2.064 - 2.345	30
	6 (Thermal IR)	10.40 - 12.50	60
Landsat-8 OLI	4 (Red)	0.64 - 0.67	30
	5 (NIR)	0.85 - 0.88	30
Landsat-8 TIRS	10 (Thermal IR)	10.60 - 11.19	100

Table 2. Landsat images used in the study.

Mission	Date	Aquisition time (GMT)	Sun Azimuth (degrees)	Sun Elevation (degrees)	Path/Row
Landsat 5	27-jun-09	10:50:18	123.55	63.88	202/32
	29-jul-09	10:50:49	128.98	59.94	202/32
	30-ago-09	10:51:18	141.13	52.63	202/32
	15-sep-09	10:51:32	147.28	47.91	202/32
	17-oct-09	10:51:53	156.52	37.36	202/32
	06-feb-10	10:52:39	151.39	29.19	202/32
	10-mar-10	10:52:43	146.85	40.13	202/32
	11-abr-10	10:52:40	141.79	52.28	202/32
	30-jun-10	10:52:19	124.31	64.00	202/32
	16-jul-10	10:52:19	126.06	62.26	202/32
	01-ago-10	10:52:10	130.34	59.61	202/32
	05-nov-10	10:51:34	159.16	31.4	202/32
	16-may-11	10:51:20	132.51	61.79	202/32
	01-jun-11	10:51:13	127.86	63.89	202/32
	04-ago-11	10:50:41	130.72	58.86	202/32
	05-sep-11	10:50:24	142.93	50.94	202/32
Landsat 7	27-jun-08	10:32:25	126.53	63.32	199/31
	30-ago-08	10:31:51	142.44	51.44	199/31
Landsat 8	16-mar-14	10:43:19	150.02	42.51	199/31
	03-may-14	10:42:31	142.22	59.45	199/31
	20-jun-14	10:42:32	131.21	65.36	199/31
	23-ago-14	10:42:54	143.84	55.02	199/31

4.1.2. MODIS LST

When working on the first objective, data from eleven MODIS LST images at a 1-km pixel spatial resolution corresponding to MOD11_L2 product were used for comparison with LST values obtained from Landsat images by methods tested in this study (Table 3). MOD11_L2 is obtained from application of the split window algorithm (Wan and Dozier, 1996) to MODIS bands 31 (10.780–11.280 μm) and 32 (11.770–12.270 μm). The images of the study area are acquired approximately 20 min earlier than those obtained by Landsat. To account for important difference in spatial resolution (1000 m versus 30 m for MODIS and Landsat, respectively), MODIS temperature value corresponding to a pixel centered in the study area was compared with the mean value of the Landsat-5 TM pixels as suggested in earlier studies (Li et al., 2010; Noyes et al., 2006). There are also important differences in the observation geometry between the two sensors with the MODIS viewing angle of the study area greater than 30 degrees versus Landsat images obtained at (almost) nadir. To minimize these effects only the images with the best quality MODIS pixel of the study area (MODIS product quality flag 0) were used for the comparison. According to the MOD11_L2 product description quality flag 0 is assigned to the cloud-free pixels with LST error less than 1 °C and the emissivity errors in channels 31 and 32 involved in LST estimation less than 0.01.

Table 3. Dates and observation geometry for MODIS images used in this study.

Date	Aquisition time (GMT)	Sun Azimuth (degrees)	Sun Elevation (degrees)
30-ago-09	10:51:18	141.13	52.63
15-sep-09	10:51:32	147.28	47.91
17-oct-09	10:51:53	156.52	37.36
06-feb-10	10:52:39	151.39	29.19
11-abr-10	10:52:40	141.79	52.28
30-jun-10	10:52:19	124.31	64.00
01-ago-10	10:52:10	130.34	59.61
05-nov-10	10:51:34	159.16	31.4
01-jun-11	10:51:13	127.86	63.89
04-ago-11	10:50:41	130.72	58.86
05-sep-11	10:50:24	142.93	50.94

4.2. Atmospheric parameters

Atmospheric water vapor content necessary for atmospheric correction was obtained from three online sources: Aerosol Robotic Network (AERONET) database, National Center for Environmental Prediction (NCEP) Reanalysis (hereafter called REANALYSIS) database and from MODIS MOD05 product. AERONET includes more than 500 sites distributed worldwide (Holben et al., 1998). Values of precipitable water content ($g \cdot cm^{-2}$) corresponding to the AERONET site closest to the testing study area were obtained from the AERONET website. The National Center for Environmental Prediction (NCEP) and the National Center of Atmospheric Research Reanalysis Project (NCAR) maintain freely accessible online database containing meteorological data at 2.5° × 2.5° spatial and 6 h temporal resolution extending back to 1948 (Kistler et al., 2001) developed and regularly updated by the US National Center for Environmental Prediction (NCEP) and the National Center of Atmospheric Research Reanalysis Project (NCAR) constitute another source of precipitable water values ($kg \cdot m^{-2}$) (http://www.esrl.noaa.gov/psd/data). The study used values registered at noon approximately an hour later than Landsat overpasses. Finally, values of precipitable water corresponding to MODIS (MOD05) product at 1-km spatial were downloaded from MODIS online archive. The study also used data from the Hurdes-Azabal meteorological station situated about 10 km from the Las Hurdes study site. The station is part of the Spanish Agroclimatic Information System for Irrigation (SIAR) (http://www.magrama.gob.es/es/agua/).

Atmospheric profiles containing information on vertical distribution of pressure, geopotential height, temperature and relative humidity served as inputs for radiative code simulation of the reference LSTs. They were generated by online Atmospheric Correction parameters Calculator (ACPC) tool based on the interpolation of the NCEP profiles resampled to 1° × 1° spatial resolution (Barsi et al., 2003). This tool was specifically designed to compute parameters for atmospheric correction of Landsat images. When using the tool the user fills in the data about the sensor and the scene to be corrected choosing whether the results will be interpolated for the specific location or the system will provide values for the closest geographic grid intersection. There is also the possibility to fill in the data on near-surface atmospheric conditions at the moment of image acquisition. In case of this study meteorological inputs came from the FLUXNET tower. The results are mailed to the electronic address provided by the user.

4.3. Field data

4.3.1. Proximal sensing reflectance measurements

Field reflectance measurements were performed using ASD spectroradiometer (ASD, 2012) during 2009-2011 field campaigns in the frame of the BIOSPEC project (*dehesa* study site), as well as in August 2014 in Zuera study area (wildfire burn) to validate results of atmospheric correction of Landsat optical bands and to generate spectral signatures of landcover types in the areas of post-fire wood treatments. ASD registers reflectance in the wave range of 350–2500 nm with spectral resolution of 3-10 nm. Reflectance measurements were performed between 12:00 and 15:00 local time with optical fiber 1 m above the plant canopy pointing vertically downwards. To prevent signal saturation the instrument was regularly calibrated using white reference Spectralon panel. For better signal-to-noise ratio each spectral signature represents the mean of 20 individual spectra.NDVI resulting from reflectances in Landsat spectral bands simulated from the continuous spectral signatures (Teillet et al., 2001) were compared with available Landsat images.

4.3.2. Land Surface temperature measurements

In situ land surface temperature measurements were performed at the *dehesa* study site to contextualize LST values derived from Landsat images and evaluate the necessary adjustments due to the time difference between the Landsat and MODIS overpasses. Measurements were realized by the infrared sensor Campbell IR120 installed on a FLUXNET tower at a height of 8 m. The sensor measures grasstemperature from the received infrared radiation in the wavelength range of 8 to 14 μm in the field of view of 20°. The values registered in a continuous mode are averaged every 10 min with an accuracy of ±0.2 °C. The *in situ* LSTs coincident with the Landsat image acquisition (10:50 a.m. GMT) were only used to assess the significance of time mismatch between Landsat and MODIS TERRA overpasses because the data are available only for one of the landcover components (grass) and for less than 25% of the images.

4.3.3. Emissivity measurements

Errors in emissivity estimation hinder the quality of LST assessment. Soil and vegetation are two main landcover components in the studied heterogeneous systems of dehesa and wildfire burns. Vegetation emissivity is quite stable and presents variation around 0.99, while variation of soil emissivity is higher, and emissivity of one soil type can be quite different from the emissivity of the other (Sobrino et al., 2008). Thus, the emissivity of bare soil was

measured in situ using box method (Rubio et al., 1997). The box built from material with lambertian surface reflectance is used to isolate the sampled surface (soil) from the surrounding environmental radiance (atmospheric descendent radiance and radiance from the adjacent materials) (Figure 4). The method is capable of estimating emissivity with an error of 0.003. Soil emissivity value of 0.984 which resulted from field measurements is similar to the values reported by previous research (Sobrino et al., 2008) and was used to adjust applied land surface emissivity estimation algorithm to local conditions.

Figure 4. Box used for emissivity measurement using box method.

4.4. Cartography of *dehesa*

Initial information on the extension and vegetation structure of *dehesa* ecosystem was obtained from the SIOSE (National Information System of Land Cover and Land Use of Spain) (http://www.siose.es). Data generated in the frame of the Spanish National Plan for Territory Observation (PNOT) at scale 1:25.000 were downloaded from the SIOSE website and contain georeferenced polygonsof established land cover types in UTM projection (datum ETRS 1989, zone 30N). Among SIOSE land cover types is *dehesa* coverage 701 with the code DHS. Its attributes include information on the percentage of the area covered by canopies of deciduous (FDC) and evergreen (FDP) tree species, shrubs (MTR) and pastures (PST). Three polygons with the tree canopies covering between 30% and 50% of the area were selected for further analysis (Figure 2).

Vegetation coverage within these polygons was classified into “tree canopy” and “pasture” based on digital orthophotography generated in June 2012 in the frame of the

Spanish National Plan for Territory Observation (PNOT). High resolution photomosaic (25 cm pixel) corresponding to the sheet number 0624 of the Spanish National Topographic Map 1: 50000 (MTN50, datum ETRS89, UTM projection zone 30N) was downloaded from the server of Spanish National Geographic Institute(http://centrodedescargas.cnig.es/CentroDescargas). Data preprocessing included conversion of the downloaded image from RGB into gray scale format. Next, the images were classified in two categories: (1) woody vegetation consisting of trees and shrubs, and (2) pasture. New classified image contains pixels with two values: 1 for "tree cover" and 0 for "pasture". Zonal statistics were applied to calculate *n*, the number of "tree cover" pixels (0.25 m pixel size) in each Landsat pixel (30m pixel size). Finally, percentage of tree cover in Landsat pixels was calculated using expression *n*100/N*, where *N*=14400 is the number of orthophoto pixels in a pixel of a satellite image.

4.5. Landscape characteristics of the studied burns

Digital elevation model from the National Center for Geographic Information (Spain) (http://centrodedescargas.cnig.es/CentroDescargas/) was used to generate grids of surface slope and orientation (aspect) at 25 m spatial resolution. Aspect calculated as the maximum rate of change in the z-value (elevation) from each cell in a raster surface is usually measured in in degrees east of north, which complicates the use of this variable in LST and vegetation modeling: north-facing slopes can have aspect values as different as 1 and 360 was. The solution consisted in application of Beers transformation (Beers et al., 1966):

$$Transformed\ aspect = cos(45 - Aspect) + 1 \quad (3)$$

This transformation rescales aspect values between zero and two, with zero corresponding to the northeast and two to the southwest direction.

The amount of incident sun energy was considered incorporating in the models "illumination" variable as the proxy. Illumination was calculated using expression suggested by Burrough and McDonnell (1998):

$$Illumination = cos\ a * cos\ b + (sin\ a * sin\ b * cos(c-d)) \quad (4)$$

where *a, b, c,* and *d* are angles (in radians): *a* – solar zenith; *b* – slope; *c* – solar azimuth and *d* – aspect. For Landsat image used for vegetation regeneration and LST estimation in this study, solar zenith (*a*) and azimuth (*c*) angles were obtained from the header file and transformed from sexagesimal degrees into radians.

Pre-fire forest composition in the Las Hurdes burn was obtained from the parcels database of the Third National Forest Inventory, Spain (http://www.magrama.gob.es/es/biodiversidad/servicios/banco-datos-naturaleza/informacion-disponible/ifn3.aspx). Information on tree cover fraction, dominant and up to two less important tree species is available for 24 inventory points within Las Hurdes study area.

5. Methodology

5.1. Pre-processing ofremotely sensed images

Preprocessing of Landsat images consisted in (i) filling of the gaps existing in parts of Landsat-7 images due to the malfunctioning of the scan-line corrector (Storey et al., 2005); (ii) conversion of original digital numbers (DN) into the top-of-the atmosphere radiance; and (iii) atmospheric correction of optical bands.

Gap-filling of Landsat-7 images was performed using localized linear histogram match method (Scaramuzza et al., 2004). Since data loss does not affect the same area on contiguous in time Landsat passes, other images of similar phenology can be used for correction. In order to fill the gap the method attempts to find a linear transformation between one image and another calculating corrective gain and bias, which are applied to the pixels in the auxiliary image. Calculated values are used to fill the pixels affected by data loss. The quality of correction mainly depends on the similarity of atmospheric conditions and phenology in the images used for gap-filling and the scenes affected by data gaps (Rulloni et al., 2012; Zhang et al., 2007).

Coefficients from image metadata were applied to convert original digital numbers (DN) into the top-of-the-atmosphere radiance using procedures recommended by NASA for Landsat-5/7 (http://landsat.usgs.gov/how_is_radiance_calculated.php) and Landsat-8 (http://landsat.usgs.gov/Landsat8_Using_Product.php).

Atmospheric correction of optical bands was performed using FLAASH (Cooley et al., 2002) and LEDAPS(Masek et al., 2006) algorithms based on radiative transfer codes MODTRAN 4 and 6S, respectively.

FLAASH is an acronym for Fast Line-of-sight Atmospheric Analysis of Spectral Hypercubes implemented as a part of the geospatial image-processing software package ENVI (http://www.exelisvis.com). The method gives the user a possibility to choose one of the MODTRAN standard atmospheres and types of aerosol environments to characterize the scene calculating unique solution for each image. It can be used for correcting multi- and hyperspectral images, acquired in conditions of vertical or oblique observation geometry. Using FLAASH is time-consuming because of the need to manually fill in the required inputs in the software interface.

LEDAPS (Landsat Ecosystem Disturbance Adaptive Processing System) overcomes this limitation. It is a stand-alone tool created by NASA Goddard Space Flight Center (GSFC) to deal with Landsat images (Masek et al., 2006). The algorithm is based on the assumptions that

the surface is Lambertian and the effects of signal absorption are separable from the effects of scattering. Transmissivty, reflectivity and albedo are calculated running 6S radiative transfer code. DDV (Dark Dense Vegetation) correction method (Kaufman and Sendra, 1988) is used to retrieve aerosol optical density from the image. Interpolated values of optical thickness, atmospheric pressure and water vapor are input into 6S for calculation of pixel-by-pixel corrections. Parameters required for atmospheric correction from the National Centers for Environmental Prediction (NCEP) reanalysis database (atmospheric water vapor) and Earth Probe Total Ozone Mapping Spectrometer (EP TOMS) (ozone) are resampled to the common spatial resolution of 1.2 km by the NOAA/OAR/ESRL PSD, Boulder, Colorado, USA, on-line (http://www.esrl.noaa.gov/psd/data/).One of the advantages of the system is that it does not require previous data transformation or scaling by the user or any other input besides original Landsat data.

5.2. LST estimation from Landsat images

Four algorithms were used to estimate LST from Landsat images: RTE inversion, single-channel method, mono-window method and simulation using radiative transfer code MODTRAN-5.

5.2.1. Radiative Transfer Equation (RTE)

When parameters for atmospheric corrections are available and the surface emissivity is known, it is possible to estimate LST from remote sensing images through direct inversion of RTE and Planck's law. One of the tested procedures obtained atmospheric correction parameters from the Atmospheric Correction Parameter Calculator (ACPC). This on-line tool based on MODTRAN 4 radiative transfer code was developed specifically for correction of Landsat thermal imagery (Barsi et al., 2003). It calculates site-specific atmospheric transmission, upwelling, and downwelling atmospheric radiances for LST estimation through RTE inversion using information on geographical coordinates, site elevation, date and time of the image acquisition provided by the user. User can also specify one of the two available choices of the standard atmospheres, midlatitude summer or midlatitude winter. The tool does not require the user to input meteorological data corresponding to the image acquisition time; it uses atmospheric profiles from NCEP databases to interpolate the profile for the specified place, date, and time. No batch processing is possible; user has to fill in data corresponding to one Landsat imageat a time; the results are forwarded to the user's e-mail address. Generated atmospheric correction parameters (atmospheric profiles, transmissivity, upwelling and

downwelling atmospheric radiance) allow LST estimation within ±2 °C for clear-sky midlatitude conditions (Barsi et al., 2005).

5.2.2. Mono-Window (MW) Method

MW algorithm is an approximation of RTE and does not require precise data on atmospheric profiles. LST is calculated through decomposition of Planck's radiance function using a Taylor's expansion and estimation of empirical coefficients *a* and *b*(Qin et al., 2001). Three a priori known parameters are required for atmospheric correction: transmissivity (τ)/water vapor content, effective mean atmospheric temperature (*Ta*) and surface emissivity (ε). The following equation is used to calculate *Ts* (in K):

$$Ts=\{a(1-C-D)+[b(1-C-D)+C+D]\times Tsensor-DTa\}/C \quad (5)$$

where a = −67.355351 and b = 0.458606 are constants, and *Tsensor* is the at-sensor brightness temperature. C and D are calculated as:

$$C=\varepsilon\tau \quad (6) \qquad \text{and} \qquad D=(1-\tau)[1+(1-\varepsilon)\tau] \quad (7)$$

Effective mean atmospheric temperature *Ta* is estimated from the relationship between *Ta* and the vertical water vapor distribution in the atmosphere: it had been demonstrated that, the distribution of the ratio of water vapor content at a particular altitude to the total is very similar for all atmospheric profiles although water vapor content differs significantly depending on the atmospheric conditions.Hence, *Ta*can be estimated from the total water vapor content and the near surface local air temperature (T_0), according to the atmospheric conditions:

$$Ta=19.2704+0.91118\,T_0 \text{(mid-latitude winter)} \quad (8a)$$

$$Ta=19.2704+0.91118\,T_0 \text{(mid-latitude summer)} \quad (8b)$$

$$Ta=17.9769+0.91715\,T_0 \text{(tropical atmosphere)} \quad (8c)$$

Expressions for estimation of atmospheric transmissivity τ were obtained from simulations using LOWTRAN 7 for high (35 °C) and low (18 °C) air temperature profiles and two ranges of atmospheric water vapor content *w*:

High temperature $\tau=0.974290-0.08007w(0.4\ g\cdot cm-2<w<1.6\ g\cdot cm^{-2})$ (9a)

$\tau=1.031412-0.11536w(1.6\ g\cdot cm-2<w<3.0\ g\cdot cm^{-2})$ (9b)

Low temperature $\tau=0.982007-0.09611w(0.4\ g\cdot cm-2<w<1.6\ g\cdot cm^{-2})$ (9c)

$\tau=1.053710-0.14142w(1.6\ g\cdot cm-2<w<3.0\ g\cdot cm^{-2})$ (9d)

MW method produces optimum results (error ~1 K) when atmospheric water vapor content varies between 0.5 and 2.5 g·cm^{-2}(Qin et al., 2001; Sobrino et al., 2004).

5.2.3. Single-Channel (SC) Method

Another RTE approximation, SC method (Jiménez-Muñoz and Sobrino, 2003)needs only one atmospheric parameter for atmospheric correction (atmospheric water vapor content). The following expression is used to calculate LST:

$$Ts=\gamma[\varepsilon^{-1}(\psi_1 L_{sensor}+\psi_2)+\psi_3]+\delta \quad (10)$$

whereε is surface emissivity, γ and δ are parameters directly depending on Planck function. ψ_1, ψ_2 and ψ_3 are atmospheric correction functions expressed as second degree polynomial equations (Eq. 11) with coefficients (c_{ij}) obtained by simulation. These coefficients for Landsat sensors used in the research are given in Table 4.

$$\begin{bmatrix}\psi_1\\ \psi_2\\ \psi_{13}\end{bmatrix}=\begin{bmatrix}c_{11} & c_{12} & c_{13}\\ c_{21} & c_{22} & c_{23}\\ c_{31} & c_{32} & c_{33}\end{bmatrix}\begin{bmatrix}w^2\\ w\\ 1\end{bmatrix} \quad (11)$$

where w is total atmospheric water vapor content in g·cm^{-2}.

Table 4. Coefficients for SC atmospheric functions following matrix notation in Eq. 11 obtained for band 6 of Landsat 5 (L5B6), band 6 of Landsat 7 (L7B6) and band 10 of Landsat 8 (L8B10).

Sensor	Cij	i=1	i=2	i=3
L5B6	j=1	0.14714	-0.15583	1.1234
	j=2	-1.1836	-0.37607	-0.52894
	j=3	-0.04554	1.8719	-0.39071
L7B6	j=1	0.07593	-0.07132	1.08565
	j=2	-0.61438	-0.70916	-0.19379
	j=3	-0.02892	1.46051	-0.43199
L8B10	j=1	0.04019	0.02916	1.01523
	j=2	-0.38333	-1.50294	0.20324
	j=3	0.00918	1.36072	-0.27514

SC algorithm demonstrates optimal performance for the atmospheres with water vapor content in the range of 0.5–2.5 g·cm^{-2}.

5.2.4. Simulation of Land Surface Temperature (LST)

When comparing the performance of different LST estimation algorithms, LSTs simulated by the latest version of the radiative transfer code MODTRAN 5 were used as a reference set.

It is generally accepted (Li et al., 2013a) that LST simulated using radiative transfer code can be an alternative for validation when field measurements at a required spatial scale are not available. Previous studies applied the procedure for validation of Landsat (Sobrino et al., 2004) and MODIS (Wan and Li, 2008) LST. MODTRAN 5 performs calculations based on the information about observation geometry and atmospheric profiles at the moment of observation. The best results are achieved when data come from in situ radiosoundings synchronized in time with image acquisition. Unfortunately, data from in situ radiosoundings synchronized in time with image acquisition were not available in this study. Instead, NCEP atmospheric profiles interpolated for the exact location and time of Landsat overpass were used in this research. This source has been successfully used for validation earlier(Coll et al., 2012; Jiménez-Muñoz et al., 2010). On-site meteorological data for the lowest atmospheric layer complemented the NCEP atmospheric profiles interpolated for the study area and conditions by ACPC tool. The profiles were incorporated into MODTRAN input file.

MODTRAN was run twice to obtain parameters for LST simulation. The first MODTRAN run is performed with 0% surface albedo. Atmospheric transmissivity (τ) and upwelling radiance (L_u) are extracted from the MODTRAN output files and integrated over the Landsat-5 TM thermal band using the sensor filter function. Then MODTRAN 5 is run for the second time with 100% surface albedo to calculate downwelling radiance (L_d). Next, the obtained atmospheric correction parameters τ, L_u and L_d together with previously estimated emissivity ε are substituted into RTE (Eq. 1) to calculate the radiance from the target (L_{Ts}). The final step consists in transformation of the calculated target radiance into LST (*LSTref*) by inversion of the Planck's law.

5.3. Emissivity estimation

Methods for emissivity estimation from remotely sensed data requiring two or more bands, e.g. TES (Gillespie et al., 1998) or TISI (Becker and Li, 1990) cannot be used with Landsat images because there is only one thermal band. In this situation it is possible to use one of the methods which take advantage of the relationship existing between emissivity and the normalized difference vegetation index (NDVI) (Li et al., 2013b). The NDVI thresholds method $NDVI^{THM}$(Sobrino and Raissouni, 2000) based on the findings of Valor and Caselles (1996) was applied to estimate surface emissivity in this study. Pixel-based emissivity is assigned based on the NDVI range. All the pixels, except those categorized as mixed pixels, are assigned fixed emissivities according to the NDVI range (Table 5).

Table 5. Emissivity values assigned to ranges of the normalized difference vegetation index (NDVI).

NDVI	Emissivity (ε)
NDVI < 0	*0.985*
0 <= NDVI <= 0.1	*f(red reflectivity)*
0.1 <= NDVI <= 0.7	$0.990\ P_V + 0.984(1- P_V) + 0.004 * P_V (1- P_V)$
NDVI > 0.7	*0.990*

In case of the mixed pixels category (vegetation and soil), the NDVI values (thresholds) selection is based on the analysis of the images histograms and the emissivty values are scaled between the ε_s and ε_v values using the expression in Table 5. In landcovers consisting mainly of different vegetation components, like in this study, soil emissivities show the greatest variation in the thermal region of the spectrum. This is why the soil emissivity was adjusted to local conditions; ε_s value of 0.984 is based on *in situ* field measurements. The vegetation emissivity $\varepsilon_v$is assigned the value of 0.990; $d\varepsilon$ = 0.01 is the term accounting for surface roughness different from zero for heterogeneous covers (Sobrino et al., 2004). Vegetation fraction *PV*is estimated from pixel NDVI according to Choudhury et al. (1994) and Gutman and Ignatov (1988):

$$PV = \frac{(NDVI - NDVI_S)}{(NDVI_{V-} - NDVI_S)} \qquad (12)$$

According to Sobrino et al. (2008) the method estimates emissivity of vegetation-soil pixels with an error less than 0.01, which would allow LST estimation with the error below 0.5 °C.

5.4. Vegetation abundance (NDVI) estimation

Vegetation abundance was assessed through NDVI calculated for each available image. The NDVI exploits the difference between the maximum reflection of radiation in the near-infrared spectral bands (0.78–0.90 μm) and the maximum absorption of radiation in the red spectral band (0.63–0.69 μm) characteristic to vegetation. The effect of shadows is reduced by normalization of the difference of the reflectances by their sum, resulting in *NDVI=(NIR−VIS)/(NIR + VIS)*.NDVIvary from -1.0 to +1.0. Because of high positive correlation with vegetation status and density, NDVI is widely used for vegetation monitoring. It is often used as a proxy for biomass although the relationship between them is often non-linear (Myneni et al., 1997), and NDVI shows saturation before biomass reaches its maximum levels. In spite of the limitations, NDVI is commonly used in assessing vegetation

recovery after fire (among others Díaz-Delgado et al., 2003; Riaño et al., 2002) and as an indicator of burn severity (Veraverbeke et al., 2012).

5.5. Burn Severity Estimation

There are several spectral indices developed for evaluation of burn severity, some of them designed for Landsat were used to study Las Hurdes and Zuera burns. These indices are Normalized Burn Difference (NBR) and Delta Normalized Burn Difference (dNBR). Close relationship of these indices with burn severity in Mediterranean conifer forest was demonstrated in previous research (DeSantis and Chuvieco, 2007). The indices were calculated following the methodology suggested by Key and Benson (2006): (1) pre- and post-fire images were transformed to reflectance and atmospherically corrected; (2) an NBR image was generated for both dates using the formula (NIR – SWIR2)/(NIR + SWIR2); (3) dNBR was calculated as NBRpre-fire − NBRpost-fire.

dNBR values were grouped into discrete classes of burn severity (e.g., low, moderate and high) using original thresholds (Key and Benson, 2006), since there applicability for similar ecosystems was confirmed in previous research (Kokaly et al., 2007). Burn severity categories were created using thedNBR values as follows: unburned (UB) (from −100 to 99), low severity (LS) (from 100 to 269), moderate-low severity (MLS) (from 270 to 439), moderate-high severity (MHS) (from 440 to 659) and high severity (HS) (from 660 to 1300).

5.6. Statistical procedures

5.6.1. Measures of difference

Comparison of values obtained by different methods of LST estimation (first research objective) with reference values was performed using bias, standard deviation and root mean-square deviation.

Bias (*B*), also referred to as mean error, is calculated as the average of deviations, i.e. the differences between LST calculated by the tested method (LST_{calc}) and reference LST (LST_{ref}).

$$B = \frac{1}{N}\sum_{1}^{N}\left(LST_{calc} - LST_{ref}\right) \qquad (13)$$

Smaller absolute bias values indicate better agreement between measured and calculated values. Positive values indicate positively biased computed values (overestimate) while negative values indicate negatively biased computed values (underestimate).

Standard deviation is often used to measure data dispersion; it is the average difference between each value in dataset and the mean. For a sample standard deviation is expressed by the following formula:

$$\sigma = \sqrt{\frac{\sum_{i=1}^{n}(x_i-\mu)^2}{n-1}} \quad (14)$$

where x_i is a value for each number within the dataset; μ is the the average for the values in the dataset; n is the number of values in the dataset; and σ is a standard deviation.

The standard deviation of a normal distribution enables calculation confidence intervals. In a normal distribution, about 68% of the values are within one standard deviation either side of the mean and about 95% of the scores are within two standard deviations of the mean.

The root mean square deviation (RMSD) is a commonly used measure of deviation of a random variable from some standard or accepted value, although sometimes the RMSD is used to compare differences between two datasets, neither of which is accepted as the "standard". RMSD is defined as the square root of the mean squared error:

$$RMSD = \sqrt{\frac{1}{N}\sum_{i=1}^{N}\delta_i^2} \quad (15)$$

where δ is the distance between N pairs of data values.

5.6.2. Correlation indices

Pearson product-moment correlation statistic also known as linear correlation coefficient is one of the measures used to assess strength and direction of linear relationship between two variables. Coefficient values vary between -1 and +1; the closer to the zero, the weaker is the measured relation. To compare two sets of values (x and y) each containing n values, Pearson correlation coefficient r is computed using formula:

$$r = \frac{\sum_{i=1}^{n}(x_i-\bar{x})(y_i-\bar{y})}{\sqrt{\sum_{i=1}^{n}(x_i-\bar{x})^2\sum_{i=1}^{n}(y_i-\bar{y})^2}} \quad (16)$$

When analyzing spatial data (events) it is also necessary to take in account spatial autocorrelation. Autocorrelation and spatial auto correlation are correlation coefficients. However, instead of assessing relation between two variables, the correlation is between two

values of the same variable at different moments in time (autocorrelation)(Box et al., 2011) or space (spatial autocorrelation) (Anselin, 1988). Spatial autocorrelation is common for spatial data; according to the First Law of Geography formulated by Tobler (1970) "everything is related to everything else, but near things are more related than distant things". High spatial autocorrelation violates the assumption of data independence required in statistical analysis and can affect its results. Similarity of spatially distributed events as a function of distance can be quantified using Moran's I coefficient (Moran, 1950). Moran's I is calculated similar to the classical Pearson correlation coefficient using expression:

$$I = \frac{n}{S_0} \frac{\sum_{i=1}^{n} \sum_{j=1}^{n} w_{i,j} z_i z_j}{\sum_{i=1}^{n} z_i^2} \quad (17)$$

where z_i is the deviation of an attribute for feature i from its mean ($x_i - X$), w_{ij} is the spatial weight between feature i and j, n is the total number of features, and S_0 is the sum of spatial weights for all the features:

$$S_0 = \sum_{i=1}^{n} \sum_{j=1}^{n} w_{i,j} \quad (18)$$

Moran's I index values vary between -1 (close events are not similar) and +1 (close events are similar, clustered distribution). When index is equal to 0, properties of spatially distributed events show random distribution.

5.6.3. Analysis of variance (ANOVA)

One-way analysis of variance (ANOVA) was applied to verify if there are statistically significant differences between the analyzed datasets. The designation of one-way is used because the datasets are observations of the single variable at two or more levels. Inferences about between-means differences are made by analyzing variance, a statistic that measures the variability about the mean. The null hypothesis tested by ANOVA states that the means are equal and the groups are subsets of the same population. Its rejection leads to the conclusion that the means of at least two groups are different. To know which groups are different ANOVA is followed by one of the post hoc test.

ANOVA requires continuous numerical data and provides reliable results when data satisfy following assumptions:

1. The populations have the same variance, i.ehomogeneity of variance is assumed.

2.The populations are normally distributed.

3. Valuesare sampled independently from each other.

ANOVA partitions the total variance in two components: between-group variability and within-group variability. The test statistic for ANOVA (*F*) is a ratio of these quantities:

F= between-group variability/within-group variability

When the null hypothesis is true, this statistic has an *F* distribution with k-1 degrees of freedom (k - the number of groups) and N-k degrees of freedom (N – total number of observations) associated with the numerator and denominator, respectively. Thus, if the calculated *F* value is greater than the critical value of the F distribution with k-1 and N-k degrees of freedom and a significance level of α, the conclusion is that statistically significant difference exists between at least two of the tested groups at (1-α) probability. Commonly acceptable significance level is p=0.05. To evaluate the differences between the pairs of means, ANOVA was followed by or post-hoc tests:Bonferroni when assumption of equal variances was satisfied, or Tamhane T2 when comparing samples with unequal variances. ANOVA results include the coefficient of determination R^2, which indicates the proportion of variance explained by the independent variable.

Contribution of multiple variables to levels of LST and NDVI in areas affected by wildfire burns (research objective 2) was evaluated by factorial ANOVA. It allows exploring the relationship between one dependent and several independent variables, which can be continuous or categorical. Besides the effect of each of the dependent variables, the procedure calculates the effect of their interactions. In this study model design included one dependent variable (LST or NDVI), a fixed factor (treatment) and various continuous independent variables (e.g. elevation and slope). The results quantified the contribution of each of the independent variables and their significance.

To obtain valid results data should satisfy common ANOVA requirements: be normally distributed, present homogeneity of variance and consist of independent values.

6. Comparison of methods for LST estimation from Landsat data

This chapter reproduces the text of the following article:

Title:
Assessment of methods for land surface temperature retrieval from Landsat-5 TM images applicable to Multiscale Tree-Grass Ecosystem Modeling.

Authors:
Vlassova, L.; Pérez-Cabello, F.; Nieto, H.; Martin, P.; Riaño, D.; de la Riva, J.

Remote Sens. **2014**, *6*, 4345-4368; doi:10.3390/rs6054345

OPEN ACCESS

remote sensing

ISSN 2072-4292

www.mdpi.com/journal/remotesensing

Article

Assessment of Methods for Land Surface Temperature Retrieval from Landsat-5 TM Images Applicable to Multiscale Tree-Grass Ecosystem Modeling

Lidia Vlassova [1,2,*], Fernando Perez-Cabello [1], Hector Nieto [3], Pilar Martín [4], David Riaño [4,5] and Juan de la Riva [1]

1 GEOFOREST Group, IUCA, Department of Geography and Spatial Management, University of Zaragoza, Spain, Pedro Cerbuna 12, Zaragoza E-50009, Spain; E-Mails: fcabello@unizar.es (F.P.-C.); delariva@unizar.es (J.R.)

2 Department of Environmental Sciences, Technical State University of Quevedo, Quevedo EC120509, Los Rios, Ecuador

3 Department of Geosciences and Natural Resource Management, University of Copenhagen, Øster Voldgade 10, Copenhagen K DK-1350, Denmark; E-Mail: hn@geo.ku.dk

4 Centre for Human and Social Sciences, Spanish Council for Scientific Research, Albasanz 26-28, Madrid 28037, Spain; E-Mails: mpilar.martin@cchs.csic.es (P.M.); david.riano@cchs.csic.es (D.R.)

5 Center for Spatial Technologies and Remote Sensing (CSTARS), Department of Land, Air and Water Resources, University of California, One Shields Avenue, Davis, CA 95616-8617, USA

* Author to whom correspondence should be addressed; E-Mail: vlassova@unizar.es; Tel.: +34-645-311-832; Fax: +34-976-761-506.

Received: 27 November 2013; in revised form: 17 April 2014 / Accepted: 21 April 2014 / Published: 12 May 2014

Abstract: Land Surface Temperature (LST) is one of the key inputs for Soil-Vegetation-Atmosphere transfer modeling in terrestrial ecosystems. In the frame of BIOSPEC (Linking spectral information at different spatial scales with biophysical parameters of Mediterranean vegetation in the context of global change) and FLUXPEC (Monitoring changes in water and carbon fluxes from remote and proximal sensing in Mediterranean "dehesa" ecosystem) projects LST retrieved from Landsat data is required to integrate ground-based observations of energy, water, and carbon fluxes with multi-scale remotely-sensed data and assess water and carbon balance in ecologically fragile heterogeneous ecosystem of Mediterranean wooded grassland (dehesa). Thus, three methods based on the Radiative Transfer Equation were used to extract LST from a series of 2009–2011 Landsat-5 TM images to assess the applicability for temperature input

Remote Sens. **2014**, *6* **4346**

generation to a Landsat-MODIS LST integration. When compared to surface temperatures simulated using MODerate resolution atmospheric TRANsmission 5 (MODTRAN 5) with atmospheric profiles inputs (LST_{ref}), values from Single-Channel (SC) algorithm are the closest (root-mean-square deviation (RMSD) = 0.50 °C); procedure based on the online Radiative Transfer Equation Atmospheric Correction Parameters Calculator (RTE-ACPC) shows RMSD = 0.85 °C; Mono-Window algorithm (MW) presents the highest RMSD (2.34 °C) with systematical LST underestimation (bias = 1.81 °C). Differences between Landsat-retrieved LST and MODIS LST are in the range of 2 to 4 °C and can be explained mainly by differences in observation geometry, emissivity, and time mismatch between Landsat and MODIS overpasses. There is a seasonal bias in Landsat-MODIS LST differences due to greater variations in surface emissivity and thermal contrasts between landcover components.

Keywords: land surface temperature; Landsat; multitemporal

1. Introduction

Land surface temperature (LST) is a state variable that plays a crucial role in many land surface processes [1]. LST is related to the transport of heat between the land surface and the atmospheric boundary layer [1–3], and makes possible estimation of sensible heat flux [4] and latent heat flux, or evapotranspiration [5,6]. It is a necessary input for ecosystem modeling [7], which can be performed at local [4], regional, and global scales. While local modeling relies heavily on field data, remote sensing has become the main source for LST estimation at the regional and global scales [8].

Radiance measured at a sensor can be transformed into LST by inverting the Radiative Transfer Equation (RTE) applied to a particular thermal IR band or wavelength:

$$L_{sensor} = \tau\varepsilon L_{Ts} + L_u + \tau(1 - \varepsilon)L_d \quad (1)$$

where L_{sensor} is the radiance registered by the sensor, also referred to as top of atmosphere radiance, L_{Ts} is the blackbody radiance related to the surface temperature by Planck's law and Ts is the LST, L_u and L_d are the upwelling and downwelling atmospheric radiances, respectively (all the radiances in $W \cdot sr^{-1} \cdot m^{-2} \cdot \mu m^{-1}$), τ is the atmospheric transmissivity and ε is the land surface emissivity. In the case of dealing with a waveband, all these parameters are integrated according to the spectral response function of this band.

The signal coming from the target to the sensor is modified as it passes through the atmosphere, which both emits and absorbs thermal radiation. The latter effect is mainly caused by the presence of water vapor. When atmospheric conditions are known, emission and absorption of radiation in the atmosphere can be quantified and corrected using one of the radiative transfer computer codes, e.g., MODerate resolution atmospheric TRANsmission (MODTRAN) [9]. Atmospheric conditions are typically assessed using *in situ* atmospheric profile data, which are often not available for the place and time the image was acquired, although on-line atmospheric databases [10,11] or estimations based on empirical models [12] can be used.

At present, there are several satellites providing global data from the thermal region of the spectrum at different scales. Among them are MODIS [13] and Spinning Enhanced Visible and Infrared Imager (SEVIRI) [14] characterized by low spatial and high temporal resolutions, for which LST products are available on a regular basis. At the medium spatial scale Landsat has provided global brightness temperatures since 1984, with Landsat 8 launched at the beginning of 2013 giving continuity to the data record [15]. The assessment of methods for LST estimation from a unique thermal band gains additional importance if we consider problems with data from one of the Landsat 8 thermal bands (band 11) and National Aeronautics and Space Administration (NASA) suggestion not to use band 11 for surface temperature retrieval [16]. The recently published reviews [8,17] mention several single-channel methods based on approximations from the RTE, which can be applied for LST retrieval from Landsat-5 unique thermal band [18–21]. These methods perform atmospheric correction based on water vapor content [19,20] or both water vapor and near-surface air temperature [18,21]. Apart from the atmospheric correction parameters, the surface emissivity (defined as the ratio between the target emitting capacity and that of a blackbody at the same temperature) is also required. A review of methods for surface emissivity estimation from satellite data is available in Li *et al.* [22]. Because of the high level of correlation between NDVI and surface emissivity, many methods proposed for estimating emissivity are based on this vegetation index [23–27].

One of the research fields with a great demand of LST data at a local scale is carbon and water fluxes modeling in terrestrial ecosystems. BIOSPEC (Linking spectral information at different spatial scales with biophysical parameters of Mediterranean vegetation in the context of global change) [28] and FLUXPEC (Monitoring changes in water and carbon fluxes from remote and proximal sensing in Mediterranean "dehesa" ecosystem) [29] projects carry out the analysis of these processes using information from ground-based measurements of fluxes and vegetation biophysical parameters, and their modeling throughout the integration of spectral data from remote sensors having different spatial, spectral and temporal resolutions (Landsat and MODIS) following the attempts of other scientific teams [30,31]. Landsat can provide LST at a spatial detail much higher than MODIS, but only once in 16 days compared to daily images acquisition by MODIS. Thus, integration of the data from these two satellites would be highly beneficial given the spatial resolution of the former and the temporal resolution of the latter. However, the challenges and persisting uncertainties related to the use of Landsat for LST estimation [32], especially in heterogeneous environments, make it necessary to evaluate the methods and atmospheric information sources looking for those more similar to MODIS. Although there are a number of studies comparing methods for LST retrieval from one thermal band [18,19,33,34], the evaluation is usually based on data from homogeneous environments. On the other hand, this study presents an assessment of the single-channel methods in heterogeneous environments common for most of the land surface.

Our main interest in this study is to compare the performance of the most common methods for LST retrieval from Landsat-5 TM images of the dehesa tree-grass ecosystem [8] and analyze the relationship between LST estimated from Landsat and LST from MODIS product (MOD11_L2), for the use in Landsat-MODIS LST fusion algorithm development to study energy and water exchange between the dehesa landcover and the atmosphere. Three procedures are applied for LST retrieval from a sequence of 13 images of Central Spain, acquired from 2009 to 2011: (1) RTE inversion with

Radiative Transfer Equation Atmospheric Correction Parameters Calculator (RTE-ACPC) from here on and two methods, which are approximations of the RTE with minimum parameters: (2) single-channel (SC) method by Jiménez-Muñoz and Sobrino [20], updated in 2009 [19], and (3) mono-window MW method by Qin *et al.* [21]. The results are compared with LSTs simulated by Radiative Transfer Code MODTRAN 5. We also assess and analyze the relationship existing between Landsat LSTs and those from MODIS LST product (MOD11_L2). *In situ* grass temperature measurements available for some of the images complete the set of reference data.

2. Study Area and Data

2.1. Study Area

The study area shown in Figure 1 is located in a dehesa ecosystem near the Las Majadas del Tietar FLUXNET site (geographic coordinates: Lat 39°56′26″N, Long 5°46′29″W), which is operated by the Mediterranean Center for Environmental Studies (CEAM). FLUXNET is a network of micrometeorological observation sites established to perform continuous measurement of exchange fluxes in the soil–vegetation–atmosphere system [35].

Figure 1. Study area: (**a**) Location of the study site (**b**) orthophoto of the study area corresponding to MODIS pixel.

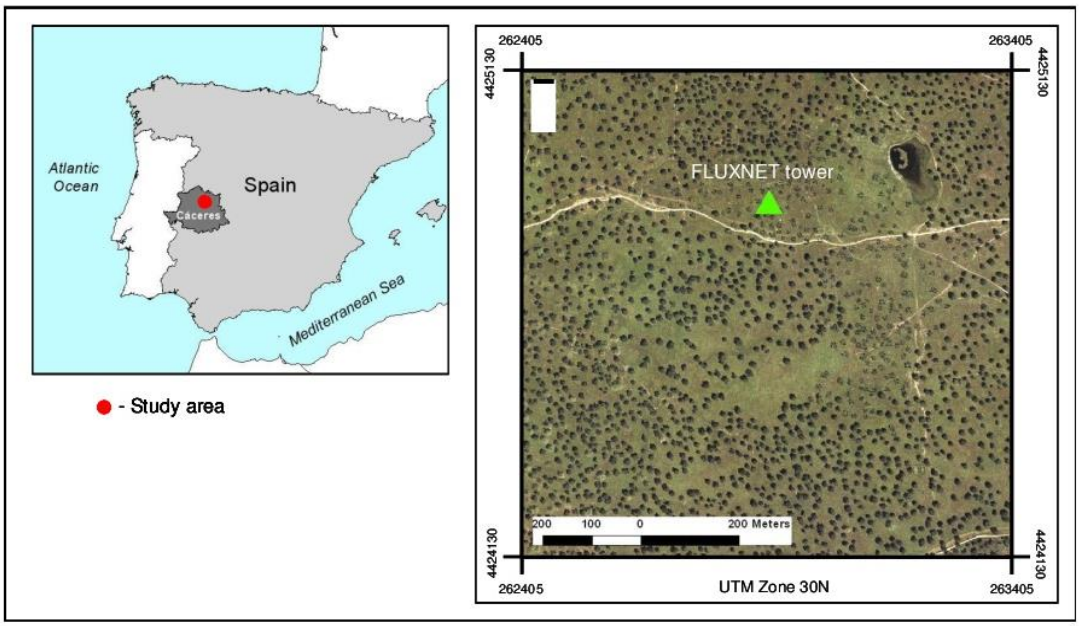

(**a**) (**b**)

The dehesa is an open savanna with an integrated agroforestry ecosystem, and has a complex vegetation structure typical of Mediterranean areas. The study site is flat, and is covered by grass (75% of the area) and holm oak trees *Quercus ilex* ssp. *rotundifolia* (25% of the area). The zone climate (Csa according to Köppen classification) is characterized by an annual average temperature of

16 °C and approximately 550 mm precipitation, and has a four-month hot dry period from June to September [36].

2.2. Datasets

2.2.1. Landsat-5 TM Images

Landsat-5 TM provides images with six bands in the optical region, and a thermal band with a bandwidth of 10.4–12.5 μm. The LST was retrieved from 13 Landsat-5 TM (path 202, row 32) clear sky images pre-processed by the NLAPS (National Land Archive Production System–USGS) and downloaded from [37] (Table 1). The images over the study area were acquired at approximately 10:50 a.m. GMT from 2009 to 2011.

Table 1. Acquisition time and observation geometry for Landsat-5 TM and MODIS satellite images used in the study.

Date	LANDSAT			MODIS TERRA		Difference in Acquisition Time
	Acquisition Time (a.m. GMT)	Sun Azimuth (degrees)	Sun Elevation (degrees)	Acquisition Time (a.m. GMT)	Viewing Angle (degrees)	(min)
27 June 2009	10:50:18	123.55	63.88	10:31:45	63.00	18
29 July 2009	10:50:49	128.98	59.94	10:35:30	63.00	15
30 August 2009	10:51:18	141.13	52.63	10:29:40	63.00	21
15 September 2009	10:51:32	147.28	47.91	10:24:00	63.00	27
17 October 2009	10:51:53	156.52	37.36	10:14:00	63.00	37
6 February 2010	10:52:39	151.39	29.19	10:43:00	63.00	7
11 April 2010	10:52:40	141.79	52.28	10:30:10	63.00	12
30 June 2010	10:52:19	124.31	64.00	10:32:25	63.00	20
1 August 2010	10:52:10	130.34	59.61	10:35:25	63.00	17
5 November 2010	10:51:34	159.16	31.40	10:12:45	63.00	38
1 June 2011	10:51:13	127.86	63.89	10:26:35	63.00	24
4 August 2011	10:50:41	130.72	58.86	10:35:10	63.00	15
5 September 2011	10:50:24	142.93	50.94	10:27:40	63.00	22

2.2.2. MODIS LST Images

The MODIS Terra LST MOD11_L2 product with a 1-km pixel spatial resolution was used for comparison. MOD11_L2 constitutes an output of the split window algorithm [38] applied to MODIS bands 31 (10.780–11.280 μm) and 32 (11.770–12.270 μm). The time difference between Landsat and MODIS passes over the study area is about 20 min (Table 1): MODIS images are acquired approximately 20 min earlier. FLUXNET tower data corresponding to the same dates show an average air temperature increase of about 0.5 °C for the same time period, while *in situ* grass surface temperature measurements available for three summer dates in 2011 (Table 2) demonstrate an average increase of 1.5 °C. Following the procedure applied by other researchers [39,40] to account for different spatial resolution of the sensors, MODIS temperature value corresponding to a pixel centered in the study area was compared with the mean value of the Landsat-5 TM pixels within that MODIS

pixel. Moreover, to minimize the effects of the differences in the observation geometry only the images with the best quality MODIS pixel of the study area (MODIS product quality flag 0) were used for the comparison. According to the MOD11_L2 product description quality flag 0 is assigned to the cloud-free pixels with LST error less than 1 °C and the emissivity errors in channels 31 and 32 involved in LST estimation less than 0.01.

2.2.3. Atmospheric Correction Parameters Sources

We obtained and compared data on the atmospheric water vapor content from three online sources: Aerosol Robotic Network (AERONET) database, National Center for Environmental Prediction (NCEP) Reanalysis (hereafter called REANALYSIS) database and from MODIS MOD05 product. AERONET is part of the NOAA Observing System Architecture, which includes more than 500 sites distributed worldwide. Precipitable water content values ($g \cdot cm^{-2}$) were downloaded from an online database [41] for Cáceres; the observation site is located approximately 50 km from the study area. The National Center for Environmental Prediction (NCEP) and the National Center of Atmospheric Research Reanalysis Project (NCAR) maintain a free access online database of gridded and continuously updated meteorological data at 2.5° × 2.5° spatial and 6 h temporal resolution extending back to 1948 [42]. Precipitable water values ($kg \cdot m^{-2}$) for 2009–2011 were downloaded from [43]. The noon values, approximately 1 h later than the Landsat-5 TM overpass, were extracted for the study area location and used in the water vapor sources comparison. Atmospheric profiles containing information on vertical distribution of pressure, geopotential height, temperature and relative humidity for simulation of the reference LSTs were generated by ACPC tool based on the interpolation of the NCEP profiles resampled to 1° × 1° spatial resolution [11]. Interpolated profiles were completed with the data from the standard atmospheres for the altitude range from 30 km to 100 km and user-supplied information for the lowest level, resulting in the 31 levels in each profile. Precipitable water from MODIS MOD05 product at 1-km spatial resolution close in time to Landsat overpass was obtained from MODIS web archive [44].

FLUXNET tower was used as the source of ACPC tool meteorological inputs. Due to the limited extension of the study site, meteorological data provided by the tower were considered characteristic for all the analyzed area.

2.2.4. *In Situ* Grass Temperature Measurements

To put the obtained results in site context and take into account the difference in LST between the overpass times of Landsat and MODIS on board of Terra (from Latin “land”) satellite, we used the data on grass temperature obtained from an infrared sensor Campbell IR120 installed on a tower at a height of 8 m (Table 2). The sensor registers data every 10 min with an accuracy of ±0.2 °C. The data are available for a part of 2011 beginning 3 March 2011. The device offers a non-contact means of measuring the surface temperature of an object by sensing the infrared radiation in the wavelength range of 8 to 14 μm in the field of view of 20°. The *in situ* LSTs coincident with the Landsat image acquisition (10:50 a.m. GMT) were only used to assess the significance of time mismatch between Landsat and MODIS TERRA overpasses because the data are available only for one of the landcover components (grass) and for less than 25% of the images.

Remote Sens. **2014**, *6* **4351**

Table 2. Time difference between Landsat and MODIS passes over the study site and corresponding increment in *in situ* Land Surface Temperature (LST) (grass) temperature between 10:30 a.m. and 10:50 a.m. GMT.

Date	MODIS (a.m. GMT)	Landsat (a.m. GMT)	Time Difference (min)	*In situ* Temperature Increment (°C)
01 June 2011	10:26:35	10:51:13	24	2.13
04 August 2011	10:35:10	10:50:41	15	1.13
05 September 2011	10:27:40	10:50:24	22	1.31

3. Methods

3.1. Land Surface Temperature (LST) Estimation

Prior to LST retrieval optical bands of Landsat images used in emissivity estimation were corrected for atmospheric effects using the Fast Line-of-sight Atmospheric Analysis of Spectral Hypercubes (FLAASH) algorithm implemented in the ENVI (software package, a geospatial imagery analysis and processing application marketed by Exelis Visual Information Solutions) [45]. The LST was retrieved from the thermal band; the digital numbers were first converted into radiance using the header files parameters and then to the at-sensor brightness temperature, which was then transformed to LST. Three procedures used to transform the at-sensor brightness temperature into LST are: (1) RTE inversion using atmospheric correction parameters from on-line ACPC tool [10] available at [46]; and two algorithms based on the approximations of RTE: (2) single-channel SC method [19,20]; and (3) mono-window MW method [21]. The most recent SC modification [18] is highly sensitive to water vapor changes and was not considered, because *in situ* measurements of water vapor content were not available. Since LST estimation methods require clear sky, only cloud-free images were used for processing.

3.1.1. Radiative Transfer Equation (RTE)

As mentioned in Section 1, LST can be obtained from RTE (Equation (1)) and Planck's law inversion once parameters for the atmospheric corrections (L_u, L_d and τ) are estimated and the surface emissivity is known. The first tested procedure used the atmospheric correction parameters from the Atmospheric Correction Parameter Calculator (ACPC). It is an on-line tool developed for atmospheric correction of the Landsat 5 and 7 thermal data using MODTRAN 4 radiative transfer code [10,11]. The tool receives as input user-provided information on geographical coordinates, site elevation, date and time of the image acquisition and calculates site-specific atmospheric transmission, upwelling, and downwelling atmospheric radiances to be used in LST estimation through RTE inversion. Henceforth, the LST values obtained in the study by this procedure are referred to as RTE-ACPC. NCEP atmospheric databases are used to interpolate the profile for the specified place, date, and time; the profiles resulting from time interpolation can be provided for the closest lat/long grid corner or interpolated for the user-specified location. The latter option was used in this study. The tool processes data corresponding to one set of conditions (one Landsat image) at a time; the results are forwarded to the user's e-mail address. The set of parameters generated by the tool for the images analyzed in this

study is presented in Table 3. According to developers, the tool provides parameters allowing LST estimation through RTE (Equation (1)) inversion within ±2 °C [11].

Table 3. Parameters provided by Atmospheric Correction Parameter Calculator (ACPC) tool for the analyzed Landsat-5 TM images: upwelling (L_u) and downwelling (L_d) radiances in $W \cdot sr^{-1} \cdot m^{-2} \cdot \mu m^{-1}$, atmospheric transmissivity (τ).

Date	τ	L_u	L_d
27/06/2009	0.790	1.430	2.400
29/07/2009	0.890	0.830	1.410
30/08/2009	0.820	1.430	2.390
15/09/2009	0.860	0.940	1.580
17/10/2009	0.930	0.500	0.860
06/02/2010	0.870	0.820	1.380
11/04/2010	0.920	0.530	0.900
30/06/2010	0.730	2.060	3.370
01/08/2010	0.820	1.440	2.380
05/11/2010	0.830	1.220	2.010
01/06/2011	0.880	0.850	1.420
04/08/2011	0.750	1.870	3.070
05/09/2011	0.810	1.430	2.370
Mean	0.838	1.181	1.965
St. dev.	0.061	0.484	0.783

3.1.2. Mono-Window (MW) Method

In the MW algorithm [21] the LST is determined through decomposition of Planck's radiance function using a Taylor's expansion and calculation of two empirical coefficients *a* and *b*. Three *a priori* known parameters are required for the algorithm: transmissivity (τ)/water vapor content, effective mean atmospheric temperature (T_a) and emissivity (ε). All the temperatures are in K. LST (Ts) is calculated from the equation (2):

$$Ts = \{a(1 - C - D) + [b(1 - C - D) + C + D] \times T_{sensor} - DT_a\} / C \quad (2)$$

where $a = -67.355351$ and $b = 0.458606$ are constants, $Tsensor$ is the at-sensor brightness temperature, C and D are calculated using Equation (2a,2b) respectively:

$$C = \varepsilon\tau \quad (2a)$$

$$D = (1 - \tau)[1 + (1 - \varepsilon)\tau] \quad (2b)$$

The suggested method for calculation of T_a is based on the relationship between T_a and the vertical water vapor distribution in the atmosphere [47]. Simulations performed using LOW resolution TRANsmission 7 (LOWTRAN 7) [21] indicate that, while water vapor content differs significantly depending on the atmospheric conditions, the distribution of the ratio of water vapor content at a particular altitude to the total is very similar for all atmospheric profiles. This enabled formulation of

the Equation (3a–3c) for calculation of T_a from the total water vapor content and the near surface local air temperature (T_0), according to the atmospheric conditions [21]:

$$T_a = 19.2704 + 0.91118\ T_0 \text{(mid-latitude winter)} \quad (3a)$$

$$T_a = 19.2704 + 0.91118\ T_0 \text{(mid-latitude summer)} \quad (3b)$$

$$T_a = 17.9769 + 0.91715 T_0 \text{(tropical atmosphere)} \quad (3c)$$

The most important parameter of the algorithm τ is estimated using the expressions obtained from simulations using LOWTRAN 7 [21] for two air temperature profiles: Equation (4a,4b) for high (35 °C) and Equation (4c,4d) for low (18 °C) [21]:

$$\tau = 0.974290 - 0.08007w \ (0.4\ \text{g·cm}^{-2} < w < 1.6\ \text{g·cm}^{-2}) \quad (4a)$$

$$\tau = 1.031412 - 0.11536\ w \ (1.6\ \text{g·cm}^{-2} < w < 3.0\ \text{g·cm}^{-2}) \quad (4b)$$

$$\tau = 0.982007 - 0.09611w \ (0.4\ \text{g·cm}^{-2} < w < 1.6\ \text{g·cm}^{-2}) \quad (4c)$$

$$\tau = 1.053710 - 0.14142w \ (1.6\ \text{g·cm}^{-2} < w < 3.0\ \text{g·cm}^{-2}) \quad (4d)$$

The algorithm performs well for atmospheric conditions where the water vapor content is 0.5–2.5 g·cm^{-2} [18,19,21].

3.1.3. Single-Channel (SC) Method

SC method [19,20] is also an approximation of RTE and requires only atmospheric water vapor content for atmospheric correction. In this method LST is obtained from the following Equation (5):

$$Ts = \gamma\left[\frac{1}{\varepsilon}\left(\psi_1 L_{sensor} + \psi_2\right) + \psi_3\right] + \delta \quad (5)$$

where: ε is surface emissivity, γ and δ are parameters directly depending on Planck function.

For Landsat TM5 band 6 γ and δ are calculated using expression (5a,5b):

$$\gamma \approx \frac{T_{sensor}^2}{1256 L_{sensor}} \quad (5a)$$

$$\delta \approx T_{sensor} - \frac{T_{sensor}^2}{1256 L_{sensor}} \quad (5b)$$

ψ_1, ψ_2 and ψ_3 are atmospheric correction functions expressed for Landsat-5 TM as Equation (6a–c):

$$\psi_1 = 0.14714w^2 - 0.15583w + 1.1234 \quad (6a)$$

$$\psi_2 = -1.1836w^2 - 0.37607w - 0.52894 \quad (6b)$$

$$\psi_3 = -0.04554w^2 + 1.8719w - 0.39071 \quad (6c)$$

where w is total atmospheric water vapor content in g·cm^{-2}.

Similar to the MW, the optimal performance of the SC algorithm is observed for the atmospheres with water vapor content in the range of 0.5–2.5 g·cm^{-2} [18,19,21].

3.1.4. Reference Land Surface Temperature (LST)

Because of the incompleteness of the *in situ* data, LSTs simulated by the latest version of the radiative transfer code MODTRAN 5 are used as a reference set. As suggested in previous studies [8,17,48,49], LSTs simulated using radiative transfer code can be an alternative for validation when field measurements at a required spatial scale are not available. The method was earlier applied for Landsat [34] and MODIS [48,49] LST assessment. Among the most important improvements in MODTRAN 5 compared to MODTRAN 4 is the incorporation of band model parameters based on HITRAN2008, with 2009 updates [9]. MODTRAN 5 performs calculations based on the information about observation geometry and atmospheric profiles at the moment of observation. The best results are achieved when data come from *in situ* radiosoundings synchronized in time with image acquisition. Unfortunately, they were not available in this study. When discussing the difficulty of obtaining local radiosounding data, multiple studies [17,50,51] suggest the use of the atmospheric profiles from the reanalysis products as a viable solution. Thus, we use NCEP atmospheric profiles interpolated for the exact location and time of Landsat overpass, the choice validated by previous research [17,50,51]. The NCEP atmospheric profiles interpolated for the study area and conditions by ACPC tool are complemented with on-site meteorological data for the lowest atmospheric layer, which together with the newer MODTRAN version (5 *vs*. 4) marks the difference with the RTE-ACPC procedure. To simulate the reference LSTs, the profiles are inserted into MODTRAN input file. Then the first MODTRAN run is performed with 0% surface albedo; atmospheric transmissivity (τ) and upwelling radiance (L_u) are extracted from the MODTRAN output files and integrated over the Landsat-5 TM thermal band using the sensor filter function. To calculate downwelling radiance (L_d) MODTRAN 5 is run for the second time with 100% surface albedo. Next, the obtained atmospheric correction parameters τ, L_u and L_d together with previously estimated emissivity ε are substituted into RTE (Equation (1)) to calculate the radiance from the target (L_{Ts}). The final step consists in transformation of the calculated target radiance into LST (LST_{ref}) by inversion of the Planck's law.

3.2. Emissivity Estimation

Most of the emissivity retrieval methods from remotely sensed data, such as TES [52] or TISI [53] cannot be used with Landsat images because there is only one thermal band. The possible solution is to apply one of the methods based on the normalized difference vegetation index (NDVI) [22]. Among the advantages of these methods is that they rely on the information from the image used for the LST retrieval [22]. The NDVI thresholds method ($NDVI^{THM}$) [25,54] based on the findings of Valor and Caselles [26] was applied to estimate surface emissivity in this study. The emissivity of the pixel is determined based on its NDVI. Different functions are applied to calculate emissivity depending on the NDVI range (Table 4).

In case of the mixed pixels category the NDVI values (thresholds) selection is based on an analysis of the images histograms. The soil emissivity ε_s value of 0.984 is based on *in situ* field measurements using box method [24] with an estimated error of 0.003 [24], and is similar to the values reported by previous research [34,55]. The vegetation emissivity ε_v is assigned the value of 0.990 [34]; $d\varepsilon = 0.01$ is the term accounting for surface roughness different from zero for heterogeneous covers [3];

and P_V is the vegetation fraction estimated from a scaled NDVI, according to Choudhury *et al.* [56] and Gutman and Ignatov [57]:

$$P_V = \frac{NDVI - NDVI_s}{NDVI_V - NDVI_s} \quad (7)$$

Table 4. Emissivity values assigned to ranges of the normalized difference vegetation index (NDVI) [26,34].

NDVI	Cover Type	Emissivity (ε)
NDVI < 0	Water	0.985
0 ≤ NDVI ≤ 0.1	Bare soil	*f* (red reflectivity)
0.1 ≤ NDVI ≤ 0.7	Vegetation mixed with soil	$0.990 P_V + 0.984(1 - P_V) + 0.04 P_V (1 - P_V)$
NDVI > 0.7	Vegetation	0.99

The validation of $NDVI^{THM}$ method performed by Sobrino *et al.* [34] gets the error of less than 0.01, which in terms of LST would mean the error below 0.5 °C [26]. Of the three dehesa landcover components, soil emissivities show the greatest variation in the thermal region of the spectrum [24,34]. As the soil emissivity measured *in situ* is high in present study, the related error should be smaller.

4. Results and Discussion

We present and discuss below the results of LST estimation in heterogeneous Mediterranean tree-grass (dehesa) ecosystem with the RTE-ACPC, MW and SC procedures described in Section 3.1. Emissivity ε is calculated using the NDVI Thresholds method presented in Section 3.2. Section 4.1 compares three sources of the atmospheric water vapor (*w*) and explains the choice of the NCEP REANALYSIS for this study. Section 4.2 analyses the differences between the LST_{ref} and LST generated by the tested procedures. Next, Section 4.3 discusses the relationship between Landsat LST and MODIS LST product. Both LST comparisons (LST_{ref} and MODIS) include the use of the *in situ* values of grass temperature measured in 2011 to assess the implications of time mismatch on the LST differences.

4.1. Atmospheric Water Vapor Content

Atmospheric conditions on the images acquisition dates are shown in Table 5. The registered mean *w* values were relatively low (1.292 g·cm^{-2}, 1.515 g·cm^{-2}, and 1.600 g·cm^{-2} for REANALYSIS, AERONET, and MODIS, respectively), and the maximum values were close to 2.5 g·cm^{-2}. Therefore, the data were considered adequate as inputs to the MW and SC methods. The average difference between *w* sources was around 0.3 g·cm^{-2}.

A detailed case-by-case analysis revealed important differences among databases on some dates. For example, the difference between MODIS and other sources was greater than 0.7 g·cm^{-2} for 4 August 2011, while AERONET exceeded *w* values from REANALYSIS in more than half a gram per square centimeter on 30 June 2010, and 17 October 2009. Although a clear pattern of differences among the data sources was not observed, the REANALYSIS water vapor values were

lower than those of the other two databases; only once the *w* value from this source was marginally greater than the value from MODIS (11 April 2010) and in two cases the *w* levels were greater than those of the AERONET database (1 August 2010, and 4 August 2011). The comparison of three different atmospheric water vapor (*w*) sources did not reveal statistically significant differences between them (*F*-Test = 1.16; *p*-value > 0.05). Hence, the REANALYSIS *w* values were used in atmospheric correction since this database is the result of modeling which assimilates data from multiple sources and is continuously updated. We did not use the MODIS product as a *w* source, because one of the objectives of the study is the comparison of the Landsat-retrieved LSTs with those from MODIS LST product, which employs MOD05 *w* values in the algorithm.

Table 5. Atmospheric water vapor content values ($g \cdot cm^{-2}$) obtained from the REANALYSIS and AERONET databases, and MODIS MOD05 product, as well as the air temperature T_{air} (°C) and relative humidity RH (%) for each date.

Date	Atmospheric Water Vapor Content Values ($g \cdot cm^{-2}$)			T_{air} (°C)	RH (%)
	REANALYSIS	AERONET	MODIS		
27/06/2009	1.770	1.796	1.791	26.80	31.59
29/07/2009	0.771	0.861	1.146	29.72	19.06
30/08/2009	2.060	2.373	2.088	31.52	32.73
15/09/2009	1.050	1.443	1.302	20.32	37.76
17/10/2009	0.390	0.967	1.080	16.34	48.66
06/02/2010	0.980	1.230	1.415	12.58	75.28
11/04/2010	0.580	0.781	0.569	17.87	41.94
30/06/2010	1.810	2.438	2.146	32.43	40.99
01/08/2010	1.590	1.410	1.674	33.51	28.1
05/11/2010	1.120	1.538	1.175	17.25	66.2
01/06/2011	1.410	1.551	1.887	20.73	43.16
04/08/2011	1.930	1.854	2.639	31.32	33.87
05/09/2011	1.330	1.448	1.887	24.78	42.43
Mean	1.292	1.515	1.600	24.24	41.67
Max	2.060	2.438	2.639	33.51	75.28
Min	0.390	0.781	0.569	12.58	19.06
St. Dev.	0.530	0.513	0.553	7.12	15.10

4.2. Landsat-5 TM Retrievals vs. Reference Land Surface Temperature (LST)

The LSTs retrieved from each Landsat-5 TM image and LST_{ref} are shown in Table 6. Among the Landsat LSTs the lowest average value of 31.36 °C is obtained using MW algorithm, followed by RTE-ACPC (32.98 °C) and SC (33.33 °C) procedures, which present the values very close to the LST_{ref} average of 33.17 °C. Minimum (around 12 °C) and maximum (around 45 °C) LSTs from RTE-ACPC and SC algorithms are also similar to the LST_{ref}; while for the MW method these statistics are lower (11.27 and 43.95 °C respectively). MW also shows standard deviations lower than other procedures.

There were no statistically significant differences between the values obtained using tested procedures (*F*-Test = 0.111; *p*-value > 0.05) and the degree of correlation between the values

obtained by different methods is very high ($R^2 > 0.986$). It is not strange considering that all the four algorithms are based on successive versions of the same radiative transfer code: LOWTRAN 7 (Mono-Window (MW)), MODTRAN 4 (RTE-ACPC and SC) and MODTRAN 5 (LST_{ref}), developed in 1988 [58], 1999 [59] and 2011 [9] respectively. Moreover, all of them employ the fewest (although different) possible number of parameters for atmospheric correction (*w* for SC; T_a and *w* for MW; profiles of *RH*, T_a and atmospheric pressure for RTE-ACPC and LST_{ref}) and the same emissivity.

Table 6. LST values retrieved from Landsat-5 TM images using Mono-Window (MW), Single-Channel (SC), Radiative Transfer Equation Atmospheric Correction Parameters Calculator (RTE-ACPC, procedure based on the online ACPC), LST_{ref} and LST from MODIS MOD11_L2 product used for comparison, as well as LST_{in_situ} (grass surface temperature at 10:50 a.m. GMT).

Date	LST (°C) Landsat			LST (°C) MODIS	LST_{ref} (°C)	LST_{in_situ} (°C)
	MW	SC	RTE-ACPC			
27/06/2009	41.92	43.79	44.91	39.87	43.55	--
29/07/2009	43.95	45.32	45.36	39.21	45.11	--
30/08/2009	41.11	45.44	42.15	38.87	45.00	--
15/09/2009	29.78	30.75	31.25	28.03	30.68	--
17/10/2009	21.85	22.59	21.33	22.23	22.32	--
06/02/2010	11.27	12.04	11.99	11.99	12.01	--
11/04/2010	21.61	22.45	22.17	22.35	22.09	--
30/06/2010	36.23	40.14	41.40	34.17	40.40	--
01/08/2010	41.49	44.76	42.96	39.51	43.82	--
05/11/2010	17.49	18.25	17.78	18.41	17.59	--
01/06/2011	27.76	29.09	27.97	25.27	28.52	33.01
04/08/2011	40.39	44.27	44.85	38.55	45.04	45.71
05/09/2011	32.79	34.38	34.57	29.29	35.03	38.11
Mean	31.36	33.33	32.98	29.83	33.17	--
Min.	11.27	12.04	11.99	11.99	12.01	--
Max.	43.95	45.44	45.36	39.87	45.11	--
St. dev.	10.69	11.68	11.71	9.34	11.76	--

When compared to LST_{ref}, the RMSDs are within 2.4 °C (Table 7): SC and RTE-ACPC present RMSDs lower than 1 °C, while the MW shows the highest RMSD (2.34 °C) with systematical LST underestimation (bias = −1.81 °C). SC values are the closest to the LST_{ref} with the RMSD of 0.50 °C (bias = 0.16); RTE-ACPC shows similar RMSD (0.85 °C) and a slight underestimation of the LST (bias = −0.19 °C).

Differences between LST_{ref} and Landsat LSTs depend on the "age" of the code version used in procedure development: greater differences with LST_{ref} correspond to procedures based on the older code version, *i.e.*, MW-LST_{ref} > SC-LST_{ref}. They are also consistent with the results of LST simulations using LOWTRAN 7 and MODTRAN 4 performed by Jiménez-Muñoz *et al.* [19], which show that MODTRAN 4 generates greater *w* values (around 1 $g \cdot cm^{-2}$ for high w values) resulting in higher LSTs. At the same time, the SC and RTE-ACPC (methods based on MODTRAN4) are closer to the *in situ* data: (averages of 5.46, 3.19, and 3.31 °C for LST_{in_situ}-LST_{MW}, LST_{in_situ}-LST_{SC}, and

LST_{in_situ}-$LST_{RTE\text{-}ACPC}$, respectively), although this comparison is not fully accurate since LST_{in_situ} corresponds only to grass component of the landcover.

Table 7. Root mean square deviation (RMSD) of the comparison between the LST_{ref}, MODIS product and LSTs obtained from Landsat-5 TM by MW, SC and RTE-ACPC (°C).

RMSD	MW	SC	RTE-ACPC	MODIS
MW	--	--	--	--
SC	2.37	--	--	--
RTE-ACPC	2.28	1.26	--	--
MODIS	2.27	4.29	4.16	--
LST_{ref}	2.34	0.50	0.85	4.27

Even though MW systematically underestimates LST, the size of the differences varies from 0.11 to 4.66 °C depending on the date (Table 8); the range of variations for SC and RTE-ACPC is much smaller (below 1 °C and 3 °C for SC and RTE-ACPC, respectively). Considering that both procedures use the same emissivity, explanation of the anomalies lies in different sensitivity of the algorithms to atmospheric variables. Good correlation of the differences between LST_{ref} and MW with w and air temperature (R = 0.8) can be appreciated in Figures 2 and 3; high atmospheric water vapor concentration and high temperatures in summer time explaining the biggest LST deviations. The same graphics reveal that there is no relationship between atmospheric parameters and the differences between SC and LST_{ref} ($R < 0.2$). Bigger errors in hot and wet conditions have already been detected in other studies [19,50]. Modeling [60] shows that a typical w error of 10% [61] may lead to LST error of 0.4 K and 0.2 K for SC and MW algorithms respectively for summer atmosphere [60]. For MW it is also necessary to consider the 0.2 °C error due to the air temperature [21]. Because in MW algorithm coefficients are developed only for two air temperature values and a reduced number of standard atmospheres, the algorithm fails to represent real atmospheric conditions in the study area correctly, especially on in summer. However, SC incorporates atmospheric functions based on extensive atmospheric profile databases allowing more precise representation of atmospheric conditions over the study site at the moment of satellite pass [19,50].

Based on statistical analysis we can conclude that SC and RTE-ACPC procedures are capable of retrieving LSTs in the study area of Mediterranean tree-grass ecosystem with an error below 1 °C, which is similar to the results of the previous studies conducted in the homogeneous areas [34,62]. Thus, Sobrino *et al.* [34] compared LSTs from MW and SC methods applied to Landsat images with LSTs simulated using radiative transfer code and *in situ* emissivity in agricultural area obtaining the errors of around 0.9 °C for SC and around 2 °C for MW procedures; similar errors were reported by Copertino *et al.* [33] who applied the same methods for estimating LST over different landcover types in Southern Italy, in this case retrieved LSTs were compared to the soil temperatures. Limin *et al.* [60] compared LST estimated from HJ-1B satellite by MW and SC with MODTRAN 4 simulations of LST registering errors below 1 °C in summer for nadiral view of the sensor.

Remote Sens. **2014**, *6* **4359**

Table 8. Differences between the LST retrieved from Landsat-5 TM using RTE-ACPC, MW and SC procedures and LST simulated using MODTRAN5 (LST_{ref}).

Date	LST_{ref} (°C)	$LST_{Landsat}$–LST_{ref} (°C)		
		MW	SC	RTE−ACPC
27/06/2009	43.55	−1.63	0.24	1.36
29/07/2009	45.11	−1.16	0.21	0.25
30/08/2009	45.00	−3.89	0.43	−2.85
15/09/2009	30.68	−0.9	0.07	0.57
17/10/2009	22.32	−0.47	0.27	−0.99
06/02/2010	12.01	−0.74	0.03	−0.02
11/04/2010	22.09	−0.48	0.36	0.08
30/06/2010	40.40	−4.17	−0.27	1.00
01/08/2010	43.82	−2.34	0.94	−0.86
05/11/2010	17.59	−0.11	0.65	0.19
01/06/2011	28.52	−0.76	0.58	−0.55
04/08/2011	45.04	−4.66	−0.77	−0.19
05/09/2011	35.03	−2.24	−0.65	−0.46
Bias		−1.81	0.16	−0.19
St. Dev		1.54	0.49	1.05

Figure 2. Relationship between *w* and $LST_{Landsat}$–LST_{ref}.

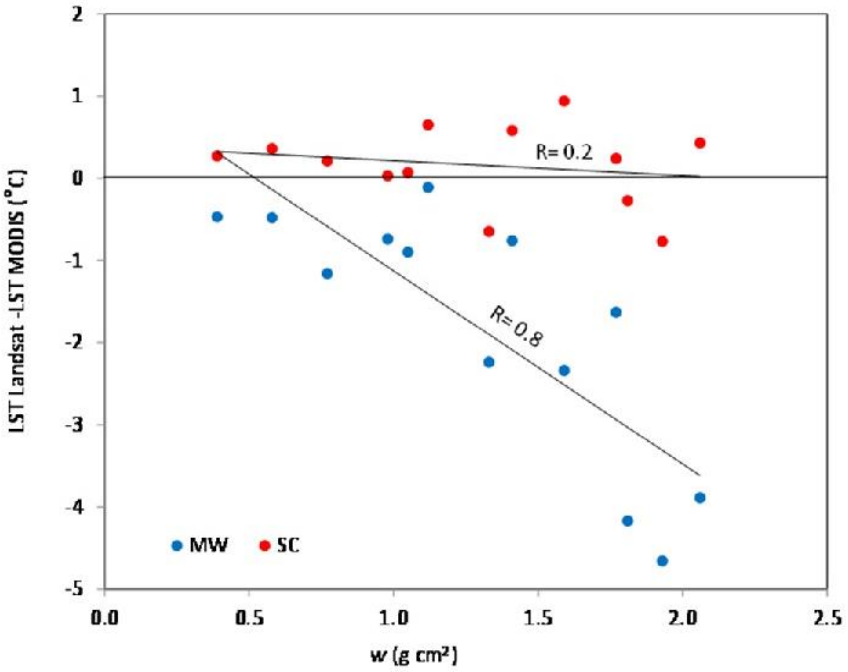

Figure 3. Relationship between near surface air temperature T_{air} and $LST_{Landsat}$–LST_{ref}.

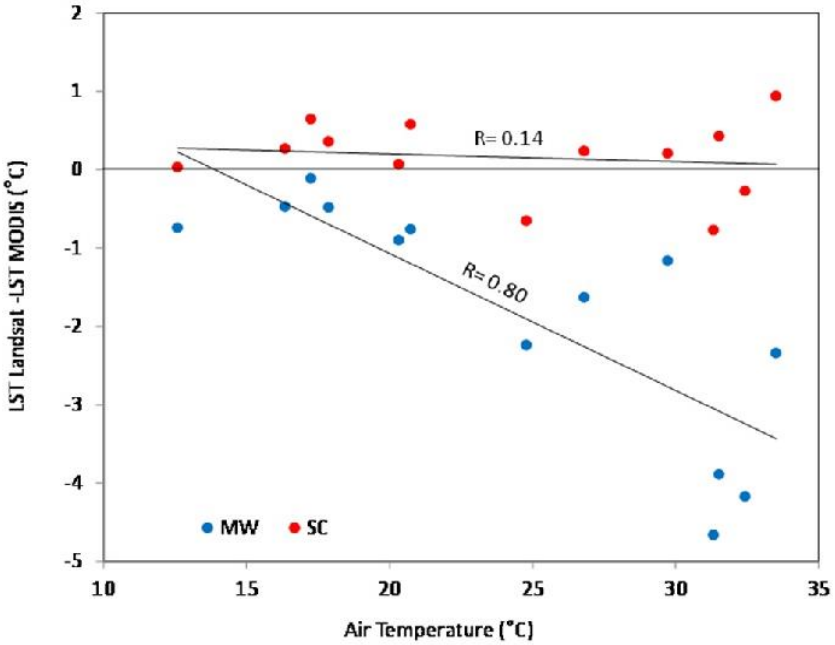

4.3. Landsat LST vs. MODIS Land Surface Temperature (LST)

We now present the comparison of Landsat LSTs and LSTs from MODIS LST product. Before the comparison some adjustment was performed to account for differences in data format and spatial resolution between Landsat and MODIS. MODIS LST images (MOD11_L2 product) were reprojected to match spatial reference of Landsat. Since the study site is in the middle of the much more extensive tree-grass ecosystem area with similar LST variability at the MODIS scale, the average LST value of the Landsat pixels inside the MODIS pixel covering the center of the study area is calculated for each date and method and is used for the comparison.

The results of the comparison with MODIS product LST and the intercomparison of the LST values retrieved by the tested methods (Table 7) show that SC and RTE-ACPC are more similar to each other than to the LSTs from MODIS product (RMSD of 4.16 and 4.29 °C for RTE-ACPC and SC respectively). On the contrary, the MW-estimated LST values are much closer to MODIS LSTs (RMSD of 2.27 °C).

Compared to Landsat-estimated values MODIS product underestimates LST, the bias is 1.5 °C for MW and 3.5 °C for SC procedures. This is in agreement with the results reported in previous studies [40,63,64], which mention that LST values from MODIS product are lower than those obtained from other sensors or *in situ* measurements. Thus, Trigo *et al.* [65] observed a negative bias of 2.6 °C in MODIS LST compared with ground values, especially at night. The underestimation also occurs when comparing MODIS with other sensors, such as SEVIRI [65] and AATSR [40]. In case of AATSR sensor, which is the most accurate infrared radiometer currently being flown in space according to [40], the biases of −0.5 and −1.2 °C were observed both during day and night respectively. So, it is evident that there is a problem related to spatial scale differences, which makes

complicated the comparison of satellite and *in situ* data [17,48,49,66], although the differences are also affected by other factors. One of the most important is the impact of the observation angles on the measurements: while Landsat angles of observation are almost nadiral, MODIS views the study area at an angle of 60°, *i.e.*, the sensor observes the surface from the west, detecting higher fraction of shadow and vegetation surfaces considerably decreasing LST. Previous studies show that the differences in the LST measured in nadir and off-nadir observations can be as large as 5 °C depending on the angle and cover type [17,67].

On the other hand, the 21 min time mismatch in the study area overpass between the sensors (ranging from 7 min to 38 min, see Table 1) also operates in the same direction. The analysis of the time differences between Landsat and MODIS is performed using data from thermal sensor installed in the study area. The average temperature increment between 10:30 and 10:50 GMT for the three dates in 2011, all of them in summer, is around 1.5 °C (Table 2). These coincide with [66] who indicate that LST difference between the LSTs at the moments of Landsat and MODIS Terra overpasses can range from 0.8 to 2 K, depending on the vegetation cover. If this time mismatch and the corresponding surface temperature increase were taken into account the gap between Landsat and MODIS would be reduced. The LSTs were not adjusted because only grass temperatures are available, not so the temperatures of tree canopies and shadows. However, even though tree canopies cover only about 20% of the area, we would expect significant decrease of the LST due to their presence within the MODIS pixel, since some studies [68] indicate that the difference between the grass and tree canopy temperatures in summer can be around 6–15 °C depending on the species and time of the day.

Although MW apparently generates LST values, which are closer to those from MODIS, they may not be more accurate than LSTs estimated by other procedures. The similarity between MW and MODIS LSTs results from two trends acting in the same direction: one is the underestimation of the LST by MW algorithm due to the use of the older radiative transfer code version (LOWTRAN) and another is the underestimation of the LSTs by MODIS due to the differences in time and observation angles between MODIS and Landsat and implications of these differences on the emissivity.

When SC results (the closest to the LST_{ref}) are compared to MODIS LST, a seasonal bias is observed: the greatest variances (above 6 °C) occur in summer (Table 9) and the lowest (0.00–0.38 °C) in winter and autumn. This fact was already mentioned in other studies [51]. Trigo *et al.* [65] observed that greater LST dispersion in summer can be related to the great thermal contrasts between landcover components (bareground, grass, tree canopy) taking place during this season. Because of higher spatial resolution and higher variability in emissivity, Landsat is more sensitive to this dispersion. Greater thermal range of around 8 °C on summer dates can be appreciated in Figure 4 showing Landsat LST variability within MODIS pixel. We should also consider that MODIS surface emissivity estimation is based on landcover types from the map updated annually [69], while NDVI Thresholds emissivity algorithm used in this study is based on NDVI (see Section 2.4).

Table 9. Differences between LST retrieved from Landsat using MW and SC methods and LST from MODIS MOD11_L2 product.

Date	LST_{MODIS} (°C)	$LST_{Landsat}$–LST_{MODIS} (°C)		
		MW	SC	RTE–ACPC
27/06/2009	39.87	2.05	3.92	5.04
29/07/2009	39.21	4.74	6.11	6.15
30/08/2009	38.87	2.24	6.57	3.28
15/09/2009	28.03	1.75	2.72	3.22
17/10/2009	22.23	−0.38	0.36	−0.90
06/02/2010	11.99	−0.72	0.05	0.00
11/04/2010	22.35	−0.74	0.10	−0.18
30/06/2010	34.17	2.06	5.97	7.23
01/08/2010	39.51	1.98	5.25	3.45
05/11/2010	18.41	−0.92	−0.16	−0.63
01/06/2011	25.27	2.49	3.82	2.70
04/08/2011	38.55	1.84	5.72	6.30
05/09/2011	29.29	3.50	5.09	5.28
Bias		1.53	3.50	3.15
St. Dev		1.74	2.59	2.82

Figure 4. Box plot showing variability of Landsat LST estimated from Landsat-5 TM images using MW (in red) and SC (in blue) within MODIS pixel.

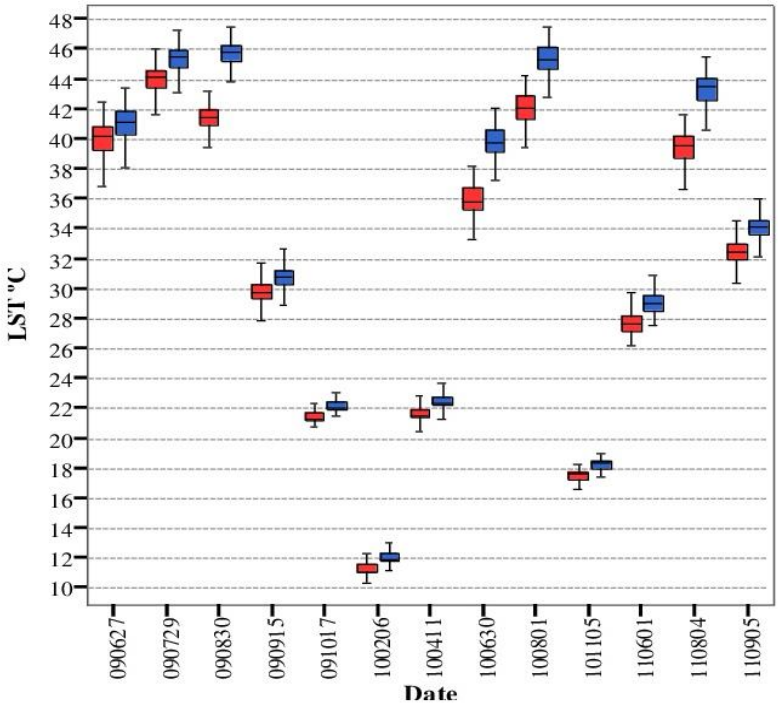

Another explanation for the magnitude of $LST_{Landsat}$–LST_{MODIS} is the greater spatial and temporal variability of emissivity values estimated from Landsat-5 TM NDVI. This wider range is caused by the

higher spatial resolution of the Landsat-5 TM, different algorithms used for emissivity estimation for two sensors and differences in viewing angles between Landsat and MODIS Terra (almost nadiral for Landsat *vs.* around 60° viewing angles for MODIS Terra) resulting in greater sensitivity of Landsat to an increase in the soil component and greater temperature contrasts between areas with and without vegetation, characteristic to summer as a consequence of grass senescence.

5. Conclusions

The study demonstrates that LST of dehesa ecosystem can be estimated from Landsat-5 TM thermal band using SC and RTE-ACPC procedures with RMSDs lower than 1 °C and the RMSD of 2.3 °C using MW algorithm, with expected uncertainties in energy fluxes modeling of around 10–30 $W \cdot m^2$ for SC and RTE-ACPC [17]. The differences with the reference LSTs (LST_{ref}) are due to the fact that the tested methods are based on the different versions of the radiative transfer code: LOWTRAN 7 for MW and MODTRAN 4 for SC and RTE-ACPC. Moreover, there is a seasonal bias in the MW results, as evident from the correlations between MW-LST_{ref} and near-surface air temperature and atmospheric water vapor w (R = 0.8), explained by the worse fit of MW coefficients to real atmospheric conditions in the study area compared to other procedures. This dependence is not evident in the LSTs obtained by the SC and RTE-ACPC procedures.

On the other hand, the existing LST mismatch between Landsat and MODIS is due mainly to (1) the time differences in the satellites overpasses and (2) the differences in the viewing angles which make Landsat much more sensitive to changes in the proportion of different landcover components with high thermal contrasts (soil and vegetation) and decrease of emissivity, especially during hot summer months.

Considering the generally-accepted error at the level of 1–2 K [70,71], the three tested procedures (SC, RTE-ACPC, and MW) can be used for LST estimation from Landsat-5 TM thermal data. RMSDs obtained for SC and RTE-ACPC procedures are below 1 °C, with the best results for SC (RMSD = 0.5 °C). This algorithm, which does not require radiosounding data, is considered the most adequate for integration with LST from MODIS MOD11_L2 product. However, the between-sensors differences due to time mismatch and observation angles should be taken into account. It was not possible to estimate the precise magnitude of Landsat-MODIS LST differences due to the lack of information on the contribution of each of the landcover components to ensemble radiance from heterogeneous and non-isothermal pixel characteristic for dehesa ecosystem.

Acknowledgments

This research has been financially supported by the BIOSPEC project “Linking spectral information at different spatial scales with biophysical parameters of Mediterranean vegetation in the context of Global Change” [28] (CGL2008-02301/CLI, Ministry of Science and Innovation, Spain), the FLUXPEC project “Monitoring changes in water and carbon fluxes from remote and proximal sensing in a Mediterranean dehesa ecosystem” [29] (CGL2012-34383, Ministry of Economy and Competitiveness, Spain), and by a collaboration agreement between the Aragón Government and the *Obra Social* “*La Caixa*” (DGA-La Caixa, GA-LC-042/2011), Spain. The authors also appreciate the financial support provided to this research by SENESCYT, Ecuador. We are grateful to Research

Group AIRE of Physics Department, University of Extremadura, for establishing and maintaining the Cáceres AERONET site database used in this research.

Author Contributions

This research was conducted by Lidia Vlassova and Fernando Perez-Cabello. Lidia Vlassova performed data processing and modelling. Hector Nieto and Pilar Martín contributed to interpretation of the results and supervision of the methods employed. David Riaño and Juan de la Riva contributed to the organization of the paper. All authors helped in editing and revision of the manuscript, and responding to reviewers comments.

Conflicts of Interest

The authors declare no conflict of interest.

References

1. Quattrochi, D.A.; Luvall, J.C. *Thermal Remote Sensing in Land Surface Processing*; CRC Press: Boca Raton, FL, USA, 2004.
2. Kustas, W.; Anderson, M. Advances in thermal infrared remote sensing for land surface modeling. *Agric. For. Meteorol.* **2009**, *149*, 2071–2081.
3. Zhan, X.; Kustas, W.P.; Humes, K.S. An intercomparison study on models of sensible heat flux over partial canopy surfaces with remotely sensed surface temperature. *Remote Sens. Environ.* **1996**, *58*, 242–256.
4. Jia, L.; Menenti, M.; Su, Z.B.; Li, Z.-L.; Djepa, V.; Wang, J.M. Modeling Sensible Heat Flux Using Estimates of Soil and Vegetation Temperatures: The HEIFE and IMGRASS Experiments. In *Remote Sensing and Climate Modeling: Synergies and Limitations*; Beniston, M., Verstraete, M., Eds.; Kluwer Academic Publishers: Berlin, Germany, 2001; pp. 23–49.
5. Kalma, J.; McVicar, T.; McCabe, M. Estimating land surface evaporation: A review of methods using remotely sensed surface temperature data. *Surv. Geophys.* **2008**, *29*, 421–469.
6. Moran, M.S.; Rahman, A.F.; Washburne, J.C.; Goodrich, D.C.; Weltz, M.A.; Kustas, W.P. Combining the Penman-Monteith equation with measurements of surface temperature and reflectance to estimate evaporation rates of semiarid grassland. *Agric. For. Meteorol.* **1996**, *80*, 87–109.
7. Gamon, J.A.; Huemmrich, K.F.; Peddle, D.R.; Chen, J.; Fuentes, D.; Hall, F.G.; Kimball, J.S.; Goetz, S.; Gu, J.; McDonald, K.C.; *et al.* Remote sensing in BOREAS: Lessons learned. *Remote Sens. Environ.* **2004**, *89*, 139–162.
8. Li, Z.-L.; Tang, B.-H.; Wu, H.; Ren, H.; Yan, G.; Wan, Z.; Trigo, I.F.; Sobrino, J.A. Satellite-derived land surface temperature: Current status and perspectives. *Remote Sens. Environ.* **2013**, *131*, 14–37.
9. Berk, A.; Anderson, G.P.; Acharya, P.K.; Shettle, E.P. *Modtran 5.2.1 User's Manual*; Spectral Sciences, Inc. & Air Force Research Laboratory: Burlington, MA, USA, 2011.

10. Barsi, J.A.; Barker, J.L.; Schott, J.R. An Atmospheric Correction Parameter Calculator for a Single Thermal Band Earth-Sensing Instrument. In Processdings of the 2003 IEEE International Geoscience and Remote Sensing Symposium. IGARSS '03. Melbourne, Australia, 21–25 July 2003; Volume 5, pp. 3014–3016.
11. Barsi, J.A.; Schott, J.R.; Palluconi, F.D.; Hook, S.J. Validation of a web-based atmospheric correction tool for single thermal band instruments. *Proc. SPIE* **2005**, doi:10.1117/12.619990
12. Precipitable Water at the VLA—1990–1998. Available online: http://legacy.nrao.edu/alma/memos/html-memos/alma237/memo237.html (accessed on 5 May 2014).
13. MODIS Website. Available online: http://modis.gsfc.nasa.gov (accessed on 5 May 2014).
14. SEVIRI Sensor WDC-RSAT. Available online: http://wdc.dlr.de/sensors/seviri (accessed on 5 May 2014).
15. Landsat Missions. Available online: http://landsat.usgs.gov (accessed on 5 May 2014).
16. Landsat 8 (L8) Operational Land Imager (OLI) and Thermal Infrared Sensor (TIRS). Available online: http://landsat.usgs.gov/calibration_notices.php (accessed on 5 May 2014).
17. Tang, H.; Li, Z.-L. Introduction. In *Quantitative Remote Sensing in Thermal Infrared*; Springer: Berlin/Heidelberg, Germany, 2014; pp. 1–4.
18. Cristóbal, J.; Jiménez-Muñoz, J.C.; Sobrino, J.A.; Ninyerola, M.; Pons, X. Improvements in land surface temperature retrieval from the Landsat series thermal band using water vapor and air temperature. *J. Geophys. Res.* **2009**, *114*, doi:10.1029/2008JD010616.
19. Jimenez-Munoz, J.C.; Cristobal, J.; Sobrino, J.A.; Soria, G.; Ninyerola, M.; Pons, X. Revision of the single-channel algorithm for land surface temperature retrieval from Landsat thermal-infrared data. *IEEE Trans. Geosci. Remote Sens.* **2009**, *47*, 339–349.
20. Jiménez-Muñoz, J.C.; Sobrino, J.A. A generalized single-channel method for retrieving land surface temperature from remote sensing data. *J. Geophys. Res.* **2004**, *108*, 46–88.
21. Qin, Z.; Karnieli, A.; Berliner, P. A mono-window algorithm for retrieving land surface temperature from Landsat TM data and its application to the Israel-Egypt border region. *Int. J. Remote Sens.* **2001**, *22*, 3719–3746.
22. Li, Z.-L.; Wu, H.; Wang, N.; Qiu, S.; Sobrino, J.A.; Wan, Z.; Tang, B.-H.; Yan, G. Land surface emissivity retrieval from satellite data. *Int. J. Remote Sens.* **2013**, *34*, 3084–3127.
23. Olioso, A. Simulating the relationship between thermal emissivity and the normalized difference vegetation index. *Int. J. Remote Sens.* **1995**, *16*, 3211–3216.
24. Rubio, E.; Caselles, V.; Badenas, C. Emissivity measurements of several soils and vegetation types in the 8–14 μm wave band: Analysis of two field methods. *Remote Sens. Environ.* **1997**, *59*, 490–521.
25. Sobrino, J.A.; Raissouni, N. Toward remote sensing methods for land cover dynamic monitoring: Application to Morocco. *Int. J. Remote Sens.* **2000**, *21*, 353–366.
26. Valor, E.; Caselles, V. Mapping land surface emissivity from NDVI: Application to European, African, and South American areas. *Remote Sens. Environ.* **1996**, *57*, 167–184.
27. Van de Griend, A.A.; Owe, M. On the relationship between thermal emissivity and the normalized difference vegetation index for natural surfaces. *Int. J. Remote Sens.* **1993**, *14*, 1119–1131.
28. BIOSPEC. Available online: http://www.lineas.cchs.csic.es/biospec (accessed on 5 May 2014).
29. FLUXPEC. Available online: http://www.lineas.cchs.csic.es/fluxpec (accessed on 5 May 2014).

30. Agam, N.; Kustas, W.P.; Anderson, M.C.; Li, F.; Neale, C.M. A vegetation index based technique for spatial sharpening of thermal imagery. *Remote Sens. Environ.* **2007**, *107*, 545–558.
31. Walker, J.J.; De Beurs, K.M.; Wynne, R.H.; Gao, F. Evaluation of landsat and MODIS data fusion products for analysis of dryland forest phenology. *Remote Sens. Environ.* **2012**, *117*, 381–393.
32. Cleugh, H.A.; Leuning, R.; Mu, Q.; Running, S.W. Regional evaporation estimates from flux tower and modis satellite data. *Remote Sens. Environ.* **2007**, *106*, 285–304.
33. Copertino, V.A.; Di Pietro, M.; Scavone, G.; Telesca, V. Comparison of algorithms to retrieve land surface temperature from Landsat-7 ETM+ IR data in the Basilicata Ionian band. *Tethys* **2012**, *9*, 25–34.
34. Sobrino, J.A.; Jiménez-Muñoz, J.C.; Paolini, L. Land surface temperature retrieval from Landsat TM 5. *Remote Sens. Environ.* **2004**, *90*, 434–440.
35. Baldocchi, D.; Falge, E.; Gu, L.; Olson, R.; Hollinger, D.; Running, S.; Anthony, P.; Bernhofer, C.; Davis, K.; Evans, R.; *et al.* FLUXNET: A new tool to study the temporal and spatial variability of ecosystem-scale carbon dioxide, water vapor and energy flux densities. *Bull. Am. Meteorol. Soc.* **2001**, *82*, 2415–2434.
36. Núñez Corchero, M.; Sosa Cardo, J.A. *Climatología de Extremadura (1961–1990)*; Ministerio de Medio Ambiente: Madrid, Spain, 2001.
37. USGS Global Visualization Viewer. Available online: http://glovis.usgs.gov (accessed on 5 May 2014).
38. Wan, Z.; Dozier, J. A generalized split-window algorithm for retrieving land-surface temperature from space. *IEEE Trans. Geosci. Remote Sens.* **1996**, *34*, 892–905.
39. Li, H.; Liu, Q.; Zhong, B.; Du, Y.; Wang, H.; Wang, Q. A Single-Channel Algorithm for Land Surface Temperature Retrieval from HJ-1B/IRS Data Based on a Parametric Model. In Proceedings of the 2010 IEEE International Geoscience and Remote Sensing Symposium (IGARSS), Honolulu, HI, USA, 25–30 July 2010; pp. 2448–2451.
40. Noyes, E.; Good, S.; Corlet, G.; Kong, X.; Remedios, J.; Llewellyn-Jones, D. AATSR LST Product Validation. In Proceedings of the Second Working Meeting on MERIS and AATSR Calibration and Geophysical Validation (MAVT-2006), Frascati, Italy, 20–24 March 2006.
41. Aerosol Robotic Network (AERONET). Available online: http://aeronet.gsfc.nasa.gov (accessed on 5 May 2014).
42. Kistler, R.; Kalnay, E.; Collins, W.; Saha, S.; White, G.; Woollen, J.; Chelliah, M.; Ebisuzaki, W.; Kanamitsu, M.; Kousky, V.; *et al. The NCEP-NCAR 50-Year Reanalysis: Monthly Means CD-ROM and Documentation*; American Meteorological Society: Boston, MA, USA, 2001.
43. NCEP/NCAR Reanalysis Monthly Means and Other Derived Variables. Available online: http://www.esrl.noaa.gov/psd/data/gridded/data.ncep.reanalysis.derived.surface.html (accessed on 5 May 2014).
44. NASA Land Data Service and Products. Available online: https://lpdaac.usgs.gov/get_data/data_pool (accessed on 5 May 2014).
45. ENVI Software. Available online: http://www.exelisvis.com/ProductsServices/ENVI/ENVI.aspx (accessed on 5 May 2014).
46. Atmospheric Correction Parameter Calculator. Available online: http://atmcorr.gsfc.nasa.gov (accessed on 5 May 2014).

47. Sobrino, J.A.; Coll, C.; Caselles, V. Atmospheric correction for land surface temperature using NOAA-11 AVHRR channels 4 and 5. *Remote Sens. Environ.* **1991**, *38*, 19–34.
48. Coll, C.; Valor, E.; Galve, J.M.; Mira, M.; Bisquert, M.; García-Santos, V.; Caselles, E.; Caselles, V. Long-term accuracy assessment of land surface temperatures derived from the Advanced Along-Track Scanning Radiometer. *Remote Sens. Environ.* **2012**, *116*, 211–225.
49. Wan, Z.; Li, Z.L. Radiance-based validation of the v5 MODIS land-surface temperature product. *Int. J. Remote Sens.* **2008**, *29*, 5373–5395.
50. Coll, C.; Caselles, V.; Valor, E.; Niclòs, R. Comparison between different sources of atmospheric profiles for land surface temperature retrieval from single channel thermal infrared data. *Remote Sens. Environ.* **2012**, *117*, 199–210.
51. Jiménez-Muñoz, J.C.; Sobrino, J.A.; Mattar, C.; Franch, B. Atmospheric correction of optical imagery from MODIS and Reanalysis atmospheric products. *Remote Sens. Environ.* **2010**, *114*, 2195–2210.
52. Gillespie, A.; Rokugawa, S.; Matsunaga, T.; Cothern, J.S.; Hook, S.; Kahle, A.B. A temperature and emissivity separation algorithm for advanced spaceborne thermal emission and reflection radiometer (ASTER) images. . *IEEE Trans. Geosci. Remote Sens* **1998**, *36*, 1113–1126.
53. Becker, F.; Li, Z.-L. Temperature-independent spectral indices in thermal infrared bands. *Remote Sens. Environ.* **1990**, *32*, 17–33.
54. Sobrino, J.A.; Raissouni, N.; Li, Z.-L. A comparative study of land surface emissivity retrieval from NOAA data. *Remote Sens. Environ.* **2001**, *75*, 256–266.
55. Sobrino, J.A.; Jiménez-Muñoz, J.C.; Soria, G.; Romaguera, M.; Guanter, L.; Moreno, J.; Plaza, A.; Martinez, P. Land surface emissivity retrieval from different VNIR and TIR sensors. *IEEE Trans. Geosci. Remote Sens* **2008**, *46*, 316–327.
56. Choudhury, B.J.; Ahmed, N.U.; Idso, S.B.; Reginato, R.J.; Daughtry, C.S.T. Relations between evaporation coefficients and vegetation indices studied by model simulations. *Remote Sens. Environ.* **1994**, *50*, 1–17.
57. Gutman, G.; Ignatov, A. The derivation of the green vegetation fraction from NOAA/AVHRR data for use in numerical weather prediction models. *Int. J. Remote Sens.* **1998**, *19*, 1533–1543.
58. Kneizys, F.X.; Shettle, E.; Abreu, L.; Chetwynd, J.; Anderson, G. *Users Guide to LOWTRAN 7*; Air Force Geophysics Lab Hanscom AFB: Saugus, MA, USA, 1988.
59. Berk, A.; Anderson, G.P.; Bernstein, L.S.; Acharya, P.K.; Dothe, H.; Matthew, M.W.; Adler-Golden, S.M.; Chetwynd, J.H., Jr.; Richtsmeier, S.C.; Pukall, B. Modtran4 Radiative Transfer Modeling for Atmospheric Correction. In Proceedings of the International Society for Optics and Photonics SPIE's International Symposium on Optical Science, Engineering, and Instrumentation, Denver, CO, USA, 18 July 1999; pp. 348–353.
60. Zhao, L.; Tian, Q.; Wan, W.; Yu, T.; Gu, X.; Chen, H. Atmospheric Sensitivity on Land Surface Temperature Retrieval Using Single Channel Thermal Infrared Remote Sensing Data: Comparison among Models. In Proceedings of the 2010 18th International Conference on Geoinformatics, Beijing, China, 18–20 June 2010; pp. 1–6.
61. Schmugge, T.; Hook, S.J.; Coll, C. Recovering surface temperature and emissivity from thermal infrared multispectral data. *Remote Sens. Environ.* **1998**, *65*, 121–131.

62. Srivastava, P.K.; Majumdar, T.J.; Bhattacharya, A.K. Surface temperature estimation in Singhbhum Shear zone of India using Landsat-7 ETM+ thermal infrared data. *Adv. Space Res.* **2009**, *43*, 1563–1574.
63. Qian, Y.-G.; Li, Z.-L.; Nerry, F. Evaluation of land surface temperature and emissivities retrieved from MSG/SEVIRI data with MODIS land surface temperature and emissivity products. *Int. J. Remote Sens.* **2012**, *34*, 3140–3152.
64. Soria, G.; Sobrino, J.A.; Atitar, M.; Jiménez-Muñoz, J.C.; Hidalgo, V.; Julien, Y.; Ruescas, A.B.; Franch, B.; Mattar, C.; Oltra, R. AATSR Land Surface Temperature Product: Comparison with SEVIRI and MODIS in the Framework of CEFLES2 Campaigns. In Proceedings of the 2nd MERIS/AATSR User Workshop, 22–26 September 2008, Frascati, Italy, 2008.
65. Trigo, I.F.; Monteiro, I.T.; Olesen, F.; Kabsch, E. An assessment of remotely sensed land surface temperature. *J. Geophys. Res. Atmos.* **2008**, *113*, doi:10.1029/2008JD010035.
66. Li, F.; Jackson, T.J.; Kustas, W.P.; Schmugge, T.J.; French, A.N.; Cosh, M.H.; Bindlish, R. Deriving land surface temperature from Landsat 5 and 7 during SMEX02/SMACEX. *Remote Sens. Environ.* **2004**, *92*, 521–534.
67. Rasmussen, M.O.; Pinheiro, A.C.; Proud, S.R.; Sandholt, I. Modeling angular dependences in land surface temperatures from the seviri instrument onboard the geostationary Meteosat second generation satellites. *IEEE Trans. Geosci. Remote Sens.* **2010**, *48*, 3123–3133.
68. Hesslerová, P.; Pokorný, J.; Brom, J.; Rejšková-Procházková, A. Daily dynamics of radiation surface temperature of different land cover types in a temperate cultural landscape: Consequences for the local climate. *Ecol. Eng.* **2013**, *54*, 145–154.
69. Snyder, W.C.; Wan, Z.; Zhang, Y.; Feng, Y.Z. Classification-based emissivity for land surface temperature measurement from space. *Int. J. Remote Sens.* **1998**, *19*, 2753–2774.
70. French, A.N.; Norman, J.M.; Anderson, M.C. A simple and fast atmospheric correction for spaceborne remote sensing of surface temperature. *Remote Sens. Environ.* **2003**, *87*, 326–333.
71. Sobrino, J.A.; Frate, F.; Drusch, M.; Jiménez-Muñoz, J.C.; Manunta, P. Review of High Resolution Thermal Infrared Applications and Requirements: The FUEGOSAT Synthesis Study. In *Thermal Infrared Remote Sensing*; Kuenzer, C., Dech, S., Eds.; Springer: Dordrecht, The Netherlands, 2013; pp. 197–214.

7. Analysis of the relationship between land surface temperature and wildfire severity in a series of Landsat images

This chapter reproduces the text of the following article:

Title:
Analysis of the relationship between land surface temperature and wildfire severity in a series of Landsat images

Authors:
Vlassova, L.; Perez-Cabello, F.; Rodrigues Mimbrero, M.; Montorio Lloveria, R.; García-Martin, A.

Remote Sens. **2014**, *6*, 6136-6162; doi:10.3390/rs6076136

OPEN ACCESS

remote sensing

ISSN 2072-4292

www.mdpi.com/journal/remotesensing

Article

Analysis of the Relationship between Land Surface Temperature and Wildfire Severity in a Series of Landsat Images

Lidia Vlassova [1,2,*], Fernando Pérez-Cabello [1], Marcos Rodrigues Mimbrero [1], Raquel Montorio Llovería [1] and Alberto García-Martín [3]

[1] GEOFOREST Group, IUCA, Department of Geography and Spatial Management, University of Zaragoza, Spain, Pedro Cerbuna 12, Zaragoza E-50009, Spain; E-Mails: fcabello@unizar.es (F.P.-C.); rmarcos@unizar.es (M.R.M.); montorio@unizar.es (R.M.L.)

[2] Department of Environmental Sciences, Technical State University of Quevedo, Quevedo EC120509, Los Rios, Ecuador

[3] Centro Universitario de la Defensa de Zaragoza, Zaragoza E-50090, Spain; E-Mail: algarcia@unizar.es

* Author to whom correspondence should be addressed; E-Mail: vlassova@unizar.es or lvlassova@uteq.edu.ec; Tel.: +34-645-311-832; Fax: +34-976-761-506.

Received: 2 January 2014; in revised form: 17 June 2014 / Accepted: 20 June 2014 / Published: 30 June 2014

Abstract: The paper assesses spatio-temporal patterns of land surface temperature (LST) and fire severity in the Las Hurdes wildfire of *Pinus pinaster* forest, which occurred in July 2009, in Extremadura (Spain), from a time series of fifteen Landsat 5 TM images corresponding to 27 post-fire months. The differenced Normalized Burn Ratio (dNBR) was used to evaluate burn severity. The mono-window algorithm was applied to estimate LST from the Landsat thermal band. The burned zones underwent a significant increase in LST after fire. Statistically significant differences have been detected between the LST within regions of burn severity categories. More substantial changes in LST are observed in zones of greater fire severity, which can be explained by the lower emissivity of combustion products found in the burned area and changes in the energy balance related to vegetation removal. As time progresses over the 27 months after fire, LST differences decrease due to vegetation regeneration. The differences in LST and Normalized Difference Vegetation Index (NDVI) values between burn severity categories in each image are highly correlated ($r = 0.84$). Spatial patterns of severity and post-fire LST obtained from Landsat time series enable an evaluation of the relationship between these variables to predict the natural dynamics of burned areas.

Remote Sens. **2014**, *6* **6137**

Keywords: land surface temperature(LST); Landsat; burn severity; Normalized Difference Vegetation Index (NDVI); remote sensing

1. Introduction

Land surface temperature (LST) is one of the most important factors controlling physical processes responsible for the land surface balance of water, energy and CO_2 [1–3]. In the context of wildfire studies, fire-induced environmental changes cause variations in the spatial distribution of LST, mainly due to a decrease in transpiration and an increase in the Bowen ratio (β = sensible heating/latent heating) [4]. The higher post-fire LST of the burned areas was observed in field data [5,6] and remotely-sensed images [7,8]. Moreover, according to Beringer *et al.* [9], there is a relationship between fire intensity and an increase in the Bowen ratio, as far as fire intensity determines the likely impact on energy and carbon fluxes. Consequently, burn severity, defined for the current study as the amount of change in a burned area with respect to the pre-fire conditions [10–12], is very dependent on fire intensity [13] and can be considered a key variable in understanding the spatial distribution of LST in the immediate post-fire environment [8]. The regrowth of vegetation is also one of the most important factors controlling LST in the years following a fire, as vegetation cover and bare ground have different emissivity, defined as the ratio between the object emitting capacity and that of a blackbody at the same temperature. That is why spatio-temporal patterns of LST can help monitor the processes that structure ecosystem development and may assist in developing appropriate management strategies following forest fires.

Satellite sensors have long been used in wildfire research [11,14] to assess variables related to burn severity and vegetation recovery in a cost-effective and time-efficient way (among others [15,16]. On the medium spatial scale, Landsat has provided global coverage since 1984, with Landsat 8 launched at the beginning of 2013, ensuring the continuity of data record [17].However, compared to optical bands, the use of Landsat thermal data presents additional challenges [1,18].

Radiance levels in the thermal region of the spectrum depend not only on the amount of solar radiation received, but also on the ability of the surface to emit energy, expressed by its emissivity and atmospheric conditions (water vapor and temperature). At present, several physically-based methods have been suggested for LST estimation based on thermal infrared data from satellites, such as the Moderate Resolution Imaging Spectroradiometer (MODIS) and Landsat [19]. In the specific case of Landsat-5 TM, with only one thermal infrared band available, atmospheric profiles of temperature and water vapor content must be known for the exact time of image acquisition, as well as the knowledge of surface emissivity for each pixel. There are several LST algorithms applicable to Landsat 5/7, including mono-window [20], single channel [21,22] and the on-line Atmospheric Correction Parameters Calculator (ACPC) [23,24]. All of the procedures report similar estimation errors of 1–2 K.

Burn severity can be assessed through the calculation of spectral indices, which are focused on reflectance changes in burned areas mainly related to vegetation removal, soil exposure, changes in water content and the deposition of carbon and ash [25]. Although the Normalized Difference Vegetation Index (NDVI) [26] yields good results for burn severity assessment [27,28], the Normalized Burn Ratio applied in a two-date approach, the delta Normalized Burn Ratio (dNBR) [12], outperforms

the other indices [29–33]. dNBR can be considered a consistent method for burn severity assessment, due to its proven relationship with field severity metrics. Empirical models have shown strong relationships (r^2 > 0.6–0.7) between dNBR and specific parameters of burn severity, such as ash cover percentage, tree mortality, or twig diameter [30,34–37], or field indices, such as the Composite Burn Index (CBI) [31,38–42]. Moreover, the bi-temporal approach, where values of the post-fire image are subtracted from values of the pre-fire image, is considered the best approach to detect change caused by fire. Spectral vegetation indices have been proven useful in monitoring seasonal variations in vegetation development (phenological cycle) [43,44], as well as post-fire plant regeneration [45,46]: strong correlations were observed between the NDVI and various biophysical vegetation parameters, such as Leaf Area Index (LAI), the fraction of photosynthetically active radiation (fPAR) or vegetation abundance [47].

Although relationships between burn severity, NDVI and LST values seem quite clear, few studies have explored these [8,48,49]. There are indications that the inclusion of thermal information in spectral indices for severity mapping improves their performance [48,49]. The post-fire LST-severity relationship was assessed by Veraverbeke *et al.* [8] using MODIS images for a two-year period after fire, detecting an increase in post-fire LST up to 8.4 °C for a conifer forest. However, Landsat images can be especially suitable, because both the severity and LST of burned areas can be estimated in a more detailed spatial resolution.Therefore, the objectives of this study are: (1) to evaluate changes in LST for several images over a two-year period after fire; (2) to analyze the relationship between LST and burn severity estimated using the dNBR index; and (3) to study the relationship between vegetation regrowth measured by NDVI and changes in LST. The working hypothesis tested in this study is that the spatial distribution of LST in the burned areas depends on burn severity and that the LST range in each image is related to the phenological cycle and the time elapsed since the fire. From a methodological perspective, this study relies on the potential of remotely-sensed data and, more specifically, Landsat data to estimate LST, burn severity and vegetation regrowth.

2. Study Area and Data

2.1. Study Area

The study area of the Las Hurdes 2009 wildfire is located in Extremadura, in the province of Cáceres, Spain (40°19′–40°24′N, 6°10′–6°15′W) (Figure 1). It is a hilly area with elevation ranging from 390 to 1280 m above the sea level. The typical acid fine-textured soils are mainly umbricLeptosols and humicCambisols formed over metamorphic bedrock [50]. The Mediterranean climate (Csa according to the Köppen classification), characterized by an annual average temperature of 16°C and approximately 550 mm of precipitation, has a four-month hot, dry period from June to September [51].

The Las Hurdes fire analyzed in this study burned more than 3000 ha of the 30–40 year-old pine forest (*Pinuspinaster*) in four days (25–28 July 2009). According to the Spanish Third National Forest Inventory [50] (sample points shown as points in Figure 1), the average tree coverage is around 40%; besides *Pinuspinaster*, otherspecies, notably*Arbutus unedo*and*Quercus ilex* are also present. In Spain, *Pinus pinaster* occupies more than 1 million ha and is highly important to Spanish forestry [52]. It is also the species most affected by wildfires (27.96% of the burned area) [50]. Growth usually occurs in spring

(early April to mid-June) and autumn (late August to early October) [53]. The seed production is generally related to the fire regime. Stands suffering recurrent, high-intensity fires show more serotinous cones and a large aerial seed bank compared to stands where crown fires are not frequent [54].

Figure 1. Map of the fire site. Points indicate the location of the Spanish National Forest Inventory parcels [50].

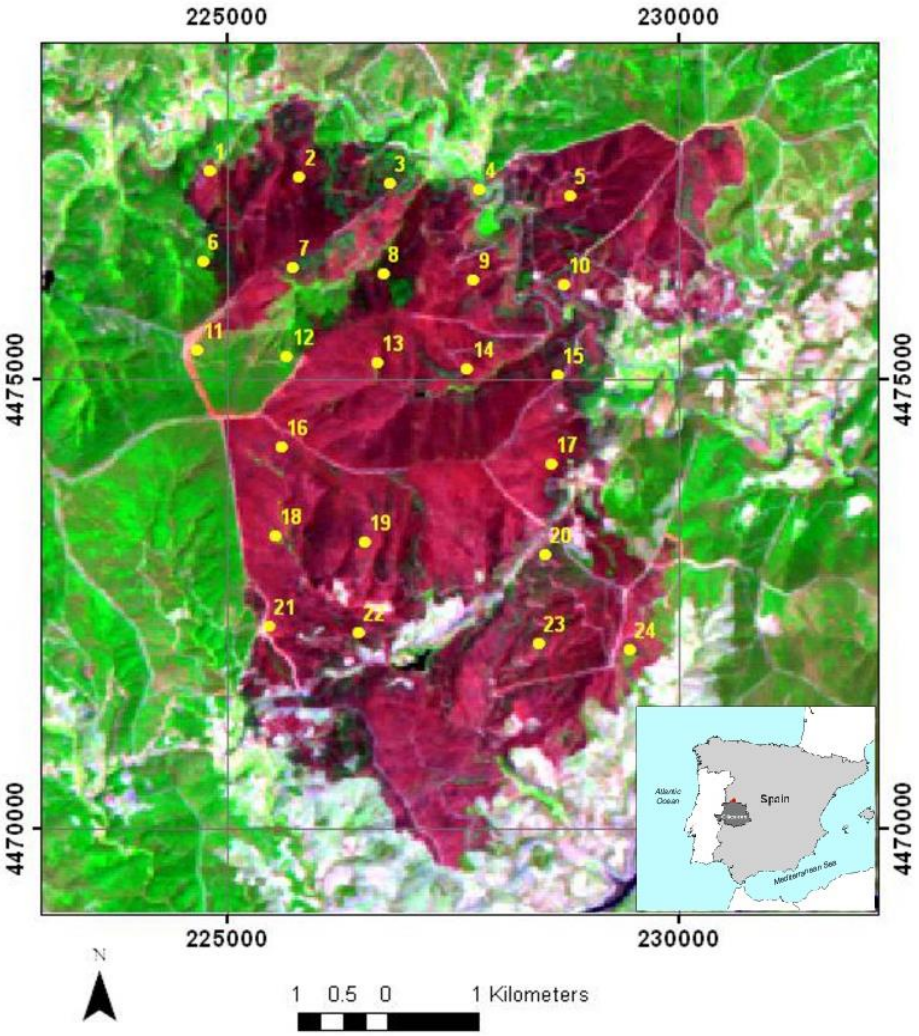

2.2. Data

Data from recently calibrated Landsat-5 TM archive [55] were used in this study. Landsat-5 TM images are composed of six optical and one thermal (bandwidth of 10.4–12.5 μm) spectral bands. Spatial resolution is 30 m for optical bands and 120 m for the thermal band.

Fifteen clear sky images, path 202/row 32, covering the period from July 2009 to September 2011, downloaded from the NASA website [56], are listed in Table 1 along with the information on the observation geometry and atmospheric conditions (near-surface air temperature T_{air} and relative humidity

RH) obtained from the Hurdes-Azabal meteorological station [57]. The station is part of the Spanish Agroclimatic Information System for Irrigation (SIAR) [58] and is about 10 km from the study site.

Table 1. Landsat-5 TM images and meteorological data on the dates involved.RH, relative humidity.

Date	Months Post-Fire	Sun Azimuth (Degrees)	Sun Elevation (Degrees)	T_{air} (Mean, °C)	RH (Mean, %)
13 July 2009	0 (Pre-fire)	125.0	62.4	25.3	41.6
29 July 2009	1	129.0	59.9	24.3	32.8
30 August 2009	2	141.1	52.6	28.7	23.7
15 September 2009	3	147.3	47.9	17.9	38.6
17 October 2009	4	156.5	37.4	11.7	40.7
10 March 2010	9	146.9	40.1	5.9	39.6
11 April 2010	10	141.8	52.9	13.4	58.0
30 June 2010	12	124.3	64.0	25.8	47.0
16 July 2010	13	126.1	62.3	24.5	41.3
1 August 2010	14	130.3	59.6	25.8	35.2
5 November 2010	17	159.2	31.4	12.8	81.9
16 May 2011	23	132.5	61.8	18.7	56.2
1 June 2011	24	127.9	63.9	17.7	40.1
4 August 2011	26	130.7	58.9	25.8	45.8
5 September 2011	27	142.9	50.9	20.2	47.3

We used preprocessed level L1T Landsatdata. The downloaded images (GeoTiff format) were available in the UTM projection (datum: WGS84). The digital elevation model with 25-m resolution in the UTM projection was downloaded from the online archive of the National Center for Geographic Information (Spain) [59]. It was processed using ArcGIS software [60] to obtain information on the surface slope and aspect.

3. Methodology

3.1. Atmospheric Correction of the Optical Bands

An open-source Landsat Ecosystem Disturbance Adaptive Processing System (LEDAPS) from NASA Goddard Space Flight Center (GSFC) [61] was used for the atmospheric correction of the optical bands. It obtains parameters required for atmospheric correction from the National Centers for Environmental Prediction (NCEP) reanalysis data provided by the NOAA/OAR/ESRL PSD, Boulder, Colorado, USA, on-line [62](atmospheric pressure and water vapor), at 2.5° spatial resolution and the Earth Probe Total Ozone Mapping Spectrometer (EP TOMS) (ozone) at 1° spatial resolution, available from [63]. The obtained values are resampled to the same spatial resolution of 1.2 km and each image is processed and corrected independently. One of the advantages of the system compared to other similar tools, is that it takes the original Landsat data (DN values) as inputs and provides atmospherically corrected reflectance values for each of the optical bands as outputs ,without the need for previous data transformation or scaling by the user.

3.2. Monitoring Vegetation Recovery

Monitoring of vegetation recovery was performed through NDVI calculated for each available image. The NDVI is based on the difference between the maximum reflection of radiation in the near-infrared spectral bands (0.78–0.90 μm) and the maximum absorption of radiation in the red spectral band (0.63–0.69 μm). The difference of the reflectances is normalized by their sum, reducing the effect of shadows, resulting in NDVI = (NIR − VIS)/(NIR + VIS).

Values of the NDVI range between −1.0 and +1.0. The wide use of NDVI for vegetation monitoring arises because of its positive correlation with characteristics of plant status and abundance. NDVI frequently serves as a proxy for biomass, although the relationship between them is often non-linear [26,44],and NDVI shows saturation before biomass reaches its maximum levels. In spite of the limitations, NDVI is commonly used in assessing vegetation recovery after fire (among others [8,16,27,64]). It is sometimes used as a metric of burn severity [8,48,65,66].

3.3. LST Estimation

LST was calculated using the mono-window (*M*w) method [20]. Prior to the LST estimation, band 6 original data were transformed first into radiance, with the help of the data from the header files, and next into the at-sensor brightness temperature. The *M*w algorithm [20] requires three *a priori* known parameters: atmospheric transmissivity (τ) calculated from the water vapor content, effective mean atmospheric temperature (T_a) and surface emissivity (ε). The formula used to calculate LST (Ts) is the approximation of the radiative transfer formula and includes two empirical coefficients a and b:

$$Ts = \{a(1-C-D)+[b(1-C-D)+C+D]\times T_{sensor} - DT_a\}/C \quad (1)$$

where $a = -67.355351$ and $b = 0.458606$ are constants, T_{sensor} is the at-sensor brightness temperature and:

$$C = \varepsilon\tau \quad (2a)$$

$$D = (1-\tau)[1+(1-\varepsilon)\tau] \quad (2b)$$

Formulas for the estimation of the atmospheric correction parameters were developed by Qin and Karnieli[20] using LOWTRAN 7 simulations. The simulation of atmospheric transmissivity τ, depending on water vapor content, yielded Equation (3a,b) for a low temperature profile (18°C) and Equation (3c,d) for a high temperature profile (35°C) [20]:

$$\tau = 0.974290 - 0.08007w \ (0.4\ \text{g·cm}^{-2} < w < 1.6\ \text{g·cm}^{-2}) \quad (3a)$$

$$\tau = 1.031412 - 0.11536w \ (1.6\ \text{g·cm}^{-2} < w < 3.0\ \text{g·cm}^{-2}) \quad (3b)$$

$$\tau = 0.982007 - 0.09611w \ (0.4\ \text{g·cm}^{-2} < w < 1.6\ \text{g·cm}^{-2}) \quad (3c)$$

$$\tau = 1.053710 - 0.14142w \ (1.6\ \text{g·cm}^{-2} < w < 3.0\ \text{g·cm}^{-2}) \quad (3d)$$

The effective mean temperature T_a is computed for specific atmospheric conditions using Formulas 4a–c based on the ratio of water vapor content at a particular altitude to total atmospheric water vapor content and near-surface local air temperature T_0 [20]:

$$T_a = 19.2704 + 0.91118T_0 \text{ (mid-latitude winter)} \quad (4a)$$

$$T_a = 19.2704 + 0.91118T_0 \text{ (mid-latitude summer)} \quad (4b)$$

$$T_a = 17.9769 + 0.91715T_0 \text{ (tropical atmosphere)} \quad (4c)$$

The empirical formula (Equation (5)) developed by Butler [67] based on Bolton [68] and adjusted for central Spain by De Vicente and Pulido [69] was used to estimate atmospheric water vapor content:

$$w = 0.013227 \frac{\exp(17.67T_0/(243.5+T_0))}{T+273.15} RH * 135 \quad (5)$$

where w is the water vapor content ($g \cdot cm^{-2}$), T_0 is the near-surface air temperature in °C and RH is the relative humidity (%).

When working with Landsat thermal data, surface emissivity estimation required for calculating LST is a challenge, because only one thermal band is available. To solve the problem, the NDVI-based methods, which rely on the information from the image used for the LST retrieval, were successfully applied [70]. One of these, the NDVI thresholds method ($NDVI^{THM}$) [71,72], based on the findings of Valor and Caselles [73], was used to calculate surface emissivity in this study. The emissivity for different NDVI ranges was estimated using different functions. For water and fully vegetated pixels, the emissivity values of 0.985 and 0.99, respectively, were assigned following the suggestion of Sobrino *et al.* [74]. The soil emissivity value of 0.984 is a result of the field measurements using the box method [75] and is similar to values reported by previous research [74,76]. As for the pixels with the mixed cover of vegetation and soil ($0.1 \leq NDVI \leq 0.7$), emissivity ε is calculated using Formula (6) [72–74], which involves vegetation fraction P_V estimated from a scaled NDVI, according to Choudhury *et al.* [77] and Gutman and Ignatov [78] (Equation (7)):

$$\varepsilon = 0.990P_V + 0.984(1-P_V) + 0.04P_V(1-P_V) \quad (6)$$

$$P_V = \frac{NDVI_{pixel} - NDVI_s}{NDVI_V - NDVI_s} \quad (7)$$

where $NDVI_{pixel}$ is the NDVI value of a pixel.

NDVI thresholds for the mixed pixels range are based on image histogram analysis.

3.4. Burn Severity Estimation

In this research, dNBR was the spectral index applied for burn severity evaluation due to the very strong association observed between dNBR and field burn severity measurements in conifer forests [34,42,79] and more specifically, in Mediterranean areas [80,81]. Likewise, as LST values were obtained from Landsat data, it was considered appropriate to use the burn severity index especially designed for Landsat spatial and spectral specifications [12]. The methodology followed for dNBR calculation was [82]: (1) pre- and post-fire images were transformed to reflectance R and atmospherically corrected; (2) an NBR image was generated for both dates using the formula $(R_4 - R_7)/(R_4 + R_7)$, where subscripts correspond to the band numbers; (3) dNBR was calculated as NBRpre-fire − NBRpost-fire; and (4) the polygon encompassing fire-affected pixels (dNBR > 100) plus a 350-m buffer was defined for the purposes of analysis.

dNBR values are sometimes grouped into discrete classes of burn severity (e.g., low, moderate and high) [12]. Original thresholds for these intervals were not thought to be used as fixed values, valid

worldwide. Several studies have used the relationship between dNBR and CBI to calculate dNBR thresholds representing breaks between burn severity classes [39,40,83], sometimes with fairly insignificant differences from the initially suggested values [84]. However, there are also studies that have adopted them in ecosystems quite different from the one for which they were created [30,31,34]. For simplicity and objectivity, thedNBR values suggested by Key and Benson [12] were used for creating the burn severity categories as follows: unburned (UB) (from −100 to 99), low severity (LS) (from 100 to 269), moderate-low severity (MLS) (from 270 to 439), moderate-high severity (MHS) (from 440 to 659) and high severity (HS) (from 660 to 1300).

3.5. Statistical Procedures

The comparison of pre- and post-fire images suffers from problems related to interannual phenological differences and time since fire [12,45,85,86]: the overall regeneration trend may vary significantly from one year to another due to climatic differences. To solve this problem, Díaz-Delgado and Pons [45] compared burned and unburned plots within the same image, while Veraverbeke *et al.* [86] used a control plot selection procedure based on Lhermite *et al.* [87], which exploits the similarity between the temporal evolution of the burned and unburned pixels. In this context, two different approaches to the temporal study of the LST-severity relationship were applied in this research. First, variations in LST and NDVI differences throughout the 27 months after the fire were identified by comparing the images captured at similar moments of the annual phenological cycle in different post-fire years. This analysis was applied to images satisfying the following criteria: (1) post-fire images from different years can be compared only if the acquisition day corresponds to the same phenological stage of *Pinuspinaster* (all of the images used for comparison in this study are acquired within the period between two active growth phenological stages between mid-June and late August [53]);and (2) the difference in atmospheric temperature between compared dates has to be lower than 1.5°C (Table 1). Thus, the following raster arithmetic calculations were applied: (1) dLST: subtraction of the post- and pre-fire LST, *i.e.*, $LST_{29\ July\ 2009} - LST_{pre}$; (2) dNDVI: subtraction of the pre- and post-fire NDVI for three dates, *i.e.*, $dNDVI_{2009} = NDVI_{pre} - NDVI_{29\ July\ 2009}$, $dNDVI_{2010} = NDVI_{pre} - NDVI_{16\ July\ 2010}$, and $dNDVI_{2011} = NDVI_{pre} - NDVI_{4\ August\ 2011}$.

Second, statistical differences were studied between the LST and NDVI values observed in the burn severity categories. To reduce the spatial auto-correlation effects, a random sample of 10% pixels by severity category, including the UB category for reference, was extracted from the pixels inside the study site perimeter (n = 4230). Sample points were analyzed independently for each date using ANOVA analysis and Tamhane'sT2 *post hoc* test algorithms. Moreover, for further study of the temporal differences between burn severity categories, the variables "fire severity differences in LST" (fsdLST) and "fire severity differences in the NDVI" (fsdNDVI) were analyzed. fsdLST specifically refers to the LST differences between areas within burn severity categories: UB, LS, MLS, MHS and HS. It was accomplished by Formula (8):

$$fsdLST = \left| \overline{LST_i} - \overline{LST_j} \right|^{date} \quad (8)$$

where $\overline{LST}$ is the mean value of the *LST* variable and *i*, *j* are a pair of burn severity categories.

A similar procedure (Equation (9)) was applied to calculate *fsdNDVI*:

$$fsdNDVI = \left| \overline{NDVI_i} - \overline{NDVI_j} \right|^{date} \quad (9)$$

where $\overline{NDVI}$ is the mean value of the *NDVI* variable and *i, j* are a pair of burn severity categories.

4. Results and Discussion

4.1. Spatial Pattern of dNBR

The RGB 7-4-3 band combination (Figure 1) depicts the Las Hurdes fire perimeter in shades of red associated with the low reflectance in the NIR band, a characteristic of zones of scarce vegetation, and high reflectance at 2.1 µm in the SWIR spectral region, typical of areas with a low moisture content. This is the typical spectral response of burned areas [79] (Figure 2). Different exposure time and different fire intensity result in the great spatial variability of burn severity in the affected ecosystem. The spatial distribution of burn severity, classified from the original dNBR threshold values, can be seen in Figure 2. Within the Las Hurdes fire, 32.9% of the burned surface presents HS, 37.4% MHS, 18% MLS and 11.7% LS. On the whole, Las Hurdes was a high severity fire, since more than 70% of the area falls within the MHS and HS categories. However, within the fire perimeter, two wide diagonals of low severity pixels divide the burned area in the north and south (Figure 2), defining four sectors: two in the north with a large number of high-severity nuclei, a very large one in the center and one of predominantly moderate-low severity in the south. The predominance of the highest burn severity intervals is also related to the initial approach applied to the burn severity assessment, by using an immediate post-fire image and not giving time for the ecosystem to show additional responses to fire [12].

4.2. Temporal Dynamics of LST and NDVI Values

This section presents the temporal dynamics of LST and NDVI throughout the study period. Descriptive statistics for LST and NDVI (Tables 2 and 3) refer to data from all of the available images: the pre-fire image (13 July 2009) and 14 post-fire images taken between July 2009 (one day after fire), and September 2011 (two years after fire), while Figure 3 shows data in the form of graphics on four different dates: 13 days before the fire on13 July 2009, and on three midsummer dates corresponding to successive post-fire summer seasons (29 July 2009,16 July 2010, and 4 August 2011). Values are grouped by severity categories. In addition, Figure 4 shows the spatial distribution of LST and NDVI on the same dates as Figure 3.

In the pre-fire image, all burn severity categories present similar average LST values (~30 °C) (Table 2). The coolest areas associated with greater biomass are those registering the highest severity levels after fire (Figures 3 and 4). The existence of this type of relationship between pre-fire biomass and further burn severity was previously reported by García-Martin *et al.* [88], who demonstrated that knowledge of crown biomass enables the prediction of the burn severity levels.

Figure 2. Burn severity map.

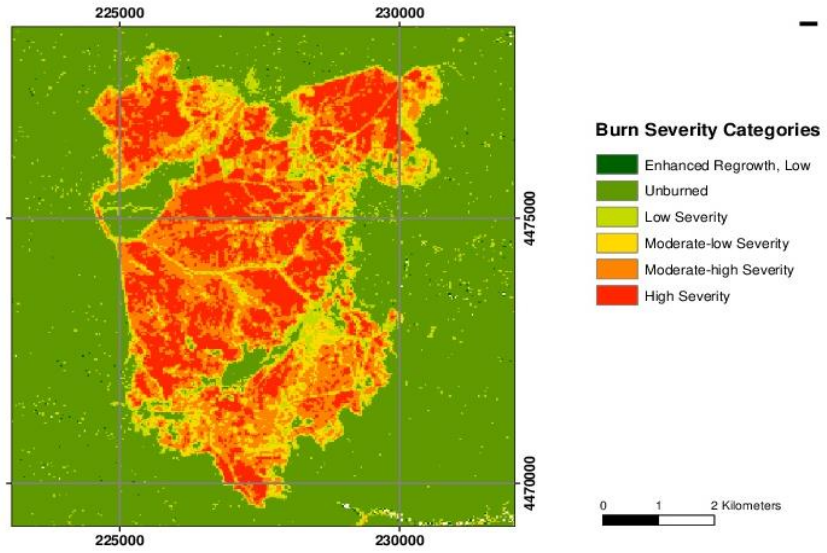

Table 2. The average LST values by fire severity category and date (MMDD). UB = unburned (n = 673); LS=low severity (n = 415); MLS = moderate-low severity (n = 640); MHS = moderate-high severity (n = 1332); HS = high severity (n = 1170).

LST	2009					2010					2011				
Severity	**Date**	**Mean**	**SD**	**Min**	**Max**	**Date**	**Mean**	**SD**	**Min**	**Max**	**Date**	**Mean**	**SD**	**Min**	**Max**
UB	*0713*	30.84	4.30	21.34	42.80	*0310*	9.84	4.1	0.54	18.55	*0516*	25.99	3.60	17.82	35.89
LS	*0713*	31.04	3.23	21.39	38.09	*0310*	11.93	3.93	0.86	21.08	*0516*	28.26	3.55	18.13	38.20
MLS	*0713*	30.10	2.74	20.75	37.47	*0310*	13.7	4.26	0.45	22.4	*0516*	30.29	3.50	18.01	39.69
MHS	*0713*	29.23	2.42	20.70	36.96	*0310*	14.38	4.87	0.89	23.18	*0516*	31.34	3.80	18.56	39.26
HS	*0713*	27.70	2.05	21.33	36.50	*0310*	14.82	5.96	1.15	23.88	*0516*	32.32	4.37	21.12	40.26
UB	*0729*	36.61	5.56	25.32	49.37	*0411*	24.34	4.12	14.78	35.17	*0601*	23.12	3.05	15.97	30.06
LS	*0729*	40.59	5.06	24.62	50.85	*0411*	27.8	4.3	15.1	40.09	*0601*	24.87	2.65	16.46	30.18
MLS	*0729*	43.23	4.91	25.08	53.74	*0411*	31.06	4.32	15.31	41.53	*0601*	26.28	2.40	16.75	33.98
MHS	*0729*	45.87	4.93	26.52	55.41	*0411*	32.79	4.85	16.48	42.01	*0601*	26.87	2.61	16.72	33.87
HS	*0729*	47.29	4.94	29.69	56.58	*0411*	34.36	5.83	19.15	44.55	*0601*	27.54	2.96	19.32	33.89
UB	*0830*	37.18	4.90	26.12	47.06	*0630*	32.59	4.72	19.44	45.12	*0804*	26.57	5.41	8.55	39.43
LS	*0830*	40.17	4.42	26.85	48.66	*0630*	35.75	4.58	18.72	47.39	*0804*	28.46	5.25	2.28	37.12
MLS	*0830*	42.19	4.59	26.91	52.41	*0630*	39.06	3.98	24.22	47.41	*0804*	30.12	4.91	11.91	39.76
MHS	*0830*	44.22	4.84	27.07	53.65	*0630*	40.45	3.91	25.17	49.21	*0804*	30.40	4.78	5.72	40.64
HS	*0830*	45.02	5.14	29.60	53.79	*0630*	41.42	4.11	30.45	49.76	*0804*	30.35	4.99	11.33	39.70
UB	*0915*	23.84	4.84	13.83	35.18	*0716*	33.13	5.09	23.05	44.03	*0905*	24.27	4.10	15.47	32.49
LS	*0915*	26.35	4.17	14.18	34.12	*0716*	36.64	4.71	23.52	46.59	*0905*	26.38	3.61	15.22	32.86
MLS	*0915*	28.01	4.21	13.71	36.13	*0716*	39.81	3.88	24.19	47.91	*0905*	27.86	3.37	15.10	35.36
MHS	*0915*	29.14	4.42	14.72	39.65	*0716*	41.2	3.79	24.22	48.22	*0905*	28.28	3.69	15.18	36.06
HS	*0915*	30.00	4.93	15.01	39.66	*0716*	41.84	4.15	30.14	48.34	*0905*	28.59	4.46	16.19	35.88
UB	*1017*	21.80	5.58	10.21	33.69	*0801*	36.51	4.87	26.37	46.65					
LS	*1017*	24.51	5.15	11.03	36.10	*0801*	39.66	4.47	27	49.62					
MLS	*1017*	27.04	5.71	11.04	39.91	*0801*	42.61	3.71	28.02	50.58					

Table 2. *Cont.*

LST	2009					2010					2011				
Severity	**Date**	**Mean**	**SD**	**Min**	**Max**	**Date**	**Mean**	**SD**	**Min**	**Max**	**Date**	**Mean**	**SD**	**Min**	**Max**
MHS	*1017*	28.88	6.72	10.16	42.69	*0801*	43.92	3.6	28.64	50.65					
HS	*1017*	29.27	7.79	10.16	41.73	*0801*	44.47	3.87	33.88	50.76					
UB						*1105*	17.24	3.46	9.82	26.75					
LS						*1105*	19.1	3.9	9.81	31.36					
MLS						*1105*	21.05	4.7	9.35	31.94					
MHS						*1105*	21.83	5.61	8.13	33.2					
HS						*1105*	22.55	6.85	8.12	33.61					

Table 3. Average NDVI values by fire severity category and date (MMDD). UB = unburned (n = 673); LS = low severity (n = 415); MLS = moderate-low severity (n = 640); MHS = moderate-high severity (n = 1332); HS = high severity (n = 1170).

NDVI	2009					2010					2011				
S	**Date**	**Mean**	**SD**	**Min**	**Max**	**Date**	**Mean**	**SD**	**Min**	**Max**	**Date**	**Mean**	**SD**	**Min**	**Max**
UB	*0713*	0.46	0.14	0.13	0.74	*0310*	0.50	0.13	0.14	0.76	*0516*	0.52	0.13	0.15	0.80
LS	*0713*	0.45	0.12	0.15	0.74	*0310*	0.38	0.12	0.13	0.73	*0516*	0.48	0.11	0.22	0.80
MLS	*0713*	0.49	0.10	0.21	0.74	*0310*	0.25	0.08	0.03	0.71	*0516*	0.43	0.10	0.19	0.72
MHS	*0713*	0.55	0.07	0.35	0.79	*0310*	0.19	0.06	0.03	0.47	*0516*	0.44	0.09	0.21	0.80
HS	*0713*	0.63	0.04	0.44	0.78	*0310*	0.16	0.04	0.08	0.38	*0516*	0.41	0.10	0.21	0.76
UB	*0729*	0.44	0.15	0.13	0.75	*0411*	0.49	0.13	0.11	0.82	*0601*	0.52	0.13	0.17	0.82
LS	*0729*	0.34	0.12	0.10	0.73	*0411*	0.37	0.12	0.05	0.75	*0601*	0.48	0.12	0.23	0.80
MLS	*0729*	0.25	0.09	0.05	0.58	*0411*	0.25	0.09	0.11	0.61	*0601*	0.43	0.09	0.21	0.71
MHS	*0729*	0.18	0.07	0.07	0.48	*0411*	0.19	0.06	0.09	0.51	*0601*	0.45	0.09	0.19	0.82
HS	*0729*	0.14	0.04	0.07	0.34	*0411*	0.16	0.04	0.08	0.49	*6001*	0.43	0.10	0.21	0.80
UB	*0830*	0.42	0.15	0.10	0.72	*0630*	0.49	0.14	0.16	0.76	*0804*	0.45	0.13	0.13	0.77
LS	*0830*	0.32	0.11	0.10	0.69	*0630*	0.39	0.13	0.08	0.79	*0804*	0.39	0.10	0.18	0.74
MLS	*0830*	0.24	0.07	0.09	0.59	*0630*	0.29	0.09	0.13	0.64	*0804*	0.36	0.07	0.18	0.70
MHS	*0830*	0.19	0.05	0.09	0.44	*0630*	0.27	0.08	0.13	0.76	*0804*	0.38	0.07	0.18	0.73
HS	*0830*	0.17	0.03	0.09	0.30	*0630*	0.25	0.07	0.13	0.74	*0804*	0.39	0.07	0.21	0.69
UB	*0915*	0.44	0.14	0.11	0.71	*0716*	0.49	0.16	0.10	0.80	*0905*	0.50	0.14	0.11	0.79
LS	*0915*	0.34	0.11	0.13	0.70	*0716*	0.37	0.14	−0.06	0.81	*0905*	0.43	0.12	0.17	0.78
MLS	*0915*	0.25	0.07	0.09	0.53	*0716*	0.27	0.09	0.11	0.63	*0905*	0.40	0.09	0.18	0.71
MHS	*0915*	0.21	0.05	0.07	0.52	*0716*	0.25	0.08	0.11	0.76	*0905*	0.42	0.08	0.20	0.80
HS	*0915*	0.19	0.03	0.07	0.32	*0716*	0.24	0.07	0.11	0.73	*0905*	0.44	0.08	0.20	0.75
UB	*1017*	0.46	0.16	0.11	0.76	*0801*	0.46	0.14	0.13	0.74					
LS	*1017*	0.35	0.12	0.12	0.71	*0801*	0.35	0.13	0.02	0.74					
MLS	*1017*	0.26	0.08	0.09	0.56	*0801*	0.26	0.08	0.11	0.61					
MHS	*1017*	0.21	0.06	0.09	0.61	*0801*	0.25	0.07	0.12	0.73					
HS	*1017*	0.18	0.04	0.04	0.39	*0801*	0.24	0.06	0.11	0.71					
UB						*1105*	0.55	0.14	0.19	0.82					
LS						*1105*	0.44	0.13	0.16	0.82					
MLS						*1105*	0.36	0.10	0.05	0.80					
MHS						*1105*	0.36	0.09	0.16	0.67					
HS						*1105*	0.36	0.10	−500.10	0.73					

Remote Sens. **2014**, *6* **6147**

Figure 3. The relationship between burn severity categories and LST in °C (**left panel**), and NDVI (**right panel**). Bars indicate confidence interval of average values ($\alpha = 0.01$). Each graphic shows data for a date specified in its title (YYYYMMDD).

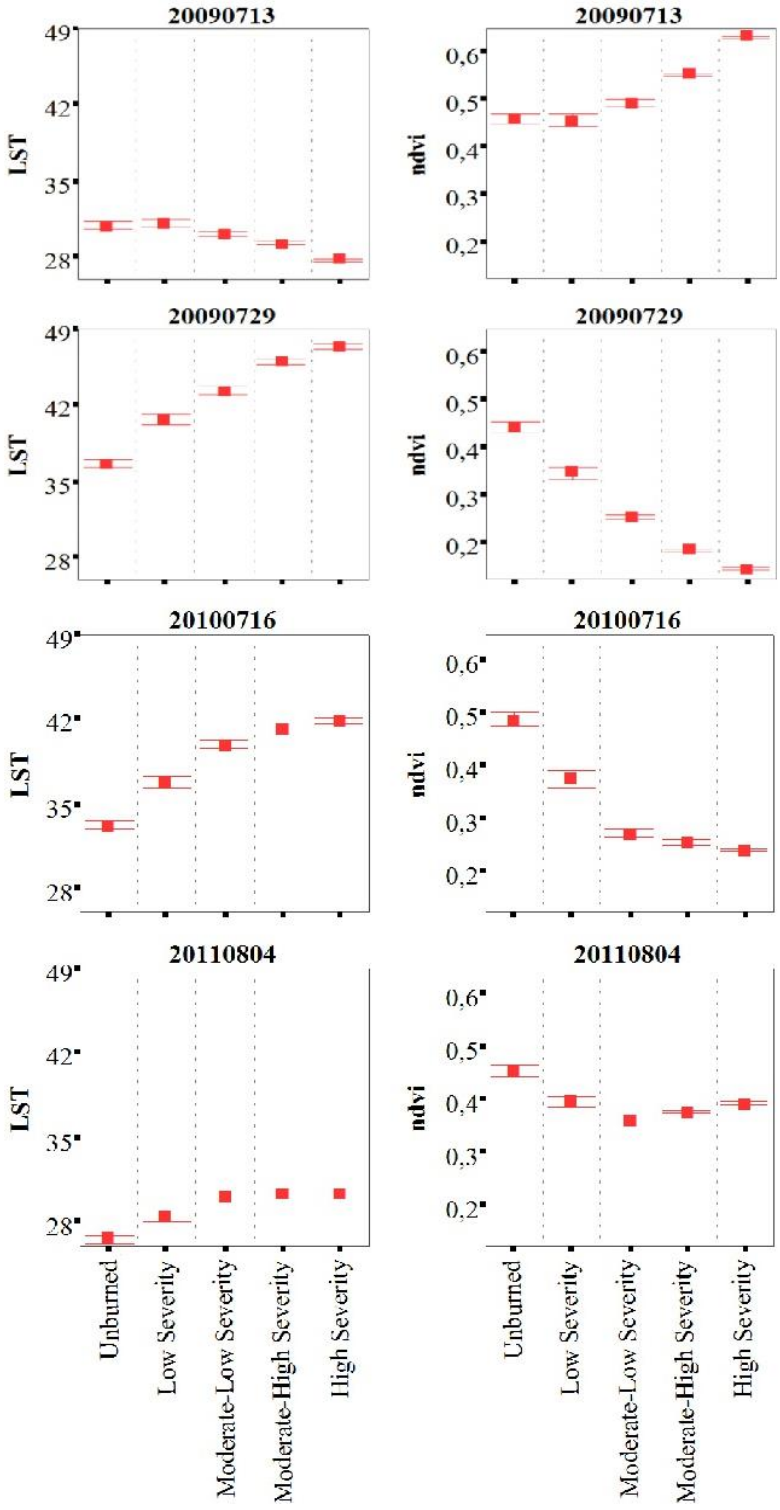

Figure 4. Spatial distribution of LST (**left panel**) and NDVI (**right panel**) before the fire event and in the three post-fire summer seasons.(**a**) 13 July 2009 (pre-fire); (**b**) 29 July 2009; (**c**) 16 July 2010;(**d**) 4 August 2011.

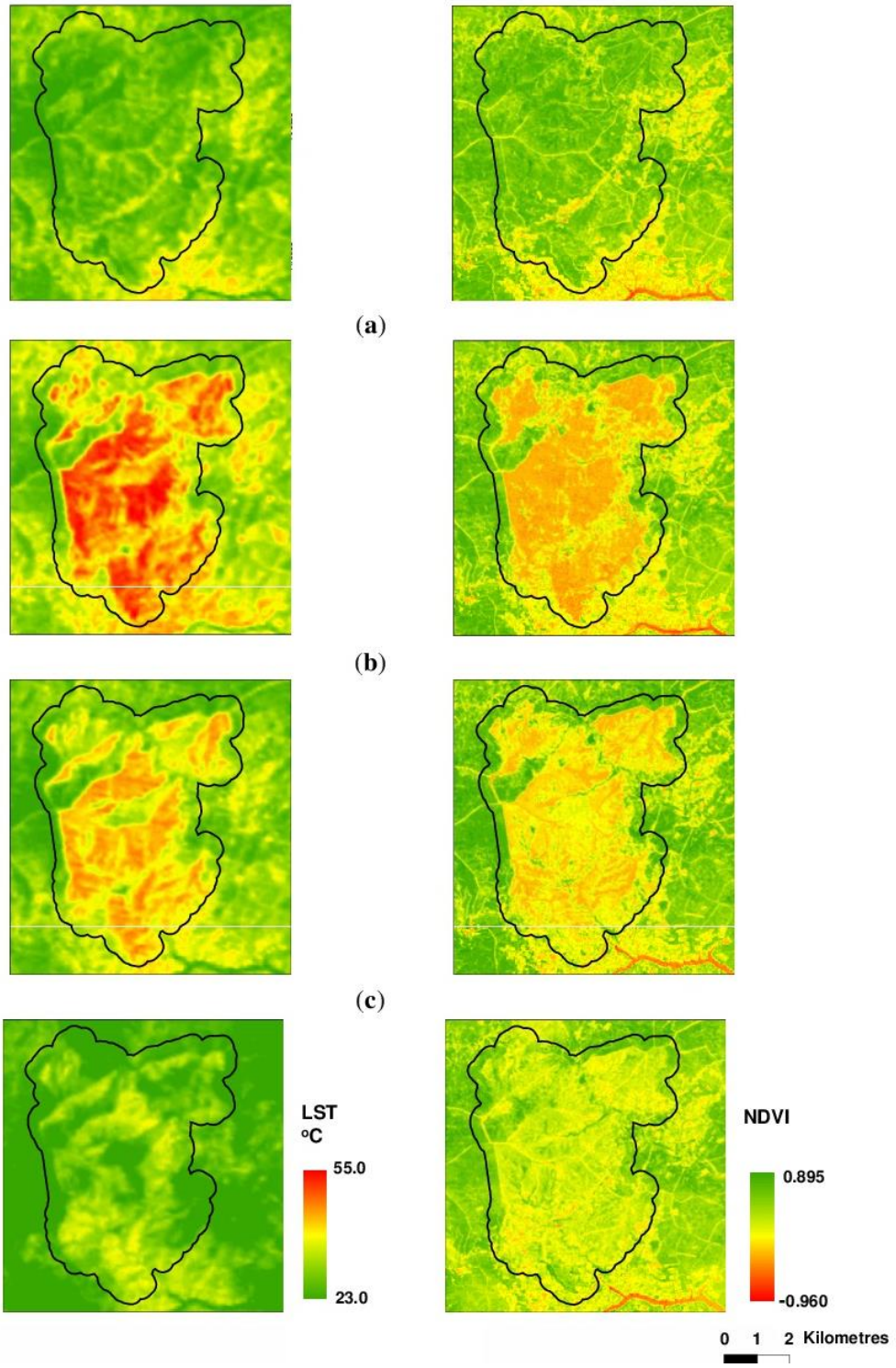

The immediate effects of the fire on the LST are reflected in the first two post-fire images (29 July and 30 August 2009) closest to the event. For the visual assessment of these effects, Figure 5 presents the spatial distribution of the dLST, where LST values of the post-fire image are subtracted from the pre-fire image. According to this formula and the assigned colors, areas with the greatest increase of LST are highlighted in red, and areas without a change are shown in green. To improve the understanding of pre- and post-fire LST changes, Figure 6 presents the confidence levels of average values for the dLST by burn severity category. The average LST increase is 13°C, reaching 20°C for the HS pixels. The generalized LST increase in the post-fire image (both in the burned and unburned areas) may be due to the fact that this image was acquired on a date closer to the middle of summer than the pre-fire image, and therefore, the air temperature was high. However, thermal differences between HS and UB categories within the post-fire image (>10°C) reveal the influence of burn severity on the spatial distribution of LST (Table 3). The decrease of aboveground green biomass in the burned zones [12], especially in those of higher severity, and the appearance of lower emissivity coverage (ash, char and mineral soils) lead to a large increase in the LST.

Figure 5. The spatial distribution of dLST between immediate post-fire (29 July 2009) and pre-fire (13 July 2009) images.

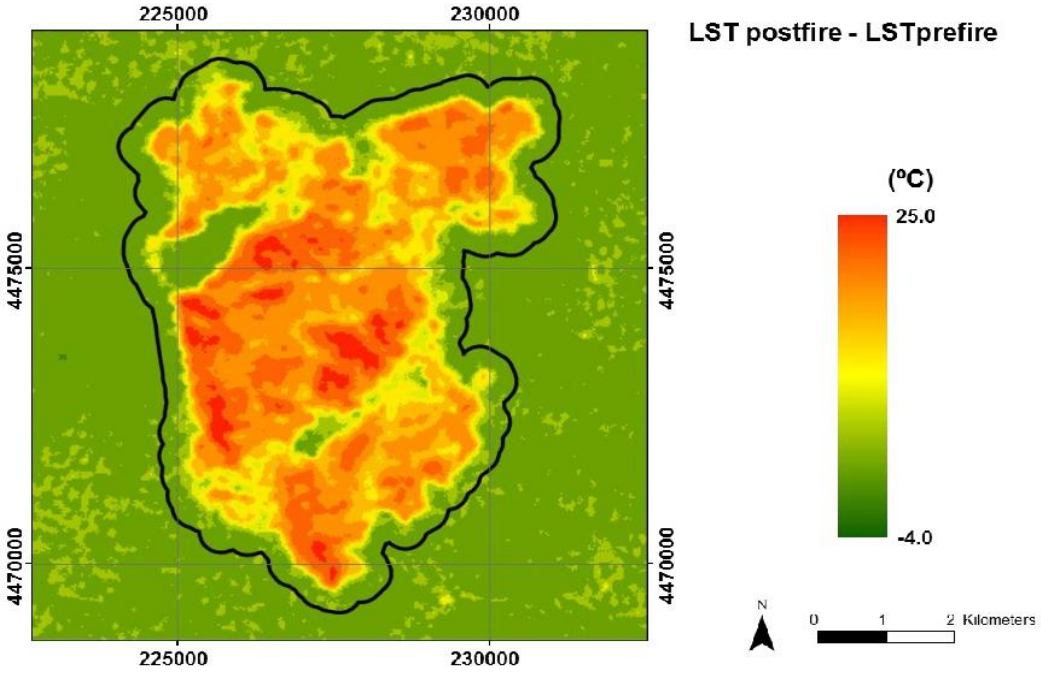

Elevated LST after fire events is mentioned by several authors (among others Lambin *et al.* [7]; Montes-Helu *et al.* [5]; Wendt *et al.* [6]). Veraverbeke *et al.* [8] studied this increase using MODIS imagery following the major Peloponnese fire in 2007. Until now, few studies have analyzed spatiotemporal patterns of post-fire surface temperature using Landsat data, although the high potential of existing single channel algorithms, such as the mono-window (MW) method by Qin *et al.* [20] or the single-channel (SC) method by Jiménez-Muñoz and Sobrino [22], has already been demonstrated [89–91]. The greater surface heterogeneity of the burned areas due to the incorporation of combustion products,

changes to lighter-colored soil and ash, char and scorched, then blackened, vegetation [12] results in an increase in post-fire thermal variability (SD values ~5, Table 2).

Figure 6. The relationship between burn severity categories and dLST between pre-fire (13 July 2009) and post-fire (29 July 2009) images. Bars indicate the confidence interval of the average values ($\alpha = 0.01$).

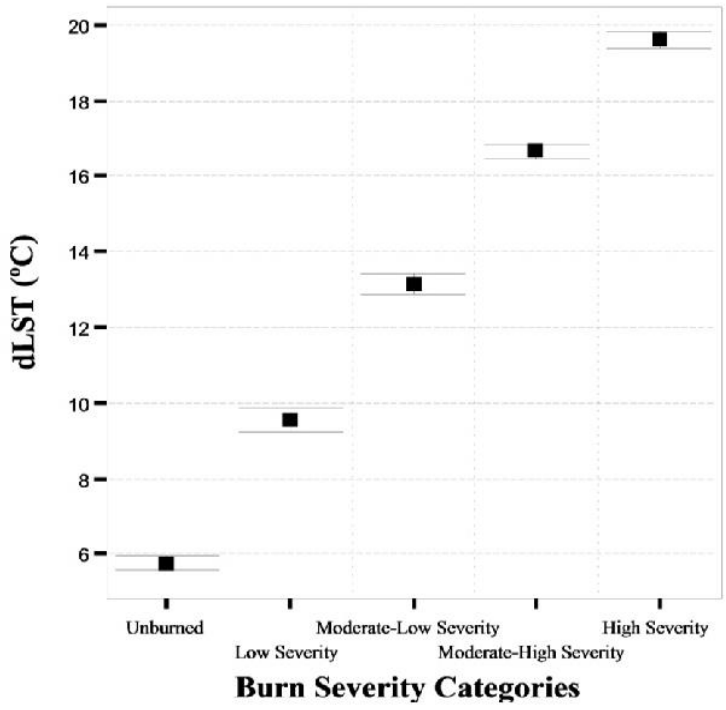

Some interesting ideas arise regarding the influence of burn severity on the LST distribution and the contrast between areas of different burn severity categories. The general decrease in LST observed in the first post-fire autumn (September and October data of 2009) is probably associated with lower solar illumination angles. When the sun is directly above the observation location and the sunlight is perpendicular to the land surface, the amount of solar radiation received by the surface is at its maximum. However, as the angle between the sun and a surface is continually changing, the surface gets only part of the incident sunlight. Topography (slope) and sun azimuth also affect the incidence angle of sunrays and the time the area is illuminated by the sun. However, burn severity remains the main factor influencing the spatial distribution of LST: higher LST values correspond to higher burn severity and *vice versa* (Table 2). Likewise, post-fire thermal variability within burn severity categories maintains the level observed in the immediate post-fire image.

The same patterns of LST changes are observed in the images from different years: (i) same season LST values (spring, summer, autumn) become lower from year to year; (ii) the spatial distribution of LST values is qualitatively in agreement with the burn severity categories; and (iii) differences between extreme severity categories in 2010 are slightly lower compared to 2009 (the year of fire) and even lower in 2011 (Table 2). This smoothing of contrast among categories can be explained by both the effects of time on the combustion products and, most of all, the effects of vegetation regeneration, reflected in

NDVI values registered in all of the temporal series in the various burn severity categories (Table 3) and a visual comparison of three dNDVI images (Figure 7): each image is calculated as the subtraction of the NDVI raster of one of the post-fire summer seasons from the pre-fire NDVI ($dNDVI_{2009}$, $dNDVI_{2010}$ and $dNDVI_{2011}$). The images show areas with higher dNDVI in red and those with lower dNDVI (similar to the pre-fire situation) in green. The progress of vegetation recovery is quite evident: while the highest differences are characteristic to the first post-fire summer, the contrast between burned and unburned areas is smoothed in 2010 and especially in 2011 data, with much lower dNDVI values in the corresponding images.

Figure 7. Temporal evolution of dNDVI.

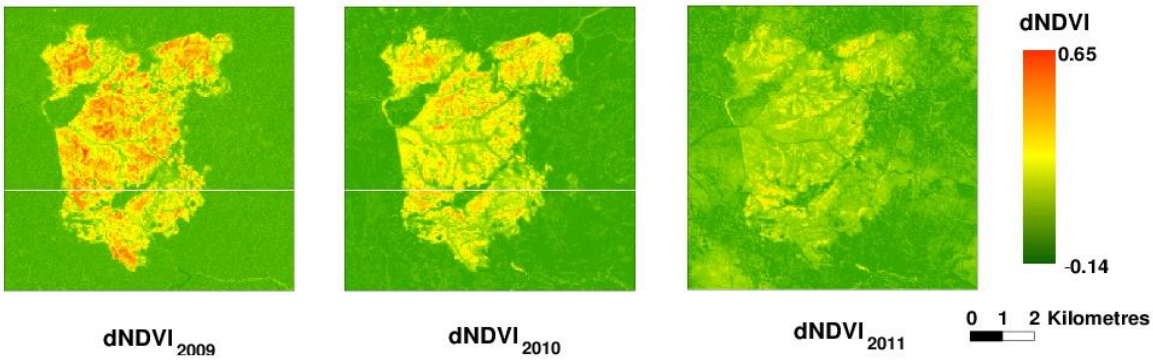

This successful regeneration process is explained by the efficient recovery mechanisms of the vegetation species dominant in this area. *Pinus pinaster*, the main species affected by the Las Hurdes fire, is highly adapted to fire-prone environments through the massive release of seeds from serotinous cones after fire forgermination [92,93]. In the same way, shrubland species observed in fire affected areas near the study site (*Erica arborea*, *Erica lusitanica*, *Cistus ladanifer*, *Phillies angustifolia*, *Cytisus scoparius*, *Calluna vulgaris* and *Lavandulastoechas*)[94]also apply efficient post-fire reproduction strategies in recolonizing burned areas.

Our results demonstrate that the LST increase in fire-affected areas was evident in the analyzed series of images, which cover all of the seasons of the two post-fire years, except winter. This is similar to the results reported by the previous research [5,6,8], although the range and the size of the differences between severity categories of the same date is much larger than that detected in the earlier studies. This is probably due to the different response of the analyzed vegetation: much more homogeneous in this study (predominantly conifer forests) than analyzed in the study by Veraverbeke *et al.* [8] (shrublands, olive groves, coniferous and deciduous forests). Immediate post-fire increment in LST calculated from Landsat is much more pronounced than that registered for similar vegetation cover at the same phenological stage registered by MODIS, because of the difference in spatial resolution between the two sensors, *i.e.*, the smoothing of contrasts in the lower resolution images.

4.3. Analysis of fsdLST and fsdNDVI

The results of the date-by-date LST-NDVI comparison by severity categories are shown below. It can be seen that the differences between burned/unburned areas increase with burn severity in terms of LST

from around 3 °C to almost 7 °C (Figure 8a) and from 0.09 to 0.21 in terms of the NDVI (Figure 8b). Mean fsdLST between the successive severity categories is 1.42°C. In fact, significant statistical differences ($p < 0.05$) were registered in all of the pairs, with the only exception being HS-MHS and MHS-MLS in the images from August and September of 2011.

A detailed date-by-date analysis of the differences between severity categories allows for the identification of common features. Each pair in Figure 8 shows the distribution of the fsdLST and fsdNDVI by date. The size of the circle reflects the between-category distance for each pair (*i.e.*, a size of four corresponds to combinations of the extreme burn severity categories UB-HS). The color in these figures represents the type of categories paired: green when one of the categories in the pair is the UB; red and orange when the HS category is involved and blue for the combinations of the intermediate categories. Pairs combining high burn severity levels (HS and MHS) and the UB class register the most pronounced differences (between 7 °C and 10 °C). A seasonal pattern is observed during 2009 and 2010, as well as a stronger decrease and temporal stabilization in 2011, two years after the fire. Pairs formed by consecutive categories (HS-MHS and MHS-MLS) (size = 1) show lower differences (<3 °C), without any specific temporal pattern.Differences below 1°C are almost exclusively observed in combinations of high severity levels (HS-MHS) on all of the dates, except in the image taken just after the fire, where they are slightly above 1 °C.Between these two groups of high and low differences, differences for the HS-LS (orange), UB-MLS (light green) and MHS-LS (blue) (size = 2–3) pairs show a large range of variation (from 2 °C to 7 °C).

The greatest fsdNDVI between 0.25 and 0.35 (Figure 8b) are always related to the comparison between UB and all of the other severity categories (green).They are mainly observed in the images of the first post-fire summer, when the effects of fire are more obvious, and especially in March and April 2010.Lower fsdNDVI (0.25–0.15) are characteristic of the pairs formed by the UB and HS (size = 4) in the last images of 2010, MHS and MLS (light blue, size = 1) and also between HS-LS (orange, size = 3) until the spring of 2010.Many pairs register differences between 0.15 and 0.05. The majority of images included in this group are from 2011. Differences below 0.05 correspond to the HS-MHS pair on all of the dates and the HS-MLS pair on the dates after June 2010.

Analysis of the fsdLST and fsdNDVI in 2011 reveals: (1) lower fsdLST compared to 2010; and (2) progressive smoothing of contrast between severity categories. fsdNDVI are below 0.10 (Figure 8b), and fsdLST values are less than 5°C (Figure 8a), except in May, when they are slightly higher. A general downward trend is observed in both the fsdLST and fsdNDVI throughout the time series, especially significant in 2011. Thus, the scatterplot in Figure 9 highlights the strong relationship between these two variables ($r = 0.84$): most of the bigger circles in the graphic are located in the upper part of the scatterplot, except those corresponding to the 2011 dates (in green), which are located in the lower part of the plot, always below the reference line, due to the minimizing effects of vegetation regeneration on fsdLST. Unusually low fsdLST values observed in March of 2010 are due to particularly low air temperature on this date.

Figure 8. Fire severity differences in LST(fsdLST_ (**a**) and fsdNDVI (**b**) by date (YYYYMMDD), combination type (color) and distance between categories (circle size).

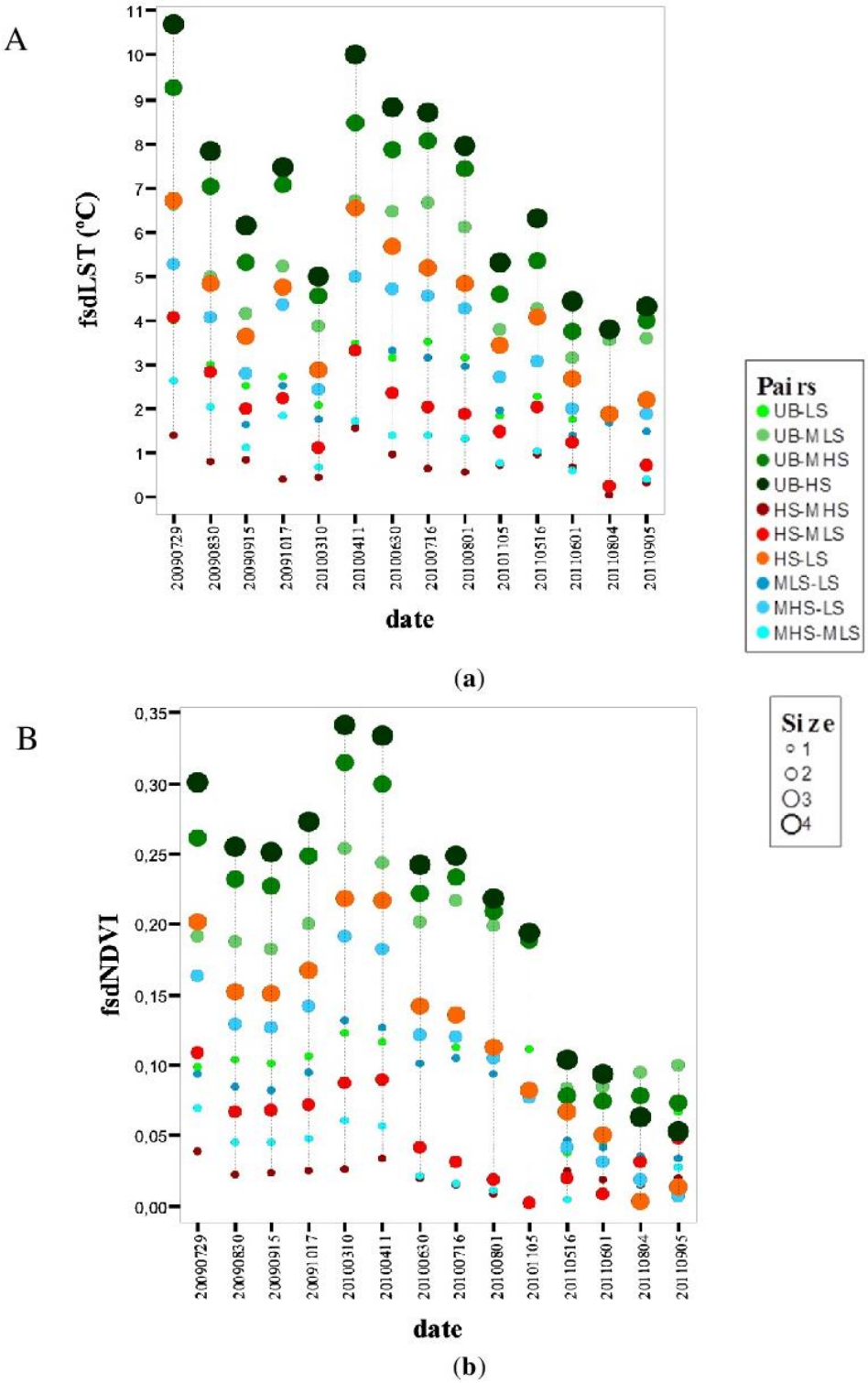

Figure 9. Scatterplot between fsdLST and fsdNDVI.The symbol color shows the dates (YYYYMMDD); the symbol size represents the distance between severity categories.

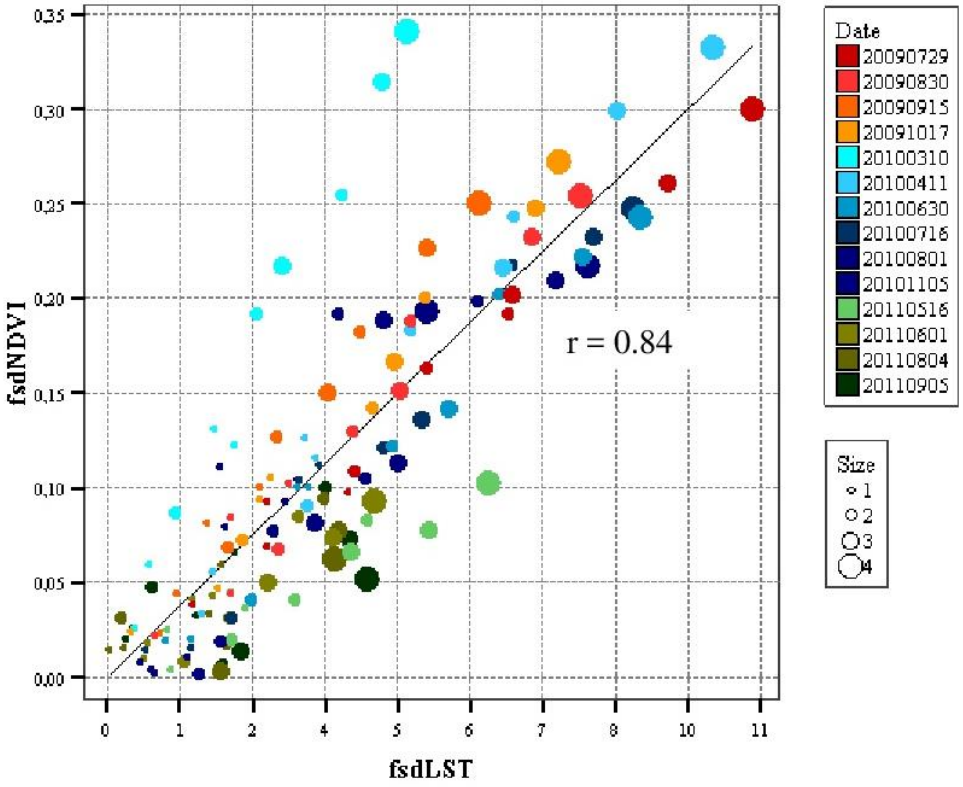

However, the spatial distribution of LST depends not only on burn severity and its interaction with local-scale variables, such as surface emissivity (vegetation regeneration).Factors explaining intra- and inter-annual LST changes also include illumination geometry controlled by solar azimuth and elevation angles and topography reflected in slope and aspect. The role of aspect in the spatial distribution of LST is shown in Figure 10. The figure presents mean LST values for eightcategories of aspects (at 45-degree intervals) grouped by burn severity levels from the pre-fire image up to the image taken 27 months after the fire in September of 2011.

At first glance, some influence of aspect on the spatial distribution of LST and its relationship with severity levels, cover type and day of the year is observed. High LST values are systematically registered on SE-facing slopes (between 90° and 180°), with slight variations depending on the image date. Conversely, values corresponding to pixels in NNE- and NW-facing slopes (between 270° and 360° and between 0° and 45°, respectively) always register lower LST. Differences between hot and cold orientations deepen in the spring and autumn images, due to the lower elevation angles of the sun. For example, in the image from July2010, the differences between the aspect intervals described above can exceed 6°C, and in October2009, they can be higher than 15°C, because of the deeply shaded areas. However, thermal contrast between pixels of different aspects is not as pronounced in the pre-fire image, where it does not exceed 4°C. Therefore, the fire and the consequent vegetation removal lead to greater thermal heterogeneity, increasing the role of aspect in the spatial distribution of LST. In later images

(those from 2011), however, vegetation regeneration reduces the differences in LST between burn severity categories and aspect intervals, as can be appreciated in the 2011 images.

Figure 10. Mean LST values in different burn severity categories by date and aspect intervals (degrees). The title of each graphic indicates the image date (YYYYMMDD).

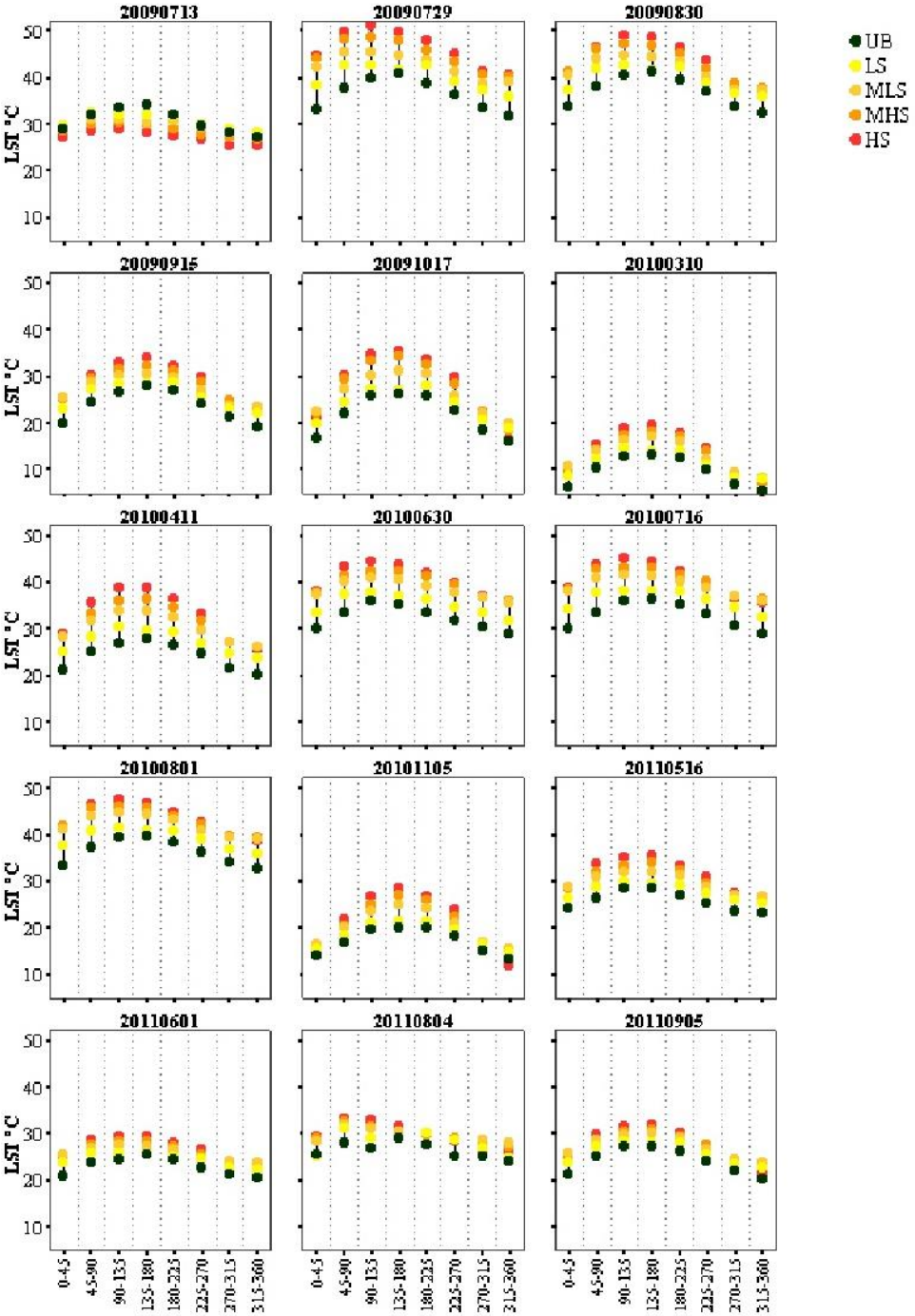

5. Conclusions

The study quantifies fire-induced changes in the spatial and temporal distribution of land surface temperature (LST) within the Las Hurdes fire in Central Spain using Landsat imagery. Immediately after the fire, the burned zones were, on average, 7.6 °C warmer than the unburned; the difference with the unburned areas was above 10 °C for the zones of high burn severity. The size of LST differences was directly related to the area's burn severity. After the first months following the fire, LST contrasts between burned and unburned areas in the same image decrease, although the LST differences between areas of different burn severity categories are still detectable for two years after fire.

The spatial distribution of post-fire LST is mainly influenced by vegetation regeneration. In the specific case of the Las Hurdes fire, study results point to the vegetation regrowth two years after the fire as a key factor in the temporal evolution of LST values, making less noticeable the consequences of fire as time elapses.

LST contrasts in the areas of different burn severity are also enhanced by the aspect and illumination geometry, being higher for the better-illuminated slopes. As vegetation recovers, the differences between aspect intervals considerably decrease.

The study draws upon the Landsat potential to provide spatially continuous quantitative estimation of land surface temperature and demonstrates the influence of burn severity and post-fire vegetation recovery, both of them assessed by spectral indices, on the spatial distribution of land surface temperature, one of the key parameters controlling physical processes in fire-altered areas.

Future research will approach the relationships between burn severity, LST and vegetation regeneration in other ecosystems and test the possibility of combining LST with commonly used metrics to improve burn severity differentiation.

Acknowledgments

This research has been financially supported by the FLUXPEC project "Monitoring changes in water and carbon fluxes from remote and proximal sensing in a Mediterranean dehesa ecosystem" (CGL2012-34383, Ministry of Economy and Competitiveness, Spain) and by a collaboration agreement between the Aragón Government (DGA) and the Obra Social "La Caixa" (Aragon Government DGA-La Caixa, GA-LC-042/2011), Spain. The authors also appreciate the financial support provided to this research by Secretariat for Higher Education, Science, Technology and Innovation (SENESCYT), Ecuador.

Author Contributions

This research was conducted by Lidia Vlassova and Fernando Perez-Cabello. Lidia Vlassova performed data processing and modelling. Raquel Montorio contributed to interpretation of the results and supervision of the methods employed. Marcos Rodrigues and Alberto García-Martín contributed to the organization of the manuscript. All authors helped in editing and revision of the manuscript, and responding to reviewers comments. All authors read and approved the final manuscript.

Conflicts of Interest

The authors declare no conflict of interest.

References

1. Kuenzer, C.; Dech, S. *Thermal Infrared Remote Sensing: Sensors, Methods, Applications*; Springer: London, UK, 2013.
2. Kustas, W.; Anderson, M. Advances in thermal infrared remote sensing for land surface modeling. *Agric. For. Meteorol.* **2009**, *149*, 2071–2081.
3. Monson, R.; Baldocchi, D. *Terrestrial Biosphere-Atmosphere Fluxes*; Cambridge University Press: Cambridge, MA, USA, 2014.
4. Bowen, I.S. The ratio of heat losses by conduction and by evaporation from any water surface. *Phys. Rev.* **1926**, *27*, 779–787.
5. Montes-Helu, M.; Kolb, T.; Dore, S.; Sullivan, B.; Hart, S.; Koch, G.; Hungate, B. Persistent effects of fire-induced vegetation change on energy partitioning and evapotranspiration in Ponderosa pine forests. *Agric.For. Meteorol.* **2009**, *149*, 491–500.
6. Wendt, C.K.; Beringer, J.; Tapper, N.J.; Hutley, L.B. Local boundary-layer development over burnt and unburnt tropical savanna: An observational study. *Bound.-Layer Meteorol.* **2007**, *124*, 291–304.
7. Lambin, E.; Goyvaerts, K.; Petit, C. Remotely-sensed indicators of burning efficiency of savannah and forest fires. *Int.J. Remote Sens.* **2003**, *24*, 3105–3118.
8. Veraverbeke, S.; Verstraeten, W.W.; Lhermitte, S.; van de Kerchove, R.; Goossens, R. Assessment of post-fire changes in land surface temperature and surface albedo, and their relation with fire–burn severity using multitemporal MODIS imagery. *Int.J. Wildland Fire* **2012**, *21*, 243–256.
9. Beringer, J.; Hutley, L.; Tapper, N.; Coutts, A.; Kerley, A.; O'grady, A. Fire impacts on surface heat, moisture and carbon fluxes from a tropical savanna in Northern Australia. *Int. J. Wildland Fire* **2003**, *12*, 333–340.
10. De Santis, A.; Chuvieco, E. Geocbi: A modified version of the composite burn index for the initial assessment of the short-term burn severity from remotely sensed data. *Remote Sens. Environ.* **2009**, *113*, 554–562.
11. Gitas, I.Z.; Santis, A.; Mitri, G.H. Remote Sensing of Burn Severity. In *Earth Observation of Wildland Fires in Mediterranean Ecosystems*;Chuvieco, E., Ed.; Springer: Berlin/Heidelberg, Germany, 2009; pp. 129–148.
12. Key, C.H.; Benson, N.C. Landscape Assessment. In *Firemon: Fire Effects Monitoring and Inventory System*; Lutes, D.C., Keane, R.E., Caratti, J.F., Key, C.H., Benson, N.C., Sutherland, S., Gangi, L.J., Eds.; USDA Forest Service, Rocky Mountain Research Station: Fort Collins, CO, USA, 2006; pp.1–55.
13. Chuvieco, E.; Riaño, D.; Danson, F.M.; Martin, P. Use of a radiative transfer model to simulate the postfire spectral response to burn severity. *J. Geophys. Res.: Biogeosci.* **2006**, *111*, doi:10.1029/2005JG000143.
14. Chuvieco, E.; Cocero, D.; Riaño, D.; Martin, P.; Martínez-Vega, J.; de la Riva, J.; Pérez, F. Combining NDVI and surface temperature for the estimation of live fuel moisture content in forest fire danger rating. *Remote Sens.Environ.* **2004**, *92*, 322–331.
15. Lentile, L.B.; Holden, Z.A.; Smith, A.M.S.; Falkowski, M.J.; Hudak, A.T.; Morgan, P.; Lewis, S.A.; Gessler, P.E.; Benson, N.C. Remote sensing techniques to assess active fire characteristics and post-fire effects. *Int.J. Wildland Fire* **2006**, *15*, 319–345.

16. Riaño, D.; Chuvieco, E.; Ustin, S.; Zomer, R.; Dennison, P.; Roberts, D.; Salas, J. Assessment of vegetation regeneration after fire through multitemporal analysis of AVIRIS images in the Santa Monica mountains. *Remote Sens.Environ.* **2002**, *79*, 60–71.
17. Landsat Missions. Available online: http://landsat.usgs.gov (accessed on 25 May 2014).
18. Tang, H.; Li, Z.-L. Introduction. In *Quantitative Remote Sensing in Thermal Infrared*; Springer: Berlin/Heidelberg, Germany, 2014; pp.1–4.
19. Li, Z.-L.; Tang, B.-H.; Wu, H.; Ren, H.; Yan, G.; Wan, Z.; Trigo, I.F.; Sobrino, J.A. Satellite-derived land surface temperature: Current status and perspectives. *Remote Sens. Environ.* **2013**, *131*, 14–37.
20. Qin, Z.; Karnieli, A.; Berliner, P. A mono-window algorithm for retrieving land surface temperature from Landsat TM data and its application to the Israel-Egypt border region. *Int. J. Remote Sens.* **2001**, *22*, 3719–3746.
21. Jimenez-Munoz, J.C.; Cristobal, J.; Sobrino, J.A.; Soria, G.; Ninyerola, M.; Pons, X. Revision of the single-channel algorithm for land surface temperature retrieval from Landsat thermal-infrared data. *IEEE Trans. Geosci. Remote Sens.* **2009**, *47*, 339–349.
22. Jiménez-Muñoz, J.C.; Sobrino, J.A. A generalized single-channel method for retrieving land surface temperature from remote sensing data. *J. Geophys. Res.* **2004**, *108*, 46–88.
23. Barsi, J.A.; Barker, J.L.; Schott, J.R. An Atmospheric Correction Parameter Calculator for a Single Thermal Band Earth-Sensing Instrument. In Proceedings of the 2003 IEEE International Geoscience and Remote Sensing Symposium, IGARSS '03, Toulouse, France, 21–25 July 2003; Volume 3015, pp. 3014–3016.
24. Barsi, J.A.; Schott, J.R.; Palluconi, F.D.; Hook, S.J. Validation of a web-based atmospheric correction tool for single thermal band instruments. *Proc. SPIE* **2005**, *5882*, doi:10.1117/12.619990.
25. Jakubauskas, M.E.; Lulla, K.P.; Mausel, P.W. Assessment of vegetation change in a fire-altered forest landscape. *Photogramm. Eng. Remote Sens.* **1990**, *56*, 371–377.
26. Kriegler, F.J.; Malila, W.A.; Nalepka, R.F.; Richardson, W. Preprocessing Transformations and Their Effects on Multispectral Recognition. In Proceedings of the Sixth International Symposium on Remote Sensing of Environment, Ann Arbor, MI, USA, 13–16 October 1969; pp. 97–131.
27. Díaz-Delgado, R.; Lloret, F.; Pons, X. Influence of fire severity on plant regeneration by means of remote sensing imagery. *Int.J. Remote Sens.* **2003**, *24*, 1751–1763.
28. Escuin, S.; Navarro, R.; Fernandez, P. Fire severity assessment by using NBR (Normalized Burn Ratio) and NDVI (Normalized Difference Vegetation Index) derived from Landsat TM/ETM images. *Int. J. Remote Sens.* **2008**, *29*, 1053–1073.
29. Brewer, C.K.; Winne, J.C.; Redmond, R.L.; Opitz, D.W.; Mangrich, M.V. Classifying and mapping wildfire severity: A comparison of methods. *Photogramm. Eng. Remote Sens.* **2005**, *71*, 1311–1320.
30. Chafer, C.J. A comparison of fire severity measures: An Australian example and implications for predicting major areas of soil erosion. *Catena* **2008**, *74*, 235–245.
31. Epting, J.; Verbyla, D.; Sorbel, B. Evaluation of remotely sensed indices for assessing burn severity in interior Alaska using Landsat TM and ETM+. *Remote Sens. Environ.* **2005**, *96*, 328–339.
32. Holden, Z.A.; Morgan, P.; Hudak, A.T. Burn severity of areas reburned by wildfires in the Gila National Forest, New Mexico, USA. *Fire Ecol.* **2010**, *6*, 77–85.

33. Hudak, A.T.; Morgan, P.; Bobbitt, M.J.; Smith, A.M.S.; Lewis, S.A.; Lentile, L.B.; Robichaud, P.R.; Clark, J.T.; McKinley, R.A. The relationship of multispectral satellite imagery to immediate fire effects. *Fire Ecol.* **2007**, *3*, 64–90.
34. Cocke, A.E.; Fulé, P.Z.; Crouse, J.E. Comparison of burn severity assessments using differenced normalized burn ratio and ground data. *Int. J. Wildland Fire* **2005**, *14*, 189–198.
35. Hudak, A.T.; Robichaud, P.; Evans, J.S.; Clark, J.; Lannom, K.; Morgan, P.; Stone, C. Field Validation of Burned Area Reflectance Classification (BARC) Products for Post Fire Assessment. In Proceedings of the Tenth Forest Service Remote Sensing Applications Conference, Salt Lake City, UT, USA, 5–9 April 2004; pp. 1–13.
36. Keeley, J.E. Fire intensity, fire severity and burn severity: A brief review and suggested usage. *Int. J. Wildland Fire* **2009**, *18*, 116–126.
37. Robichaud, P.R.; Lewis, S.A.; Laes, D.Y.M.; Hudak, A.T.; Kokaly, R.F.; Zamudio, J.A. Postfire soil burn severity mapping with hyperspectral image unmixing. *Remote Sens. Environ.* **2007**, *108*, 467–480.
38. Allen, J.L.; Sorbel, B. Assessing the differenced normalized burn ratio's ability to map burn severity in the boreal forest and tundra ecosystems of Alaska's national parks. *Int. J. Wildland Fire* **2008**, *17*, 463–475.
39. Hall, R.J.; Freeburn, J.; de Groot, W.; Pritchard, J.; Lynham, T.; Landry, R. Remote sensing of burn severity: Experience from Western Canada boreal fires. *Int. J. Wildland Fire* **2008**, *17*, 476–489.
40. Picotte, J.J.; Robertson, K.M. Validation of remote sensing of burn severity in South-Eastern US ecosystems. *Int. J. Wildland Fire* **2011**, *20*, 453–464.
41. Soverel, N.O.; Perrakis, D.D.; Coops, N.C. Estimating burn severity from Landsat dNBR and RdNBR indices across Western Canada. *Remote Sens.Environ.* **2010**, *114*, 1896–1909.
42. Wimberly, M.C.; Reilly, M.J. Assessment of fire severity and species diversity in the Southern Appalachians using Landsat TM and ETM+ imagery. *Remote Sens.Environ.* **2007**, *108*, 189–197.
43. Schwartz, M.D. *Phenology: An Integrative Environmental Science*; Kluwer Academic Publishers: Dordrecht, The Netherlands, 2011.
44. Myneni, R.B.; Keeling, C.; Tucker, C.; Asrar, G.; Nemani, R. Increased plant growth in the northern high latitudes from 1981 to 1991. *Nature* **1997**, *386*, 698–702.
45. Díaz-Delgado, R.; Pons, X. Spatial patterns of forest fires in Catalonia (NE of Spain) along the period 1975–1995: Analysis of vegetation recovery after fire. *For. Ecol. Manag.* **2001**, *147*, 67–74.
46. Viedma, O.; Melia, J.; Segarra, D.; García-Haro, J. Modeling rates of ecosystem recovery after fires by using Landsat TM data. *Remote Sens. Environ.* **1997**, *61*, 383–398.
47. Jones, H.G.; Vaughan, R.A. *Remote Sensing of Vegetation: Principles, Techniques, and Applications*; Oxford University Press: New York, NY, USA, 2010.
48. Harris, S.; Veraverbeke, S.; Hook, S. Evaluating spectral indices for assessing fire severity in chaparral ecosystems (Southern California) using MODIS/ASTER (MASTER) airborne simulator data. *Remote Sens.* **2011**, *3*, 2403–2419.
49. Veraverbeke, S.; Harris, S.; Hook, S. Evaluating spectral indices for burned area discrimination using MODIS/ASTER (MASTER) airborne simulator data. *Remote Sens. Environ.***2011**, *115*, 2702–2709.

50. Forestal, S.D.I., 3rd; Spanish National Forest Inventory (IFN3). *Dirección General de Medio Natural y Política Forestal del Ministerio de Medio Ambiente*; Medio Rural y Marino: Madrid, Spain, 2011.
51. Núñez Corchero, M.; Sosa Cardo, J.A. *Climatología de Extremadura* (*1961–1990*); Ministerio de Medio Ambiente: Madrid, Spain, 2001; p. 232.
52. Gil, L.; Gordo, J.; Alía, R.; Catalán, G.; Pardos, J. Pinus pinaster Aiton en el paisaje vegetal de la peninsula Iberica. *Ecología* **1990**, *1*, 469–495.
53. Miguel Pérez, I.; González Martínez, S.; Alía Miranda, R.; Gil Sánchez, L. Growth phenology and mating system of Maritime pine (*Pinus pinaster Aiton*) in Central Spain. *Investig. Agrar. Sist. Recur. For.* **2002**, *11*, 193–204.
54. Tapias, R.; Gil, L.; Fuentes-Utrilla, P.; Pardos, J.A. Canopy seed banks in Mediterranean pines of South-Eastern Spain: A comparison between Pinus halepensis mill., P. pinaster ait., P. nigra arn. and P. pinea l. *J. Ecol.* **2001**, *89*, 629–638.
55. Schott, J.R.; Hook, S.J.; Barsi, J.A.; Markham, B.L.; Miller, J.; Padula, F.P.; Raqueno, N.G. Thermal infrared radiometric calibration of the entire Landsat 4, 5, and 7 archive (1982–2010). *Remote Sens. Environ.* **2012**, *122*, 41–49.
56. USGS Global Visualization Viewer. Available online: http://glovis.usgs.gov (accessed on 25 May 2014).
57. REDAREX. Available online: http://sw-aperos.juntaex.es/redarex/fs_estaciones.asp?lug=cc (accessed on 25 May 2014).
58. SIAR. Available online: http://www.magrama.gob.es/es/agua/temas/gestion-sostenible-de-regadios/sistema-informacion-agroclimatica-regadio/Red-Estaciones-Agroclimaticas.aspx (accessed on 25 May 2014).
59. Centro de Descargas de CNIG. Available online: http://centrodedescargas.cnig.es/CentroDescargas (accessed on 25 May 2014).
60. ArcGIS Software. Available online: http://www.esri.com/software/arcgis (accessed on 25 May 2014).
61. Masek, J.G.; Vermote, E.F.; Saleous, N.E.; Wolfe, R.; Hall, F.G.; Huemmrich, K.F.; Gao, F.; Kutler, J.; Lim, T.-K. A Landsat surface reflectance dataset for North America, 1990–2000. *IEEE Geosci. Remote Sens. Lett.* **2006**, *3*, 68–72.
62. ESRL:PSD:PSD Data: NCEP/NCAR Reanalysis Monthly Means and Other Derived Variables. Available online: http://www.esrl.noaa.gov/psd/data/gridded/data.ncep.reanalysis.derived.surface.html (accessed on 25 May 2014).
63. NASA—Space-Based Measurements of Ozone and Air Quality in the Ultraviolet and Visible. Available online: http://ozoneaq.gsfc.nasa.gov/measurements.md (accessed on 25 May 2014).
64. Lanorte, A.; Lasaponara, R.; Lovallo, M.; Telesca, L. Fisher–Shannon information plane analysis of SPOT/Vegetation Normalized Difference Vegetation Index (NDVI) time series to characterize vegetation recovery after fire disturbance. *Int. J. Appl. Earth Obs.Geoinf.* **2014**, *26*, 441–446.
65. Fox, D.; Maselli, F.; Carrega, P. Using SPOT images and field sampling to map burn severity and vegetation factors affecting post forest fire erosion risk. *Catena* **2008**, *75*, 326–335.
66. Petropoulos, G.P.; Griffiths, H.M.; Kalivas, D.P. Quantifying spatial and temporal vegetation recovery dynamics following a wildfire event in a Mediterranean landscape using EO data and GIS. *Appl. Geogr.***2014**, *50*, 120–131.
67. Butler, B. *Precipitable Water at the VLA—1990–1998*; MMA Memo: Charlottesville, VA, USA, 1998.

68. Bolton, D. The computation of equivalent potential temperature. *Mon. Weather Rev.* **1980**, *108*, 1046–1053.
69. De Vicente, P.; Pulido, A.D. *The Atmosphere in the 40 m RT Environment*; Water Vapour and Opacity; 2012-18; IT-OAN: Madrid, Spain, 2012.
70. Li, Z.-L.; Wu, H.; Wang, N.; Qiu, S.; Sobrino, J.A.; Wan, Z.; Tang, B.-H.; Yan, G. Land surface emissivity retrieval from satellite data. *Int. J. Remote Sens.* **2013**, *34*, 3084–3127.
71. Sobrino, J.A.; Raissouni, N. Toward remote sensing methods for land cover dynamic monitoring: Application to Morocco. *Int. J. Remote Sens.* **2000**, *21*, 353–366.
72. Sobrino, J.A.; Raissouni, N.; Li, Z.-L. A comparative study of land surface emissivity retrieval from NOAA data. *Remote Sens.Environ.* **2001**, *75*, 256–266.
73. Valor, E.; Caselles, V. Mapping land surface emissivity from NDVI: Application to European, African, and South American areas. *Remote Sens. Environ.* **1996**, *57*, 167–184.
74. Sobrino, J.A.; Jiménez-Muñoz, J.C.; Paolini, L. Land surface temperature retrieval from Landsat TM 5. *Remote Sens. Environ.* **2004**, *90*, 434–440.
75. Rubio, E.; Caselles, V.; Badenas, C. Emissivity measurements of several soils and vegetation types in the 8–14 μm wave band: Analysis of two field methods. *Remote Sens. Environ.* **1997**, *59*, 490–521.
76. Sobrino, J.A.; Jiménez-Muñoz, J.C.; Sòria, G.; Gómez, M.; Ortiz, A.B.; Romaguera, M.; Zaragoza, M.; Julien, Y.; Cuenca, J.; Atitar, M.; *et al.*Thermal remote sensing in the framework of the SEN2FLEX project: Field measurements, airborne data and applications. *Int.J. Remote Sens.* **2008**, *29*, 4961–4991.
77. Choudhury, B.J.; Ahmed, N.U.; Idso, S.B.; Reginato, R.J.; Daughtry, C.S.T. Relations between evaporation coefficients and vegetation indices studied by model simulations. *Remote Sens. Environ.* **1994**, *50*, 1–17.
78. Gutman, G.; Ignatov, A. The derivation of the green vegetation fraction from NOAA/AVHRR data for use in numerical weather prediction models. *Int. J. Remote Sens.* **1998**, *19*, 1533–1543.
79. Van Wagtendonk, J.W.; Root, R.R.; Key, C.H. Comparison of AVIRIS and Landsat ETM+ detection capabilities for burn severity. *Remote Sens. Environ.* **2004**, *92*, 397–408.
80. De Santis, A.; Chuvieco, E. Burn severity estimation from remotely sensed data: Performance of simulation *vs.* empirical models. *Remote Sens. Environ.* **2007**, *108*, 422–435.
81. Tanase, M.; de la Riva, J.; Pérez-Cabello, F. Estimating burn severity at the regional level using optically based indices. *Can. J. For. Res.* **2011**, *41*, 863–872.
82. Key, C.H.; Benson, N.C. *Remote Sensing Measure of Severity: The Normalized Burn Ratio, FIREMON Landscape Assessment (LA) v4, Sampling and Analysis Methods*; USFS Rocky Mountain Research Station: Collins, CO, USA, 2004.
83. Parks, S.; Dillon, G.; Miller, C. A new metric for quantifying burn severity: The relativized burn ratio. *Remote Sens.* **2014**, *6*, 1827–1844.
84. Kokaly, R.F.; Rockwell, B.W.; Haire, S.L.; King, T.V.V. Characterization of post-fire surface cover, soils, and burn severity at the Cerro Grande fire, New Mexico, using hyperspectral and multispectral remote sensing. *Remote Sens. Environ.* **2007**, *106*, 305–325.
85. Lhermitte, S.; Verbesselt, J.; Verstraeten, W.W.; Veraverbeke, S.; Coppin, P. Assessing intra-annual vegetation regrowth after fire using the pixel based regeneration index. *ISPRS J. Photogramm. Remote Sens.* **2011**, *66*, 17–27.

86. Veraverbeke, S.; Lhermitte, S.; Verstraeten, W.; Goossens, R. The temporal dimension of Differenced Normalized Burn Ratio (dNBR) fire/burn severity studies: The case of the large 2007 Peloponnese wildfires in Greece. *Remote Sens. Environ.* **2010**, *114*, 2548–2563.
87. Lhermitte, S.; Verbesselt, J.; Verstraeten, W.W.; Coppin, P. A pixel based regeneration index using time series similarity and spatial context. *Photogramm. Eng. Remote Sens.* **2010**, *76*, 673–682.
88. García-Martín, A.; Pérez-Cabello, F.; de la Riva Fernández, J.; Llovería, R.M. Estimation of crown biomass in the context of forest-fire management in Mediterranean areas. *Towar. Oper. Use Remote Sens. For. Fire Manag.* **2007**, *84*, 78–82.
89. Copertino, V.A.; di Pietro, M.; Scavone, G.; Telesca, V. Comparison of algorithms to retrieve land surface temperature from Landsat-7 ETM+ IR data in the Basilicata Ionian band. *Tethys* **2012**, *12*, 25–34.
90. Srivastava, P.K.; Majumdar, T.J.; Bhattacharya, A.K. Surface temperature estimation in Singhbhum Shear Zone of India using Landsat-7 ETM+ thermal infrared data. *Adv. Space Res.* **2009**, *43*, 1563–1574.
91. Vlassova, L.; Perez-Cabello, F.; Nieto, H.; Martín, P.; Riaño, D.; de la Riva, J. Assessment of methods for land surface temperature retrieval from Landsat-5 TM images applicable to multiscale tree-grass ecosystem modeling. *Remote Sens.* **2014**, *6*, 4345–4368.
92. Barbero, M.; Loisel, R.; Quezel, P.; Richardson, D.M.; Romane, F. Pines of the Mediterranean Basin. In *Ecology and Biogeography of Pinus*; Richardson, D., Ed.; Cambridge University Press: Cambridge, UK, 2000; pp. 153–170.
93. Pérez-Cabello, F.; Echeverría, M.; Ibarra, P.; Riva, J. Effects of Fire on Vegetation, Soil and Hydrogeomorphological Behavior in Mediterranean Ecosystems. In *Earth Observation of Wildland Fires in Mediterranean Ecosystems*; Chuvieco, E., Ed.; Springer: Berlin/Heidelberg, Germany, 2009; pp. 111–128.
94. Junta de Extremadura. Plan de Ordenación de los Recursos Forestales de las Hurdes. In *Plan Forestal de Extremadura*; Government of Extremadura: Extremadura, Spain, 2011.

8. Effects of post-fire wood management strategies on vegetation recovery and land surface temperature (LST) estimated from Landsat images

This chapter reproduces the text of the following article:

Title:
Effects of post-fire wood management strategies on vegetation recovery and land surface temperature (LST) estimated from Landsat images

Authors:
Vlassova, L.; Pérez-Cabello, F.

International Journal of Applied Earth Observation and Geoinformation 44 (2016) 171–183

Contents lists available at ScienceDirect

International Journal of Applied Earth Observation and Geoinformation

journal homepage: www.elsevier.com/locate/jag

Effects of post-fire wood management strategies on vegetation recovery and land surface temperature (LST) estimated from Landsat images

Lidia Vlassova[a,b,*], Fernando Pérez-Cabello[a]

[a] GEOFOREST Group, IUCA, Department of Geography and Spatial Management, University of Zaragoza, Spain, Pedro Cerbuna 12, E-50009, Zaragoza, Spain
[b] Department of Environmental Sciences, Technical State University of Quevedo, Quevedo EC120509, Los Ríos, Ecuador

ARTICLE INFO

Article history:
Received 8 April 2015
Received in revised form 27 July 2015
Accepted 31 August 2015
Available online 12 September 2015

Keywords:
Post-fire wood management
Salvage logging
Ecosystem recovery
Landsat-8
NDVI
Land surface temperature (LST)

ABSTRACT

The study contributes remote sensing data to the discussion about effects of post-fire wood management strategies on forest regeneration. Land surface temperature (LST) and Normalized Differenced Vegetation Index (NDVI), estimated from Landsat-8 images are used as indicators of *Pinus halepensis* ecosystem recovery after 2008 fire in areas of three post-fire treatments: (1) salvage logging with wood extraction from the site on skidders in suspended position (SL); (2) snag shredding in situ leaving wood debris in place (SS) performed two years after the event; and (3) non-intervention control areas (CL) where all snags were left standing. Six years after the fire NDVI values ~0.5 estimated from satellite images and field radiometry indicate considerable vegetation recovery due to efficient regeneration traits developed by the dominant plant species. However, two years after management activities in part of the burnt area, the effect of SL and SS on ecosystem recovery is observed in terms of both LST and NDVI. Statistically significant differences are detected between the intervened areas (SL and SS) and control areas of non-intervention (CL); no difference is registered between zones of different intervention types (SL and SS). CL areas are on average 1 °C cooler and 10% greener than those corresponding to either SL or SS, because of the beneficial effects of burnt wood residuals, which favor forest recovery through (i) enhanced nutrient cycling in soils, (ii) avoidance of soil surface disturbance and mechanical damage of seedlings typical to the managed areas, and (iii) ameliorated microclimate. The results of the study show that in fire-resilient ecosystems, such as *P. halepensis* forests, NDVI is higher and LST is lower in areas with no management intervention, being an indication of more favorable conditions for vegetation regeneration.

1. Introduction

Wildfire is one of the main disturbance causes of Mediterranean forests (Pausas et al., 2009) being a main driver of vegetation and landscape dynamics (Agee, 1998; Lloret and Zedler, 2009). According to authors who have reviewed effects of fire on soils and vegetation (Cerdà and Robichaud, 2009; Certini, 2005; Pausas et al., 2009; among others), fires consume above surface biomass (trees, understory, litter) partly or completely, and modify physical, chemical and microbial properties of soils. The loss of vegetation canopies alters hydrological cycle modifying conditions for evapotranspiration and changing parameters controlling runoff and infiltration (DeBano, 2000; Wagenbrenner et al., 2015), which results in important increase of soil erosion (Badía et al., 2011; Pérez-Cabello et al., 2009). The degree of damage depends on several factors, which include fire severity (Lentile et al., 2006) and the type of survival strategy developed by predominant plant species (Vallejo et al., 2012).

Short term priority of the emergency post-fire activities is to prevent soil degradation and tree pests, and decrease risks to people from the burnt trees (Robichaud, 2009; Vallejo et al., 2012). Long-term objectives often consider reestablishment of the pre-fire structure and processes in the burned forests. At present forest restoration is not limited to reforestation and afforestation as earlier (Pausas et al., 2004). Besides active intervention, which consists in planting the trees, available approaches include indirect restoration, either passive (natural regeneration protecting against further disturbances) or assisted, when natural regeneration is complemented with management activities. The success

* Corresponding author at: GEOFOREST Group, IUCA, Department of Geography and Spatial Management, University of Zaragoza, Spain, Pedro Cerbuna 12, E-50009, Zaragoza, Spain. Fax: +34 976 761 506
E-mail address: vlassova@unizar.es (L. Vlassova).

http://dx.doi.org/10.1016/j.jag.2015.08.011
0303-2434/

of different management techniques varies a lot from one experience to another, and there is a great demand of objective and unbiased data from monitoring. Difficulties in generalization of fire effects and a great variation in natural capacity of environmental response explain the lack of consensus on the efficiency of current forest restoration strategies (Pausas et al., 2004).

One of the most controversial aspects is the role of the burnt wood. Strategy of post-fire wood management is a topic of ongoing intense scientific discussion. Recent examples include the controversy raised by the article from (Donato et al., 2006a) with the following responses and contra-responses (Baird, 2006; Donato et al., 2006b; Newton et al., 2006), and reports by McIver et al. (2000), Bautista et al. (2004) or Lindenmayer et al. (2008). In Spain, post-fire salvage logging is a common practice (Fernández et al., 2008; Hernández Jimenez, 2014; Vallejo et al., 2012). However, multiple studies show that burnt wood extraction can have multiple negative ecological consequences. It affects key ecosystem processes altering water, carbon and nutrients cycles (Serrano-Ortiz et al., 2011). When logs and other woody debris are removed, fire-affected areas are left without part of their biological legacies vital for forest regeneration (Perera and Buse, 2014). Removal of snags reduces the amount of seeds available for regeneration of serotinous tree species (Greene et al., 2013). Greater exposure to sunlight due to clear-cutting modifies microclimate and limits the number and variety of sites suitable for germination (Marañón-Jiménez et al., 2013b; Marzano et al., 2013); elevated temperatures and wind reduce soil moisture content and cause hydric stress of seedlings, sprouts and young trees (Martínez-Sánchez et al., 1999; Vacchiano et al., 2014). Among the effects of salvage logging are vegetation homogenization (Purdon et al., 2004), loss of complexity in the forest structure (Lindenmayer et al., 2008) and changes in species composition (Leverkus et al., 2014; Marzano et al., 2013).

Recovery after wild fire is a slow process requiring scientific short- and longtime monitoring (Pausas et al., 2009). Ecological effects of salvage logging are usually evaluated based on field studies, but the use of alternative techniques, such as satellite remote sensing, in studying the influence of wood removal on vegetation regeneration can complement fieldwork results and provide another spatial dimension to analysis. Remote sensing is a valuable tool for environmental monitoring because it provides systematic coverage of extensive areas (Lentile et al., 2006; Schroeder et al., 2010). Remotely sensed data have been widely applied in fire science and management for detecting active fires (Roy, 1999); assessing active fire behavior (Smith and Wooster, 2005); and evaluating post-fire vegetation response (Díaz-Delgado et al., 2003; Hernández Clemente et al., 2009). Data from Landsat satellites are especially suitable because of their temporal and spatial resolution (16 days and 30 m, respectively). The potential of Landsat data in detecting patterns of post-fire forest recovery resulting from application of different management strategies has been reported by Chen et al. (2014). Landsat images provide data from visible, near infrared, shortwave infrared and thermal spectral regions, which makes possible the analysis of biophysical variables using LST synchronous with spectral indices.

One of the most popular spectral indices used for vegetation assessment from the satellite images is the Normalized Difference Vegetation Index (NDVI) (Rouse et al., 1973). It is based on the contrasting reflectance values in near-infrared and red wavelengths characteristic to plants and has been often used as indicator of management success in post-fire vegetation regeneration. Multiple studies (Van Leeuwen et al., 2010; Vila and Barbosa, 2010 among others) observed that NDVI has higher correlation with post-fire vegetation recovery estimated from the field data than other vegetation indices.

Changes in land surface energy balance due to the vegetation loss are reflected in modified LST values and distribution (Quintano et al., 2015; Veraverbeke et al., 2012; Vlassova et al., 2014). LST is a key factor conditioning soil physical environment since it determines the speed and direction of physico-chemical processes and energy/matter interchanges with the atmosphere (Quattrochi and Luvall, 2004). It affects soil microbiological activity; controls root development, levels of seed germination and plant growth rates (Mexal and South, 1991; Spanos et al., 2000). Moreover, increased temperature is a clear indication of plant moisture stress, which occurs when demand for water exceeds available soil moisture level (Liang, 2004). As vegetation transpires, the evaporated water cools the leaves so that their temperatures are below air temperature. When the plant becomes water stressed, transpiration decreases and the canopy temperature increases (Jackson, 1982). Because it affects photosynthesis and respiration (Hatfield, 1997), transpiration rate is a primary indicator of adequate functioning of any plant ecosystem, including forests (Vidal and Devaux-Ros, 1995). The direct link between the process of transpiration and the vegetation thermal response explains the potential of the use of LST as a metric of plant ecosystem health in monitoring of the fire-affected zones (Moran, 2004).

Monitoring of NDVI and LST as indicators of post-fire landscape regeneration can be performed using remote sensing, which provides a cost-efficient alternative for estimation of these variables on a regular basis with precision required for assessment of post-fire landscape recovery (Gitas et al., 2008; Vicente-Serrano et al., 2008).

The objective of this research is to study the effect of different post-fire wood treatments on vegetation recovery (through NDVI) and LST. Precise information on spatio-temporal distribution of surface temperature in areas of salvage logging can help understand its role in processes taking place in soil and vegetation after fire.

2. Materials and methods

2.1. Study area

The study area (Fig. 1) is situated in the Zuera Mountains, NE Spain (41°56′- 4°58′N, 0°55′- 1°0′W), where in four days between 5 and 8 of August 2008 a wildfire consumed more than 2500 ha of forest managed by Forest Administration of Aragon Autonomous Region DGA causing damage to Special Bird Protection Zone (ZEPAS) and Places of Community Importance (LIC) (EGIF, 2008).

The burnt area located at 500–740 m above sea level is characterized by Mediterranean climate with average annual temperature of 12.5 °C and average annual precipitation ~560 mm with summer minimum (Cuadrat et al., 2007). The fire destroyed forests dominated by *Pinus halepensis Mill* on sandy-loam soils over Rendzic Phaeozem (Badía et al., 2013). The understory is rich in typical Mediterranean species, such as *Quercus coccifera L.*, *Juniperus oxycedrus L.*, *Rosmarinus officinalis L.* and *Genista Scorpius (L.)DC.* Forests are interspersed with patches of shrublands dominated by *Q. coccifera, G. scorpius* and *Brachipodium retusum.*

Three different burnt wood treatments were implemented in the fire-affected area (Fig. 1) between November 2009 and September 2011: (1) salvage logging (SL): felling of the snags, their removal from the burnt site on the skidder in suspended position with following branch cutting and wood shredding outside the site; (2) shredding of snags in situ (SS): mastication of the standing burnt trees with a mulching head attached to a retroexcavator, leaving wood debris on site; (3) non-intervention/control (CL): areas where burnt trees were not logged and no management activities were realized.

Fig. 2 shows typical vegetation cover in the study area at the moment of sampling in August of 2014. Vegetation in Salvage

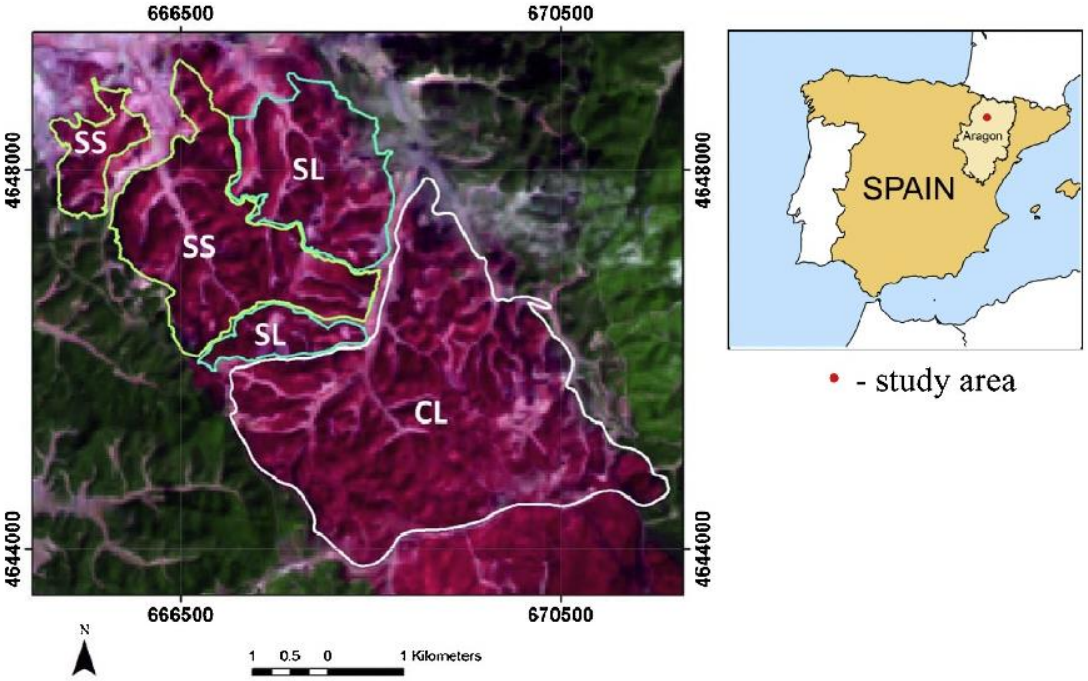

Fig. 1. Map of the fire site (color RGB composite of Landsat-7 bands 7-4-3; burnt area appears in tones of red). Polygons indicate areas of different post-fire wood treatments: Salvage Logging (SL); Snag Shredding (SS); and Control (CL). (For interpretation of the references to colour in this figure legend, the reader is referred to the web version of this article.)

Logging (SL) and Snag Shredding (SS) areas (Fig. 2A and 2B, respectively) is characterized by the presence of evergreen sclerophyllous shrublands (<1.5 m tall), sclerophyllous pastures dominated by *Brachypodium retosum* (a rhizomatous perennial grass resprouting after fire), areas of bare soil, and *P. halepensis* saplings (<1 m tall) (~75 plants per hectare). Shrub species with the highest contribution to the vegetation cover are those typical for a garrigue plant community: *Q. coccifera* (kermes oak) (~30%) — an obligate resprouter-, and *R. officinalis* (~20%) and *G. scorpius* (15–20%) — obligate seeders-. Among other plant species identified in both SL and SS areas are *Prunus spinosa*, *J. oxycedrus*, *Staehelina dubia*, *Rhamnus lycioides*, *Rubia peregrina*, *Bupleurum rigidum*, *Quercus ilex*, *Phyllerea angustifolia*, *Pistacea terebinthus*, *Lonicera implexa*, *Thymus* sp. and *Euphorbia* sp. Control areas (CL) at the moment of sampling were characterized by the presence of snags (3-5 per hectare), logs and other coarse wood debris, sometimes forming a 1–1.5 m layer (Fig. 2C), and the greater vigor of the regenerated vegetation in these areas consisting mainly of *P. halepensis* saplings and *Q. coccifera*.

2.2. Data

2.2.1. Remotely and proximally sensed data

Six clear sky Landsat images of the area (path 199/row 31) taken between 10:30 and 10:45 GMT (Table 1) were downloaded from the USGS Global Visualization Viewer (http://glovis.usgs.gov). Level 1T scenes in UTM projection are provided after geometric and radiometric correction. Two scenes were acquired by Landsat-7 before and a short time after the fire (June 27 and August 30 of 2008, respectively); four other images were taken by Landsat-8 in 2014 and give information on the present state of the fire-affected area. Both satellites produce images of similar spectral and spatial characteristics. Optical and thermal data are used in the study. There are two thermal bands (10 and 11) in Landsat-8 images, but only band 10 (10.60–11.19 μm) was used for LST estimation, because of elevated uncertainties detected in the data from another band (http://landsat.usgs.gov/calibration_notices.php).

Table 1
Acquisition time and observation geometry of Landsat images.

Mission	Date	Aquisition time (GMT)	Sun Azimuth	Sun Elevation
			(Degrees)	(Degrees)
Landsat 7	27-Jun-08	10:32:25	126.53	63.32
	30-Aug-08	10:31:51	142.44	51.44
Landsat 8	16-Mar-14	10:43:19	150.02	42.51
	03-May-14	10:42:31	142.22	59.45
	20-Jun-14	10:42:32	131.21	65.36
	23-Aug-14	10:42:54	143.84	55.02

Reflectance spectra of landcover in treated and control areas were measured during field campaign in August 2014 using ASD spectroradiometer (ASD, 2012). The instrument registered reflectance in the wave range of 350–2500 nm with spectral resolution of 3–10 nm. Reflectance measurements were performed between 12:00 and 15:00 local time with optical fiber 1 m above the plant canopy pointing vertically downwards. 44 SL and 59CL spectral signatures were obtained. Each spectral sample was calculated as the mean of 20 individual spectra to improve signal-to-noise ratio. Reflectance in Landsat spectral bands was simulated from the continuous spectral signatures (Teillet et al., 2001) and used to calculate NDVI for comparison with available Landsat images.

2.2.2. Ancillary data

Surface slope and aspect were generated at 25 m spatial resolution using digital elevation model from the National Center for Geographic Information (Spain) (http://centrodedescargas.cnig.es/CentroDescargas/). To overcome the difficulty present when aspect is measured in degrees east of north, and north-facing slopes can have aspect values as different as 1 and 360 Beerís transformation (Beers et al., 1966) was applied rescaling aspect between zero and

SL

SS

CL

Fig. 2. Vegetation regeneration in areas of different post-fire treatments (August 7, 2014): SL- salvage logging, SS — snag shredding and CL — non-intervention/control.

two, with zero corresponding to the northeast and two to the southwest direction. calculated according to Burrough and McDonnell (1998) was considered a proxy for the amount of incident sun energy.

2.3. Methods

2.3.1. Pre-processing of remotely sensed data

As a first step, gap-filling was applied to the parts of Landsat-7 images affected by data loss due to the malfunctioning of the scan-line corrector (Storey et al., 2005). Localized linear histogram match method (Scaramuzza et al., 2004) was used for filling the gaps. It takes advantage of the fact that the area of data loss is not the same on contiguous in time Landsat passes, so other images of similar phenology can be used for gap-filling. When the gap is detected, the linear histogram matching methodology attempts to find a linear transformation between one image and another. Fill values for the gap pixels are generated by applying a corrective gain and bias to the pixels in the auxiliary image. The quality of the correction mainly depends on the similarity of atmospheric conditions and phenology in the images used for gap-filling and the scenes affected by data gaps (Rulloni et al., 2012 Zhang et al., 2007). Thus, the correction of the pre-fire (June 27, 2008) and post-fire (August 30, 2008) Landsat images was performed using July 8, 2007 and September 15, 2008 scenes acquired at atmospheric visibility of ~12 km and average NDVI within the burn perimeter around 0.6 and 0.2 for pre- and postfire images, respectively.

Next, original digital numbers (DN) were converted to the top-of-the-atmosphere radiance using coefficients from image file and procedure recommended by NASA for Landsat-7 and Landsat-8 (http://landsat.usgs.gov/how_is_radiance_calculated.php and http://landsat.usgs.gov/Landsat8_Using_Product.php).

Finally, atmospheric correction of optical bands was performed by Fast Line-of-sight Atmospheric Analysis of Hypercubes (FLAASH) algorithm (Cooley et al., 2002). Atmospheric water vapor content from the National Center for Environmental Prediction (NCEP) Reanalysis database (http://www.esrl.noaa.gov/psd/data) was used for the algorithm adjustment.

2.3.2. Vegetation recovery and land surface temperature (LST) estimation

Vegetation regeneration was assessed from the NDVI, which is one of the most popular metrics for assessment of post-fire vegetation recovery (Díaz-Delgado et al., 2003; Lanorte et al., 2014; Riaño et al., 2002).

LST was estimated using Single-Channel (SC) method (Jiménez-Muñoz et al., 2014; Jiménez-Muñoz and Sobrino, 2004). Multiple studies have successfully applied this method for LST estimation from Landsat-5 and Landsat-7 thermal data. For atmospheres with water content in the range of 0.5–2.5 g cm^{-2} the method provides LST values from Landsat 5/7 with an error of around 1 K (Jiménez-Muñoz et al., 2014); software simulations for Landsat-8 thermal band 10 performed by the algorithm developers (Jiménez-Muñoz et al., 2014) estimate the expected error around 1.5 K. The algorithm requires only total water vapor content for atmospheric correction.

Surface emissivity (ratio between the target emitting capacity and that of a blackbody at the same temperature) necessary for LST calculation cannot be estimated from the Landsat image (Li et al., 2013). It is highly correlated with the NDVI and was calculated in this study using the NDVI Thresholds Method ($NDVI^{THM}$) (Sobrino and Raissouni, 2000) based on the findings of Valor and Caselles (1996). Emissivity is assigned to a pixel based on its NDVI range. Thus, fully vegetated pixels with $NDVI \geq 0.7$ are assigned emissivity of 0.990, whereas bare soil pixels with $NDVI \leq 0.1$ are assumed to have average emissivity of 0.973, as suggested in Sobrino et al.

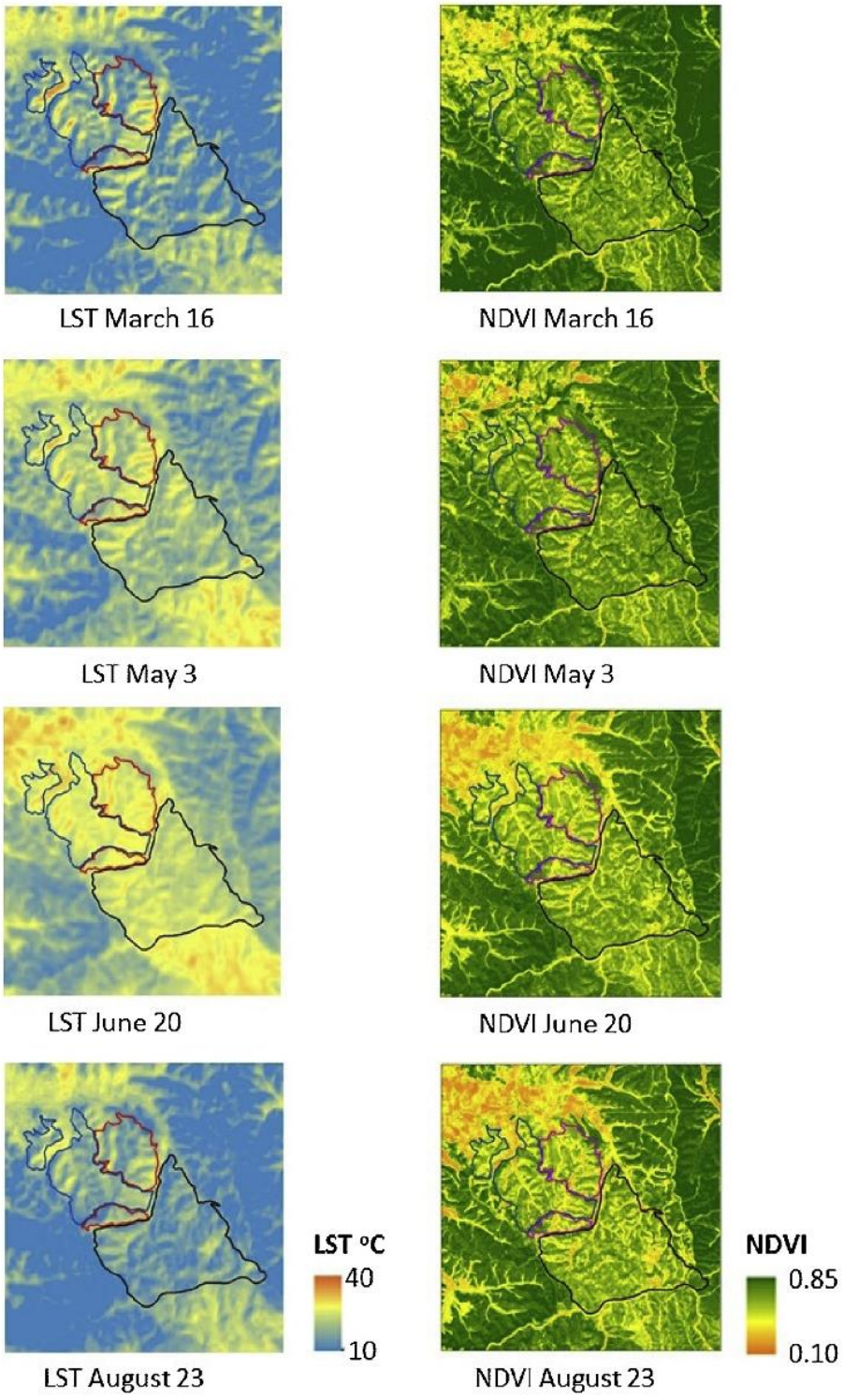

Fig. 3. Spatial distribution of LST (left column) and NDVI (right column) on four spring and summer dates in 2014. Areas of SL and SS management activities are delimited by red and blue lines, respectively; black line encircles control (CL) area. (For interpretation of the references to colour in this figure legend, the reader is referred to the web version of this article.)

Table 2
Mean and standard deviation (in parenthesis) for land surface biophysical variables. S1, S2, S3 are random samples ($N = 300$); SL, SS and CL are treatment types ($n = 100$).

Variable	Treatment	S1	S2	S3
Elevation (m)	CL	652 (23)	656 (23)	653 (23)
	SL	623 (16)	625 (22)	628 (20)
	SS	613 (22)	616 (22)	616 (21)
Slope (degrees)	CL	15.7 (5.6)	14.8 (6.2)	15.0 (5.6)
	SL	14.2 (6.4)	14.3 (6.2)	13.2 (6.4)
	SS	15.8 (5.7)	15.7 (5.7)	15.2 (5.9)
Aspect	CL	0.85 (0.68)	0.86 (0.76)	0.86 (0.70)
	SL	1.00 (0.76)	0.97 (0.71)	1.00 (0.73)
	SS	1.01 (0.71)	0.94 (0.67)	1.02 (0.70)
Illumination (March 16, 2014)	CL	0.58 (0.13)	0.59 (0.12)	0.58 (0.13)
	SL	0.60 (0.11)	0.60 (0.12)	0.60 (0.11)
	SS	0.57 (0.13)	0.61 (0.13)	0.59 (0.13)
Illumination (May 3, 2014)	CL	0.77 (0.09)	0.78 (0.09)	0.78 (0.10)
	SL	0.79 (0.08)	0.79 (0.09)	0.80 (0.08)
	SS	0.77 (0.10)	0.79 (0.09)	0.78 (0.10)
Illumination (June 20, 2014)	CL	0.83 (0.08)	0.84 (0.08)	0.83 (0.08)
	SL	0.84 (0.08)	0.84 (0.08)	0.85 (0.08)
	SS	0.83 (0.08)	0.85 (0.08)	0.84 (0.08)
Illumination (August 23, 2014)	CL	0.73 (0.10)	0.74 (0.10)	0.73 (0.11)
	SL	0.75 (0.09)	0.75 (0.10)	0.75 (0.09)
	SS	0.73 (0.11)	0.75 (0.10)	0.74 (0.11)
Pre-fire NDVI (June 27, 2008)	CL	0.68 (0.04)	0.69 (0.04)	0.69 (0.04)
	SL	0.67 (0.04)	0.67 (0.05)	0.68 (0.03)
	SS	0.69 (0.05)	0.68 (0.05)	0.69 (0.05)
Pre-fire LST (June 27, 2008)	CL	24.6 (1.1)	24.4 (1.1)	24.5 (1.2)
	SL	24.4 (1.0)	24.0 (0.9)	24.4 (1.1)
	SS	24.3 (1.3)	24.2 (1.4)	24.4 (1.1)
dNBR	CL	793 (86)	799 (85)	801 (83)
	SL	787 (90)	791 (93)	801 (79)
	SS	810 (95)	802 (98)	810 (96)

(2004). Emissivity of the pixels containing both soil and vegetation ($0.1 < NDVI < 0.7$) is scaled between these two extremes.

2.3.3. Burn severity assessment

Burn severity was estimated using Delta Normalized Burn Ratio Index (dNBR). Multiple studies have demonstrated that dNBR is closely related to burn severity of conifer forests in the Mediterranean (Gitas et al., 2009; Tanase et al., 2011; Veraverbeke et al., 2011). dNBR calculation followed the methodology suggested by Key and Benson (2006) and involved (1) transformation of the digital numbers into reflectance (R) of the pre- and post-fire images; (2) generation of the Normalized Burn Ratio (NBR) image for each date using the formula $(R_4 - R_7)/(R_4 + R_7)$, where subscripts correspond to band numbers; and (3) calculation of the dNBR subtracting pre- and post-fire NBR images.

2.3.4. Statistical procedures

Data were grouped in three classes according to wood treatment: (1) salvage logging (SL); (2) snag shredding (SS); and non-intervention/control (CL). For statistical analysis 100 points per class were randomly selected forming a sample of 300 points. The procedure was repeated three times obtaining samples S1, S2, and S3. Spatial distribution of the points in S1, S2 and S3 is shown in Fig. A1 of Appendix A. Furthermore, to prevent bias due to the influence of the adjacent agricultural areas, only pixels farther than 60 m from the edge of the treated area were considered. Spatial autocorrelation was estimated using Moranís I index, which quantifies similarity of spatially distributed events (pixels) as a function of distance (Moran, 1950). In case of CL pixels Moranís I index is close to zero for pre- and post-fire NDVI revealing random distribution. As for the SL and SS, positive Moranís I values are 0.2–0.3 for pre-fire NDVI and 0.25–0.35 for post-fire NDVI, which is an indication of a slight tendency for clustering.

One-way ANOVA was performed to test (1) similarity of environmental factors between classes and (2) to verify if there are significant differences in analyzed land surface variables (LST and NDVI) between treatments. For greater robustness the analysis was realized on S1, S2 and S3.

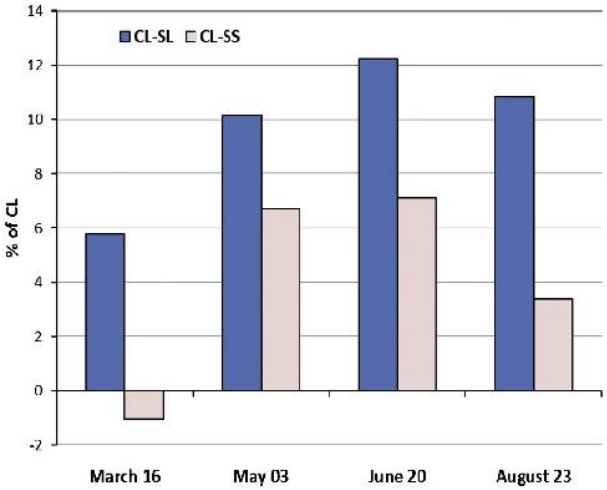

Fig. 4. NDVI differences between control (CL) and intervened (SL and SS) areas in 2014 (data for S1).

Contribution of different post-fire wood management treatments to vegetation regeneration (NDVI) and land surface temperature (LST) was evaluated by factorial ANOVA, widely used in environmental research (e.g., Wheater and Cook, 2000). All of the predictors fully satisfy ANOVA assumptions (Chapman et al., 1976).

3. Results

3.1. Environmental variables

Comparison of post-fire treatments requires knowledge of environmental characteristics in terms of pre-fire vegetation

Table 3
ANOVA results for land surface biophysical variables in three analyzed samples (S1, S2 and S3).

Variable	S1		S2		S3	
	F	Sig.	F	Sig.	F	Sig.
Elevation (m)	90.695	0.000	82.179	0.000	69.704	0.000
Slope (degrees)	2.524	0.082	1.442	0.238	3.411	0.054
Aspect	1.480	0.229	0.637	0.530	1.575	0.209
Illumination (March 16, 2014)	1.515	0.221	0.766	0.466	1.274	0.281
Illumination (May 3, 2014)	1.494	0.226	0.455	0.635	1.072	0.344
Illumination (June 20, 2014)	1.210	0.300	0.182	0.833	0.700	0.497
Illumination (August 23, 2014)	1.470	0.232	0.521	0.594	1.090	0.337
Pre-fire NDVI (June 27, 2008)	1.745	0.176	1.653	0.193	1.720	0.181
Pre-fire LST (June 27, 2008)	1.090	0.338	1.232	0.294	0.545	0.581
dNBR	1.638	0.196	0.407	0.666	0.307	0.736

p-Value < 0.05.

Table 4
Mean values and standard deviation (in parenthesis) for LST (°C) estimated from Landsat 8 images for samples S1, S2 and S3.

Date	Treatment	S1	S2	S3
March 16, 2014	CL	15.95 (1.19)	15.93 (1.17)	15.99 (1.19)
	SL	16.68 (1.18)	16.74 (1.31)	16.66 (1.22)
	SS	16.99 (1.26)	16.86 (1.42)	16.99 (1.36)
May 3, 2014	CL	22.98 (1.18)	22.90 (1.16)	22.98 (1.26)
	SL	23.90 (1.18)	23.94 (1.31)	23.86 (1.24)
	SS	24.00 (1.21)	23.90 (1.37)	23.99 (1.31)
June 20, 2014	CL	35.35 (0.94)	35.38 (0.81)	35.41 (0.99)
	SL	37.24 (1.01)	37.20 (1.07)	37.21 (1.02)
	SS	37.04 (0.86)	37.01 (0.94)	37.06 (0.86)
August 23, 2014	CL	25.00 (1.09)	24.99 (1.15)	24.99 (1.16)
	SL	26.25 (1.18)	26.27 (1.32)	26.20 (1.24)
	SS	26.31 (1.21)	26.24 (1.24)	26.34 (1.26)

Table 5
Mean LST differences (°C) between CL, SL and SS areas for samples S1, S2 and S3.

Dependent variable	(I)	(J)	Difference of means (I-J)		
			S1	S2	S3
LST_March_16	CL	SL	**−0.73**	**−0.80**	**−0.67**
	CL	SS	**−1.04**	**−0.93**	**−1.00**
	SL	SS	−0.31	-0.12	−0.33
LST_May_03	CL	SL	**−0.93**	**−1.05**	**−0.88**
	CL	SS	**−1.03**	**−1.00**	**−1.02**
	SL	SS	-0.10	0.04	−0.13
LST_June_20	CL	SL	**−1.88**	**−1.82**	**−1.80**
	CL	SS	**−1.69**	**−1.63**	**−1.65**
	SL	SS	0.19	0.19	0.16
LST_August_23	CL	SL	**−1.23**	**−1.29**	**−1.21**
	CL	SS	**−1.30**	**−1.26**	**−1.35**
	SL	SS	−0.07	0.03	−0.14

abundance and LST, land surface topographical and illumination conditions and fire severity, to prevent contamination of the post-fire vegetation regeneration analysis with effects of these variables. Table 2 presents descriptive statistics of elevation, slope, aspect, solar illumination, dNBR and pre-fire NDVI and LST.

ANOVA results demonstrate that there are no statistically significant differences among SS, SL and CL, except for elevation (Table 3), which is ~620 m for SL and SS, and ~650 m for CL points. This mismatch, although not very relevant, is statistically significant and its effect on vegetation recovery and spatial distribution of LST is further analyzed using factorial ANOVA (see Sections 3.3 and 3.4).

Slope and exposition together with solar elevation angle were used to estimate illumination geometry at the moment of satellite overpass. These conditions are homogeneous in the three samples (Table 3). Pre-fire vegetation cover (pre-fire NDVI ~0.68) and fire severity (dNBR ~800) are similar for SL, SS and CL. Similarity in most of the environmental characteristics ensures the comparability of LST and NDVI, indicators of landscape regeneration.

3.2. Land surface temperature (LST)

Table 4 shows descriptive statistics for LST in S1, S2 and S3 by analyzed treatment categories in March, May, June and August of 2014. In addition, left column in Fig. 3 presents spatial distribution of LST on the same dates. The lowest values correspond to pixels in the burnt areas without intervention (CL) on all dates and in all samples. LST differences between control and intervened areas (Table 5) increase from 0.84 °C in March to 1.23 °C in June and are statistically significant on all tested dates. However, the differences between SL and SS areas are minimal; they range from 0.13 °C in May to 0.33 °C in March. The pattern is the same for the three samples

Differences between control and intervened areas increase with temperature. Moreover, LST variability and standard deviations in not intervened part of the burn (CL) are notably lower than in the intervened areas on three of four dates (except June).

3.3. Vegetation status (NDVI)

Descriptive statistics of NDVI for 2014 images (Table 6) reveal that vegetation abundance in the burned area six years after the fire is lower than the pre-fire level (Table 2): 0.5–0.55 versus 0.68. Fig. 2 (right column) shows spatial distribution of NDVI in four analyzed images from 2014. NDVI values observed in the control areas are the highest, except the difference between CL and SS in March (SS 0.01 higher than CL, not significant at 0.05 level). NDVI differences between CL and SL range from 0.03 in March to above 0.06 in June (Table 7), being significant for the three samples; NDVI differences between CL and SS are much lower (vary from 0.005 average in March to 0.04 average in June; Table 7), they are statistically significant at 0.05 level on all the dates, except March. Observed differences in vegetation recovery (NDVI) between areas with dif-

Table 6
Mean and standard deviation (in parenthesis) for NDVI estimated from Landsat-8 images for three samples (S1, S2 and S3).

Date	Treatment	S1	S2	S3
March 16, 2014	CL	0.56 (0.07)	0.56 (0.07)	0.57 (0.07)
	SL	0.53 (0.07)	0.53 (0.07)	0.54 (0.07)
	SS	0.57 (0.07)	0.55 (0.08)	0.56 (0.07)
May 3, 2014	CL	0.56 (0.06)	0.55 (0.06)	0.56 (0.05)
	SL	0.50 (0.06)	0.50 (0.06)	0.50 (0.06)
	SS	0.52 (0.06)	0.50 (0.07)	0.52 (0.06)
June 20, 2014	CL	0.53 (0.05)	0.53 (0.05)	0.53 (0.05)
	SL	0.46 (0.05)	0.47 (0.05)	0.47 (0.06)
	SS	0.49 (0.06)	0.47 (0.06)	0.49 (0.06)
August 23, 2014	CL	0.53 (0.07)	0.53 (0.07)	0.54 (0.06)
	SL	0.47 (0.06)	0.48 (0.06)	0.48 (0.06)
	SS	0.51 (0.07)	0.49 (0.08)	0.51 (0.07)

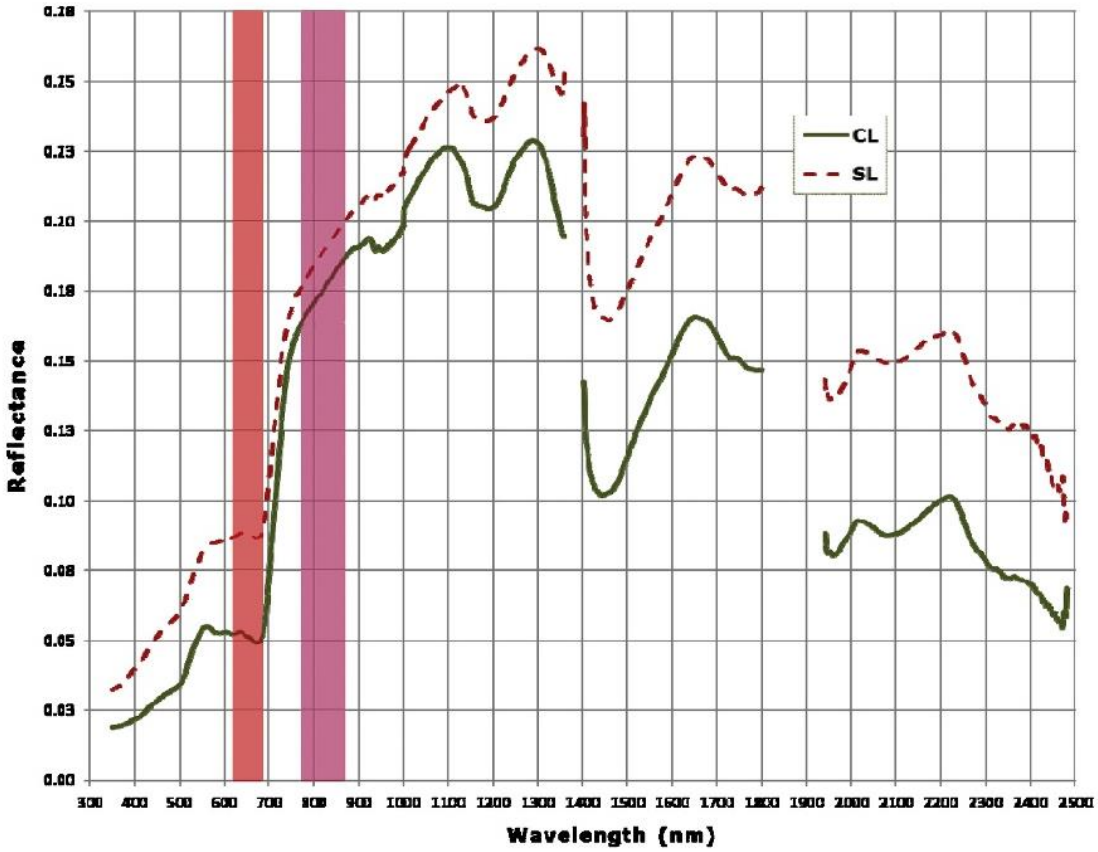

Fig. 5. Mean field spectra of the intervened (SL) and not intervened (CL) areas. Spectral regions corresponding to Landsat-8 Band 4 (RED) and Band 5 (NIR) are highlighted in red and purple, respectively. (For interpretation of the references to colour in this figure legend, the reader is referred to the web version of this article.)

ferent post-fire wood management activities (SL and SS) are much smaller than the difference of these areas and those not intervened in May and June (Table 7).

NDVI variation between dates is notably smaller for CL, than for SL or SS. Fig. 4 shows differences between intervened and not intervened areas in terms of percent of NDVI in control areas. The figure shows results for S1, since S2 and S3 present similar pattern: (1) differences between CL and SL exceed 10% in May, June and August; (2) they are greater than CL-SS on all the dates; (3) differences between CL and SS are smaller, even though in May and June they are statistically significant (>5%).

Table 7
Mean NDVI differences between treatments.

Dependent variable	(I)	(J)	Difference of means (I–J)		
			S1	S2	S3
NDVI_March_16	CL	SL	**0.033**	**0.028**	**0.030**
	CL	SS	−0.006	0.008	0.005
	SL	SS	**−0.039**	−0.020	−0.025
NDVI_May_03	CL	SL	**0.057**	**0.048**	**0.052**
	CL	SS	**0.038**	**0.051**	**0.039**
	SL	SS	−0.019	0.003	−0.013
NDVI_June_20	CL	SL	**0.065**	**0.061**	**0.066**
	CL	SS	**0.038**	**0.055**	**0.045**
	SL	SS	**−0.027**	−0.006	**−0.021**
NDVI_August_23	CL	SL	**0.058**	**0.050**	**0.058**
	CL	SS	0.018	**0.033**	**0.030**
	SL	SS	**−0.040**	−0.017	**−0.028**

Values significant at 0.05 level are in bold cursive

3.4. Spectral signatures

Fig. 5 shows mean spectral signatures obtained from field measurements in intervened (SL) and not intervened (CL) areas in August of 2014. The overall shape of the CL and SL spectra is similar: low reflectance levels in VIS are followed by sharp increase in NIR and overall decrease with some absorption features in SWIR spectral regions. In spite of these similarities, there are important differences between the spectra, too. Compared to the CL, the "treated" spectrum presents: (1) higher reflectance levels in 400–700 nm wavelengths; (2) shorter red edge and lower reflectance in the 750–1130 nm; and (3) higher reflectance in the 1400–2450 nm wavelengths (Fig. 5). NDVI values computed from the field spectra resampled to the Landsat-8 bands highlighted in Fig. 4 are higher in CL areas compared to SL (0.54 vs 0.34).

3.5. Relevance of environmental variables and type of wood treatment for spatial patterns of NDVI and LST

Because initial analysis detected statistically significant differences in *Elevation* between SL, SS and CL (see Section 3.1) factorial ANOVA was applied to assess the influence of this variable on NDVI and LST, especially in comparison with the effect of applied wood management strategy (*Treatment*). Since similar results were obtained for three samples, only those related to Sample 1 are presented in Tables 8 and 9, which show statistics for variables significant on one or more dates.

In case of LST models, explanatory variables in addition to *Elevation* and *Treatment* included date-specific *Illumination* and *NDVI*. The models explain between 53% (May 2014) and almost 70%

Table 8
Factorial ANOVA results for LST. Significant values are in bold cursive.

	March 16			May 3			June 20			August 23		
	R^2 = 0.573			R^2 = 0.529			R^2 = 0.696			R^2 = 0.597		
Independent variable	F	Sig.	η^2	F	Sig.	η^2	F	Sig.	η^2	F	Sig.	η^2
Treatment	**23.955**	**0.000**	**0.141**	**16.172**	**0.000**	**0.100**	**94.588**	**0.000**	**0.393**	**36.549**	**0.000**	**0.200**
Illumination[a]	**236.025**	**0.000**	**0.447**	**225.995**	**0.000**	**0.436**	**180.746**	**0.000**	**0.382**	**243.458**	**0.000**	**0.455**
NDVI[(a)]	0.601	0.439	0.002	0.595	0.441	0.002	**13.590**	**0.000**	**0.044**	2.062	0.152	0.007

p-Value < 0.05.
[a] Corresponding to a specific date.

Table 9
Factorial ANOVA results for NDVI.

	March 16			May 3			June 20			August 23		
	R^2 = 0.337			R^2 = 0.33			R^2 = 0.394			R^2 = 0.355		
Independent variable	F	Sig.	η^2	F	Sig.	η^2	F	Sig.	η^2	F	Sig.	η^2
Treatment	**7.430**	**0.001**	**0.049**	**20.039**	**0.000**	**0.121**	**26.475**	**0.000**	**0.154**	**20.229**	**0.000**	**0.122**
$NDVI_{June2008}$	**34.162**	**0.000**	**0.105**	**23.961**	**0.000**	**0.076**	**32.813**	**0.000**	**0.102**	**30.996**	**0.000**	**0.097**
Slope	1.001	0.318	0.003	**17.033**	**0.000**	**0.055**	**6.771**	**0.010**	**0.023**	3.027	0.083	0.010
elevation	1.349	0.246	0.005	0.888	0.347	0.003	0.052	0.820	0.000	**4.498**	**0.035**	**0.015**

p-Value < 0.05.

(June 2014) of LST variance (Table 8). The proportion of variance explained by each of the independent variables was estimated from eta squared (η^2). The highest contribution comes from *Illumination* and *Treatment*, significant on all the dates. While *Illumination* explains ~40% or more in all the models, the importance of *Treatment* varies, with the maximum of explained variance in June (39%). NDVI is significant only in June explaining 4% of variance, on other dates its contribution is less than 1%. Contribution of *Elevation* to LST explanation is not significant.

The set of independent variables in NDVI models included *Treatment*, *pre-fire NDVI* estimated from June 2008 image, *Slope*, *Aspect*, *dNBR* and *Elevation*. Models explain 33–39% of NDVI variance (Table 9). Similar to LST, the model run on June data yielded the highest R^2 (0.39). Among the most important independent variables are *Treatment* and *pre-fire NDVI*, which explain 5–15% and 8–10% of NDVI variance, respectively. *Treatment* has the highest contribution in June, and *pre-fire NDVI* exercises maximum influence in August. *Slope* is significant in May and June explaining 2% and 5% of variance on these dates. As in the case of LST modeling, *Elevation* is among the tested variables, but its power in explaining NDVI variance does not exceed 1.5%.

Zones of higher NDVI are associated with lower LST; the strength of the relation varies from date to date with the highest values observed in June (Fig. 6), the date with the highest relevance of treatment type for explanation of distribution of both NDVI and LST (Tables 8 and 9).

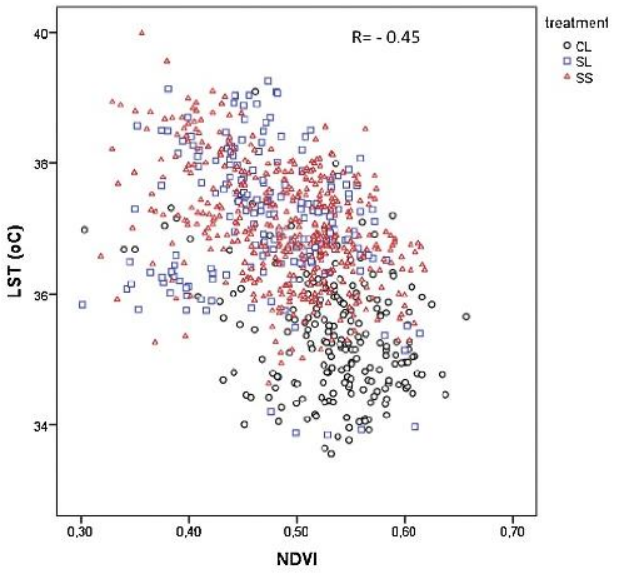

Fig. 6. Scatterplot of NDVI and LST (June 2014, Sample 1).

4. Discussion

Land surface temperature (LST) and vegetation cover (through NDVI), which control hydrological and biochemical cycles (Bonan et al., 2002), can be used as indicators of surface processes and were analyzed in this research to assess the consequences of post-fire wood treatments in an area of Zuera fire dominated by *P. halepensis*.

Different management strategies were applied by regional administration in emergency context to prevent surface erosion due to the sudden loss of vegetation and soil degradation after forest fire. The study based on Landsat-8 data compared LST and NDVI in the intervened (SL and SS) and control (CL) areas. The SS and SL strategies vary in degree of intervention: while salvage logging (SL) involves removal of the wood debris, it is left on site when snag shredding (SS) is performed.

NDVI values of ~0.5 in the analyzed areas estimated from satellite images and field radiometry indicate considerable vegetation recovery with the consequent reduction of ecosystem degradation risks. Visual field inspection of the site (Fig. 2) gives way to the conclusion that recovery is due to the effective "reseeder" mechanism developed by Aleppo pine (Trabaud et al., 1985) consisting in stimulation of post-fire seed release and germination by smoke or heat. This trait is typical to Mediterranean pine forests, where recruitment of serotinous pines is related to fire (De las Heras et al., 2012; Pausas, 1999). Another effective recovery trait of "resprouter" is observed in *Q. coccifera*, which survives by producing new growth from underground lignotubers, so that dead plants seem to revive (Trabaud, 1991). Field observations are in agreement with existing research on vegetation regeneration of the burns close to the study area (Vicente-Serrano et al., 2011).

CL zones are characterized by higher proportion of vegetation recovery. On the three of four analyzed dates NDVI values here are significantly higher than those in the intervened zones (SL and

SS), although observed differences are not large (~7%). This is not strange since there is ample evidence that snag and other coarse wood residuals present in zones with no post-fire intervention promote and facilitate the post-fire forest regeneration (Beschta et al., 1995; Lindenmayer et al., 2008; McIver et al., 2000; Perera and Buse, 2014) through greater nutrient availability due to soil retention and wood decomposition (Marañón-Jiménez et al., 2013a), better microclimate (lower temperatures and higher soil moisture content) in a great number of shelters for plants germination and survival (Devine and Harrington, 2007; Marañón-Jiménez et al., 2013b), and preventing mechanical damage of seedlings which may occur as a result of delayed salvage logging (Greene et al., 2006).

Higher proportion of vegetation cover is accompanied by lower LST in CL compared to the intervened zones (Table 4). The differences in LST vary from 0.5 °C in March to almost 2 °C in June (Table 5), when atmospheric temperature is higher and there is a greater proportion of exposed bare ground in the intervened areas (NDVI 12% and 7% lower than CL for SL and SS, respectively). These results are in agreement with data from the field study by Fontaine et al. (2010), who observed higher near-surface temperature values around midday due to earlier and accelerated heating in salvage-logged areas of the burn compared to the non-intervened areas. Distribution of lower LST values in zones of higher NDVI has also been mentioned in previous research based on multitemporal satellite data (Veraverbeke et al., 2012; Vlassova et al., 2014). Both green (photosynthetically active vegetation) and dead (snags, logs and other coarse wood debris) biomass contribute to lower LST in the CL areas: the former through the transpiration process (Jones and Vaughan, 2010) and the latter through much greater surface shading (Devine and Harrington, 2007). Thus, higher NDVI and lower LST in the non-intervened zones are indicators of a more successful reestablishment of ecological processes because of the beneficial effects of wood residuals on recovery of biochemical dynamics and microclimate. In areas without post-fire human disturbance soil is less exposed to sunlight and wind (Perera and Buse, 2014), and burnt wood enhances nutrient cycling processes and improves soil ecological functions (Marañón-Jiménez, 2012).

Differences in NDVI identified from Landsat images were also evident in the spectral signatures collected in the field. Higher reflectance in VIS of the spectrum from the intervened area is possibly related to the lower content of the photosynthetic pigments and higher proportion of bare soil in the areas where snags and other wood debris have been removed; shorter red edge and lower reflectance in the NIR wavelength range of the treated spectrum is caused by reduction of vegetation cover in the intervened areas; finally, higher reflectance in the SWIR spectral region is explained by higher water absorption by leaf structures of more abundant vegetation in the control areas. NDVIs computed using Landsat bands simulated from field spectra are in agreement with data from image analysis: differences in NDVI levels between control and intervened zones in this case are much greater (>30%) due to the time lag between data acquisition and differences in spatial resolution of the two methods. No statistically significant differences in LST and NDVI have been detected between SL and SS, which is probably explained by the fact that applied intervention strategies are not ecologically aggressive. According to Hernández Jiménez (2014) the performed intervention activities are classified as "low impact" because of the effort taken to minimize generation of skid trails and soil compaction to reduce soil scarification and degradation.

Initial analysis of environmental conditions (Section 3.1) revealed statistically significant differences in elevation among SS, SL and CL. In order to assess the possible effect of elevation on LST and NDVI, we used factorial ANOVA. Date by date analysis detected that elevation was not statistically significant in any LST model; in case of NDVI, elevation was significant only in August, when it explained <1.5% of variance.

Factorial ANOVA provided additional insight on importance of other factors, such as *Pre-fire NDVI* and *Illumination*, for LST and NDVI levels in the studied area. *Pre-fire NDVI* is relevant in explaining vegetation regeneration (NDVI) because recovery of the burnt plant communities does not start from zero point. Only part of the biological content is destroyed and some conditions necessary for recovery are conserved. Moreover, adaptive vegetation traits of "resprouters" and "reseeders" help in reestablishment of plant communities in Mediterranean ecosystems (Vallejo et al., 2012). In case of the LST, *Illumination* emerges as the major explanatory variable due to the relationship between LST distribution and sun-sensor-surface observation geometry at the moment of satellite overpass. However, naturally outstanding role of *Illumination* in LST models should not dim the relevance of treatment type: its influence on LST distribution is statistically significant, and in June its explanatory power equals that of *Illumination*.

Post-fire regeneration takes time and requires short- and long-term monitoring (Pausas and Vallejo, 2008). From this perspective, remote sensing, which allows observation of land surface processes over extensive areas and time periods, is a valuable complement of field data. Few studies have used information from remote sensing to study impacts of post-fire salvage logging on forest regeneration, although there is an extensive research exploring this topic based on field observations (Castro et al., 2011; Marañón-Jiménez et al., 2013b). The relationship between land surface temperature and vegetation recovery/fire severity and salvage logging has been earlier mentioned in studies based on field (Fontaine et al., 2010) and remotely-sensed data (Quintano et al., 2015; Veraverbeke et al., 2012; Vlassova et al., 2014). This study uses satellite images to analyze the effect of post-fire wood management activities on land surface biophysical characteristics providing additional data for understanding of the complicated relationship.

5. Conclusions

The influence of post-fire wood management was assessed from remotely-sensed data. Two land surface biophysical variables (LST and NDVI) were analyzed on 4 dates in 2014 in the areas of three wood treatments in the Zuera burn.

LST and NDVI demonstrate great post-fire vegetation recovery capacity of *P. halepensis* ecosystem, and confirm low aggressiveness of the analyzed wood management treatments, even though their effects are still detectable from the satellite images three years after being applied.

Statistically significant, albeit not very relevant, differences have been detected between intervened and not intervened zones; there were no differences between the intervened zones. The results of the study show that in ecosystems with high regeneration capacity, such as *P. halepensis* forests, post-fire recovery in terms of NDVI is higher and LST is lower in areas where no management activities were realized, being an indication of more favorable conditions for vegetation regeneration.

Acknowledgements

The research was financially supported by Secretariat for Higher Education, Science, Technology and Innovation (SENESCYT), Ecuador through the educational Grant awarded to the first author. The authors would like to thank the Department of Forest Management of the Government of Aragón (Dirección General de Gestión Forestal, Diputación General de Aragón) for sharing information about forest fires and management activities in the fire-affected areas.

Appendix A.

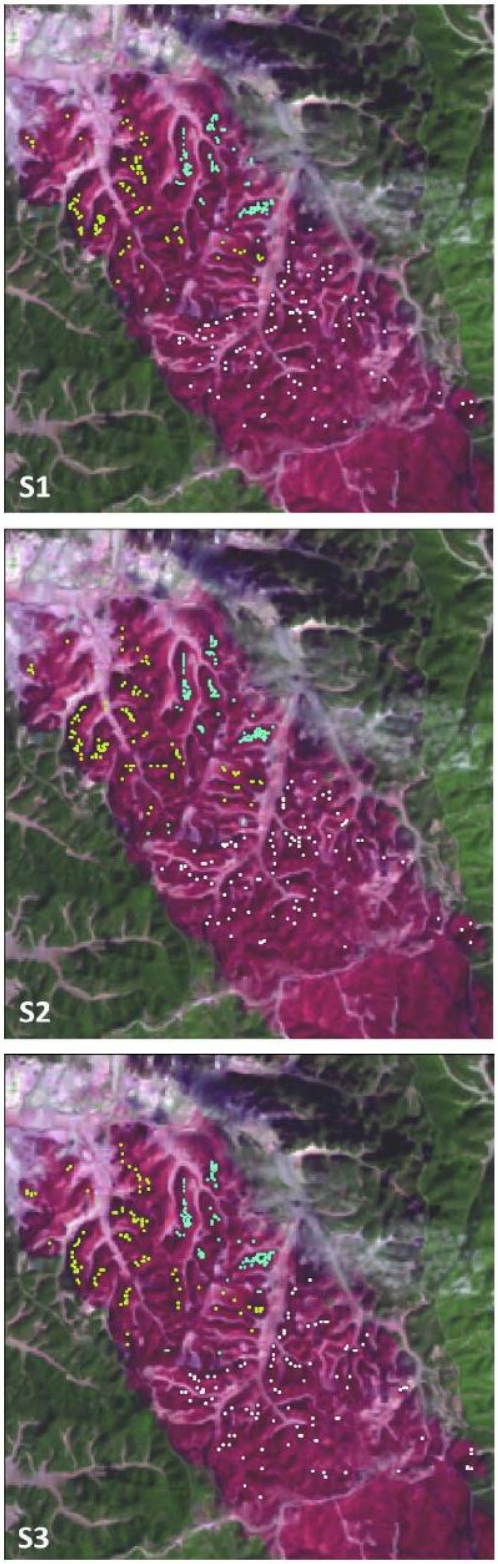

Fig. A1. Location of sampling points in the study area over the color RGB composite of Landsat-7 bands 7-4-3: Sample 1 (S1), Sample 2 (S2) and Sample 3 (S3). Point color indicates the type of treatment: SL – light blue, SS – green, and CL – white. (For interpretation of the references to colour in this figure legend, the reader is referred to the web version of this article.)

References

Agee, J.K., 1998. Fire and pine ecosystems. In: Richardson, D.M. (Ed.), Ecology and Biogeography of Pinus. Cambridge University Press, Cambridge, pp. 193–218.

ASD, 2012. FieldSpec pro user's guide. ASDInc, Boulder.

Badía, D., Martí, C., Aznar, J.M., León, J., 2013. Influence of slope and parent rock on soil genesis and classification in semiarid mountainous environments. Geoderma 193–194, 13–21.

Badía, D., Martí, C., Charte, R., 2011. Soil erosion and conservation measures in semiarid ecosystems affected by wildfires. In: Godone, D. (Ed.), Soil Erosion Studies. INTECH Open Access Publisher, pp. 87–110.

Baird, B.N., 2006. Comment on post-wildfire logging hinders regeneration and increases fire risk. Science 313, 615.

Bautista, S., Gimeno, T., Mayor, A.G., Gallego, D., 2004. El tratamiento de la madera quemada tras los incendios forestales. In: Vallejo, V.R., Alloza, J.A. (Eds.), Avances en el Estudio de la Gestión del Monte Mediterráneo. Fundación Centro de Estudios Ambientales del Mediterráneo, Valencia, pp. 547–570.

Beers, T.W., Dress, P.E., Wensel, L.C., 1966. Notes and observations: aspect transformation in site productivity research. J. For. 64, 691–692.

Beschta, R.L., Frissell, C.A., Gresswell, R., Hauer, R., Karr, J.R., Minshall, G.W., Perry, D.A., Rhodes, J.J., 1995. Wildfire and Salvage Logging: Recommendations for Ecologically Sound Post-fire Salvage Management and Other Post-fire Treatments on Federal Lands in the West. Oregon State University, Corvallis.

Bonan, G.B., Oleson, K.W., Vertenstein, M., Levis, S., Zeng, X., Dai, Y., Dickinson, R.E., Yang, Z.-L., 2002. The land surface climatology of the community land model coupled to the NCAR community climate model. J. Clim. 15, 3123–3149.

Burrough, P.A., McDonnell, R.A., 1998. Principles of GIS. Oxford University Press, London.

Castro, J., Allen, C.D., Molina-Morales, M., Marañón-Jiménez, S., Sánchez-Miranda, Á., Zamora, R., 2011. Salvage logging versus the use of burnt wood as a nurse object to promote post-fire tree seedling establishment. Restor. Ecol. 19, 537–544.

Cerdà, A., Robichaud, P., 2009. Fire effects on soil infiltration. In: Cerdá, A., Robichaud, P. (Eds.), Fire Effects on Soils and Restoration Strategies. Science Publishers, New Hampshire, pp. 81–103.

Certini, G., 2005. Effects of fire on properties of forest soils: a review. Oecologia 143 (1), 1–10.

Chapman, M.A., Lewis, M.H., Stout, V.M., 1976. Introduction to the Freshwater Crustacea of New Zealand. Collins, New Zealand.

Chen, W., Moriya, K., Sakai, T., Koyama, L., Cao, C., 2014. Monitoring of post-fire forest recovery under different restoration modes based on time series Landsat data. Eur. J. Remote Sens. 47, 153–168.

Cooley, T., Anderson, G.P., Felde, G.W., Hoke, M.L., Ratkowski, A.J., Chetwynd, J.H., Gardner, J.A., Adler-Golden, S.M., Matthew, M.W., Berk, A., Bernstein, L.S., Acharya, P.K., Miller, D., Lewis, P., 2002. FLAASH, a MODTRAN4-based atmospheric correction algorithm, its application and validation. IGARSS '02. 2002 IEEE International In: Geoscience and Remote Sensing Symposium, 2002, vol. 1413, pp. 1414–1418.

Cuadrat, J.M., Saz, M.A., Vicente-Serrano, S.M., 2007. Atlas climático de Aragón. Gobierno de Aragón, Aragón.

De las Heras, J., Moya, D., Vega, J.A., Daskalakou, E., Vallejo, V.R., Grigoriadis, N., Tsitsoni, T., Baeza, J., Valdecantos, A., Fernández, C., 2012. Post-fire management of serotinous pine forests. In: Moreira, F., Arianoutsu, M., Corona, P., De las Heras, J. (Eds.), Post-Fire Management and Restoration of Southern European Forests. Springer, pp. 121–150.

DeBano, L.F., 2000. The role of fire and soil heating on water repellency in wildland environments: a review. J. Hydrol. 231, 195–206.

Devine, W.D., Harrington, C.A., 2007. Influence of harvest residues and vegetation on microsite soil and air temperatures in a young conifer plantation. Agric. For. Meteorol. 145, 125–138.

Díaz-Delgado, R., Lloret, F., Pons, X., 2003. Influence of fire severity on plant regeneration by means of remote sensing imagery. Int. J. Remote Sens. 24, 1751–1763.

Donato, D.C., Fontaine, J.B., Campbell, J.L., Robinson, W.D., Kauffman, J.B., Law, B.E., 2006a. Post-wildfire logging hinders regeneration and increases fire risk. Science 311, 352.

Donato, D.C., Fontaine, J.B., Campbell, J.L., Robinson, W.D., Kauffman, J.B., Law, B.E., 2006b. Response to comments on post-wildfire logging hinders regeneration and increases fire risk. Science 313, 615.

EGIF, 2008. National database of Forest Fires. Ministry of Agriculture, Food and Environment, Spain.

Fernández, C., Vega, J.A., Fonturbel, T., Jiménez, E., Pérez-Gorostiaga, P., 2008. Effects of wildfire, salvage logging and slash manipulation on Pinus pinaster Ait. recruitment in Orense (NW Spain). For. Ecol. Manag. 255, 1294–1304.

Fontaine, J.B., Donato, D.C., Campbell, J.L., Martin, J.G., Law, B.E., 2010. Effects of post-fire logging on forest surface air temperatures in the Siskiyou Mountains, Oregon, USA. Forestry 83, 477–482.

Gitas, I.Z., De Santis, A., Mitri, G.H., 2009. Remote sensing of burn severity. In: Chuvieco, E. (Ed.), Earth Observation of Wildland Fires in Mediterranean Ecosystems. Springer, Berlin, pp. 129–148.

Gitas, I.Z., Polychronaki, A., Katagis, T., Mallinis, G., 2008. Contribution of remote sensing to disaster management activities: a case study of the large fires in the Peloponnese, Greece. Int. J. Remote Sens. 29, 1847–1853.

Greene, D.F., Gauthier, S., Noel, J., Rousseau, M., Bergeron, Y., 2006. A field experiment to determine the effect of post-fire salvage on seedbeds and tree regeneration. Front. Ecol. Environ. 4, 69–74.

Greene, D.F., Splawinski, T.B., Gauthier, S., Bergeron, Y., 2013. Seed abscission schedules and the timing of post-fire salvage of *Picea mariana* and *Pinus banksiana*. For. Ecol. Manage. 303, 20–24.

Hatfield, J.L., 1997. Plant-water interactions. In: Wang, W., Gorsuch, J., Hughes, J. (Eds.), Plants for Environmental Studies. CRC Press, USA, pp. 81–103.

Hernández Clemente, R., Navarro Cerrillo, R.M., Gitas, I.Z., 2009. Monitoring post-fire regeneration in Mediterranean ecosystems by employing multitemporal satellite imagery. Int. J. Wildland Fire 18, 648–658.

Hernández Jiménez, A. 2014. Actuaciones de emergencia post-incendio en Aragón, IV Jornada sobre conservación y rehabilitación de suelos en ecosistemas afectados por incendios forestales. Zaragoza, Spain.

Jackson, R.D., 1982. Canopy temperature and crop water stress. Adv. Irrig. 1, 43–85.

Jiménez-Muñoz, J.C., Sobrino, J.A., Skokovic, D., Mattar, C., Cristóbal, J., 2014. Land surface temperature retrieval methods from Landsat-8 Thermal Infrared Sensor data. IEEE Geosci. Remote Sens. Lett. 11 (10), 1840–1843.

Jiménez-Muñoz, J.C., Sobrino, J.A., 2004. A generalized single-channel method for retrieving land surface temperature from remote sensing data. J. Geophys. Res. 108, 46–88.

Jones, H.G., Vaughan, R.A., 2010. Remote Sensing of Vegetation: Principles, Techniques, and Applications. Oxford University Press, New York.

Key, C.H., Benson, N.C., 2006. Landscape Assessment: Ground measure of severity, the Composite Burn Index; and Remote sensing of severity, the Normalized Burn Ratio. In: Lutes, D.C., Keane, R.E., Caratti, J.F., Key, C.H., Benson, N.C., Sutherland, S., Gangi, L.J. (Eds.), FIREMON: Landscape Assessment (LA) V4, Sampling and Analysis Methods. USDA Forest Service, Rocky Mountain Research Station,Collins, CO, pp. 1–51.

Lanorte, A., Lasaponara, R., Lovallo, M., Telesca, L., 2014. Fisher–Shannon information plane analysis of SPOT/VEGETATION Normalized Difference Vegetation Index (NDVI) time series to characterize vegetation recovery after fire disturbance. Int. J. Appl. Earth Observ. Geoinf. 26, 441–446.

Lentile, L.B., Holden, Z.A., Smith, A.M.S., Falkowski, M.J., Hudak, A.T., Morgan, P., Lewis, S.A., Gessler, P.E., Benson, N.C., 2006. Remote sensing techniques to assess active fire characteristics and post-fire effects. Int. J. Wildland Fire 15, 319–345.

Leverkus, A.B., Lorite, J., Navarro, F.B., Sánchez-Cañete, E.P., Castro, J., 2014. Post-fire salvage logging alters species composition and reduces cover, richness, and diversity in Mediterranean plant communities. J. Environ. Manag. 133, 323–331.

Li, Z.-L., Wu, H., Wang, N., Qiu, S., Sobrino, J.A., Wan, Z., Tang, B.-H., Yan, G., 2013. Land surface emissivity retrieval from satellite data. Int. J. Remote Sens. 34, 3084–3127.

Liang, S., 2004. Quantitative Remote Sensing of Land Surfaces. Wiley, New Jersey, USA.

Lindenmayer, D.B., Burton, P.J., Franklin, J.F., 2008. Salvage Logging and Its Ecological Consequences. Island Press, USA.

Lloret, F., Zedler, P.H., 2009. The effect of forest fire on vegetation. In: Cerdá, A., Robichaud, P.R. (Eds.), Fire Effect on Soils and Restoration Strategies. Science publisher, New Hampshire, USA, pp. 257–285.

Marañón-Jiménez, S., 2012. Efecto del manejo de la madera quemada después de un incendio sobre el ciclo del carbono y nutrientes en un ecosistema de montaña mediterránea. Flamma 3, 43–49.

Marañón-Jiménez, S., Castro, J., Fernández-Ondoño, E., Zamora, R., 2013a. Charred wood remaining after a wildfire as a reservoir of macro-and micronutrients in a Mediterranean pine forest. Int. J. Wildland Fire 22, 681–695.

Marañón-Jiménez, S., Castro, J., Querejeta, J.I., Fernández-Ondoño, E., Allen, C.D., 2013b. Post-fire wood management alters water stress, growth, and performance of pine regeneration in a Mediterranean ecosystem. For. Ecol. Manag. 308, 231–239.

Martínez-Sánchez, J.J., Ferrandis, P., de las Heras, J., Herranz, J.M., 1999. Effect of burnt wood removal on the natural regeneration of *Pinus halepensis* after fire in a pine forest in Tus valley (SE Spain). For. Ecol. Manag. 123 (1), 1–10.

Marzano, R., Garbarino, M., Marcolin, E., Pividori, M., Lingua, E., 2013. Deadwood anisotropic facilitation on seedling establishment after a stand-replacing wildfire in Aosta Valley (NW Italy). Ecol. Eng. 51, 117–122.

McIver, J.D., Starr, L., Portland, O., 2000. Environmental Effects of Postfire Logging: Literature Review and Annotated Bibliography. US Dept. of Agriculture, Forest Service, Pacific Northwest Research Station.

Mexal, J.G., South, D.B., 1991. Bareroot seedling culture. In: Duryea, M.L., Dougherry, Ph.M. (Eds.), Forest Regeneration Manual. Kluwer Academic Publishers, Netherlands, pp. 89–115.

Moran, P.A.P., 1950. Notes on continuous stochastic phenomena. Biometrika 37, 17–23.

Moran, M., 2004. Thermal infrared measurement as an indicator of plant ecosystem health. In: Dale, A., Quattrochi, D., Luvall, J.C. (Eds.), Thermal Remote Sensing in Land Surface Processing. CRC Press, USA, pp. 257–282.

Newton, M., Fitzgerald, S., Rose, R.R., Adams, P.W., Tesch, S.D., Sessions, J., Atzet, T., Powers, R.F., Skinner, C., 2006. Comment on post-wildfire logging hinders regeneration and increases fire risk. Science 313, 615.

Pausas, J.G., 1999. Response of plant functional types to changes in the fire regime in Mediterranean ecosystems: a simulation approach. J. Veg. Sci. 10, 717–722.

Pausas, J.G., Bladé, C., Valdecantos, A., Seva, J.P., Fuentes, D., Alloza, J.A., Vilagrosa, A., Bautista, S., Cortina, J., Vallejo, R., 2004. Pines and oaks in the restoration of Mediterranean landscapes of Spain: new perspectives for an old practice—a review. Plant Ecol. 171, 209–220.

Pausas, J.G., Llovet, J., Rodrigo, A., Vallejo, R., 2009. Are wildfires a disaster in the Mediterranean basin?–a review. Int. J. Wildland Fire 17, 713–723.

Pausas, J.G., Vallejo, R., 2008. Bases ecológicas para convivir con los incendios forestales en la Región Mediterránea: decálogo. Ecosistemas 17, 128–129.

Perera, A., Buse, L., 2014. Ecology of Wildfire Residuals in Boreal Forests. Wiley, New Jersey, USA.

Pérez-Cabello, F., Echeverría, M., Ibarra, P., Riva, J., 2009. Effects of fire on vegetation, soil and hydrogeomorphological behavior in Mediterranean ecosystems. In: Chuvieco, E. (Ed.), Earth Observation of Wildland Fires in Mediterranean Ecosystems. Springer, Berlin, pp. 111–128.

Purdon, M., Brais, S., Bergeron, Y., van der Maarel, E., 2004. Initial response of understorey vegetation to fire severity and salvage-logging in the southern boreal forest of Québec. Appl. Veg. Sci. 7, 49–60.

Quattrochi, D.A., Luvall, J.C., 2004. Thermal Remote Sensing in Land Surface Processing. CRC Press, Boca Raton.

Quintano, C., Fernández-Manso, A., Calvo, L., Marcos, E., Valbuena, L., 2015. Land surface temperature as potential indicator of burn severity in forest Mediterranean ecosystems. Int. J. Appl. Earth Observ. Geoinf. 36, 1–12.

Riaño, D., Chuvieco, E., Ustin, S., Zomer, R., Dennison, P., Roberts, D., Salas, J., 2002. Assessment of vegetation regeneration after fire through multitemporal analysis of AVIRIS images in the Santa Monica Mountains. Remote Sens. Environ. 79, 60–71.

Robichaud, P.R., 2009. Post-fire stabilization and rehabilitation. In: Cerdá, A., Robichaud, P. (Eds.), Fire Effects on Soils and Restoration Strategies. Science Publishers, New Hampshire, pp. 299–320.

Rouse, J.W., Haas, R.H., Schell, J.A., Deering, D.W., 1973. Monitoring vegetation systems in the Great Plains with ERTS. In: 3rd ERTS Symposium, NASA SP-351 I, pp. 309–317.

Roy, D.P., 1999. Multi-temporal active-fire based burn scar detection algorithm. Int. J. Remote Sens. 20, 1031–1038.

Rulloni, V., Bustos, O., Flesia, A.G., 2012. Large gap imputation in remote sensed imagery of the environment. Comput. Stat. Data Anal. 56, 2388–2403.

Scaramuzza, P., Micijevic, E., Chander, G., 2004. SLC Gap-filled Products Phase One Methodology. Landsat Technical Notes.

Schroeder, W., Csiszar, I., Giglio, L., Schmidt, C.C., 2010. On the use of fire radiative power, area, and temperature estimates to characterize biomass burning via moderate to coarse spatial resolution remote sensing data in the Brazilian Amazon. J. Geophys. Res. 115, 2156–2202.

Serrano-Ortiz, P., Marañón-Jiménez, S., Reverter, B.R., Sánchez-Cañete, E.P., Castro, J., Zamora, R., Kowalski, A.S., 2011. Post-fire salvage logging reduces carbon sequestration in Mediterranean coniferous forest. For. Ecol. Manag. 262, 2287–2296.

Smith, A.M.S., Wooster, M.J., 2005. Remote classification of head and backfire types from MODIS fire radiative power and smoke plume observations. Int. J. Wildland Fire 14, 249–254.

Sobrino, J.A., Jiménez-Muñoz, J.C., Paolini, L., 2004. Land surface temperature retrieval from LANDSAT TM 5. Remote Sens. Environ. 90, 434–440.

Sobrino, J.A., Raissouni, N., 2000. Toward remote sensing methods for land cover dynamic monitoring: application to Morocco. Int. J. Remote Sens. 21, 353–366.

Spanos, I.A., Daskalakou, E.N., Thanos, C.A., 2000. Postfire, natural regeneration of *Pinus brutia* forests in Thasos island, Greece. Acta Oecol. 21, 13–20.

Storey, J., Scaramuzza, P., Schmidt, G., Barsi, J., 2005. Landsat 7 scan line corrector-off gap filled product development, pp. 23–27.

Tanase, M., de la Riva, J., Pérez-Cabello, F., 2011. Estimating burn severity at the regional level using optically based indices. Can. J. For. Res. 41, 863–872.

Teillet, P.M., Barker, J.L., Markham, B.L., Irish, R.R., Fedosejevs, G., Storey, J.C., 2001. Radiometric cross-calibration of the Landsat-7 ETM+ and Landsat-5 TM sensors based on tandem data sets. Remote Sens. Environ. 78, 39–54.

Trabaud, L., 1991. Fire regimes and phytomass growth dynamics in a *Quercus coccifera* garrigue. J. Veg. Sci. 2, 307–314.

Trabaud, L., Michels, C., Grosman, J., 1985. Recovery of burnt *Pinus halepensis* Mill. forests. II. Pine reconstruction after wildfire. For. Ecol. Manag. 13, 167–179.

Vacchiano, G., Stanchi, S., Marinari, G., Ascoli, D., Zanini, E., Motta, R., 2014. Fire severity, residuals and soil legacies affect regeneration of Scots pine in the Southern Alps. Sci. Total Environ. 472, 778–788.

Valor, E., Caselles, V., 1996. Mapping land surface emissivity from NDVI: application to European, African, and South American areas. Remote Sens. Environ. 57, 167–184.

Vallejo, V.R., Arianoutsou, M., Moreira, F., 2012. Fire ecology and post-fire restoration approaches in Southern European forest types. In: Moreira, F., Arianoutsu, M., Corona, P., De las Heras, J. (Eds.), Post-Fire Management and Restoration of Southern European Forests. Springer, pp. 93–119.

Van Leeuwen, W.J.D., Casady, G.M., Neary, D.G., Bautista, S., Alloza, J.A., Carmel, Y., Wittenberg, L., Malkinson, D., Orr, B.J., 2010. Monitoring post-wildfire vegetation response with remotely sensed time-series data in Spain, USA and Israel. Int. J. Wildland Fire 19, 75–93.

Veraverbeke, S., Lhermitte, S., Verstraeten, W.W., Goossens, R., 2011. Evaluation of pre/post-fire differenced spectral indices for assessing burn severity in a Mediterranean environment with Landsat Thematic Mapper. Int. J. Remote Sens. 32, 3521–3537.

Veraverbeke, S., Verstraeten, W.W., Lhermitte, S., Van De Kerchove, R., Goossens, R., 2012. Assessment of post-fire changes in land surface temperature and surface albedo, and their relation with fire–burn severity using multitemporal MODIS imagery. Int. J. Wildland Fire 21, 243–256.

Vicente-Serrano, S.M., Pérez-Cabello, F., Lasanta, T., 2008. Assessment of radiometric correction techniques in analyzing vegetation variability and change using time series of Landsat images. Remote Sens. Environ. 112, 3916–3934.

Vicente-Serrano, S.M., Pérez-Cabello, F., Lasanta, T., 2011. *Pinus halepensis* regeneration after a wildfire in a semiarid environment: assessment using multitemporal Landsat images. Int. J. Wildland Fire 20, 195–208.
Vidal, A., Devaux-Ros, C., 1995. Evaluating forest fire hazard with a Landsat TM derived water stress index. Agric. For. Meteorol. 77, 207–224.
Vila, J.P.S., Barbosa, P., 2010. Post-fire vegetation regrowth detection in the Deiva Marina region (Liguria-Italy) using Landsat TM and ETM+ data. Ecol. Model. 221, 75–84.
Vlassova, L., Pérez-Cabello, F., Mimbrero, M., Llovería, R., García-Martín, A., 2014. Analysis of the relationship between land surface temperature and wildfire severity in a series of landsat images. Remote Sens. 6, 6136–6162.
Wagenbrenner, J.W., MacDonald, L.H., Coats, R.N., Robichaud, P.R., Brown, R.E., 2015. Effects of post-fire salvage logging and a skid trail treatment on ground cover, soils, and sediment production in the interior western United States. For. Ecol. Manag. 335, 176–193.
Wheater, C.P., Cook, P.A., 2000. Using Statistics to Understand the Environment. Routledge, New York.
Zhang, C., Li, W., Travis, D., 2007. Gaps-fill of SLC-off Landsat ETM+ satellite image using a geostatistical approach. Int. J. Remote Sens 28, 5103–5122.

9. Application of Landsat LST in tree-grass woodlands (*dehesas*)

This chapter reproduces the text of the following article:

Title:
Variabilidad espacio-temporal de la temperatura de superficie en ecosistemas de dehesa estimada mediante imágenes Landsat TM: el papel del arbolado

Authors:
Vlassova, L.; Rosero Tufiño, P.; Montorio Llovería, R.

VARIABILIDAD ESPACIO-TEMPORAL DE LA TEMPERATURA DE SUPERFICIE EN ECOSISTEMAS DE DEHESA ESTIMADA MEDIANTE IMÁGENES LANDSAT TM: EL PAPEL DEL ARBOLADO

L. VLASSOVA[1,3], P. ROSERO TUFIÑO[2], R. MONTORIO LLOVERÍA[3]

[1] *Facultad de Ciencias Ambientales, Universidad Técnica Estatal de Quevedo. Vía a Sto. Domingo km.1.5, EC120509 Quevedo, Ecuador.*
[2] *Facultad de Ciencias Agrarias, Universidad Técnica Estatal de Quevedo. Vía a Sto. Domingo km.1.5, EC120509 Quevedo, Ecuador.*
[3] *Departamento de Geografía y Ordenación del Territorio-IUCA. Universidad de Zaragoza. Pedro Cerbuna, 12, 50006.*

lvlassova@uteq.edu.ec,prosero@uteq.edu.ec, montorio@unizar.es

RESUMEN: Las dehesas son sistemas agro-forestales en los que se producen complejos mecanismos de intercambio de carbono y agua debido a la presencia de estratos de vegetación con comportamiento eco-fisiológico contrastado: arbolado/herbáceo. Una de las variables clave en la parametrización del balance energético en estos ecosistemas es la temperatura de superficie (Ts). Este trabajo analiza su variación espacio-temporal en función de la cobertura arbórea en una dehesa al norte de Cáceres. La Ts se obtiene a partir de una serie de 14 imágenes Landsat-5 TM (2009-2011) que se agrupan en 3 compuestos estacionales (primavera, verano y otoño). La cobertura arbórea se estima a partir de ortofotografía e información del SIOSE. La distribución espacial de la Ts se relaciona con los niveles de cobertura en los compuestos de otoño y, especialmente, en verano momento en el que las diferencias medias entre las categorías extremas de arbolado (<10% y >60%) alcanzan los 2,5ºC.

Palabras-clave: temperatura de superficie, cobertura arbórea, LANDSAT, dehesa.

1. Introducción

El término *dehesa* refiere a un tipo de monte arbolado de uso agrosilvopastoril (San Miguel, 1994) resultado de un largo proceso de transformación (Blanco *et al*., 1997; Díaz *et al*., 1997). Principalmente se localiza en la parte suroccidental de la Península Ibérica, extendiéndose en España sobre una superficie de más de 3,5 millones de hectáreas (Olea *et al*., 2005). Su alto valor ecológico, socio-cultural y económico (Pulido *et al*., 2001; Montero *et al*., 1998) hace que estos hábitats estén incluidos en la Directiva 92/43 de la Unión Europea para su preservación. En este sentido,algunos estudios expresan dudas respecto a su sostenibilidad (Pulido *et al*., 2001 y Díaz *et al*., 1997) debido a los problemas derivados del sobrepastoreo, la intensificación del laboreo agrícola o la escasez de regeneración del arbolado (Moreno y Pulido, 2009). En relación con este último extremo, el predominio de los árboles de edad intermedia/avanzada y la ausencia de plantas jóvenes constituye uno de los problemas más importantes (Montero *et al*., 1998; Plieninger *et al*., 2004, entre otros). Según datos del Tercer Inventario Forestal Nacional (IFN3) en la provincia de Cáceres, la regeneración se considera insuficiente o nula en 2/3 de la superficie evaluada a nivel nacional (Pulido y Picardo, 2010).

La dehesa se caracteriza por su estructura en dos estratos: arbolado/matorral disperso y pastizal o cultivo. La fracción de cabida cubierta más habitual oscila entre el 5% y el 60% con una densidad promedio de 40-90 pies por hectárea que puede ser más baja (10) o más alta (200) dependiendo del tipo de dehesa (Huntsinger *et al*., 2013; Pulido *et al*., 2010; Carreiras *et al*., 2006). Las especies comúnmente encontradas en el estrato leñoso son *Quercus ilex* L. subsp. *ballota, Quercus suber, Quercus faginea* Lam.y diferentes arbustos perennifolios. El pastizal presenta un reducido potencial productivo que depende de la pluviometría. Entre los taxones más representativos de la fracción herbácea encontramos especies de gramíneas como *Aira caryophyllea* L., *Airopsis tenella* (Cav.) Asch. & Graebn.,*Psilurus incurvus* (Gouan) Schinz & Tell y *Bromus* sp., algunos especies de *Trifolium* entre leguminosas, y *Echium plantagineum* L., *Spergula arvensis* L., *Rumexacetosella* L., *Erygium campestre* L. o *Erodium cicutarium* L. de otras familias (Devesa, 1995; Olea *et al*., 2005).

En las dehesas los mecanismos de intercambio de carbono y agua son complejos debido a la presencia de estratos de vegetación diferenciados desde el punto de vista eco-fisiológico. En gran medida los ciclos de carbono y agua son controlados por los flujos de energía que son distintos en las copas de árboles y pastizal (Baldocchi *et al*., 2004). De esta manera, los estudios de balance de energía son necesarios para validación de los modelos de dehesa que buscan predecir estados de equilibrio entre vegetación y la humedad de suelo (Eagleson, 1982) y el efecto que puede ejercer en estos ecosistemas el cambio climático (Rodriguez-Iturbe *et al*., 1999; Volder *et al*., 2013; Zeng y Neelin, 2000).

La temperatura de superficie (Ts) constituye una de las claves en la modelización de los intercambios de energía, agua y carbono que se producen entre la vegetación, el suelo y la atmósfera, debido a su influencia sobre la tasa metabólica de las plantas y la descomposición de la materia orgánica del suelo, dos aspectos muy importantes en relación con la transferencia neta de carbono a la atmósfera (Miquelajauregui, 2013). A su vez, la presencia y, más específicamente, el tipo de vegetación juegan un rol importante en el control de la Ts, debido a las diferencias en emisividad entre los componentes bióticos y abióticos que conforman la dehesa (Quattrochi y Luvall, 2000).

Tanto la temperatura de la superficie (Ts) como la abundancia de la vegetación pueden ser analizadas a partir de la información proporcionada por sensores remotos, entre los cuales se destacan los datos de las misiones Landsat. Las imágenes Landsat-5 TM (*Thematic Mapper)* han sido utilizadas profusamente en el estudio de la distribución espacio-temporal de

vegetación a través de los diferentes índices espectrales a partir de la información captada en la región óptica del espectro electromagnético. El más ampliamente usado es el índice de vegetación de diferencia normalizada NDVI, que se relaciona con diferentes propiedades biofísicas de la vegetación (clorofila, cubrimiento, LAI, fAPAR, etc.) (Daughtry et al., 2000; Hwang et al., 2011; Turner et al., 1999). Las imágenes Landsat también poseen una banda en el infrarrojo térmico que posibilita la espacialización de la Ts (Vlassova et al., 2014; Weng et al., 2004).

El objetivo de este trabajo consiste en analizar la variabilidad espacio-temporal de la Ts, estimada a partir de las imágenes Landsat, en función de la densidad de arbolado en una zona de dehesa situada al norte de la provincia de Cáceres. La utilización conjunta de índices de vegetación procedentes de información multiespectral, de cartografía de la Ts y de información sobre las proporciones que ocupan diferentes estratos ofrece la posibilidad de crear modelos de la dehesa más precisos. Los resultados de estos modelos pueden ser integrados en el diseño de planes que aseguren la sostenibilidad y el mantenimiento de las funciones productivas y ecológicas (protección frente a la erosión, mantenimiento de la biodiversidad y regulación de los flujos de carbono y agua) de la dehesa (Moreno y Pulido, 2009).

2. Material y métodos

2.1. Área de estudio

La zona de estudio de 70 km^2 se localiza en un ecosistema de dehesa en el noreste de la provincia de Cáceres (Figura 1), muy cerca del área de estudio del proyecto de investigación FLUXPEC (CGL2012-34383): "Seguimiento de flujos de agua y carbono mediante teledetección en ecosistemas mediterráneos de dehesa" (http://www.lineas.cchs.csic.es/fluxpec/) que incluye una torre de medición de flujos de agua y carbono por el sistema *Eddy Covariance* (Lat. 39,9415º N, Lon. 5,7734º W) gestionada por el CEAM (Centro de Estudios Ambientales del Mediterráneo) desde el año 2003. El área se caracteriza por un clima típico mediterráneo con veranos secos y calurosos e inviernos húmedos y templados. La temperatura y precipitación media anual son 16,7º C y 572 mm, respectivamente. La altitud media sobre el nivel del mar es de 256 m. Las especies perennifolias de *Quercus ilex* L. subsp. *Ballota* y *Quercus suber* predominan en el estrato arbóreo y las de *Trifolium glomeratum* L., *Echium plantagineum* L., y *Spergula arvensis* son los más comunes en el pastizal.

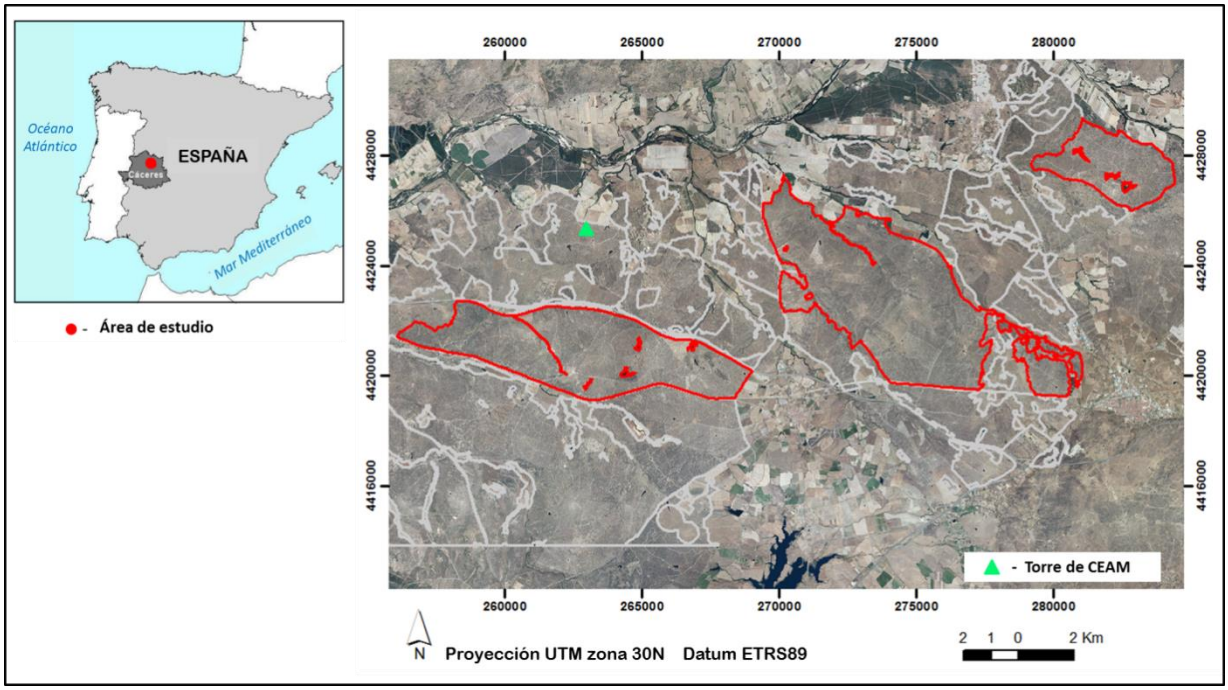

Figura 1. Ubicación y ortofotografía del área de estudio (límites en rojo). Las líneas de color gris claro delimitan el ecosistema de dehesa (Sistema de Información de Ocupación del Suelo en España, SIOSE).

2.2. Imágenes de satélite

El estudio se basa en una serie multitemporal de 14 imágenes Landsat-5 TM adquiridas sobre el área de estudio entre junio de 2009 y septiembre de 2011 (Tabla 1). Las imágenes georreferenciadas se descargaron del servidor del Servicio Geológico de los Estados Unidos o USGS por sus siglas en inglés (https://lpdaac.usgs.gov/get_data). En el trabajo se utilizaron las bandas ópticas en las regiones espectrales de rojo (0,63-0,69 µm) e infrarrojo cercano (0,76-0,90 µm), con una resolución espacial de 30 m, y la banda térmica (10,4-12,5 µm), con una resolución de 120 m.

Para la corrección atmosférica de las reflectividades se ha utilizado la herramienta LEDAPS (*Landsat Ecosystem Disturbance Adaptive Processing System*), basada en el código de transferencia radiativa 6S (Wolfe *et al*., 2004). El algoritmo emplea datos auxiliares (ozono, vapor de agua, grosor óptico de la atmósfera) para corregir en las imágenes las distorsiones causadas por la dispersión y absorción atmosférica. En el caso de los datos térmicos, los niveles digitales originales fueron transformados primero a valores de radiancia y luego en temperatura de brillousando las constantes de calibración proporcionadas en los metadatos

(Chander *et al*., 2009).

Tabla 1. Fechas y condiciones de iluminación en el momento de adquisición de las imágenes utilizadas.

FECHA	*Hora (UTC)*	*Azimut solar (grados)*	*Elevación solar (grados)*	*Estación climática*
27-jun-09	10:50:18	123,55	63,88	verano
29-jul-09	10:50:49	128,98	59,94	verano
30-ago-09	10:51:18	141,13	52,63	verano
17-oct-09	10:51:53	156,52	37,36	otoño
10-mar-10	10:52:43	146,85	40,13	primavera
11-abr-10	10:52:40	141,79	52,28	primavera
30-jun-10	10:52:19	124,31	64,00	verano
16-jul-10	10:52:16	126,06	62,26	verano
01-ago-10	10:52:10	130,34	59,61	verano
05-nov-10	10:51:34	159,16	31,40	otoño
16-may-11	10:51:20	132,51	61,79	primavera
01-jun-11	10:51:13	127,86	63,89	verano
04-ago-11	10:50:41	130,72	58,86	verano
05-sep-11	10:50:24	142,93	50,94	otoño

2.3. Estimación de la temperatura de superficie (Ts) e índice de vegetación

La temperatura de superficie (Ts) ha sido estimada mediante el método de monocanal (Jiménez-Muñoz *et al*., 2010) que, aparte de la emisividad de la superficie ε requerida por cualquier algoritmo de Ts, sólo necesita el contenido de vapor en la atmósfera como dato auxiliar. La Ts se calcula usando la ecuación:

(1) $$Ts = \gamma\left[\frac{1}{\varepsilon}\left(\psi_1 L_{sensor} + \psi_2\right) + \psi_3\right] + \delta$$

donde γ andδ son parámetros calculados a partir de la radiancia (L_{sensor}) y temperatura de brillo (T_{sensor}) usando las expresiones:

(2) $$\gamma \approx \frac{T_{sensor}^2}{1256 L_{sensor}}$$ (3) $$\delta \approx T_{sensor} - \frac{T_{sensor}^2}{1256 L_{sensor}}$$

y $\psi 1$, $\psi 2$, $\psi 3$son funciones atmosféricas, que para Landsat-5 TM vienen dadas por:

(4a) $$\psi_1 = 0.14714w^2 - 0.15583w + 1.1234$$

(4b) $$\psi_2 = -1.1836w^2 - 0.37607w - 0.52894$$

$$\psi_3 = -0.04554w^2 + 1.8719w - 0.39071 \quad (4c)$$

donde w es el contenido total del vapor en la atmósfera en g cm^{-2}.

En este estudio se utilizaron los valores de vapor atmosférico de la base de datos del Centro

Nacional para Análisis Atmosférico de EEUU (http://www.esrl.noaa.gov/psd/data/). El método es capaz de estimar la Ts con un margen de error ±1ºC cuando el contenido de vapor atmosférico se encuentra en el rango de 0,5 – 2,5 g cm^{-2} (Jiménez-Muñoz *et al*., 2010).

Para el análisis temporal de la vegetación se ha utilizado el índice de vegetación de diferencia normalizada NDVI (Rouse *et al*., 1974), que se basa en la diferencia de la reflectividad entre las bandas de las regiones espectrales rojo (banda 3) e infrarrojo cercano (banda 4) característica para la vegetación. El NDVI también se aplicó para estimar la emisividad por el método de umbrales de NDVI de Sobrino y Raissouni (2000), que asigna los valores de emisividad de acuerdo a los rangos de este índice.

2.4. Cartografía de la distribución espacial de la densidad del arbolado

Para la identificación de la dehesa se han utilizado los datos del Sistema de Información de Ocupación del Suelo en España (SIOSE) incluido en el Plan Nacional de Observación del Territorio en España (PNOT), coordinado por el Instituto Geográfico Nacional (IGN). La información consiste en capas de polígonos georeferenciados en proyección UTM (huso 30N, datum ETRS89) con escala de referencia 1:25000 (http://www.siose.es). A partir de la cobertura 701 dehesa (código DHS) se ha extraído la información referente al porcentaje de cubrimiento de frondosas caducifolias (FDC), frondosas perennifolias (FDP), matorral (MTR) y pastizal (PST). Dentro de la zona de estudio se han seleccionado para su análisis los tres polígonos más extensos cuya fracción leñosa (arbolado y matorral) se encuentra en el rango de 30-50% característico de la dehesa (Figura 1).

Dentro de los polígonos seleccionados se ha analizado la variabilidad espacial del arbolado mediante el uso de la ortofotografía digital generada en el marco del PNOT a partir de los datos de junio 2012. El fotomosaico (píxel de 0,25 m) correspondiente a la hoja 0624 del MTN50 (Mapa Topográfico Nacional 1:50.000) fue descargado del servidor del CNIG (http://centrodedescargas.cnig.es/CentroDescargas) en formato ECW, sistema geodésico de referencia ETRS89 y proyección UTM huso 30N. En la etapa de pre-procesamiento la imagen RGB fue convertida a escala de grises.

Las imágenes (Figura 2A) fueron clasificadas en dos categorías: vegetación leñosa de árboles/matorral (píxeles con niveles de gris menor de 130) y pastizal (píxeles con niveles de gris mayor o igual a 130). Como resultado de la clasificación se ha obtenido una nueva imagen ráster con píxeles de dos valores: 1 para "cobertura arbórea" y 0 para "pastizal" (Figura 2B). Tras ello, aplicando funciones de estadística zonal, se calculó la cantidad de

píxeles de "cobertura arbórea" en píxeles Landsat y, finalmente, el porcentaje de cobertura arbórea en píxeles Landsat ($CA_{\%}$) a través de la expresión:

(5) $$CA_{\%} = \frac{n*100}{N}$$

donde *n* es la cantidad de píxeles con cobertura arbórea dentro del píxel Landsat y *N*=14400 es la cantidad de píxeles de ortofoto en un píxel de la imagen satelital.

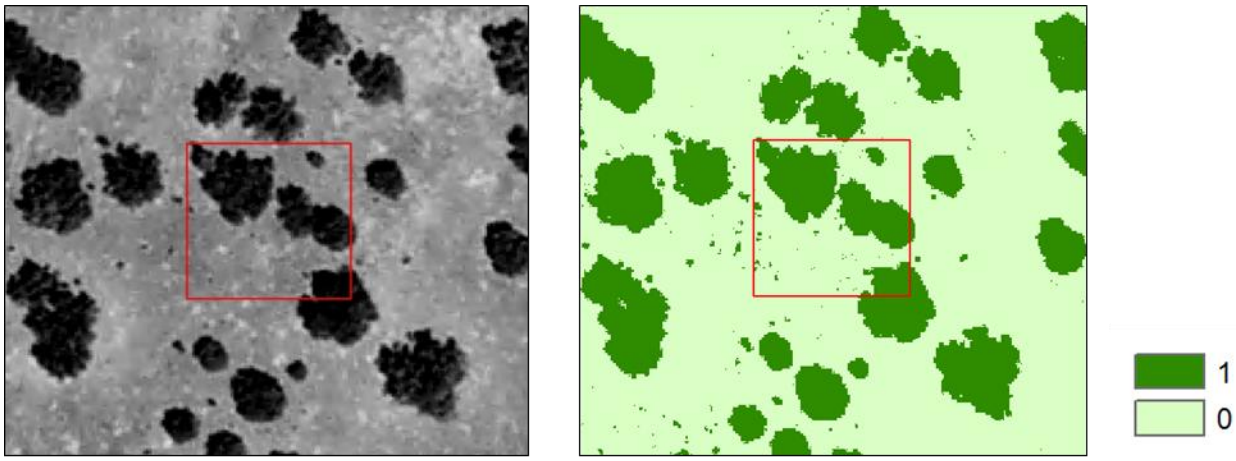

Figura 2. (A) Identificación de un píxel de Landsat-5 TM sobre la ortofotografía del PNOA; (B) Raster de clasificación de ortofotografía en "cobertura arbórea" (píxeles de valor 1) y "pastizal" (píxeles de valor 0).

2.5. Análisis estadístico

Se han establecido 7 categorías de dehesa en función del porcentaje de la cobertura arbórea: <10%; 10-20%; 20-30%; 30-40%; 40-50%; 50-60%; >60%. La determinación de los intervalos se basó en dos criterios: (1) generar intervalos regulares de cobertura arbórea dentro del rango de mayor representación de estos ecosistemas, entre 10% y 60% (Moreno y Pulido, 2009; Pulido y Picardo, 2010); y (2) disponer de suficiente número de píxeles en cada categoría para hacer posible el equilibrio de las submuestras en el análisis estadístico. Para evitar la contaminación de los resultados por la influencia de las áreas adyacentes y de los componentes no propios de la dehesa, se han excluido del análisis los píxeles situados a menos de 120 m de los límites de polígonos, así como los pertenecientes a otras cubiertas diferentes a la dehesa (láminas de agua, cultivos, edificios). El análisis se concentró en los dos componentes estructurales de la dehesa: el estrato con presencia del material leñoso (árboles y matorral) y el estrato herbáceo.

En cada categoría se ha identificado una muestra aleatoria de 1000 puntos (píxeles de la

imagen) que representan de manera equilibrada las 7 categorías de dehesa. Considerando los ciclos anuales de las variables climáticas y fenología del componente herbáceo de la dehesa, se han generado los compuestos de los datos correspondientes a los valores promedio de imágenes de cada estación climática (primavera, verano y otoño) (Tabla 1), realizándose la prueba de ANOVA y la prueba *post hoc* de Tamhane T2 para determinar la existencia de diferencias significativas de Ts y NDVI entre categorías.

3. Resultados y discusión

3.1. Cartografía de la cobertura arbórea

La figura 3 representa la distribución espacial de los porcentajes de cobertura arbórea en el área de estudio. La clasificación digital de la ortofotografía permite identificar espacialmente el desigual reparto del arbolado en cada uno de los tres polígonos del SIOSE.

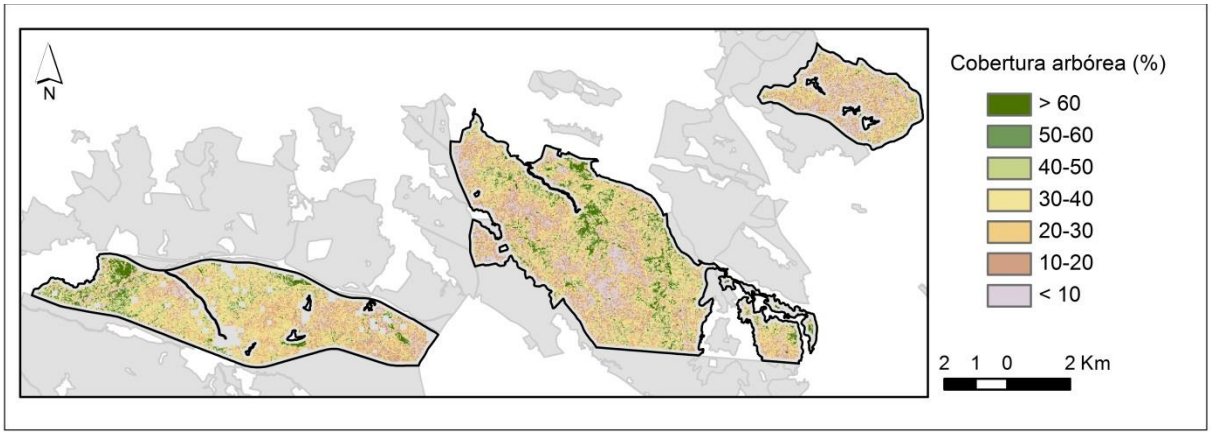

Figura 3. Distribución espacial de la cobertura arbórea en el área de estudio.

Los tonos marrones, correspondientes a las categorías en las que el recubrimiento del arbolado es intermedio (20-30% y 30-40%) son predominantes, ocupando en torno al 50% de la superficie analizada, lo que coincide con las descripciones del SIOSE para estas unidades (30% de cobertura arbórea y hasta 15% de matorral). En el otro extremo, el color verde oscuro, que representa las zonas en las que la ocupación del arbolado es superior al 60%, es poco representativo (~3.5% de la superficie), siendo más profuso en el extremo occidental del polígono situado al Oeste y en zonas específicas del polígono que ocupa la posición central. En el polígono oriental los píxeles de esta categoría son casi inexistentes.

3.2. Patrones de distribución espacio-temporal del NDVI y Ts

La distribución espacial de la Ts y el NDVI correspondientes a los compuestos de primavera, verano y otoño se muestra en la figura 4. Los valores más elevados de NDVI (con un valor

promedio de ~0,57) se observan en el compuesto de primavera, presentando un reparto bastante homogéneo sobre la superficie analizada. Sin embargo, a nivel térmico, se aprecia una mayor heterogeneidad espacial que se concreta en un gradiente moderado con dirección este-oeste.

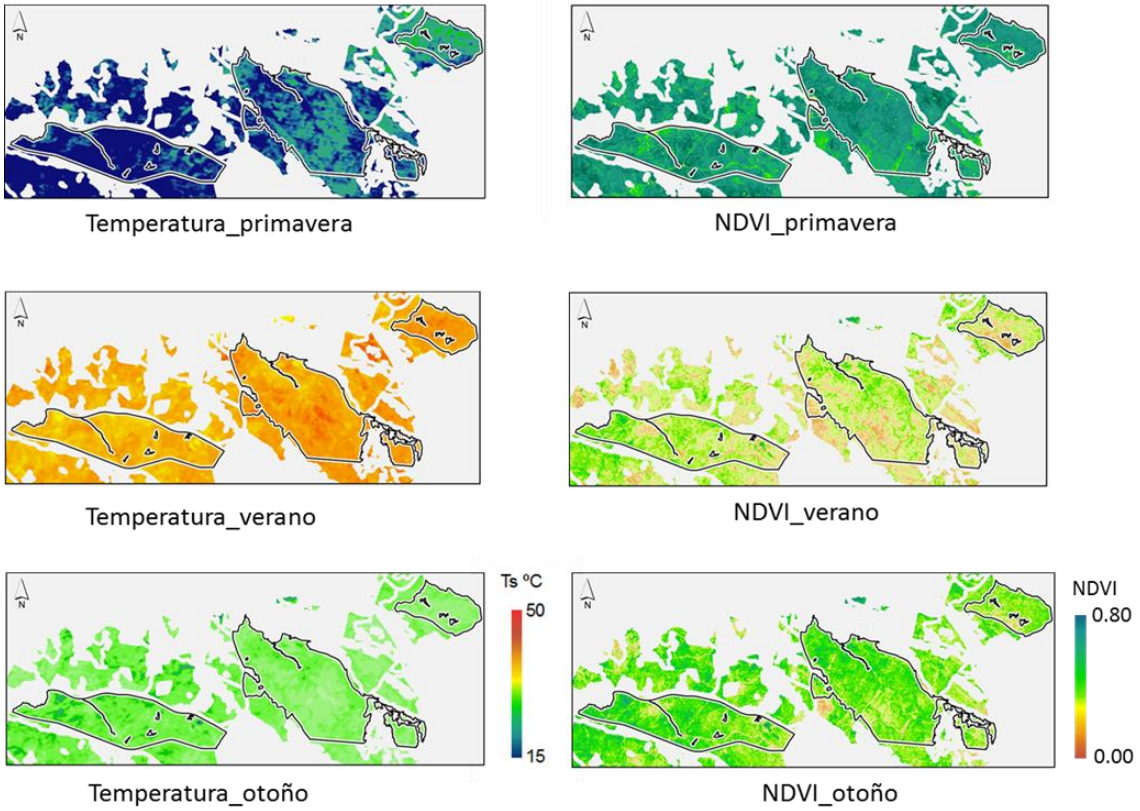

Figura 4. Distribución de la Ts (izquierda) y NDVI (derecha) estimados a partir de las imágenes Landsat-5 TM en el área de estudio.

Los valores más bajos de NDVI, tal como se esperaba, se recogen en el compuesto de verano. Su distribución presenta una gran variabilidad espacial, de tal modo que se reconocen sectores específicos en los que los valores de NDVI alcanzan valores elevados (~0,5) y otros en donde los valores de NDVI se aproximan a 0 (núcleo del polígono central). Este patrón se reproduce a nivel térmico al observarse diferencias considerables entre zonas en las que los valores de NDVI también son reseñables. Los valores de Ts más elevados se observan en el núcleo del polígono central y, en el extremo contrario, las Ts más bajas se recogen en la zona occidental, reproduciendo groseramente la distribución de los valores de NDVI y la de los porcentajes de cobertura arbórea. El compuesto de otoño (parte inferior de la figura 4) representa espacialmente una situación intermedia entre las dos anteriormente descritas.

A nivel estadístico, la Tabla 2 y la Figura 5 (A-C) recogen, respectivamente, algunos indicadores descriptivos de la Ts y los intervalos de confianza para la media al 95%, extraídos de las distintas categorías de dehesa para los tres compuestos (primavera, verano y otoño).

Tabla 2. Estadísticos descriptivos de la Ts (ºC) por categorías de dehesa y estaciones climáticas.

	Categoría (% de cobertura arbórea)	*Media*	*Desviación típica*	*Mínimo*	*Máximo*
Ts_primavera	<10	22.10	0.77	19.01	23.86
	10-20	21.94	0.77	19.59	23.83
	20-30	21.79	0.82	19.52	23.85
	30-40	21.60	0.88	19.19	23.89
	40-50	21.45	0.88	18.88	23.89
	50-60	21.41	0.85	19.02	24.53
	>60	21.31	0.84	19.22	24.24
Ts_verano	<10	42.11	1.03	38.48	44.38
	10-20	41.80	1.01	38.68	44.45
	20-30	41.46	1.06	38.14	44.35
	30-40	41.11	1.04	37.58	43.68
	40-50	40.76	1.10	37.43	43.59
	50-60	40.50	1.10	36.14	43.47
	>60	39.85	1.35	36.01	43.14
Ts_otoño	<10	26.26	0.76	23.96	28.22
	10-20	25.97	0.77	23.52	28.17
	20-30	25.68	0.79	23.45	28.12
	30-40	25.44	0.80	23.19	28.07
	40-50	25.18	0.80	23.07	27.56
	50-60	25.05	0.82	22.19	27.17
	>60	24.74	0.88	22.03	27.05

En términos generales, se advierte una clara relación entre los valores de Ts y los niveles de densidad del arbolado, de tal modo que un aumento del porcentaje de la fracción leñosa conlleva una disminución en los valores de la Ts. Esta relación inversa es muy evidente en los compuestos de verano y otoño, recogiéndose diferencias estadísticamente significativas entre todas las categorías ($p \leq 0{,}01$). En cambio, en el compuesto de primavera sólo las categorías en las que la cobertura arbórea es inferior al 40% presentan diferencias estadísticamente significativas. De hecho, mientras que en los compuestos de verano y otoño las diferencias entre los valores promedio en las categorías extremas (<10% y >60%) adquieren cierta significación (~2,5º C), en el compuesto de primavera apenas alcanzan 1º C.

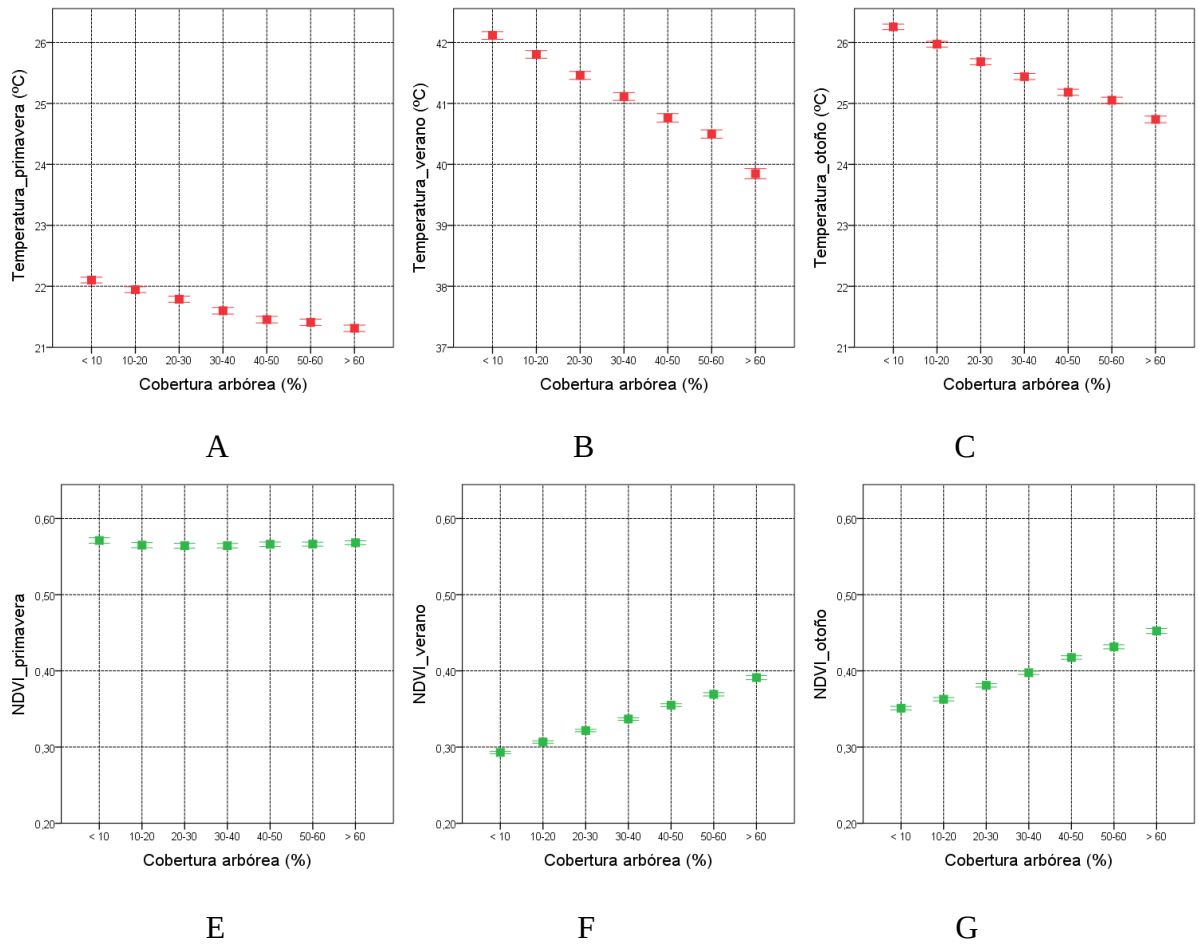

Figura 5. Distribución de la Ts (A-C) y NDVI (D-F) por categorías de dehesa (según intervalos de cobertura arbórea) en primavera (izquierda), verano (centro) y otoño (derecha). Las barras indican el intervalo de confianza 95% para el valor medio.

Teniendo en cuenta el carácter perennifolio de *Quercus ilex*, la especie arbórea con mayor representación espacial en la dehesa de Cáceres, es precisamente la diferente contribución del estrato herbáceo y su variabilidad fenológica interanual el principal factor explicativo de la variabilidad espacial de la Ts en los diferentes compuestos. Concretamente, los procesos de senescencia del estrato herbáceo durante el verano y el incremento de la contribución del suelo desnudo a la radiación emitida explicarían el mayor contraste térmico que se produce entre diferentes categorías de densidad de arbolado. Además, la menor presencia de zonas con sombra en los píxeles con escaso arbolado también contribuye de manera positiva en el incremento de la Ts. En términos generales, en verano una disminución del 10% en la cobertura arbórea (con el consiguiente aumento porcentual de la cobertura de pastizal) se asocia con un aumento de 0,4º C en la Ts. En cambio, en primavera, cuando el estrato herbáceo se sitúa fisiológicamente en su máximo productivo, especialmente a finales de abril

(San Miguel, 2009), se produce una reducción en la exposición de suelo desnudo y, sobre todo, un incremento de los procesos de transpiración que explicarían la disminución de gradientes térmicos entre categorías de dehesa. En otoño, a pesar de existir un máximo secundario en la producción de biomasa a principios de noviembre (Moreno y Pulido, 2009), se recoge un patrón de distribución semejante al de verano, aunque los contrastes térmicos entre densidades de arbolado son más moderadas. En este caso se aprecia un decremento de 0,25º C por cada incremento del 10% en la cobertura arbórea.

Por tanto, son las variaciones fisiológicas del estrato herbáceo, complemento del arbóreo en los sistemas de dehesa, las que parecen explicar en gran medida los patrones de distribución espacial de la Ts. El análisis de la distribución de los valores de NDVI en las categorías de dehesa permite comprobar este extremo (Tabla 3, Figura 5 D-F).

Tabla 3. Estadísticos descriptivos de NDVI por categorías de dehesa y estaciones climáticas.

	Categoría (% de cobertura arbórea)	*Media*	*Desviación típica*	*Mínimo*	*Máximo*
Ts_primavera	<10	0.57	0.06	0.24	0.71
	10-20	0.56	0.05	0.33	0.69
	20-30	0.56	0.05	0.31	0.72
	30-40	0.56	0.05	0.39	0.69
	40-50	0.57	0.05	0.37	0.70
	50-60	0.57	0.04	0.35	0.69
	>60	0.57	0.04	0.40	0.67
Ts_verano	<10	0.29	0.03	0.20	0.39
	10-20	0.31	0.02	0.23	0.39
	20-30	0.32	0.03	0.23	0.46
	30-40	0.34	0.03	0.25	0.45
	40-50	0.35	0.03	0.23	0.47
	50-60	0.37	0.03	0.18	0.52
	>60	0.39	0.04	0.28	0.55
Ts_otoño	<10	0.35	0.04	0.23	0.48
	10-20	0.36	0.04	0.24	0.49
	20-30	0.38	0.04	0.27	0.51
	30-40	0.40	0.03	0.27	0.51
	40-50	0.42	0.04	0.26	0.55
	50-60	0.43	0.04	0.27	0.59
	>60	0.45	0.05	0.30	0.62

El NDVI, al ser un índice espectral muy correlacionado con variables biofísicas como la actividad clorofílica, la densidad y el vigor de la vegetación, presenta valores muy homogéneos (valor medios ~ 0,57, Tabla 2) en el compuesto de primavera independientemente de la densidad del arbolado. De este modo, no se recogen diferencias significativas entre las categorías ($p>0,05$). Por el contrario, en los compuestos de otoño y,

especialmente, en el verano, se recogen diferencias significativas en los valores de NDVI entre categorías de arbolado. Los niveles de NDVI más altos se observan en la categoría con el máximo porcentaje de cobertura arbórea (>60%) disminuyendo en forma progresiva hasta llegar a los niveles más bajos en las categorías con predominio de pastizal, lo que demuestra un patrón de distribución completamente diferente (aunque relacionado) al presentado por la Ts.

Los diagramas de dispersión de la figura 6 representan las relaciones, píxel a píxel, entre los valores promedio de la Ts y los promedios de NDVI en los compuestos de primavera (6A), verano (6B) y otoño (6C). El color de los puntos hace referencia a los porcentajes de cobertura arbórea.

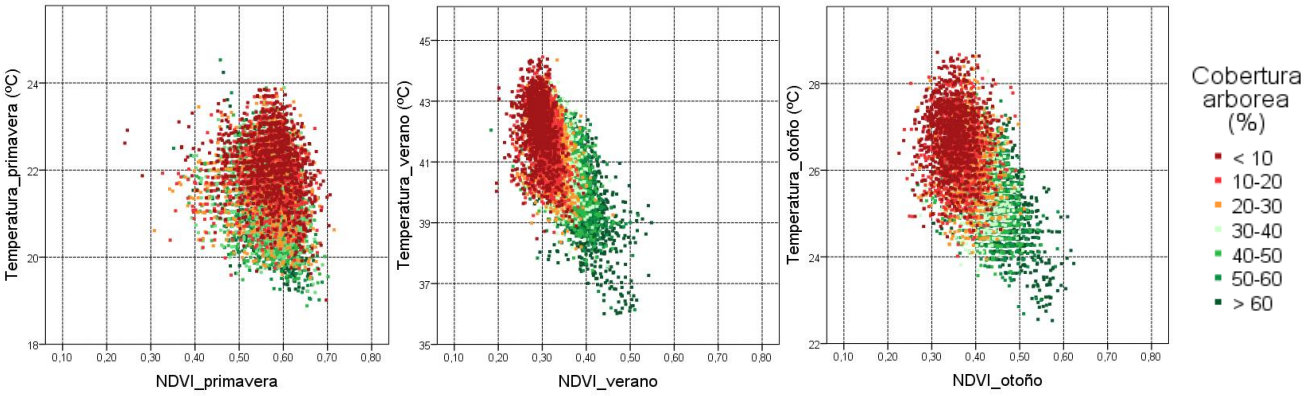

A B C

Figura 6. Diagramas de dispersión de NDVI y Ts en primavera (A), verano (B) y otoño (C).

De acuerdo con la interpretación del espacio formado por las variables NDVI-Ts sugerida por Jiang e Islam (2001), los puntos correspondientes a zonas de suelo desnudo se localizarían en el extremo superior izquierdo, lugares donde la fracción leñosa es muy baja; en cambio, los puntos correspondientes a los píxeles completamente cubiertos por vegetación se localizarían en el extremo inferior derecho.

De esta manera, en los diagramas de los compuestos de verano y otoño se advierte una relación negativa entre los valores de NDVI y Ts y una organización de los píxeles acorde a los parámetros preestablecidos. Sin embargo, en el compuesto de primavera esta relación es inexistente y las diferentes clases de arbolado se solapan en el espacio del diagrama NDVI-Ts generando una distribución más homogénea en la que los píxeles rojos, correspondientes a las categorías con porcentajes inferiores al 10% de cobertura arbórea, aparecen en toda la nube de

puntos. Esto es debido a que en esta fecha la vegetación muestra una elevada actividad fotosintética, independientemente de la proporción del estrato arbóreo o del pastizal.

4. CONCLUSIONES

El análisis cartográfico de los polígonos de dehesa (obtenidos a partir de SIOSE) mediante ortofotografía de alta resolución espacial permite evaluar la heterogeneidad de los niveles de cubrimiento del arbolado dentro de los ecosistemas de dehesa, proporcionando un mayor nivel de precisión en el análisis de las relaciones con la Ts.

Se analizan los patrones espacio-temporales de la Ts estimada a partir de la serie de imágenes Landsat-5 TM del período 2009-2011 y su relación con las categorías de dehesa. La distribución espacial de la Ts está estrechamente relacionada con la cobertura de la superficie por la vegetación: la Ts más baja se observa en las áreas con mayor cobertura de la vegetación y la más elevada en las zonas de vegetación senescente o suelo desnudo. Por esa razón, en el ecosistema de dehesa el patrón espacial de Ts depende del ciclo fenológico del pastizal, que es el componente más dinámico. El ciclo de desarrollo del estrato herbáceo contiene momentos de intenso vigor en la primavera, así como estado de senescencia en verano. Esto explica la relación negativa que existe entre la cobertura arbórea y la Ts. Esta relación es más pronunciada en verano (diferencia entre los promedios de las categorías extremas (<10% y >60%) se acerca a 2,5ºC) debido al estado senescente de las herbáceas y a la menor importancia de las sombras proyectadas por el estrato arbóreo, observándose un aumento de Ts de 0,4 ºC con cada disminución de 10% en la cobertura arbórea. Las diferencias en la Ts entre los tipos de dehesa se mantienen en primavera, aunque son de menor magnitud (~1ºC) por cuanto la vegetación de los dos estratos de la dehesa (arbóreo y pastizal) está en el máximo vigor y el promedio de las diferencias en Ts con la disminución de 10% en la cobertura arbórea se reduce a 0,1 ºC.

El estudio en su conjunto responde a la necesidad de generar información que pueda ser integrada en los modelos de respuesta del ecosistema de dehesa a los efectos del cambio climático (Moreno y Pulido, 2009; Joffre *et al*., 1999). En este contexto, se ha demostrado la capacidad de los sensores remotos para monitorizar la variabilidad espacio-temporal de la temperatura de la superficie (Ts), una de las variables destacadas en otras investigaciones (a.o. Plieninger *et al*., 2004), y contribuir así a la definición de estrategias para mantener la sostenibilidad de este ecosistema.

AGRADECIMIENTOS

Este trabajo se ha realizado en el marco del proyecto FLUXPEC (CGL2012-34383) financiado por el Ministerio de Economía y Competitividad. Los autores también agradecen la financiación de la investigación predoctoral de Lidia Vlassova por parte de SENESCYT-Ecuador.

5. BIBLIOGRAFÍA

Baldocchi, D.D., Xu, L., Kiang, N., 2004. How plant functional-type, weather, seasonal drought, and soil physical properties alter water and energy fluxes of an oak–grass savanna and an annual grassland. *Agricultural and Forest Meteorology* 123, 13-39.

Blanco, E., Casado, M.A., Costa, M., Escribano, R., García, M., Génova, M., Gómez, A., Gómez, F., Moreno, J.C., Morla, C., 1997. *Los bosques ibéricos. Una interpretación geobotánica.* Planeta, Barcelona.

Carreiras, J., Pereira, J.M., Pereira, J.S., 2006. Estimation of tree canopy cover in evergreen oak woodlands using remote sensing. *Forest ecology and management* 123, 45-53.

Chander, G., Markham, B.L., Helder, D.L., 2009. Summary of current radiometric calibration coefficients for Landsat MSS, TM, ETM+, and EO-1 ALI sensors. *Remote sensing of environment* 113, 893-903.

Daughtry, C. S. T., Walthall, C. L., Kim, M. S., De Colstoun, E. B., McMurtrey, J. E., 2000. Estimating corn leaf chlorophyll concentration from leaf and canopy reflectance. *Remote Sensing of Environment* 74(2), 229-239.

Devesa J.A.,1995. *Vegetación y flora de Extremadura*. Universitas, Badajoz.

Díaz M, Campos P, Pulido F.J., 1997. Spanish Dehesas: a diversity in land-use and wildlife. En: Pain D.J., Pienkowski M.W. (Eds). *Farming and birds in Europe*. Academic, London.

Eagleson, P.S., Tellers, T.E., 1982. Ecological optimality in water-limited natural soil-vegetation systems. *Water Resources Research* 18, 341-354.

Hwang, T., Song, C., Bolstad, P. V., Band, L. E., 2011. Downscaling real-time vegetation dynamics by fusing multi-temporal MODIS and Landsat NDVI in topographically complex terrain. *Remote Sensing of Environment* 115(10), 2499-2512.

Huntsinger, L., Campos, P., Starrs, P.F., Oviedo, J.L., Díaz, M., Standiford, R.B., Montero, G., 2013. Working Landscapes of the Spanish Dehesa and the California Oak Woodlands: An Introduction. En: P. Campos, L. Huntsinger, J.L. Oviedo, P.F. Starrs, M. Diaz, R. Standiford y G. Montero (Eds.) *Mediterranean oak woodland working landscapes*. Springer, Netherlands.

Jiang, L., Islam, S., 2001. Estimation of surface evaporation map over southern Great Plains using remote sensing data. *Water Resources Research* 37(2), 329-340.

Jiménez-Muñoz, J.C., Sobrino, J.A., Cristobal, J., Soria, G., Niyerola, M., Pons, X., Hidalgo, V., Franch, B., Romaguera, M., Oltra-Carrió, R., Julien, Y., Mattar, C., 2010. Obtención de la temperatura de la superficie terrestre a partir de la serie histórica de LANDSAT. *Revista de Teledetección* 33, 53-63.

Joffre, R., Rambal, S., Ratte, J.-P., 1999. The dehesa system of southern Spain and Portugal as a natural ecosystem mimic. *Agroforestry systems* 45, 57-79.

Miquelajauregui, Y., 2013. Modelos de simulación de la dinámica del carbono. En J.A. Blanco (Ed.). *Aplicaciones de modelos ecológicos a la gestón de recursos naturales*. Barcelona, OmniaScience.

Montero, G., San Miguel, A., Cañellas, I., 1998. System of Mediterranean silviculture La Dehesa. En R.M. Jiménez Díaz, J. Lamo de Espinos (Eds.) *Agricultura Sostenible*. Mundi Prensa, Madrid.

Moreno, G., Pulido, F., 2009. The functioning, management and persistence of dehesas. En A. Rigueiro-Rodríguez, J. McAdam, M.R. Mosquera-Losada (Eds.). *Agroforestry in Europe*, 127-160. Springer.

Olea, L., López-Bellido, R.J., Poblaciones, M.J., 2005. Europe types of silvopastoral systems in the Mediterranean area: dehesa. En M.R. Mosquera, A. Rigueiro, J. McAdam (Eds.). *Silvopastoralism and Sustainable Land Management*. CABI Publishing.

Plieninger, T., Pulido, F.J., Schaich, H., 2004. Effects of land-use and landscape structure on holm oak recruitment and regeneration at farm level in Quercus ilex L. Dehesas. *Journal of Arid Environments* 57, 345-364.

Pulido, F.J., Díaz, M., de Trucios, S.J.H., 2001. Size structure and regeneration of Spanish holm oak Quercus ilex forests and dehesas: effects of agroforestry use on their long-term sustainability. *Forest Ecology and Management* 146, 1-13.

Pulido, F., Picardo, A. (Coords.), 2010. *Libro verde de la dehesa. Documento para el debate hacia una Estrategia Ibérica de gestión*. Recuperado el 1 de octubre de 2015, de http://www.pfcyl.es/documento/libro-verde-de-la-dehesa.

Quattrochi, D.A., Luvall, J.C., 2000. *Thermal remote sensing in land surface processes*. CRC Press.

Rodriguez-Iturbe, I., D'Odorico, P., Porporato, A., Ridolfi, L., 1999. On the spatial and temporal links between vegetation, climate, and soil moisture. *Water Resources* 35 (12), 3709–3722.

Rouse, J.W., Haas, R.W., Shell, J.A., Deering, D.W., Harlan, J.C., 1974. *Monitoring the vernal advancement and retrogradation of natural vegetation*. *NASA/GSFCT Type III final report*. Greenbelt, EUA.

San Miguel, A., 1994. *La dehesa española. Origen, tipología, características y gestión*. Fundación Conde del Valle de Salazar, Madrid.

San Miguel, A. (Coord.), 2009. *Los pastos de la comunidad de Madrid. Tipología, cartografía y evaluación*. Comunidad de Madrid, Madrid.

Sobrino, J.A., Raissouni, N., 2000. Toward remote sensing methods for land cover dynamic monitoring: Application to Morocco. *International Journal of Remote Sensing* 2, 353-366.

Tamhane, A.C., 1977. Multiple comparisons in model I one-way ANOVA with unequal variances. *Communications in StatisticsSeries B* 9, 167–178.

Turner, D. P., Cohen, W. B., Kennedy, R. E., Fassnacht, K. S., & Briggs, J. M., 1999. Relationships between leaf area index and Landsat TM spectral vegetation indices across three temperate zone sites. *Remote Sensing of Environment* 70(1), 52-68.

Vlassova, L., Pérez-Cabello, F., Mimbrero, M., Llovería, R., García-Martín, A., 2014. Analysis of the Relationship between Land Surface Temperature and Wildfire Severity in a Series of Landsat Images. *Remote Sensing* 6(7), 6136-6162.

Volder, A., Briske, D.D., Tjoelker, M.G., 2013. Climate warming and precipitation redistribution modify tree–grass interactions and tree species establishment in a warm-temperate savanna. *Global Change Biology* 19, 843-857.

Weng, Q., Lu, D., Schubring, J., 2004. Estimation of land surface temperature–vegetation abundance relationship for urban heat island studies. *Remote Sensing of Environment* 89(4), 467-483.

Wolfe, R., Masek, J., Saleous, N., Hall, F., 2004. LEDAPS: mapping North American disturbance from the Landsat record. En: *Proceedings of the IEEE International*

Geoscience and Remote Sensing Symposium, September 19-26, 2004. Anchorage, Alaska, EUA.

Zeng, N., Neelin, J.D., 2000. The role of vegetation–climate interaction and interannual variability in shaping the African savanna. *J. Clim.* 13, 2665–2669.

10. Conclusions and future research

10.1 Main findings

The present research analyzes the potential of Landsat images as a source of land surface temperature (LST) data. Spatio-temporal patterns of LST estimated from Landsat images and their relationship with vegetation cover are studied in areas affected by forest fires and in tree-grass woodlands (dehesas) located in central and northeastern Spain. The most important results of the study are presented below:

1. Comparison of single band algorithms for LST estimation from Landsat images in Mediterranean ecosystems of dehesa:

- Single-Channel method and inversion of Radiative Transfer Equation with atmospheric correction parameters from ACPC on-line tool can be used for LST estimation from Landsat-5 TM thermal band with an error of ~1 K.

- There is a seasonal bias in the results obtained by Mono-Window method due to the worse fit of the coefficients to real atmospheric conditions in the study area.

- The best results (RMSD = 0.5 °C) were obtained using Single-Channel method. This algorithm, which does not require radiosounding data, is considered the most adequate for integration with MODIS LST product MOD11_L2.

2. Analysis of spatio-temporal patterns of Landsat LST in Mediterranean forests affected by wildfires and its relationship with burn severity

- This study generates cartography of LST, one of the parameters controlling physical processes in areas affected by wildfires, and describes relations between burn severity and post-fire vegetation recovery.

- In Las Hurdes burn (Extremadura, Spain), LST values in the zones of high burn severity were 10 °C higher than in the unburned areas. Although these differences decrease with the pass of time, they are still detectable two years after fire.

- LST contrasts in the areas of different burn severity are enhanced by the aspect and illumination geometry, being higher for the better-illuminated slopes.

3. *Analysis of the effects of different post-fire wood treatments on vegetation recovery (through NDVI) and LST*

- The study leads to the conclusion that in ecosystems highly resilient to fire, such as Pinus halepensis forests, post-fire recovery in terms of NDVI is high with or without application of active strategies for burnt wood management. However, in terms of vegetation recovery and LST distribution, statistically significant differences were observed between intervened and not intervened areas. Intervened areas showed lower levels of vegetation cover and higher values of LST. On the other hand, no statistically significant differences have been detected between the zones of two treatments.

- Remotely assessed levels of vegetation cover and LST distribution in burnt areas can be used as indicators in diagnostics of recovery and efficiency of applied treatments, since they synthesize important processes taking place in soil-vegetation-atmosphere systems.

4. *Analysis of spatio-temporal patterns of Landsat LST in Mediterranean tree-grass ecosystem (dehesa) and their relationship with vegetation fenology*

- In dehesa spatial patterns of LST depend on phenology of pasture, tree density and shadows projected by tree canopies. There is negative relation between the tree cover and LST; 0.4 ºC temperature increase is observed for each 10% of decreasein tree cover.

- In spring negative relation between LST and tree cover is less pronounced, because vegetation greenness is at its maximum. At this moment the observed rate of LST increase per 10% decrease of tree cover constitutes only 0.1 ºC.

10.2 New research lines derived from the thesis:

- Application of Landsat LST in modeling of carbon and water fluxes in heterogeneous ecosystems.

- Analyze relationship between LST, burn severity and vegetation regeneration in other ecosystems.

- Combine LST with traditional burn severity metrics in order to improve spatial differentiation of severity levels in fire-affected areas.

- Assess methods for LST estimation from Landsat images in tropical coastal ecosystems of Ecuador; combine Landsat LST with data from high-resolution remote sensing images to assess status of tropical agricultural crops.

11. Conclusiones y trabajos futuros

11.1 Principales hallazgos

La presente investigación se enmarca en el análisis del potencial de las imágenes Landsat para obtener cartografía de la temperatura de superficie (LST). Los patrones espacio-temporales de LST y su relación con la cobertura vegetal se estudian en áreas afectadas por incendios forestales y en ecosistemas de dehesa, situados en el centro y noreste de España. Los resultados más importantes de este estudio se presentan a continuación:

1. Comparación de los algoritmos de una banda para la estimación de la LST desde las imágenes Landsat en los ecosistemas Mediterráneos de dehesa:

- El método mono-banda (SC) y la inversión de la Ecuación de la Transferencia Radiativa (RTE) con los parámetros de corrección atmosférica de la herramienta web ACPC pueden ser utilizados para la estimación de la LST a partir de la banda térmica de Landsat-5 TM con el error de ~1 K.

- Existe un sesgo estacional en los resultados obtenidos por el método de mono-ventana (MW) debido al peor ajuste de los coeficientes a las condiciones atmosféricas reales en el área de estudio.

- Los mejores resultados (RMSD = 0.5 ºC) se obtuvieron con el método mono-banda (SC). Este algoritmo, que no requiere de datos de radiosondeos, es considerado el más adecuado para la integración con el producto de temperatura de superficie de MODIS MOD11_L2.

2. Análisis de los patrones espacio-temporales de la LST de Landsat en bosques mediterráneos afectados por los incendios forestales y su relación con la severidad de fuego:

- En este estudio se genera cartografía multitemporal deLST, uno de los parámetros clave en el control de los procesos físicos en las áreas afectadas por incendios, y se describen las relaciones entre la severidad del incendio y la recuperación post-incendio de la vegetación.

- En el incendio de Las Hurdes (Extremadura), en las zonas de severidad alta se registraron valores de LST hasta 10 ºC superiores a las no quemadas. Estas diferencias disminuyen con el paso de tiempo, aunque siguen siendo detectables dos años después del fuego.

- Los contrastes de LST en las áreas de diferente severidad de incendio se acentúan en función de la orientación y la geometría de iluminación, siendo más altos para las laderas mejor iluminadas.

3. Análisis de los efectos de los diferentes tratamientos post-incendio de madera sobre la recuperación de vegetación (a través de NDVI) y la temperatura de superficie:

— A partir de este estudio se concluye que en ecosistemas muy resilientes, como los bosques de *Pinus halepensis*, la recuperación post-incendio en términos de NDVI es elevada, independientemente de que se apliquen o no medidas para la gestión activa de la madera quemada. Sin embargo, en términos de recubrimiento vegetal y en relación con la distribución de la LST, se constatan diferencias estadísticamente significativas entre las áreas intervenidas y las no-intervenidas. Las últimas muestran niveles más bajos de recubrimiento vegetal y valores de LST más altos. Por otro lado, entre las zonas en las que se han aplicado los dos tratamientos no se recogen diferencias significativas.

— Los niveles de recubrimiento vegetal y la distribución de la LST en zonas quemadas, medidas mediante teledetección, pueden ser utilizados como indicadores en el diagnósticos de la recuperación y eficacia de los tipos de tratamiento aplicados, en la medida de que sintetizan importantes procesos que protagonizan las interacciones suelo-planta-atmósfera.

4. Análisis de los patrones espacio-temporales de la LST en los ecosistemas de dehesas Mediterráneas y su relación con la fenología de vegetación:

— El patrón espacial de LST depende del ciclo fenológico del pastizal, de la densidad del arbolado y de la sombraproyectada por el estrato arbóreo. Se observa un aumento de la LST de 0,4 ºC con cada disminución de 10% en la cobertura arbórea.

— In spring negative relation between LST and tree cover is less pronounced, because vegetation greenness is at its maximum. At this moment the observed rate of LST increase per 10% decrease of tree cover constitutes only 0.1 ºC.

11.2 Nuevas líneas de investigación derivadas de la tesis:

— Aplicación de los productos cartográficos de LST en los modelos de flujos de carbono y agua en ecosistemas heterogéneos.

— Análisis de la relación entre LST, la severidad de incendios y la regeneración de vegetación en otros ecosistemas.

— Combinar la LST con las métricas tradicionales para mejorar la diferenciación espacial de los niveles de severidad en áreas afectadas por fuegos forestales.

— Evaluación de los métodos para la estimación de LST a partir de las imágenes Landsat en ecosistemas tropicales de las áreas costeras de Ecuador; combinar la LST derivada de datos Landsat con los datos de los sensores remotos de alta resolución para detectar el estatus de los cultivos agrícolas tropicales

References

Ambast, S.K., Keshari, A.K., Gosain, A.K., 2008. Estimating Regional Evapotranspiration Using Remote Sensing: Application to Sone Low Level Canal System, India. Journal of Irrigation and Drainage Engineering 134, 13-25.

Anderson, M.C., Allen, R.G., Morse, A., Kustas, W.P., 2012. Use of Landsat thermal imagery in monitoring evapotranspiration and managing water resources. Remote Sensing of Environment 122, 50-65.

Anding, D., Kauth, R., 1970. Estimation of sea surface temperature from space. Remote Sensing of Environment 1, 217-220.

Anselin, L., 1988. Lagrange multiplier test diagnostics for spatial dependence and spatial heterogeneity. Geographical analysis 20, 1-17.

ASD, 2012. FieldSpec pro user's guide. ASD Inc, Boulder.

Badía, D., Martí, C., Aguirre, A.J., Aznar, J.M., González-Pérez, J., De la Rosa, J., León, J., Ibarra, P., Echeverría, T., 2014. Wildfire effects on nutrients and organic carbon of a Rendzic Phaeozem in NE Spain: changes at cm-scale topsoil. Catena 113, 267-275.

Baldocchi, D., Falge, E., Gu, L., Olson, R., Hollinger, D., Running, S., Anthony, P., Bernhofer, C., Davis, K., Evans, R., Fuentes, J., Goldstein, A., Katul, G., Law, B., Lee, X., Malhi, Y., Meyers, T., Munger, W., Occhel, W., PawU, K., Pilegaard, K., Schmid, H., Valentini, R., Verma, S., Vesala, T., 2001. FLUXNET: a new tool to study the temporal and spatial variability of ecosystem-scale carbon dioxide, water vapor and energy flux densities. Bull. Am. Meteorol. Soc. 82, 2415-2434.

Bandeen, W.R., Hanel, R.A., Licht, J., Stampfl, R.A., Stroud, W.G., 1961. Infrared and reflected solar radiation measurements from the Tiros II meteorological satellite. National Aeronautics and Space Administration.

Barsi, J.A., Barker, J.L., Schott, J.R., 2003. An Atmospheric Correction Parameter Calculator for a single thermal band earth-sensing instrument, Geoscience and Remote Sensing Symposium, 2003. IGARSS '03. Proceedings. 2003 IEEE International, pp. 3014-3016 vol.3015.

Barsi, J.A., Schott, J.R., Palluconi, F.D., Hook, S.J., 2005. Validation of a web-based atmospheric correction tool for single thermal band instruments, in: Butler, J.J. (Ed.), 1 ed. SPIE, San Diego, CA, USA, pp. 58820E-58827.

Becker, F., Li, Z.-L., 1990. Temperature-independent spectral indices in thermal infrared bands. Remote Sensing of Environment 32, 17-33.

Beers, T.W., Dress, P.E., Wensel, L.C., 1966. Notes and observations: aspect transformation in site productivity research. Journal of Forestry 64, 691-692.

Box, G.E.P., Jenkins, G.M., Reinsel, G.C., 2011. Time series analysis: forecasting and control. John Wiley & Sons.

Burrough, P.A., McDonnell, R.A., 1998. Principles of GIS. Oxford University Press, London.

Chavez, P.S., 1996. Image-based atmospheric corrections-revisited and improved. Photogrammetric engineering and remote sensing 62, 1025-1035.

Chedin, A., Scott, N.A., Berroir, A., 1982. A single-channel, double-viewing angle method for sea surface temperature determination from coincident Meteosat and TIROS-N radiometric measurements. Journal of Applied Meteorology 21, 613-618.

Choudhury, B.J., Ahmed, N.U., Idso, S.B., Reginato, R.J., Daughtry, C.S.T., 1994. Relations between evaporation coefficients and vegetation indices studied by model simulations. Remote Sensing of Environment 50, 1-17.

Chuvieco, E., 2010. Teledetección ambiental. Ariel, Barcelona, España.

Chuvieco, E., Cocero, D., Riaño, D., Martin, P., Martínez-Vega, J., de la Riva, J., Pérez, F., 2004. Combining NDVI and surface temperature for the estimation of live fuel moisture content in forest fire danger rating. Remote Sensing of Environment 92, 322-331.

Cleugh, H.A., Leuning, R., Mu, Q., Running, S.W., 2007. Regional evaporation estimates from flux tower and MODIS satellite data. Remote Sensing of Environment 106, 285-304.

Coll, C., Hook, S.J., Galve, J.M., 2009. Land surface temperature from the Advanced Along-Track Scanning Radiometer: Validation over inland waters and vegetated surfaces. Geoscience and Remote Sensing, IEEE Transactions on 47, 350-360.

Coll, C., Valor, E., Galve, J.M., Mira, M., Bisquert, M., García-Santos, V., Caselles, E., Caselles, V., 2012. Long-term accuracy assessment of land surface temperatures derived from the Advanced Along-Track Scanning Radiometer. Remote Sensing of Environment 116, 211-225.

Cooley, T., Anderson, G.P., Felde, G.W., Hoke, M.L., Ratkowski, A.J., Chetwynd, J.H., Gardner, J.A., Adler-Golden, S.M., Matthew, M.W., Berk, A., Bernstein, L.S., Acharya, P.K., Miller, D., Lewis, P., 2002. FLAASH, a MODTRAN4-based atmospheric correction algorithm, its application and validation, Geoscience and Remote Sensing Symposium, 2002. IGARSS '02. 2002 IEEE International, pp. 1414-1418 vol.1413.

DaCamara, C.C., 2006. The Land Surface Analysis SAF: one year of pre-operational activity, p. 48.

Dash, P., Göttsche, F.M., Olesen, F.S., Fischer, H., 2002. Land surface temperature and emissivity estimation from passive sensor data: theory and practice-current trends. International Journal of remote sensing 23, 2563-2594.

De Santis, A., Chuvieco, E., 2007. Burn severity estimation from remotely sensed data: Performance of simulation versus empirical models. Remote Sensing of Environment 108, 422-435.

Díaz-Delgado, R., Lloret, F., Pons, X., 2003. Influence of fire severity on plant regeneration by means of remote sensing imagery. International Journal of Remote Sensing 24, 1751-1763.

EGIF, 2008. National database of Forest Fires. Ministry of Agriculture, Spain.

French, A.N., Schmugge, T.J., Kustas, W.P., 2000. Estimating surface fluxes over the SGP site with remotely sensed data. Physics and Chemistry of the Earth, Part B: Hydrology, Oceans and Atmosphere 25, 167-172.

Gamon, J.A., Huemmrich, K.F., Peddle, D.R., Chen, J., Fuentes, D., Hall, F.G., Kimball, J.S., Goetz, S., Gu, J., McDonald, K.C., Miller, J.R., Moghaddam, M., Rahman, A.F., Roujean, J.L., Smith, E.A., Walthall, C.L., Zarco-Tejada, P., Hu, B., Fernandes, R.,

Cihlar, J., 2004. Remote sensing in BOREAS: Lessons learned. Remote Sensing of Environment 89, 139-162.

García, M., Chuvieco, E., Nieto, H., Aguado, I., 2008. Combining AVHRR and meteorological data for estimating live fuel moisture content. Remote Sensing of Environment 112, 3618-3627.

Gillespie, A., Rokugawa, S., Matsunaga, T., Cothern, J.S., Hook, S., Kahle, A.B., 1998. A temperature and emissivity separation algorithm for Advanced Spaceborne Thermal Emission and Reflection Radiometer (ASTER) images. Geoscience and Remote Sensing, IEEE Transactions on 36, 1113-1126.

Gutman, G., Ignatov, A., 1998. The derivation of the green vegetation fraction from NOAA/AVHRR data for use in numerical weather prediction models. International Journal of Remote Sensing 19, 1533-1543.

Holben, B.N., Eck, T.F., Slutsker, I., Tanre, D., Buis, J.P., Setzer, A., Vermote, E., Reagan, J.A., Kaufman, Y.J., Nakajima, T., 1998. AERONET—A federated instrument network and data archive for aerosol characterization. Remote sensing of environment 66, 1-16.

Hook, S.J., Chander, G., Barsi, J., Alley, R.E., Abtahi, A., Palluconi, F.D., Markham, B.L., Richards, R.C., Schladow, S.G., Helder, D.L., 2004. In-flight validation and recovery of water surface temperature with Landsat-5 thermal infrared data using an automated high-altitude lake validation site at Lake Tahoe. Geoscience and Remote Sensing, IEEE Transactions on 42, 2767-2776.

Houborg, R., Anderson, M.C., Daughtry, C.S.T., Kustas, W.P., Rodell, M., 2011. Using leaf chlorophyll to parameterize light-use-efficiency within a thermal-based carbon, water and energy exchange model. Remote Sensing of Environment 115, 1694-1705.

Howell, J.R., Siegel, R., Menguc, M.P., 2010. Thermal radiation heat transfer. CRC press.

Jensen, J.R., 2009. Remote sensing of the environment: An earth resource perspective 2/e. Pearson Education India.

Jia, L., Menenti, M., Su, Z.B., Li, Z.-L., Djepa, V., Wang, J.M., 2001. Modeling sensible heat flux using estimates of soil and vegetation temperatures: the HEIFE and IMGRASS experiments, in: Beniston, M., Verstraete, M. (Eds.), Remote sensing and climate modeling: Synergies and limitations. Kluwer academic publishers, pp. 23-49.

Jiménez-Muñoz, J.C., Sobrino, J.A., 2003. A generalized single-channel method for retrieving land surface temperature from remote sensing data. J. Geophys. Res. 108, 46-88.

Jiménez-Muñoz, J.C., Sobrino, J.A., Mattar, C., Franch, B., 2010. Atmospheric correction of optical imagery from MODIS and Reanalysis atmospheric products. Remote Sensing of Environment 114, 2195-2210.

Kalma, J., McVicar, T., McCabe, M., 2008. Estimating Land Surface Evaporation: A Review of Methods Using Remotely Sensed Surface Temperature Data. Surveys in Geophysics 29, 421-469.

Kaufman, Y.J., Sendra, C., 1988. Algorithm for automatic atmospheric corrections to visible and near-IR satellite imagery. International Journal of Remote Sensing 9, 1357-1381.

Kerr, Y.H., Lagouarde, J.P., Nerry, F., Ottlé, C., 2004. Land surface retrieval techniques and applications: Case of AVHRR, in: Quatrocci, D.A., Luvall, J.C. (Eds.), Thermal remote sensing in land surface processes. CRC Press, Florida, USA, pp. 33-109.

Key, C.H., Benson, N.C., 2004. Remote Sensing Measure of Severity: The Normalized Burn Ratio, FIREMON Landscape Assessment (LA) V4, Sampling and Analysis Methods. Collins, CO: USFS Rocky Mountain Research Station.

King, J.I., 1956. Scientific use of Earth satellites – "the radiative heat transfer of planet Earth". University of Michigan Press, Ann Arbor, Michigan.

Kistler, R., Kalnay, E., Collins, W., Saha, S., White, G., Woollen, J., Chelliah, M., Ebisuzaki, W., Kanamitsu, M., Kousky, V., Van der Dool, H., Jenne, R., Fiorino, M., 2001. The NCEP-NCAR 50-year reanalysis : Monthly means CD-ROM and documentation. American Meteorological Society, Boston, MA, ETATS-UNIS.

Kokaly, R.F., Rockwell, B.W., Haire, S.L., King, T.V.V., 2007. Characterization of post-fire surface cover, soils, and burn severity at the Cerro Grande Fire, New Mexico, using hyperspectral and multispectral remote sensing. Remote Sensing of Environment 106, 305-325.

Kustas, W., Anderson, M., 2009. Advances in thermal infrared remote sensing for land surface modeling. Agricultural and Forest Meteorology 149, 2071-2081.

Li, H., Qinhuo, L., Bo, Z., Yongming, D., Heshun, W., Qiao, W., 2010. A single-channel algorithm for land surface temperature retrieval from HJ-1B/IRS data based on a parametric model, Geoscience and Remote Sensing Symposium (IGARSS), 2010 IEEE International, pp. 2448-2451.

Li, Z.-L., Tang, B.-H., Wu, H., Ren, H., Yan, G., Wan, Z., Trigo, I.F., Sobrino, J.A., 2013a. Satellite-derived land surface temperature: Current status and perspectives. Remote Sensing of Environment 131, 14-37.

Li, Z.-L., Wu, H., Wang, N., Qiu, S., Sobrino, J.A., Wan, Z., Tang, B.-H., Yan, G., 2013b. Land surface emissivity retrieval from satellite data. International Journal of Remote Sensing 34, 3084-3127.

Liang, S., 2004. Quantitative Remote Sensing of Land Surfaces Wiley & Sons, Hoboken, NJ, USA

Liu, L., Zhang, Y., 2011. Urban heat island analysis using the Landsat TM data and ASTER data: A case study in Hong Kong. Remote Sensing 3, 1535-1552.

Masek, J.G., Vermote, E.F., Saleous, N.E., Wolfe, R., Hall, F.G., Huemmrich, K.F., Gao, F., Kutler, J., Lim, T.-K., 2006. A Landsat surface reflectance dataset for North America, 1990-2000. Geoscience and Remote Sensing Letters, IEEE 3, 68-72.

McMillin, L.M., 1975. Estimation of sea surface temperatures from two infrared window measurements with different absorption. Journal of Geophysical Research 80, 5113-5117.

Miller, H.M., Richardson, L., Koontz, S.R., Loomis, J., Koontz, L., 2013. Users, uses, and value of Landsat satellite imagery—Results from the 2012 survey of users. US Geological Survey Open-File Report 1269.

Moran, M., 2004. Thermal infrared measurement as an indicator of plant ecosystem health, in: Dale, A., Quattrochi, D., Luvall, J.C. (Eds.), Thermal Remote Sensing in Land Surface Processing. CRC Press, pp. 257-282.

Moran, P.A.P., 1950. Notes on continuous stochastic phenomena. Biometrika, 17-23.

Moreno, G., Pulido, F.J., 2009. The functioning, management and persistence of dehesas, Agroforestry in Europe. Springer, pp. 127-160.

Myneni, R.B., Dong, J., Tucker, C.J., Kaufmann, R.K., Kauppi, P.E., Liski, J., Zhou, L., Alexeyev, V., Hughes, M.K., 2001. A large carbon sink in the woody biomass of northern forests. Proceedings of the National Academy of Sciences 98, 14784-14789.

Nieto, H., Sandholt, I., Aguado, I., Chuvieco, E., Stisen, S., 2011. Air temperature estimation with MSG-SEVIRI data: Calibration and validation of the TVX algorithm for the Iberian Peninsula. Remote Sensing of Environment 115, 107-116.

Njoku, E.G., Barnett, T.P., Laurs, R.M., Vastano, A.C., 1985. Advances in Satellite Sea Surface Temperature Measurement and Oceanographic Applications. J. Geophys. Res. 90, 11573-11586.

Neteler, M., 2010. Estimating Daily Land Surface Temperatures in Mountainous Environments by Reconstructed MODIS LST Data. Remote Sensing 2, 333-351.

Norman, J.M., Becker, F., 1995. Terminology in thermal infrared remote sensing of natural surfaces. Remote Sensing Reviews 12, 159-173.

Noyes, E., Good, S., Corlet, G., Kong, X., Remedios, J., Llewellyn-Jones, D., 2006. AATSR LST product validation, Second working meeting on MERIS and AATSR calibration and geophysical validation. 20-24 March, 2006. ESRIN, Frascati, Italy.

Núñez Corchero, M., Sosa Cardo, J.A., 2001. Climatología de Extremadura (1961 - 1990). Ministerio de Medio Ambiente, Madrid.

Olea, L., López-Bellido, R.J., Poblaciones, M.J., 2005. European types of silvopastoral systems in the Mediterranean area: dehesa. Silvopastoralism and sustainable land management. CABI, Oxfordshire, 30-35.

Pausas, J.G., Vallejo, V.R., 1999. The role of fire in European Mediterranean ecosystems, Remote sensing of large wildfires. Springer, pp. 3-16.

Peres, L.F., DaCamara, C.C., 2004. Land surface temperature and emissivity estimation based on the two-temperature method: sensitivity analysis using simulated MSG/SEVIRI data. Remote Sensing of Environment 91, 377-389.

Prata, A.J., 1993. Land Surface Temperatures Derived From the Advanced Very High Resolution Radiometer and the Along-Track Scanning Radiometer 1. Theory. J. Geophys. Res. 98, 16689-16702.

Prata, A.J., Caselles, V., Coll, C., Sobrino, J.A., Ottle, C., 1995. Thermal remote sensing of land surface temperature from satellites: Current status and future prospects. Remote Sensing Reviews 12, 175-224.

Price, J.C., 1984. Land Surface Temperature Measurements From the Split Window Channels of the NOAA 7 Advanced Very High Resolution Radiometer. J. Geophys. Res. 89, 7231-7237.

Prihodko, L., Goward, S.N., 1997. Estimation of air temperature from remotely sensed surface observations. Remote Sensing of Environment 60, 335-346.

Qin, Z., Karnieli, A., Berliner, P., 2001. A mono-window algorithm for retrieving land surface temperature from Landsat TM data and its application to the Israel-Egypt border region. International Journal of Remote Sensing 22, 3719-3746.

Riaño, D., Chuvieco, E., Ustin, S., Zomer, R., Dennison, P., Roberts, D., Salas, J., 2002. Assessment of vegetation regeneration after fire through multitemporal analysis of AVIRIS images in the Santa Monica Mountains. Remote Sensing of Environment 79, 60-71.

Roy, D.P., Wulder, M.A., Loveland, T.R., Woodcock, C.E., Allen, R.G., Anderson, M.C., Helder, D., Irons, J.R., Johnson, D.M., Kennedy, R., 2014. Landsat-8: Science and product vision for terrestrial global change research. Remote Sensing of Environment 145, 154-172.

Rubio, E., Caselles, V., Badenas, C., 1997. Emissivity measurements of several soils and vegetation types in the 8–14, μm Wave band: Analysis of two field methods. Remote Sensing of Environment 59, 490-521.

Rulloni, V., Bustos, O., Flesia, A.G., 2012. Large gap imputation in remote sensed imagery of the environment. Computational Statistics & Data Analysis 56, 2388-2403.

Salisbury, J.W., D'Aria, D.M., 1992. Emissivity of terrestrial materials in the 8–14 μm atmospheric window. Remote Sensing of Environment 42, 83-106.

Salomonson, V.V., Barnes, W.L., Maymon, P.W., Montgomery, H.E., Ostrow, H., 1989. MODIS: Advanced facility instrument for studies of the Earth as a system. Geoscience and Remote Sensing, IEEE Transactions on 27, 145-153.

Scaramuzza, P., Micijevic, E., Chander, G., 2004. SLC gap-filled products phase one methodology. Landsat Technical Notes.

Schott, J.R., Hook, S.J., Barsi, J.A., Markham, B.L., Miller, J., Padula, F.P., Raqueno, N.G., 2012. Thermal infrared radiometric calibration of the entire Landsat 4, 5, and 7 archive (1982–2010). Remote Sensing of Environment 122, 41-49.

Snyder, W.C., Wan, Z., Zhang, Y., Feng, Y.Z., 1998. Classification-based emissivity for land surface temperature measurement from space. International Journal of Remote Sensing 19, 2753-2774.

Snyder, W.C., Zhengming, W., 1998. BRDF models to predict spectral reflectance and emissivity in the thermal infrared. Geoscience and Remote Sensing, IEEE Transactions on 36, 214-225.

Sobrino, J., Coll, C., Caselles, V., 1991. Atmospheric correction for land surface temperature using NOAA-11 AVHRR channels 4 and 5. Remote sensing of environment 38, 19-34.

Sobrino, J.A., Jiménez-Muñoz, J.C., Paolini, L., 2004. Land surface temperature retrieval from LANDSAT TM 5. Remote Sensing of Environment 90, 434-440.

Sobrino, J.A., Jiménez-Muñoz, J.C., Soria, G., Romaguera, M., Guanter, L., Moreno, J., Plaza, A., Martinez, P., 2008. Land Surface Emissivity Retrieval From Different VNIR and TIR Sensors. Geoscience and Remote Sensing, IEEE Transactions on 46, 316-327.

Sobrino, J.A., Jiménez-Muñoz, J.C., Zarco-Tejada, P.J., Sepulcre-Cantó, G., de Miguel, E., 2006. Land surface temperature derived from airborne hyperspectral scanner thermal infrared data. Remote Sensing of Environment 102, 99-115.

Sobrino, J.A., Li, Z.L., Stoll, M.P., Becker, F., 1996. Multi-channel and multi-angle algorithms for estimating sea and land surface temperature with ATSR data. International Journal of Remote Sensing 17, 2089-2114.

Sobrino, J.A., Raissouni, N., 2000. Toward remote sensing methods for land cover dynamic monitoring: Application to Morocco. International Journal of Remote Sensing 21, 353-366.

Song, C., Woodcock, C.E., Seto, K.C., Lenney, M.P., Macomber, S.A., 2001. Classification and Change Detection Using Landsat TM Data: When and How to Correct Atmospheric Effects? Remote Sensing of Environment 75, 230-244.

Storey, J., Scaramuzza, P., Schmidt, G., Barsi, J., 2005. Landsat 7 scan line corrector-off gap filled product development, pp. 23-27.

Sun, D., Pinker, R.T., 2003. Estimation of land surface temperature from a Geostationary Operational Environmental Satellite (GOES-8). J. Geophys. Res. 108, 4326.

Tang, H., Li, Z.-L., 2014. Quantitative Remote Sensing in Thermal Infrared. Springer Berlin Heidelberg.

Tapias, R., Gil, L., Fuentes-Utrilla, P., Pardos, J.A., 2001. Canopy seed banks in Mediterranean pines of south-eastern Spain: a comparison between Pinus halepensis Mill., P. pinaster Ait., P. nigra Arn. and P. pinea L. Journal of Ecology 89, 629-638.

Teillet, P.M., Barker, J.L., Markham, B.L., Irish, R.R., Fedosejevs, G., Storey, J.C., 2001. Radiometric cross-calibration of the Landsat-7 ETM+ and Landsat-5 TM sensors based on tandem data sets. Remote sensing of Environment 78, 39-54.

Thome, K.J., Crowther, B.G., Biggar, S.F., 1997. Reflectance-and irradiance-based calibration of Landsat-5 Thematic Mapper. Canadian Journal of Remote Sensing 23, 309-317.

Tobler, W.R., 1970. A computer movie simulating urban growth in the Detroit region. Economic geography, 234-240.

Townshend, J.R.G., Justice, C.O., 2002. Towards operational monitoring of terrestrial systems by moderate-resolution remote sensing. Remote Sensing of Environment 83, 351-359.

Townshend, J.R.G., Justice, C.O., Skole, D., Malingreau, J.P., Cihlar, J., Teillet, P., Sadowski, F., Ruttenberg, S., 1994. The 1 km resolution global data set: needs of the International Geosphere Biosphere Programme†. International Journal of Remote Sensing 15, 3417-3441.

Vallejo, V.R., Arianoutsou, M., Moreira, F., 2012. Fire ecology and post-fire restoration approaches in Southern European forest types, Post-Fire Management and Restoration of Southern European Forests. Springer, pp. 93-119.

Valor, E., Caselles, V., 1996. Mapping land surface emissivity from NDVI: Application to European, African, and South American areas. Remote Sensing of Environment 57, 167-184.

Van de Griend, A.A., Owe, M., 1993. On the relationship between thermal emissivity and the normalized difference vegetation index for natural surfaces. International Journal of Remote Sensing 14, 1119-1131.

Van den Hurk, B.J.J.M., Li, J., Menenti, M., 2002. Assimilation of land surface temperature data from ATSR in an NWP environment-case studies with ATSR data in Spain and The Netherlands, Geoscience and Remote Sensing Symposium, 2002. IGARSS '02. 2002 IEEE International, pp. 36-38 vol.31.

Veraverbeke, S., Verstraeten, W.W., Lhermitte, S., Van De Kerchove, R., Goossens, R., 2012. Assessment of post-fire changes in land surface temperature and surface albedo, and their relation with fire–burn severity using multitemporal MODIS imagery. International Journal of Wildland Fire 21, 243-256.

Wan, Z., Dozier, J., 1996. A generalized split-window algorithm for retrieving land-surface temperature from space. IEEE Transactions on Geosciences and Remote Sensing 34, 892–905.

Wan, Z., Li, Z.L., 2008. Radiance-based validation of the V5 MODIS land-surface temperature product. International Journal of Remote Sensing 29, 5373-5395.

Wan, Z., Zhang, Y., Zhang, Q., Li, Z.L., 2004. Quality assessment and validation of the MODIS global land surface temperature. International Journal of Remote Sensing 25, 261-274.

Westermann, S., Langer, M., Boike, J., 2011. Spatial and temporal variations of summer surface temperatures of high-arctic tundra on Svalbard — Implications for MODIS LST based permafrost monitoring. Remote Sensing of Environment 115, 908-922.

Wild, M., 2005. Solar radiation budgets in atmospheric model intercomparisons from a surface perspective. Geophysical Research Letters 32.

Zarco-Tejada, P.J., Rueda, C.A., Ustin, S.L., 2003. Water content estimation in vegetation with MODIS reflectance data and model inversion methods. Remote Sensing of Environment 85, 109-124.

Zhang, C., Li, W., Travis, D., 2007. Gaps-fill of SLC-off Landsat ETM+ satellite image using a geostatistical approach. International Journal of Remote Sensing 28, 5103-5122.

APPENDICES

Appendix A

Contribution of PhD student to the published research articles

1. Vlassova, L.; Perez-Cabello, F.; Nieto, H.; Martin, P.; Riaño, D.; de la Riva, J. (2014). Assessment of methods for land surface temperature retrieval from Landsat-5 TM images applicable to MultiscaleTree-Grass Ecosystem Modeling. Remote Sensing6, 4345-4368, DOI:10.3390/rs6054345.

As the first author of this article, Lidia Vlassova contributed to all the stages of the research, from planning and data collection to analysis of the results and writing the draft.The coauthors contributed in reviewing the results.

2. Vlassova, L.; Perez-Cabello, F.; Rodrigues Mimbrero, M.; Montorio Lloveria, R.; García-Martin, A. (2014). Analysis of the relationship between land surface temperatureand wildfire severity in a series of Landsat images. Remote Sensing 6, 6136-6162, DOI:10.3390/rs6076136.

As the first author of this article, Lidia Vlassova contributed to all the stages of the research, from planning and data processing to analysis of the results and writing the draft. The coauthors contributed in reviewing the results.

3. Vlassova, L.; Perez-Cabello, F. (2016). Effects of post-fire wood management strategies on vegetation recovery and land surface temperature (LST) estimated from Landsat images. International Journal of Applied Earth Observation and Geoinformation 44, 171-183, DOI: 10.1016/j.jag.2015.08.011.

As the first author of this article, Lidia Vlassova contributed to all the stages of the research, from planning and data collection to analysis of the results and writing the draft. Dr. Fernando Pérez Cabello is listed as a coauthor is a director of this PhD research.

4. Vlassova, L.; Rosero Tufiño, P.; Montorio Llovería, R. (2016). Variabilidad espacio-temporal de la temperatura de superficie en ecosistema de dehesa estimada mediante imágenes Landsat TM: el papel del arbolado. Geographicalia 68.

As the first author of this article, Lidia Vlassova contributed to all the stages of the research, from planning and data processing to analysis of the results and writing the draft. The coauthors contributed in reviewing the results.

Appendix B

Certifications